مدينة الملك عبدالعزيز
للعلوم والتقنية KACST

المملكة العربية السعودية

مدينة الملك عبدالعزيز للعلوم والتقنية
الإدارة العامة لبرامج المنح البحثية

المشروع البحثي التطبيقي أت -٢٨ -٩٥

دراسة النشاط الزلزالي والبركاني الحديث في حرة لونير- منطقة المدينة المنورة

التقرير النهائي المنقح

أ.د. عبدالله بن محمد العمري (الباحث الرئيسي)
د. سعد بن مقرن المقرن (الباحث المشارك)

جامعة الملك سعود

رجب ١٤٣٢ هـ - يونيو ٢٠١١ م

Kingdom of Saudi Arabia
King Abdulaziz City for Science and Technology
General Directorate of Research Grants Programs

AR – 28 - 95

Seismo-Volcanic Investigation of the Current Activity in Harrat Lunayyir, Al-Madinah Al-Munawwarah area.

REVISED FINAL REPORT

Prof. Abdullah M. Al-Amri, KSU **(P - I)**

Dr. Saad M. Al-Mogren **(Co –I)**

KING SAUD UNIVERSITY

RAJAB 1432 H – JUNE 2011 A.D

جميع حقوق الطبع محفوظة لمدينة الملك عبدا لعزيز للعلوم والتقنية. غير مسموح بطبع أي جزء من أجزاء هذا التقرير أو خزنه في أي نظام لخزن المعلومات واسترجاعها أو نقله على أي هيئة أو بأي وسيلة سواء كانت إلكترونية أو ممغنطة أو ميكانيكية، أو استنساخا، أو تسجيلاً، أو غيرها إلا بإذن من صاحب الطبع. إن كافة الآراء والنتائج والاستنتاجات والتوصيات المذكورة في هذا التقرير هي خاصة بالباحثين ولا تعكس وجهة نظر المدينة.

All Rights Are Reserved to King Abdulaziz City for Science and Technology. No Part of this publication may be reproduced, stored in a retrieval system or transmitted in any form or by any means- electronic, electrostatic magnetic tape, mechanical, photocopying, recording or otherwise - without the permission of the copyright holders in writing. All views, results, conclusions, and recommendations in this report represent the opinions of the authors and do not reflect opinions of KACST.

ACKNOWLEDGMENTS

This is the final progress report of the research project **AR-28 - 95**. The authors would like to express their thanks and gratitude to King Abdulaziz City for Science and Technology for funding this project. This work would not have been possible without the generous assistance of **KACST.**

Drs. John Roobol and Ghaleb Jarrar, the project consultants, whose expert guidance and continuing advice made this work possible. Their willingness to devote their time greatly facilitated the completion of the project we owe them a deep debt of gratitude and a great deal of thanks. Grateful acknowledgment is also extended to the anonymous referees for their helpful suggestions and criticism of previous progress reports.

Finally and most importantly, we would like to extend our sincerest thanks to Engineer Mostafa Hemeda from **KACST** and Dr. Kamal Abdulrahman from KSU for providing this project with the earthquake data collection and processing.

الملخص العربي

ينتج عن الزلازل البركانية – في الغالب- خليط من الموجات السيزمية عالية ومنخفضة التردد، والتي يمكن اعتبارها بمثابة دلائل على موعد حدوث الثوران البركاني. تتبلد هذه الإشارات في كثير من الأحيان بسبب طبيعية الأرض التي تمر فيها، لكن عندما نأتي لطبيعة الزلازل التي تحدث بالصفيحة العربية - خلال صخور متبلورة نجد أن هذه الموجات واضحة تماما. تشير الموجات منخفضة التردد والتي تم تسجيلها أثناء زلازل حرة لونيير لتدفق اللابا تحت الأرض، بينما الموجات السيزمية عالية التردد فهي تشير إلى تكسير الصخور البلورية كلما تسللت اللابا نحو السطح.

حرة لونيير منطقة بركانية بازلتية تقع في شمال غرب المملكة العربية السعودية. تدفقات اللابا بازلتية - بازانتيك التركيب، وتدفقات العصر الرباعي تتكون من بازلت أوليفينى قلوي. تحتوى حرة لونيير على ٥٠ مخروط بركاني وقد تكونت فوق الصخور المتبلورة التابعة لحقب ما قبل الكامبرى على محور يمتد شمال- جنوب.

هذه الحرة تعتبر واحدة من أصغر حقول اللابا الحديثة في المملكة العربية السعودية، ولكن تنتشر التدفقات الفردية على مسافات بعيدة من مركز الحرة، وقد وصلت هذه التدفقات إلى البحر الأحمر في مكانين. أحد هذه المخاريط يمكن أن يكون قد اندلع خلال القرن العاشر الميلادي أو قبل ذلك. يقع حقل اللابا على بعد ٢٠٠كم من مركز الأتساع التكتونى الممتد تحت البحر الأحمر، حيث يمكن للصهارة البركانية الاندفاع بامتداد حواف هذه المناطق.

بدأت فى ١٨ أبريل ٢٠٠٩ م حشود زلزالية بالحافة الشرقية من حقل اللابا الحديثة بحرة لونيير وبالقرب من مركز العيص. تم فحص صور الأقمار الاصطناعية وخرائط المغناطيسية الجوية لحقل اللابا بحرة لونيير ومقارنتها بالبيانات السيزمية والمعلومات الجيولوجية والجغرافية المتاحة عن الحرة. وتم تثبيت شبكة محلية من محطات الرصد الزلزالى حول المنطقة البركانية، والتي سجلت عدد هائل من الزلازل المحلية والتي خضعت بعد ذلك لعمليات من تحليل ونمذجة الشكل الموجي.

كانت تعتبر حرة لونيير فى الماضى حرة غير نشطة وذلك بسبب موقعها على حواف الغور القارى حيث تبعد حوالى ٢٠٠ كم عن مركز الأتساع النشط لقاع البحر الأحمر. ولكن خلال الفترة من أبريل إلى يونيو ٢٠٠٩ ضرب حرة لونيير حوالي ٣٠,٠٠٠ زلزال، كان من بينها حوالي ١٩ زلزال بقدر زلزالي أكبر من أو يساوى ٤ درجات على مقياس ريختر. وقد حدثت الهزة الرئيسية فى ١٩ مايو ٢٠٠٩م والتي تسببت في تكسير حوائط بعض المباني والمنشآت بمركز العيص، وعلى أثر ذلك فقد تم إخلاء حوالي ٤٠,٠٠٠ مواطن من المنطقة ونقلهم لمدينة ينبع والمدينة المنورة. وبعد انحسار النشاط الزلزالي بنهاية شهر أغسطس ٢٠٠٩، تم السماح للمواطنين بالعودة لمنازلهم وممارسة حياتهم اليومية.

أوضحت عمليات تحليل البيانات الزلزالية ومقارنتها بالمظاهر التركيبية بخرائط المغناطيسية الجوية والمعلومات الجيولوجية أن النشاط الزلزالي الذي حدث بحرة لونيير يعتبر من الزلزالية الضحلة، وعموما كان هناك تطابق جيد بين توزيع الزلازل مع المظاهر التكتونية العظمى بالمنطقة. يشير النشاط الزلزالي الحديث إلى

النمط الدوري فى السلوك وقد ظهر ذلك جليا على شكل دورات صغرى – وهى تمثل فترات تراكم الطاقة، ودورات عظمى تمثل انطلاقا أو تحررا لهذه الطاقة، والتي يمكنها أن تتراكم وتسبب زلازل كبيرة في المستقبل.

دلت نتائج توزيع أعماق النشاط الزلزاليفي الحرة أنه ينحصر بين ٥-١٠ كم والعمق الاخر بين ١٥-٢٠ كم. يزداد أعماق هذه الزلازل كلما اتجهنا جنوب الحرة ويقل كلما اتجهنا شمالها مع عدم تأكيد في الموقع يتراوح مابين ٠.٥ - ١.٠ كم وعدم تأكيد في العمق يتراوح مابين ٠.٨ - ١.٥ كم . تم حساب العزم الزلزالي للعواصف الزلزالية التي حدثت في الحرة من واقع السجلات الزلزالية المتوفرة وقدرت ب $M_0 = 8.64 \times 10^{24}$ داين.سم.

أظهرت المشاهدات الجيولوجية الحقلية وجود فالق يمتد بطول ٣ كم بحرة لونيير، وقد أتسع هذا التمزق ليصل طوله حوالي ٨ كم. وقد اقترحت صور الأقمار الاصطناعية الرادارية أن سبب ظهور هذا الفالق هو اندفاع اللابا لأعلى بامتداد جانبي قدره ١٠ كم.

تشير نتائج تحليل مجال الإجهاد الإقليمي- الذي تبينه القواطع الموجودة بالمنطقة- إلى أن محور الشد يمتد باتجاه شمال شرق – جنوب غرب، وهذا ما أكدته حلول ميكانيكية البؤرة للزلزال الرئيسي وعدد من التوابع والتي أظهرت تصدعا عاديا في اتجاهين هما شمال شرق – جنوب غرب و شمال غرب – جنوب شرق. تتوافق هذه الاتجاهات مع الاتجاه العام لانفتاح البحر الأحمر و يتفق أيضا مع اتجاهات التكتونية الإقليمية للغور العربي – الإفريقي، وكذلك يتطابق جيدا مع اتجاهات التشققات السطحية الخطية التي ظهرت بالمنطقة المتأثرة بالنشاط الزلزالي. وبناءا على هذه النتائج نستطيع القول أن مجال إجهاد البحر الأحمر يمتد على الأقل لمسافة ٢٠٠ كم من المحور الرئيسي للغور داخل الصفيحة العربية.

عموما، يمكن اعتبار النشاطات الزلزالية التي حدثت في أكتوبر ٢٠٠٧ و مايو ٢٠٠٩ بحرة لونيير على أنها تمثل أزمة بركانية- زلزالية. وقد أشارت دراسات سابقة على أن البداية المفاجئة للحشود زلزالية التي تحدث على أعماق ضحلة بالمنطقة التي سبق وأن تعرضت في الماضي لنشاط زلزالي قليل أو لم تتعرض نهائيا لنشاط

زلزالي، يدل على دورة جديدة من النشاط الزلزالي بالمنطقة. يمكن أن تستمر هذه الأحداث لمدة سنة أو أثنتين وبعد ذلك تموت نهائيا، أو يمكنها أن تستمر وتتصاعد إلى أن تؤدى لحدوث زلازل محسوسة ذات قدر لا يزيد عن ٥ درجات على مقياس ريختر مصحوبا بظهور طفوح بازلتية. بالإضافة إلى ذلك، إنه من المستحيل أن نؤكد بوضوح ما إذا كان هذا النشاط الزلزالي نتيجة اندفاع اللابا لأعلى بدلا من انطلاق أو تحرر الإجهاد التكتونى، على الرغم من أن زيادة الإجهاد بالقرب من منطقة النشاط الزلزالي ما من شك أنه نتيجة لتحركات اللابا السابقة.

دلت النتائج الجيوكيميائية أن تبلور الصهاره في الحرة مابين ٨٥٠ الى ١٢٠٠ درجة ولكن الطفوحات البركانية أخذت مكانها قبل تشبع الصهارة بالكلينوبايروكسين عند درجات حرارة ١١٤٠ درجة. يبدو من العلاقات بين الكالسيوم والبوتاسيوم للعينات الست أنها غنية بالكالسيوم عند درجات الحرارة العالية وأن معظم الإنسياب تعرض للتبلور الجزئي للأولوفين والبلاجيوكليز بدرجة أقل.

سبق وأن تم تعيين أعمار العينات الصخرية حيث أفادت أن أعمارها تمتد من العصرالثلاثى – العصرالرباعى. وقد أكدت هذه الدراسة أن أعمار كل العينات الصخرية ترجع للعصر الرباعى، فقد تم تحديد أعمار ٦ عينات صخرية باستخدام عنصر الأرجون المشع (Ar^{40}/Ar^{39}). تم فحص المظهر العام والخواص الفيزيائية لكل العينات، ومن ثم الأجزاء المختارة للتحليل بعنصر الأرجون، حيث كانت غالبية هذه العينات دقيقة الحبيبات بدرجة تكفى لمتطلبات عملية التشعيع. وقد كانت درجة الدقة فى تحديد الأعمار - بهذه الدراسة- مرتبطة بالكميات الصغيرة من عنصر الأرجون المشع مقارنة بالكميات الكبيرة من عنصر الأرجون الغير مشع، أو الأرجون النموذجى الموجود بكل العينات الصخرية البازلتية. كانت الاختلافات بين الأعمار والوضع الإستراتجرافى نتيجة للكميات الصغيرة من الأرجون المتراكم على فترة زمنية قصيرة جدا.

عموما، بينت هذه الدراسة أن النشاط البركاني فى حرة لونيير بدأ منذ حوالي ٥٠٠,٠٠٠ سنة، ونظرا لأنه من الضروري أن تكون هناك فترة زمنية بين أقدم وحدة صخرية (التي تنتمي للعصر الثلاثي كما

ذكر سابقا) وأحدث وحدة، فقد ظهر سطح عدم التوافق بين الوحدتين، وفى النهاية يمكننا القول بأن آخر نشاط بركاني بالمنطقة كان منذ حوالي ٥٠٠٠ سنة.

مما سبق ذكره فإن هذه الدراسة توصي بانشاء شبكة جيوديسية دائمة في مواقع شبكة الرصد الزلزالي لمراقبة اتجاه التحركات والتشوهات القشرية في الحرة على المدى البعيد وعلاقتها بمراكز التمدد في البحر الأحمر. بالإ ضافة الى ذلك وضع شبكة مكونة من راصدات ذات الحركة الارضية القوية مع محطات الزلازل للاستفادة منها في حساب علاقات التعتيم السيزمي والتسارع الأرضي لتقدير مستوى الخطر الزلزالي في المنطقة بدقة عالية.

ABSTRACT

Volcanic quakes often generate a mix of high- and low-frequency seismic waves that could yield clues as to when an eruption might occur. These signals are often dulled by the nature of the earth they pass through, but when it came to the nature of the Arabian plate earthquakes, they were detected through the crystalline rocks of the area quite clearly. The low-frequency seismic waves detected during the quakes in Harrat Lunayyir seemed to show magma flowing under the earth, while the high-frequency waves indicated fracturing of crystalline rocks as magma crept toward the surface.

Harrat Lunayyir is a basaltic volcanic field in NW Saudi Arabia. Lava flows are basaltic to basanitic in composition, and the Holocene flows are alkali olivine basalts. It contains about 50 volcanic cones that were constructed over Precambrian crystalline rocks along a N-S axis. Harrat Lunayyir is one of the smallest of the Holocene lava fields of Saudi Arabia, but individual flow lobes radiate long distances from the center of the Harrat, and flows reached the Red Sea in two places. One of the cones may have erupted around the 10th century AD or earlier. The lava field lies about 200 kilometers from the tectonic spreading center under the Red Sea. Magma can rise along the margins of such areas.

On 18th of April 2009 A.D., a swarm of earthquakes began in the eastern side of the Cenozoic lava field of Harrat Lunayyir and in the vicinity of the town of Al-Ays. Satellite imageries and aeromagnetic features of Harrat Lunayyir lava field were verified by comparison and integration from findings obtained from seismic data and from existing geologic and geographic information. A seismic sub-network was deployed around the volcanic area and local seismicity was undergo data processing and waveform modeling.

Harrat Lunayyir was previously considered inactive because of its location on the margins of the continental rift, nearly 200 kilometers away from the active center of spreading beneath the Red Sea. Pre-2009 interferograms (InSAR) show no deformation, indicating that the 2007 swarm was too small to produce detectable movements by InSAR. Between April and June 2009, more than 30,000 earthquakes struck Harrat Lunayyir, with 19 earthquakes of magnitude 4 or greater striking at the swarm's peak on May 19, including a magnitude 5.4 quake that fractured walls in the town of Al Ays and 40,000 people evacuated from the region. By August 2009, the seismic activity subsided and residents were allowed to return to their homes and daily lives.

Analysis of the seismicity data in conjunction with aeromagnetic and geologic information indicates that the seismicity is shallow and the correlation of the epicentral distribution with the major tectonic features is, in general, quite good. The recent seismic activity indicates a cyclic pattern of events consisting of seismic minima which may represent episodes of accumulation of energy, and seismic maxima which represent the release of energy that can be accumulated to cause larger events in the future.

Hypocentral distribution of swarm activities seem to be confined to 5–10 and 15–20 km depth intervals, with deeper earthquakes in the southern part of Harrat Lunayyir and shallower earthquakes in the north with uncertainty of 0.5–1 km in location and 0.8–1.5 km in depth. Seismic moment release during the entire swarm, calculated from all published earthquake catalogues, is about $M_0 = 8.64 \times 10^{24}$ dyne.cm and the stress drop ($\Delta\sigma$) is about 18.1 Bars.

Geological observations showed 3-km-long rupture had opened up in Harrat Lunayyir and widened to 8 km long. Satellite radar images suggested the most likely cause of this fault was magma intruding upward over a 10-km-long stretch. The regional stress field deduced

from the orientation of the observed dike indicates NE - SW tension, which is also implied by focal mechanism solutions which indicated normal faulting with two major structural trends of NE-SW and NW-SE. These trends are consistent with the opening of the Red Sea and with broad-scale tectonics of the Arabian-African rifting as well as in good agreement with linear surface cracking observed in the affected areas. Moreover, this shows that the Red Sea ridge stress field extends at least 200 km from the rift axis into the Arabian plate

Generally speaking, seismic activities of October 2007 and May 2009 in Harrat Lunayyir can be termed a volcano-seismic crisis. In an area where previously there has been little or no seismic activity, the sudden commencement of swarms of activity at shallow depths taken with the presence of fumaroles indicates a possible new cycle of activity. Such events can last for a year or two and then die out. Alternatively they can continue and escalate leading to felt earthquakes probably no greater than magnitude 5 and result in a basaltic eruption. In addition, it is impossible to state definitely if the seismic activity is due to magma upwelling rather than just release of tectonic stress, although any increase of stress near the present activity was no doubt caused by the earlier magmatic movements.

Geochemically, crystallization of the magmas took place at temperatures in the range of 1200 to about 850 °C. But eruption took place mostly before the magmas got saturated with clinopyroxene at about 1140 degrees. It is apparent from the plots of Ca/K that in all six samples Ca-rich phases predominate at the highest temperatures. This is a common feature in basaltic rocks. Only in sample HL-26 is there an indication that a high Ca/K phase may be correlated with a relict or older age. The other samples yield uniform apparent ages throughout their respective age-spectra in spite of the widely varying Ca/K ratios. Thus, the ages can be considered to be representative. The most primitive samples are well below the composition of primary magmas in terms of mg# and the concentration of compatible

elements (Ni, Cr). Therefore, most of the flows have suffered fractional crystallization of olivine and plagioclase to a less degree. The strong enrichment in the incompatible elements is a function of lower degree of partial melting of a mantle source that did not change over time and that lacks garnet as a residual phase; the enrichment has been furthered by fractionation. The process identification diagrams using magmatophile and hypermagmatophile elements supports the assumption that chemical variability is due to fractionation rather than different degrees of partial melting.

Prior to this study, estimates of the ages of the samples were cited as Tertiary to Quaternary. This work places the ages of all samples firmly in the Quaternary period. The $^{40}Ar/^{39}Ar$ age determination has been carried out in this study for six selected samples. The general appearance and physical characteristics of the samples have been examined, and then selected portions for argon analysis. Most of these were fine-grained enough that whole-rock fragments were chosen for irradiation. The precision of the ages calculated in this study are limited by the small amounts of radiogenic argon compared to the larger amounts of non-radiogenic, or background argon typical in basaltic whole rocks of this age. The discrepancies in ages and stratigraphic position are due to the small amounts in accumulated argon over the relatively very short period of time.

In general, this study showed that volcanic activity at Harrat Lunayyir started about 500 000 years. There must have been a substantial time between the lowest unit (which has previously assigned a Tertiary age) and youngest so that an unconformity has been developed. The last activity could have taken place at about 5000 years ago.

Generally speaking, a permanent geodetic network along with existing seismographic network is recommended in order to identify and quantify very recent neotectonic activity and thus, provide prediction of specific future event. Geodetic techniques range from ground technique using strain meters and laser-ranging devices to space technique using very-long-baseline radio interferometry (VLBI) and the global positioning system (GPS). It should also be pointed out that installation of strong ground-motion instruments will lead to better estimates of the attenuation relationships and accelerations for seismic hazard and risk assessment.

TABLE OF CONTENTS

LIST OF TABLES

LIST OF FIGURES

CHAPTER 1

INTRODUCTION

The study area is known as Harrat Lunayyir and is located NW of Al-Madinah Al Munawwarah, north of Yanbu and in the immediate vicinity of the town of Al Ays between Latitudes $25^{o}.1$- $25^{o}.17$ N and Longitudes $37^{o}.45$ - $37^{o}.75$ E, occupying a surface area of about 3575 Km^2 (Fig. 1.1). It is oriented northwest–southeast and morphologically, there are great variations in the altitudes between hills and wadies through the area (Fig. 1.2 and 1.3).

Harrat Lunayyir area is characterized by geothermally warm groundwater where temperatures up to 32 degrees Centigrade were measured in April 2007 before the earthquake swarm began. Farmers in the Harrat Lunayyir area report seeing steam in many places on cold winter mornings. The geothermal anomalies and reports of stream were first noted by Saudi Geological Survey staff in 2001. Harrat Lunayyir is therefore considered to have been active since at least 2001. The amazing amount of microseismic activity and signs of prolific volcanism (Kinkar et al. 1994; Roobol et al. 1994, Roobol and Al-Rehaili 1997) needs overall digital assessment of long-term geohazards related to volcanic, seismic and tectonic activities in the region.

On 11th October 2007 A.D. / 29th Ramadan 1428 A.H. a swarm of earthquakes began located on the immediate eastern side of the Cenozoic lava field of Harrat Lunayyir situated to the north of Yanbu and the Yanbu Industrial Estate and in the immediate vicinity of the town of Al Ays. Epicentral distribution shows two adjacent clusters each aligned NE to SW. This direction corresponds to the direction of transform faults crossing the Red Sea and offsetting the median trench and spreading axis of the Red Sea.

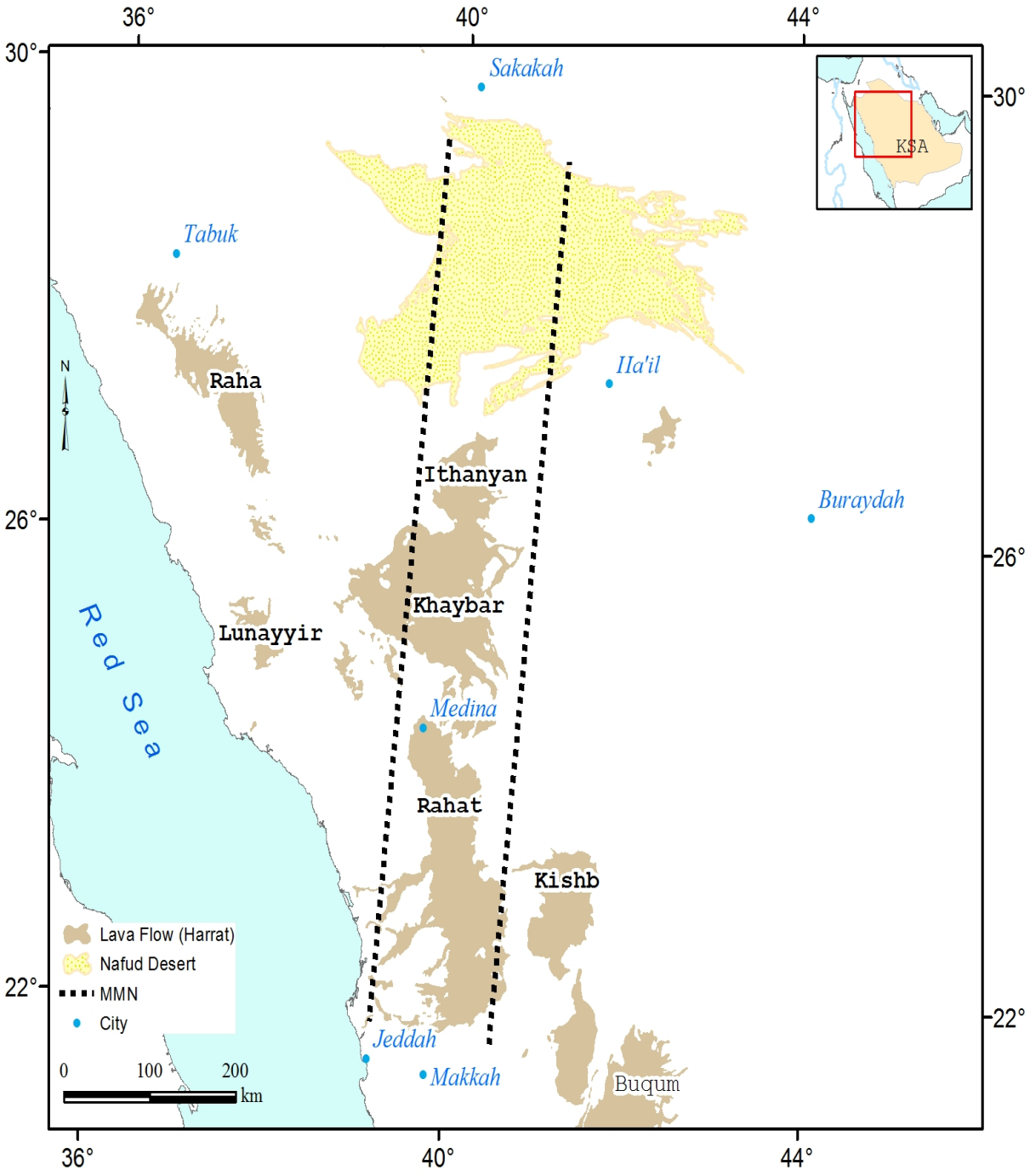

Fig. 1.1 Location map of Harrat Lunayyir and MMN line.

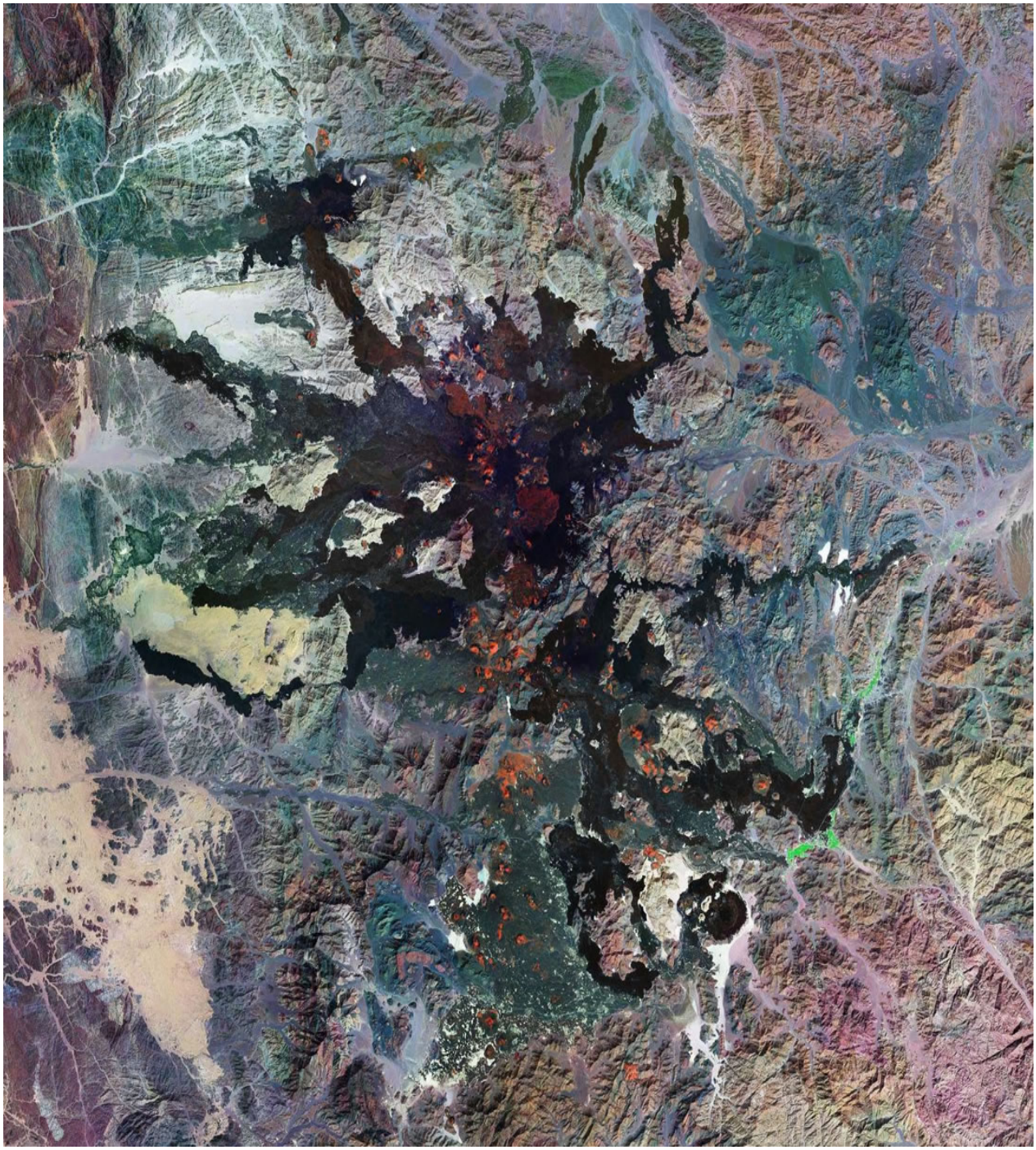

Fig. 1.2 Landsat image (Thematic Mapper) of Harrat Lunayyir volcanic area.

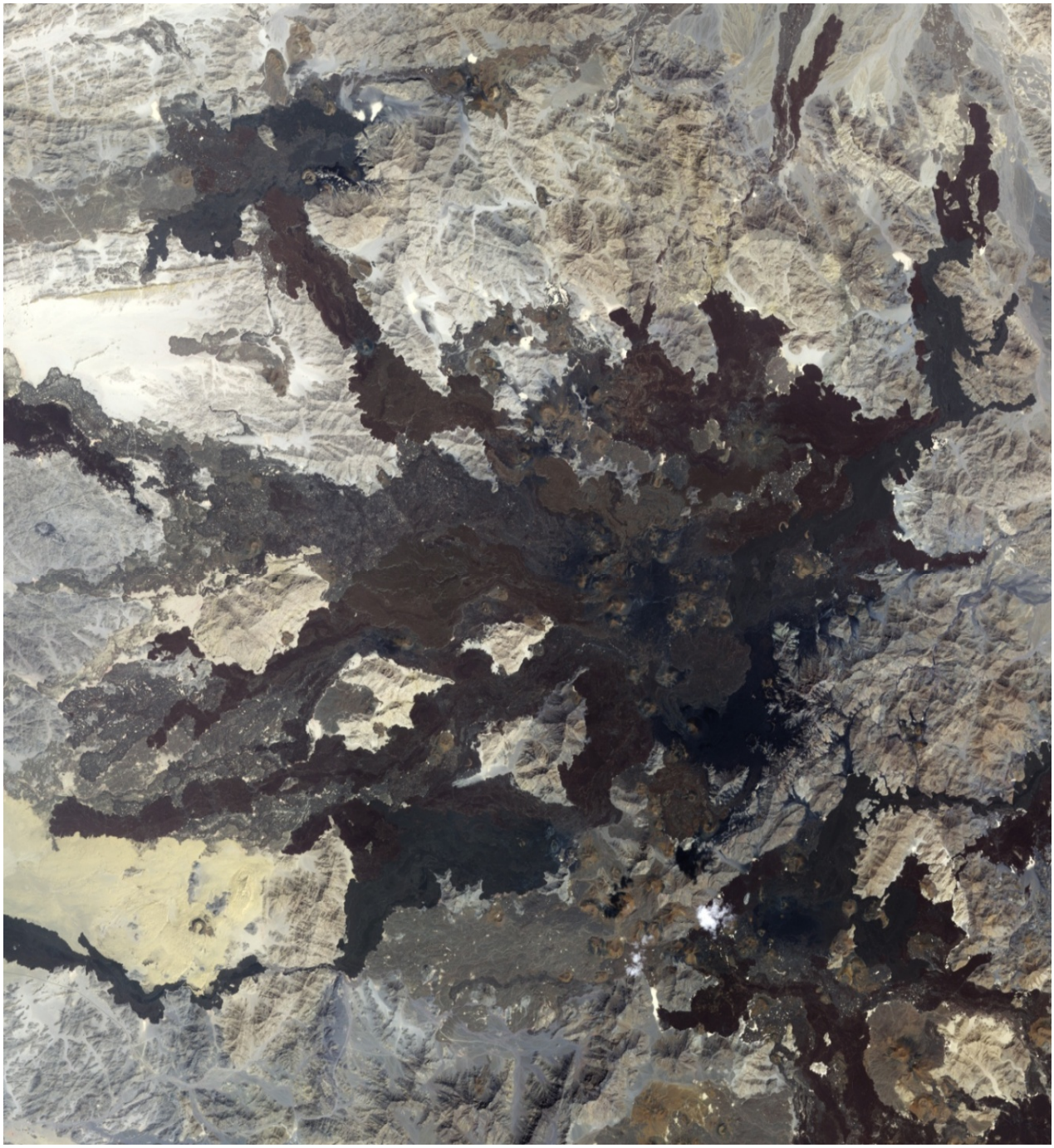

Fig. 1.3 The Advanced Space borne Thermal Emission and Reflection Radiometer (ASTER) on NASA's Terra satellite captured this false-color image of Harrat Lunayyir on October 8, 2006. The image is made from a combination infrared and visible light. Old lava flows appear as irregular, dark stains on an otherwise light-colored landscape. Like ink on an uneven surface, the lava has formed rivulets of rock that flow out in all directions.

The main cluster of epicenters corresponds to a cluster of hills composed of ancient Precambrian rocks. The hills were the site of two prehistoric basaltic eruptions as there are two chains of scoria cones sitting on top of them. One chain has five cones and the other three and both are aligned East–West.

On 19th of April, 2009 an earthquake swarm reactivated and increased gradually till its maximum on 19th of May where the main shock was occurred (M_w 5.7). The main shock was followed by great number of aftershocks with maximum magnitude (M 4.8) reported on 20 May after some hours from the mainshock occurrence. The origin of this earthquake swarm was volcano-tectonic due to the magmatic dyke intrusions into the crust (Al-Amri and Fnais 2009). This earthquake activity was close to some urban communities (e.g. Al Ays town, 40 km southeast of the epicenter). Accordingly, Saudi government evacuated more than 40,000 people (Pallister et al., 2010) from the affected region into Yanbu Al-Bahr (along the Red Sea coast) and Al-Madinah Al-Monawarah.

The researchers discovered a roughly 3-km-long rupture had opened up in the area and widened to 8 km long during the most powerful quake. Satellite radar images suggested the most likely cause of this fault was magma intruding upward over a 10-km-long stretch. Based on these findings, on June 19, 2009, the researchers forecast a moderate chance of a volcanic eruption and a low probability of magnitude 5 or greater earthquakes in the two months following.

The present activity can be termed a volcano-seismic crisis. In an area where previously there has been little or no seismic activity, the sudden commencement of swarms of activity at shallow depths taken with the presence of fumaroles indicates a possible new cycle of activity. Such events can last for a year or two and then die out. Alternatively they can continue and escalate leading to felt earthquakes (probably no greater than magnitude

5) and result in a basaltic eruption similar to that which occurred near Al Madinah city in 1256 A.D./ 654 A.H. At the Hawaiian Volcanic Observatory the passage of basalt magma has been followed as it rises from depths of around 50 km using seismometers, until an eruption commences around ten months later. Basaltic eruptions are considered the safest type of volcanic activity and do not usually involve the loss of life and the lava flows can today be diverted away from settlements by building earth banks using bulldozers. Harrat Lunayyir is today undergoing a volcano-seismic crisis which is a very unusual event in the Saudi Arabian lava field. Community awareness about the possible future volcanic activity is very low among land-use planners as well as local people. The lava field is poorly known. Due to the aforementioned points and in order to fully understand the seismicity and volcanic characteristics of Harrat Lunayyir and its relation to the spreading centers in the Red Sea.

1.1 Objectives

The main objectives of the proposed study, therefore, are to :

- *Generate and establish a preliminary integrated baseline data in volcano observation in the Harrat Lunayyir lava field composed of remote sensing imageries, existing geologic/aeromagnetic maps, and volcanic data profile from a temporary surveillance operation of a sub-network of portable seismographs. This will include the production of a geological map of the lava field.*

- *Conduct preliminary statistical study pertaining to spatio-temporal distribution of the defined micro-events when sufficient materials are available, for initial volcano assessment analysis.*

- *To carry out geothermal monitoring in the Harrat Lunayyir area, in particular looking for sudden rapid rise in ground water temperature as might preceed renewed volcanic activity.*

- *Establish a geodetic network over the seismically active area using differential GPS instrumentation with the objective of monitoring for lateral and vertical extension. Such inflation of the ground is a precursor to future volcanic activity*

- *Produce a geological map of the Harrat Lunayyir lave field and identify stratigraphy, age of past eruptions, and the mineralogy and the mineralogical and chemical characteristics of the lavas. The map will show the sites of youngest of volcanic activities which is where future activity is likely to occur. With this data an interpretation can be made of the present volcano-seismic events and their probable conclusion.*

- *Identify causes (e.g., regional tectonic stress, hot spot, volcano-tectonic, man-made, etc.) and effects (ground motion, landslides, displacement of the land surface along fault lines, etc.) of microseismicity.*

- *Suggest a mechanism for application of results and recommendations of the project. This mechanism is based primarily on the resultant models obtained from magnetic and earthquake findings.*

1.2 Literature Review

The Arabian Peninsula presents several interesting seismological problems. On the west, rifting in the Red Sea has split a large Precambrian Shield. Active rifting is responsible for the geometry of the plate margins in the west and southwest. To the south, similar rifting running in a more east-west direction through the Gulf of Aden has separated the Arabian Peninsula from Africa. In the northwest, the Gulf of Aqabah forms the southernmost continuation of the Dead Sea transform. The northern and northeastern boundaries of the Arabian Plate are areas of continental collision, with the Arabian Plate colliding with the Persian Plate (Fig. 1.4).

The western part of the Arabian Shield is made up of three major accreted tectonostratigraphic terranes (Asir, Jeddah and Hijaz) consisting mainly of variously metamorphosed layered volcano-sedimentary assemblages of older Baish, Bahah and Jeddah groups (950-800 Ma) and younger Halaban (Hulayfah) and Al Ays groups (800-650

Ma old: e.g.,) with arc-related plutonic rocks of diorite to tonalite compositions, which generally have intrusive relationship with the volcano-sedimentary sequences (Stoeser and Camp 1985, Johnson 2000). The Cenozoic to Recent basaltic lava fields (harrats) of Saudi Arabia are resting directly on the so-called stable Precambrian Arabian Shield.

The Red Sea is a region of current tectonic activity where continental lithosphere is being rupture to form oceanic lithosphere. Opening of the Red Sea split the Arabian-Nubian Shield. While much work has been done to understand the uplift and volcanism of the Arabian Shield little is known about the structure of the underlying upper mantle. The Arabian Shield consists of at least five Precambrian terranes separated by suture zones. During the late Oligocene and early Miocene, the Arabian Shield was disrupted by the development of the Red Sea and Gulf of Aden rifts, and from the mid-Miocene to the present, the region experienced volcanism and uplift. The uplift and volcanism are generally assumed to be the result of hot, buoyant material in the upper mantle that may have eroded the base of the lithosphere (Camp and Roobol, 1992). However details about the nature of the upper mantle, such as its thermal and compositional state, are not known. The Arabian Peninsula contains extensive Cenozoic lava fields of about 180,000 km^2, forming one of the largest alkali basalt provinces in the world. The presence of lava fields in western Saudi Arabia, from Yemen in the south up to Syria in the north (Camp and Roobol 1989), and with the historical records of volcanic eruptions (Ambraseys 1988) can be considered as an indication of the future possibility of recurring volcanic hazards in the western region of the Kingdom.

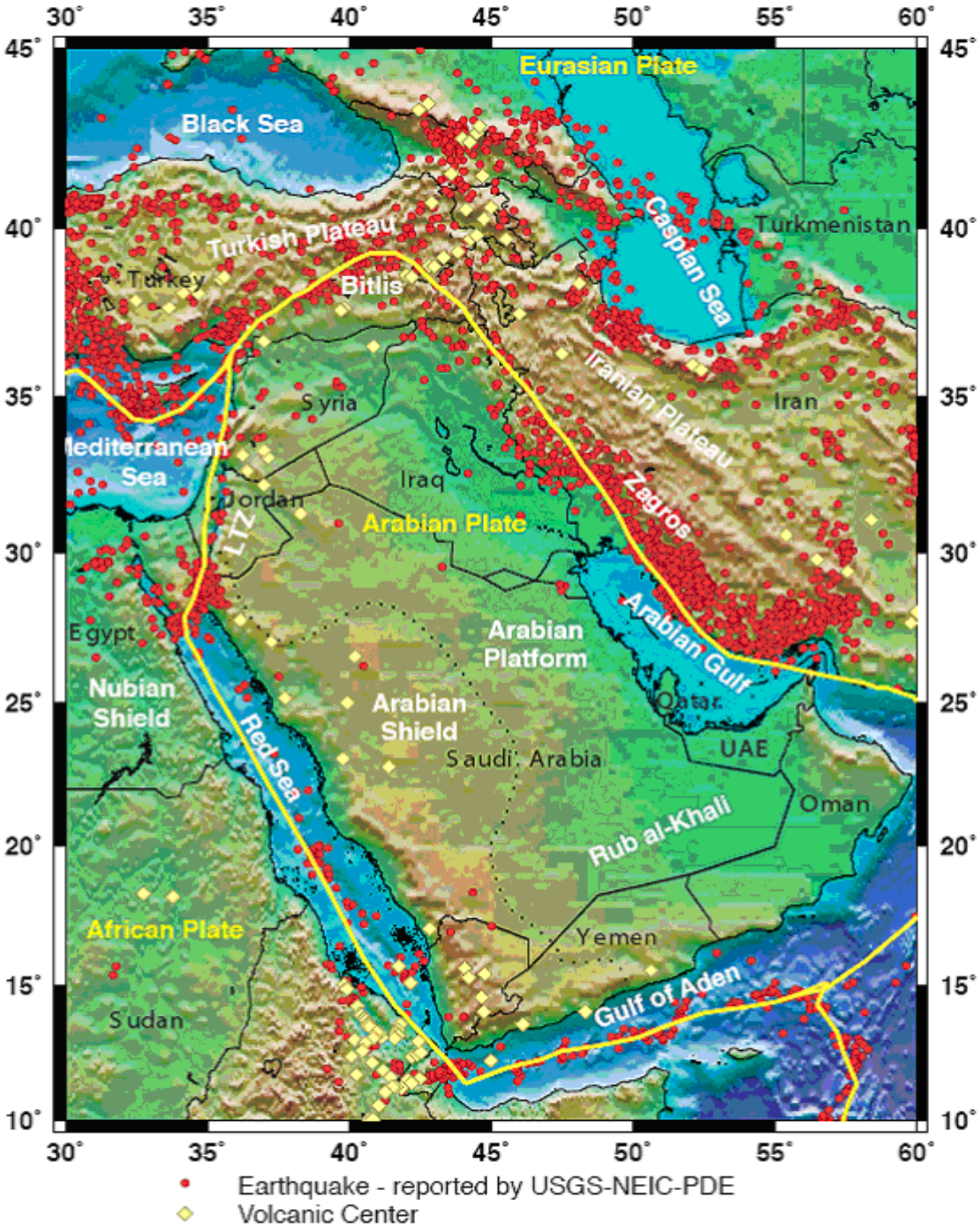

Fig. 1.4 Tectonic map of the Arabian Plate boundaries showing the distribution of seismicity and volcanic centers marked in red and yellow respectively.

Historical records of seismic (Poirier and Taher 1980; Barazangi 1981) and volcanic activity suggest that within plate volcanism has resulted in at least 21 eruptions in the Arabian Peninsula during the past 1500 years (Camp et al. 1987) including one on Harrat Lunayyir about 1000 years ago. The eruption in 1256 near the holy city of Madinah, Saudi Arabia is of particular historical and futuristic importance, for the lava flowed to within 8 km of the ancient city (Camp et al 1987). Some volcanoes which are thought to be dormant over the years become active again, and these pose danger to the environment and to the foreseeable urbanization of nearby areas. This observation among dormant volcanoes may also happen in the northern part of the Harrat Rahat and Harrat Lunayyir lava field so that basic preparations are required to be done to mitigate the imposing danger. To minimize the future probable disastrous effects of this geologic hazard in this area, it is imperative that precautionary measures and basic preparations for the minimization of losses be undertaken as early as possible.

The origin of the seismic waves from volcano activities can be attributed to two fundamentally different sources (Zobin 1979). These are the pressure variations associated with the unsteady fluid flow of magma and volatiles generating volcanic tremors, and the stress changes by sudden dislocations of shear/tensile cracks within the rigid parts of the volcanoes causing volcanic earthquakes. Volcanic tremors were first studied with eruptions at Mt. Vesuvius (1855) in Italy. Decades of major eruptions: Mt. St. Helens (1984), USA; Izu-Oshima (1986), Japan; Mt. Etna (1989), Italy; and Mt. Pinatubo (1991), Phil., etc have shown that volcanic tremors are always associated with any eruptive volcanic activity. Earthquakes and volcanic actions have always been linked. Frequently, volcanic eruptions are reported to have been preceded by strong earthquakes or earthquake swarms occurring in a focal zone which is assumed to be common for the driving mechanism of

earthquakes and eruption, but seldom in the reverse order. In a gross scale, many volcanoes are clearly connected to rift or Benioff zones, and volcanic belts follow seismifocal zones. However, tectonic earthquakes in these zones are not related to the immediate behaviour of volcanic activities. No physical processes can be specified which might be common in the crust and mantle for the occurrence of earthquakes and volcanic eruptions. But the pattern of the seismic activity close to a volcano are in space and in time among the strongest concomitants of present and future eruptive activity.

The application of remote sensing to the lava fields of Saudi Arabia has been realized on Harrat Rahat (Camp and Roobol, 1991), Harrats Khaybar, Ithnayn and Kura (Roobol and Camp, 1991a) and Harrat Kishb (Roobol and Camp, 1991b). No such study has yet been made of Harrat Lunayyir and there is no detailed geological map of the lava field.

Satellite imagery maps of the lava fields in western Saudi Arabia particularly in the northern part of Harrat Lunayyir can be verified and identified possibly through volcano monitoring data coupled with existing geologic and geographic information in this area.

The existence of mantle plume beneath the western part of the Arabian plate including Al-Madinah Al-Munawwarah region including Harrat Lunayyir has been recognized (e.g., Moufti and Hashad 2005, Al-Damegh et al. 2005, Julia et al. 2003, Benoit et al. 2003, Daradich et al.2003). About 600 km long Makkah-Madinah-Nafud (MMN) active volcanic line, consisting of Harrats Rahat, Khaybar, and Ithnayn, is the surface expression of the plume-related ocean-island basalt (OIB) volcanism (e.g., Moufti and Hashad 2005) and northward propagating nascent rift system (Camp and Roobol 1992). The last two historic volcanic eruptions, close to the city of Al-Madinah Al-Munawwarah occurred at about 641 A.D. and then again at 1256 A.D. Since 1985, instruments have recorded frequent seismic

activity within and around the City of Al-Madinah Al-Mounwwarah, especially the recent 1999 earthquake swarms (SGS 2005) and the ground deformation (Kinkar et al. 1994b). The signs of geothermal anomalies such as fumarolic emission and elevated well-water temperature within the City limits and also on Harrat Lunayyir also indicate the dynamic role of mantle plume occurring beneath the Harrat Al-Madinah (Roobol et al. 1994) and Harrat Lunayyir.

Plume dynamic beneath the western Arabian plate will be inferred the geologic mapping, structural, geochronological (e.g., relative dating of lava flows using stratigraphy, cinder cone geomorphology, radiometric (Ar-Ar) age determination), geophysical (e.g., paleomagnetism, seismic, gravity leveling, GPS geodetic) and geochemical (major and trace elements and isotopic ratios of He, Sr, Nd, and Pb) studies of the volcanic rocks of Harrat Al-Madinah, adjacent remnants of Harrat Ishara-Khirsat and Harrat Lunayyir. We will integrate all new and existing geological, structural, geochronological, geophysical and geochemical data and apply GIS methodology to create and analyze dynamic digital datasets and maps, reports, and various processes of plume dynamics and related geohazards on the surface including recurrence rate of volcanism.

Results of Hansen et al. (2006) indicate that the observed splitting parameters are the result of a complex interaction of mantle flow in the asthenosphere. Shear caused by the absolute plate motion, which is directed approximately 40° east of north at about 22 mm/yr, may affect the alignment of mantle minerals. However, it has also been suggested that flow radiating from the mantle plume beneath Afar is channelized towards the Red Sea Rift, which is oriented approximately 30° west of north. Assuming that the strain caused by the plume flow is comparable to that of the plate motion, they we combined these two flow orientations, similar to the vector approach of Silver and Holt (2002). This gives an overall

resultant that is oriented with a north-south alignment. Hansen et al. (2007) indicate that the motion is slightly more westerly, and Red Sea Rift parallel, fast directions, is the alignment of magma filled cracks that form perpendicular to the least compressive stress direction resulting in rift parallel fast polarization directions. This mechanism has been suggested as the dominant cause of anisotropy beneath other rift zones.

Al-Amri et al. (2008) suggest that low velocity beneath the Gulf of Aqabah and southern Arabian Shield and Red Sea at depths below 200 km are related to mantle upwelling and seafloor spreading. Low velocities beneath the northern Arabian Shield below 200 km may be related to volcanism. The low velocity feature near the eastern edge of the Arabian Shield and western edge of the Arabian Platform could be related to mantle flow effects near the interface of lithosphere of different thickness.

The results for crustal structure (Al-Amri et al. (2008) are consistent with previous studies where applicable. Their results for the lithosphere suggest that the mantle lithosphere is thin and the LVZ is significant near the Red Sea, where rifting is active. The mantle lid thickens away from the Red Sea in the Arabian interior. Furthermore our results indicate the presence of polarization anisotropy in the lithospheric upper mantle, in the vicinity, as well as farther away from the Red Sea. (Al-Amri et al. (2008) suggests $v_{SV} > v_{SH}$ in the southern part of the Red Sea, consistent with vertical flow, and $v_{SH} > v_{SV}$ in the northern part of the Red Sea and the continental interior, as is commonly reported in the continents. The Moho appears to be gradational, but the crustal thickness does not exceed 40 km, which is consistent with v_p/v_s analysis and inconsistent with a grid search analysis for receiver functions fits only. The mantle velocities are consistent with stable continental values.

More recently, Pallister et al. (2010) documented a surface fault rupture of 8 km long with 91 cm of offset in Harrat Lunayyir and modeled as surface deformation by the shallow intrusion of a north-west trending dyke that is about 10 km long. Seismic waves generated during the earthquakes exhibit overlapping very low- and high-frequency components. They also interpreted the low frequencies to represent intrusion of magma and the high frequencies to represent fracturing of the crystalline basement rocks. Rather than extension being accommodated entirely by the central Red Sea rift axis. Moreover, they suggested that the broad deformation observed in Harrat Lunayyir indicated that rift margins can remain as active sites of extension throughout rifting. Their analyses allowed them to forecast the likelihood of a future eruption or large earthquake in the region and informed the decisions made by the Saudi Arabian government to return the evacuees.

CHAPTER 2

GEOLOGIC & TECTONIC SETTING

The western part of the Arabian Shield is made up of three major accreted tectonostratigraphic terranes (Asir, Jeddah and Hijaz) consisting mainly of variously metamorphosed layered volcano-sedimentary assemblages of older Baish, Bahah and Jeddah groups (950-800 Ma) and younger Halaban (Hulayfah) and Al Ays groups (800-650 Ma old: e.g.,) with arc-related plutonic rocks of diorite to tonalite compositions, which generally have intrusive relationship with the volcano-sedimentary sequences (Stoeser and Camp 1985; Johnson 2000).

The great Lava Fields or harrats of flood basalt erupted on the western Shield during the Late Oligocene and Early Miocene at the same time a 2,000 km long continental rift valley developed along the future Red Sea axis. During the late Early Miocene time, the Red Sea opened at a rate of 4.4 cm/yr in the first stage movement while continental dikes and swarms of oceanic tholetiitic dikes, gabbro, and granophyres plutonic rocks were intruded into the rift sedimentary and volcanic rocks at the newly formed continental margin.

Geologically, Harrat Lunayyir is a very young volcanic region composed of late Neogene and Quaternary basaltic lavas and pyroclastics directly overlying deeply eroded Neoproterozoic rocks of the Arabian Shield (Johnson, 2005). The basement rocks surrounding Harrat Lunayyir belong to two different lithostratigraphic units: Midyan terrane located NW and Hijaz terrane in SE (Johnson, 1998). A complex of fault-bounded belt of ultramafic to mafic ophiolitic rocks known as Jabal Wask ophiolite lay between these two terranes and make the Yanbu suture.

The oldest lavas of Harrat Lunayyir, most probably Pliocene in age (Fig.2.1). The younger Quaternary lavas are much fresher, black in color and show a rugged surface topography that is unaffected by erosion. These younger lavas were erupted during at least five stages of volcanic activity. The first two stages produced very fluid basic lavas, which were able to travel long distances (more than 30 km), while the last three stages erupted more viscous and more felsic lavas that are lighter in color, and which cover a more restricted area. The fourth episode was associated with additional explosive activity which gave birth to numerous cinder cones formed from pyroclastics deposits.

The Precambrian rocks that crop out in the area of investigation include the following units:

- The Farri group. This unit appear in the map as patches and isolated outcrops, the Farri group is comprised of lavas, tuff, clastic sediments and limestone.
- Al Ays group out crops in the northern part of the study area. It is composed of gneisses and schist.
- Haja complex. The rocks of Haja complex are found in the northeastern portion of the area. The complex which is a layered is ultramafic consists of dunite, chromitite lenses, pyroxenite, layered gabbro and unlayered gabbro with trondjehmite.
- The post tectonic intrusive rocks.

The Cenozoic to Recent basaltic lava fields (harrats) of Saudi Arabia are resting directly on the so-called stable Precambrian Arabian Shield. Harrat Lunayyir is characterized by Cenozoic flood basaltic flows which can be differentiated into different cycles of metamorphism and tectonism with variable intensities during Tertiary-Quaternary age. It was suffered from series of volcanic eruptions that took place along related fissures and cinder cones forming a zone of N-S and NW-SE trends. Magmatic lavas reached the ground

surface through the prevailing deep crakes and fissures. These basaltic flows have exposed throughout western Saudi Arabia since Miocene time and extend to about 150-200 km inland from the Red Sea coast.

Tectonically, Harrat Lunayyir was affected by two episodes of tectonic movements synchronized with the Red Sea floor spreading through pre-early Miocene rifting period (Girdler 1969). Furthermore, it is controlled-to great extent-by the regional stress regime of the western Arabian plate associated with the Cenozoic development of the Red Sea. Harrat Lunayyir probably faulted during Cenozoic rift time where the up arching period was parallel to the Red Sea coast. During Late Miocene – Pliocene, the alkalic basalt invaded into the Harrat Lunayyir. According to the above-mentioned, there are different fault trends prevailing the area and oriented NE- SW, NNW-SSE, and NW-SE. (Fig. 2.1).

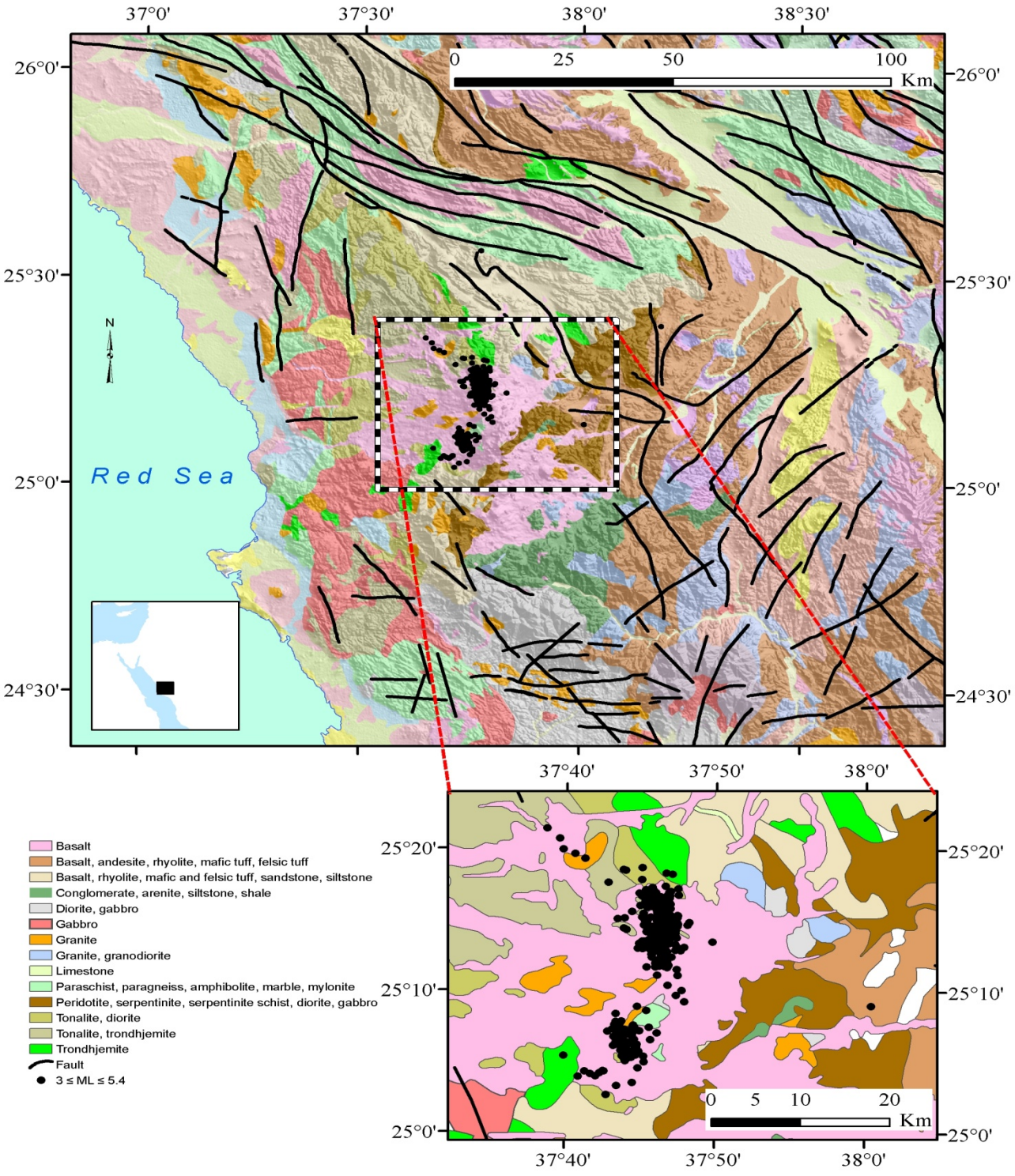

Fig. 2.1 Geotectonic map of the NW Arabian Shield. The map shows different geologic units along with structural lineaments and epicentral locations.

Detailed geological investigation is shown on Fig. 2.2 (Part 1, II and 111). The Precambrian rocks occupy the north and the south parts together with the eastern periphery of the mapped area. In the central zone the Precambrian rocks form isolated inliers. During volcanic activity episodes the relief of the Precambrian rock was high enough to hinder the basalt flow westwards. Detailed investigation of the basalts lead to the identification of the following succession :

5- Historic to Late Prehistoric lava flows.
4- Prehistoric lava flows and scoria cones.
3- Non eroded lava flows and scoria cones.
2- Eroded lava flows and scoria cones.
1- Eroded lava flows
Unconformity
Tertiary basalt.

LUNAYYIR STRATIGRAPHY

The dominantly basaltic lavas of Harrat Lunayyir have been divided on lack of erosion and erosional characteristics into two major units – an older Tertiary unit – the Jarad basalt, and a younger Quaternary unit – the Magrah basalt. The Jarad basalt (stratigraphic code Tj) is named after a large area of eroded Tertiary basalt with a prominent eroded red scoria cone of Jabal Abu Jarad which rises to 1169 m (1:50,000 topographic sheet Hirad No. 3724-11). The Maqrah basalt (stratigraphic code Qm) is named after a large area of Quaternary basalt (which may be the historic eruption of around 1000 AD and is named Harrat Maqrah on 1:50,000 topographic sheet Abar Al Hurayyidah – No. 3725-22). The Quaternary Maqrah basalt has been subdivided into five stratigraphic subunits, Qm1 and Qm2 forming the Lower Maqrah basalt and Qm3, Qm4 and Qm5 forming the Upper Maqrah basalt. The characteristics of the stratigraphic units are summarized below in stratigraphic order.

QUATERNARY UPPER MAQRAH BASALT (lacking erosion)

Qm5 Historic to late prehistoric lava flows and scoria cones. The subunit comprises the products of four eruption sites of black scoria cones with lava flows with surrounding mantles of black air fall ash still covering adjacent steep hillsides often of Precambrian basement standing through the lava field. One of these sites is believed to have erupted in the 10th Century, about 1000 years ago (Catalogue of the Active Volcanoes of the World, Part XVI Arabia and the Indian Ocean - International Association of Volcanology, 1963). The present field study suggests this is most likely Harrat Maqrah but care needs to be exercised as all older cones nearby are mantled in air fall ash and look like the youngest cone which can be distinguished by a ring of large rounded cannon-ball basaltic bombs around its base.

Qm4 Prehistoric lava flows and scoria cones, lacking erosion, dust ponds to 3m in diameter. Very black color on aerial photographs and satellite images.

QUATERNARY LOWER MAQRAH BASALT (with erosion)

Qm3 Non-eroded lava flows, slight gulling on scoria cones, dust ponds up to 100m in diameter.

Qm2 Eroded lava flows and scoria cones, surface structures on flows such as flow ridges intact, but erosional rivulets are present. Scoria cones have distinct gullies and dust ponds are up to 400m in diameter.

Qm1 Eroded lava flows, surface structures on flows are removed by erosion, but edges of flows are distinct. Scoria cones are deeply eroded but the craters remain distinct.

UNCONFORMITY (with laterite surface)

TERTIARY JARAD BASALT

Tj Deeply eroded and smoothed lava flows, individual flows no longer distinct. Scoria cones are deeply eroded to red scoria interiors with craters indistinct or removed by erosion.

SEDIMENTS

Qal Wadi gravels

Qe Aeolian sands

Qsb Sabkah/ dust pond

QTu Quaternary to Tertiary terrace deposits of rounded boulders , gravels and sand.

PRECAMBRIAN SHIELD

Pc Upper Proterozoic metavolcanic rocks and plutons mainly granitic. These rise as rugged hills around and through the lavas of Harrat Lunayyir. Scoria cones are commonly found on the tops of granite hills with lava flows draping the sides of the hills. The light colored granite hills clearly show their remnant mantles of black basaltic air fall ashes from the historic to late prehistoric eruptions.

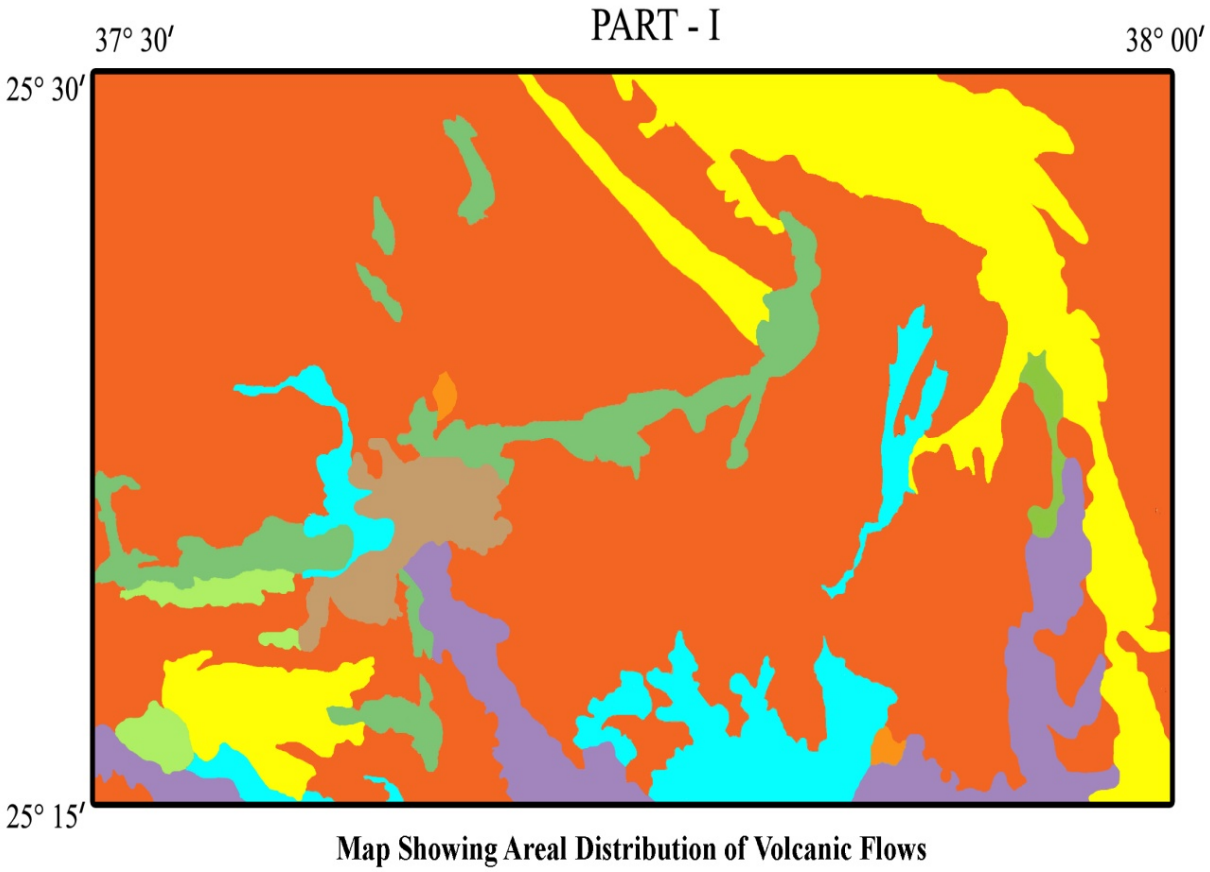

Fig. 2.2 Geological maps of harrat Lunayyir show areal distribution of volcanic flows (Part 1, II and 111). The Precambrian rocks occupy the north and the south parts together with the eastern periphery of the mapped area.

PART - II

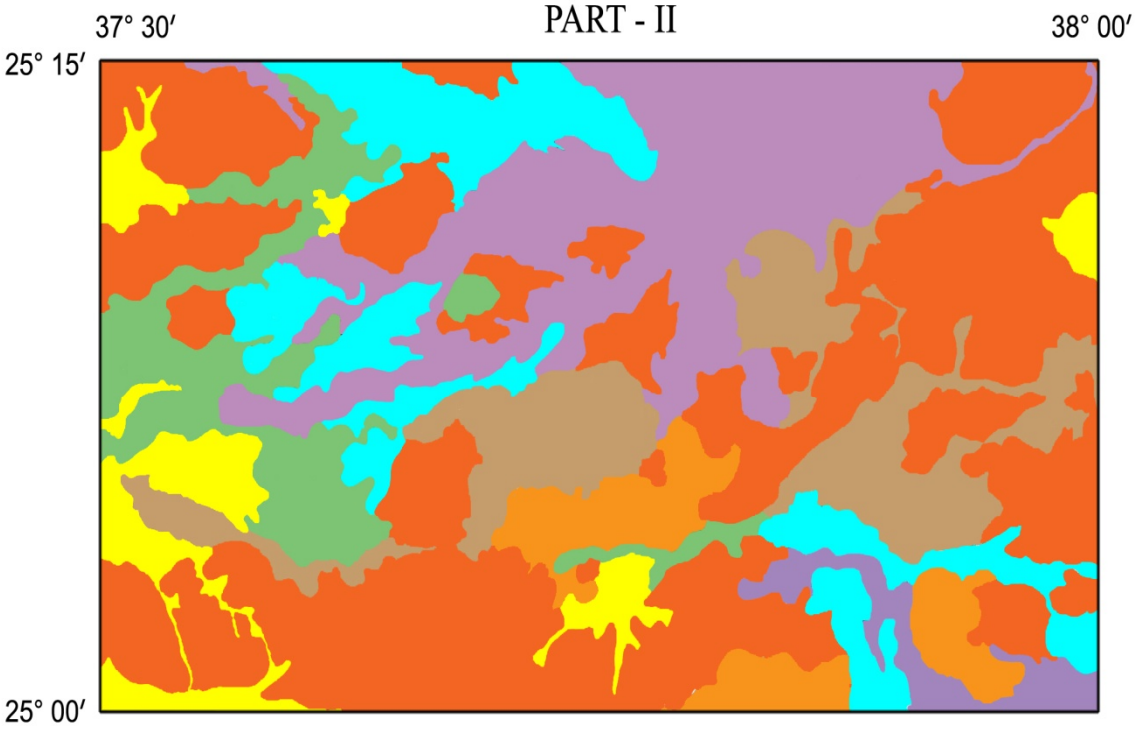

Map Showing Areal Distribution of Volcanic Flows

PART - III

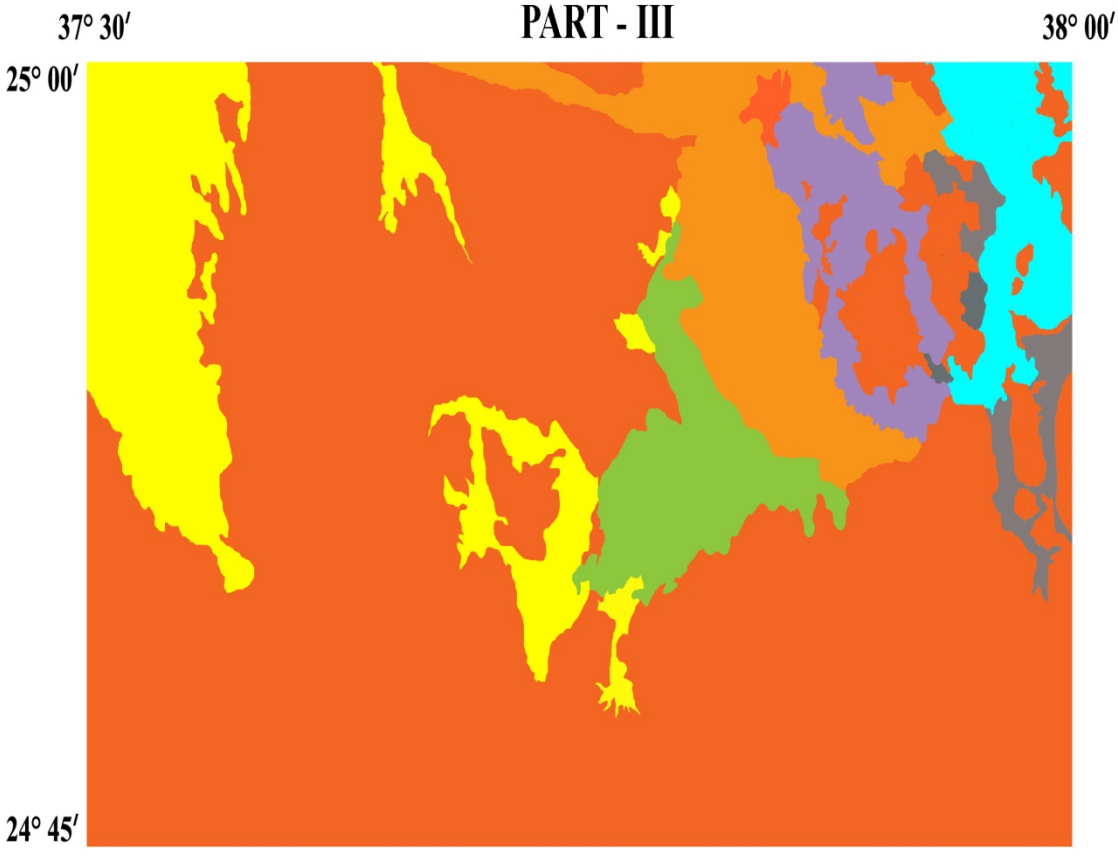

Map Showing Areal Distribution of Volcanic Flows

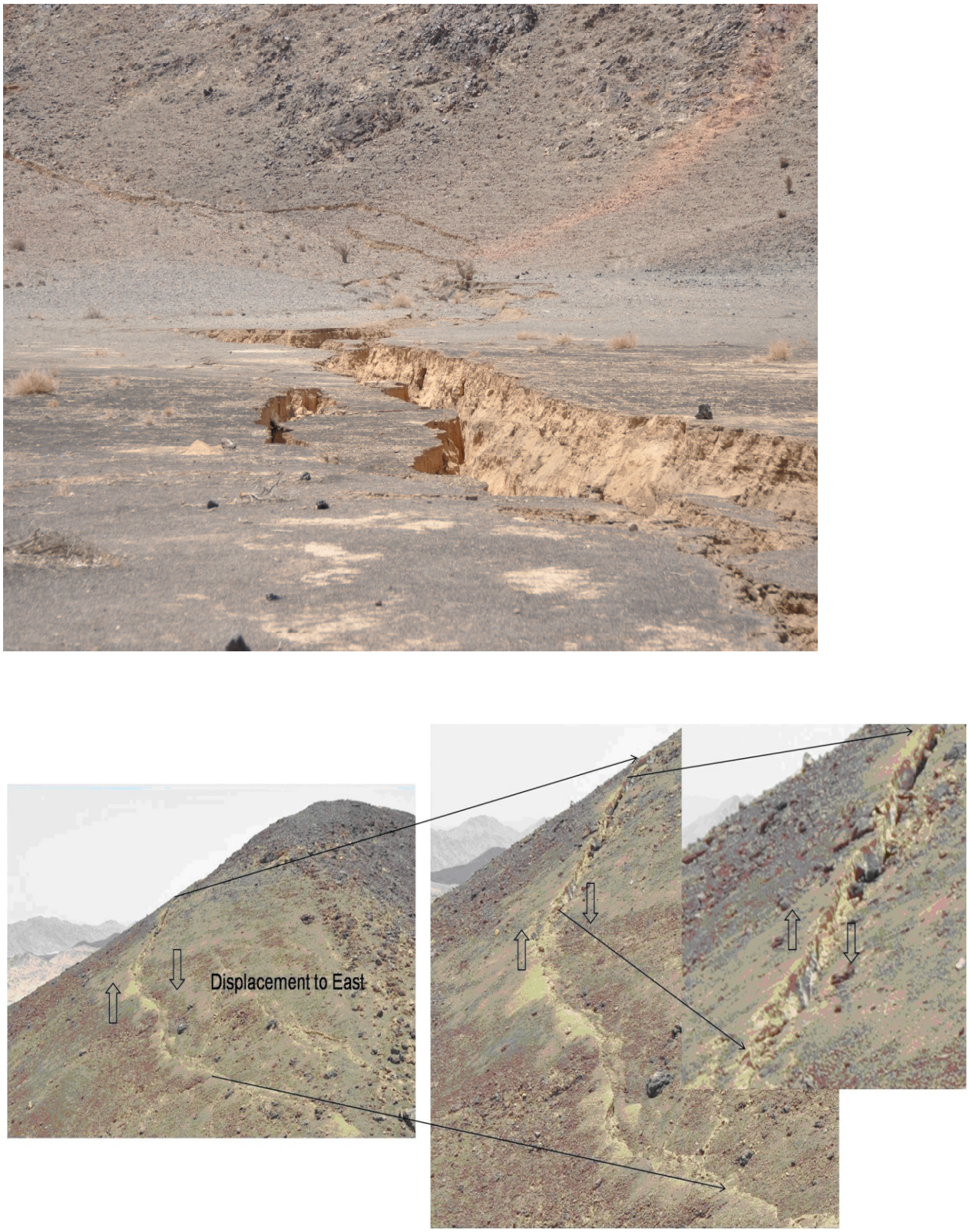

Fig. 2.3 Surface fault ruptures formed in Harrat Lunayyir during the earthquake swarm. The ground displacements in the soft sediments of the foreground are greater than in basement rocks of the background.

2.1 InSAR Observations in Harrat Lunayyir

A number of satellite radar interferograms (InSAR) of seismic activities have been analyzed for two different periods: the first one was approximately one year prior the main event and the second one within aftershock sequences using C-band with a wavelength of 5.7 cm. Pre-2009 interferograms show no deformation, indicating that the 2007 swarm was too small to produce detectable movements by In SAR. To investigate the relationship between old and new structural tectonics in harrat Lunayyir, SRTM maps along with Landsat images with 15 m resolution were analyzed as well. Unpublished report carried out by Saudi Geological Survey and US Geological Survey in June 2009 on applications of InSAR and SRTM on Harrat Lunayyir is available at SGS and in Appendix E.

Interferograms spanning the activity in April-May of 2009 exhibit strong deformation that extends across a large 40 km x 40 km area, showing over a meter of SW-NE extension. (Jonsson et al., 2010). In addition, the data show clear signs of surface faulting and graben-like subsidence in the middle of the deformed area with the graben subsidence exceeding 50 cm. Extensive faulting can be seen in the field, at least on the southwestern side of the graben, showing normal faulting of almost 1 meter in some places (Jonsson et al., 2010). They believe that the deformation appears to be caused by a near-vertical dike intrusion with a NW-SE orientation, parallel to the Red Sea rift, and the intruded volume is of the order of 0.1 cubic km. The dike triggered faulting on graben-forming normal faults. The shallowest part of the dike appears to have reached within only 2-3 km of the surface, right below where the graben is the narrowest and under an area with a number of cinder cones from previous volcanic events. Geological observations showed a roughly 3-km-long rupture had opened up in the area and widened to 8 km long during the swarm activity (Fig. 2.3).

Satellite radar images suggested the most likely cause of this fault was magma intruding upward over a 10-km-long stretch.

Baer and Hamiel (2010) combine Interferometric Synthetic Aperture Radar (InSAR) measurements and elastic modelling with seismic moment calculations to resolve the evolution of surface deformation associated with Harrat Lunayyir. Phase discontinuities and low-coherence lineaments are used to infer the location of the main active structures during the various deformation stages and descending-track interferograms that span the entire period are inverted to resolve the slip and opening distributions along two graben-bounding normal faults and a dyke, respectively. Assuming negligible rift-parallel displacements, they combine ascending- and descending-track interferograms to derive the vertical and rift-perpendicular deformation, which add up to a maximum surface extension of 1.5 m across the rift and subsidence of 0.8 m. The far-field deformation is dominated by the dyke opening, whereas the near-field displacements are mostly associated with movements along the faults. The deformation during the rifting event was controlled by an ~12-km long dyke, with maximum thickness of 2.5 m, and two normal faults that bound a wedge-shaped graben above the dyke.

Baer and Hamiel (2010) believe that Harrat Lunayyir event is juvenile in the sense that rifting is still limited to a single volcanic edifice, extension rate is low and the crust is only slightly attenuated, yet the shallow faults and the low seismic / geodetic moment partitioning indicate that some progress towards maturity has already been made.

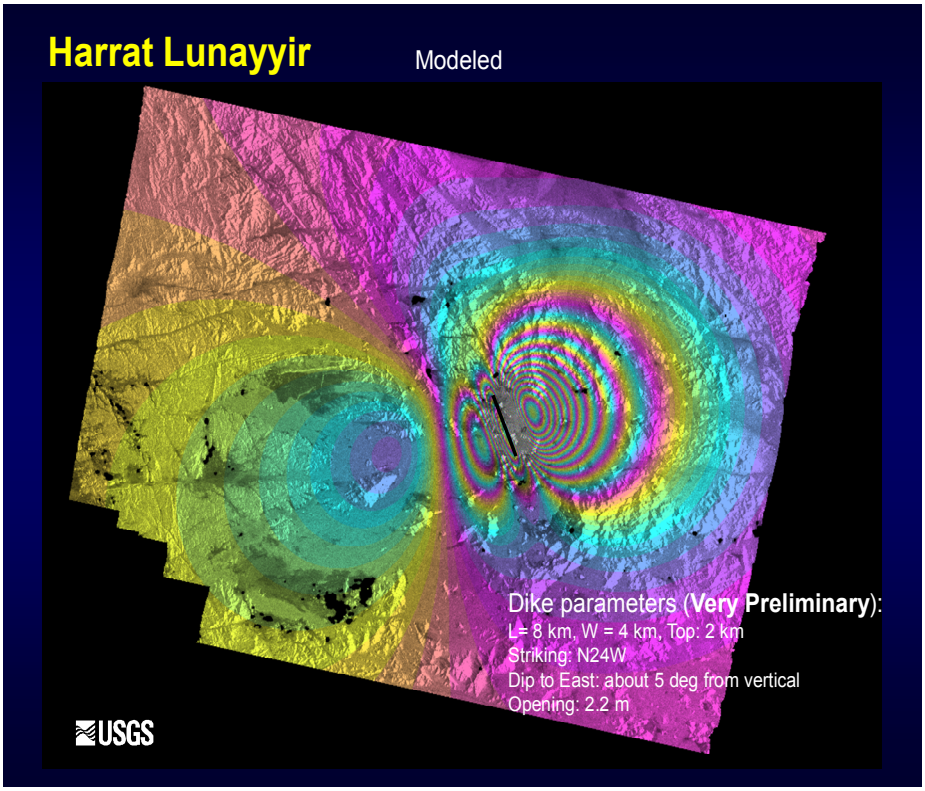

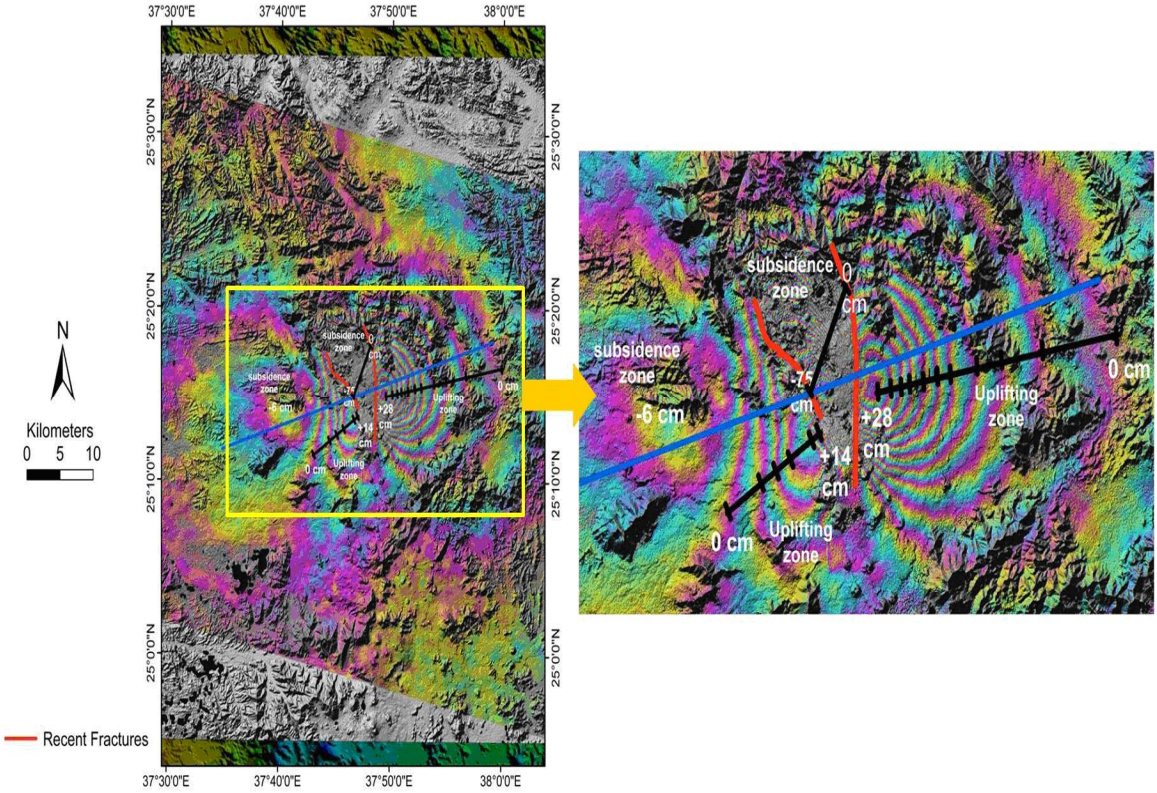

2.4 Analysis of Interferograms (InSAR) for Swarm activity in Harrat Lunayyir (SGS, 2009)

CHAPTER 3

PROCESSING OF AEROMAGNETIC DATA

The study area is covered by two aeromagnetic surveys. This chapter describes the process of integrating the two surveys into a single coherent highest resolution grid for these data (200m) and describes also the generation of the regional total magnetic intensity (TMI) grid its transformation to reduced to pole (RTP), and the tracing of maxima of the Tilt derivative of the RTP, for the purpose of evaluating the tectonic fabrics of the Al Ays area.

Data Acquisition

Aeromagnetic of Al Ays and Area 2 surveys were flown in 1962 and 1965 respectively by Hunting Geology and Geophysics Ltd., Lockwood Survey Corp. Ltd. and ARGAS using Fluxgate Gulf Mark 3 Magnetometers., using Fluxgate Gulf Mark III magnetometers with analogue recording. Al Ays and Area 2 surveys were flown with the same flight line direction N. 30° E. but at different altitude Al Ays 150 meter above ground level while Area 2 survey were flown at 300 meter above ground level. The two magnetic coverage for this study and the outline of the individual surveys are shown in Fig. 3.1.

Data Corrections

The Saudi Arabian Ministry of petroleum provided data used in this study as a digital data base of flight lines. The geomagnetic and the diurnal variation corrections were already applied to the data. However, the data in their original form lack the quality needed for advanced computer processing. Therefore, the aeromagnetic surveys have been enhanced using various methods including editing to correct some flight lines, continuation to a

common height (150m above ground level), and decorrugation to reduce line to line leveling errors. Data were provided in geographical co-ordinates referenced to the Saudi Arabia datum "Ain el Abd 1970", therefore it was necessary in some stages of the processing to re-project the data to UTM coordinates, which was essential for magnetic filtering applications such reduction to pole (RTP) and decorrugation. Flight lines for each survey were visualized and corrected using Geosoft Oasis-Montaj™ 6 software.

Gridding

Each individual aeromagnetic survey was gridded by Nearest Neighbours gridding algorithm included in the Intrepid™ 4 software with a cell size of approximately 1/4 and 1/3 of the line spacing. (i.e. cell size ranges from 500 meter to 200 meter). Grids were constructed from the traverse line data by first running Intrepid Nearest Neighbors Initial gridding which uses a mathematical interpolation/extrapolation process to calculate values for the cells within the edge regions and also within enclosed gaps and uses two-point and three-point planar interpolation (triangulation method). For image smoothing refinement the Laplace convolution and Minimum Curvature were applied.

The Nearest Neighbors gridding involves a radial search that seeks at most, three well conditioned observations nearest to each grid node. However, for the Nearest Neighbors to work perfectly and for some methods of micro leveling oblique traverse lines must be rotated to north-south or east-west direction. The Intrepid gridding function makes a number of passes through the grid. It works along the rows of the grid one by one starting alternately at the most northerly row working south and the most southerly row working north. For blank cells, Nearest Neighbors gridding locates nearby original data cells and uses a triangulation process to calculate values. When it locates a neighboring original data

cell, it records this for the blank cell. On the first pass through the grid, Nearest Neighbors gridding searches for original data cells that are immediate neighbors. On subsequent passes, it searches for original data cells one cell further away each time from the blank cell. This process is called shelling. Nearest Neighbors gridding searches a minimum of 20 shells around each cell. When Nearest Neighbors gridding has recorded three neighboring original data cells for a blank cell, it immediately locates all blank cells whose nodes lie within the triangle formed by the three original data points.

Nearest Neighbors gridding interpolates values for all cells within the triangle and marks all of the cells in the triangle as processed. Nearest Neighbors gridding uses an 'honour original data' process for this interpolation, since it uses the actual positions of the original data points rather than their cell nodes. One of the advantages of the Nearest Neighbors gridding is avoiding aliasing, which is a traditional problem in gridding geophysical data that occurs when the sample density along lines is greater than the line spacing leading to effects such as ellipsoidal between lines in gridded data.

Decorrugation

Each individual survey has been decorrugated to remove line-to-line leveling errors, which are visible as linear anomalies parallel to the flight lines see Fig. 3.2. Corrugation is a low amplitude component of flight line noise still remaining in the aeromagnetic survey data after tie line leveling. These residual errors show significant streaking or corrugations when the grid is visualized and amplified with shading artifacts. If uncorrected then the computation of derivatives becomes dominated by these line-orientated noise effects.

Therefore the gridded dataset should be filtered to reduce or remove non-geological effects caused by long-wavelength noise along survey lines. Some sources of corrugations are not

very clear, however, in this study the most important source of errors in the aeromagnetic data is due to line to line differences in flying heights. Other sources of errors may arise from; inaccuracy in the measured positions of crossover points of acquisition and tie lines. If an error arises here, it may introduce an error covering a region that extends one line spacing in each direction. The dimensions of this region would therefore be twice the tie line separation by twice the acquisition line separation. A further error could arise from inadequate compensation for the magnetic field resulting from the aircraft. Corrugation also occurs if the (time-varying) diurnal fluctuations are not accurately measured at the base station, thus affecting part of the measurements along an acquisition line. Finally, corrugation can occur when adjacent flight lines are in opposite flight directions. Although the contractor performed standard compensation and diurnal corrections and leveling, the rugged terrain and widely spaced tie lines prevented complete removal of flight line noise.

In this study micro leveling were performed using a combination of Naudy non-linear filter and the Fuller hanned band pass convolution filter that works in the space domain and is implemented by the Intrepid™ software. The mechanism of Decorrugation by Naudy-Fuller filters is that after removing the noise and spikes from the flight line data and gridding the individual aeromagnetic surveys (with rotating the flight line if they are oblique in direction to E-W or N-S directions), an input grid for the decorrugation tools is produced. Grids were decorrugated using Intrepid™ Decorrugation tools, which were designed to remove anomalies (in these case errors) with precisely defined characteristics, and to specify corrections for corrugation. These corrections do not remove geophysical information related to the geology since they extract residual errors with: the longest possible wavelength along the flight lines, the shortest wavelength perpendicular to the lines and the smallest dynamic range.

In this study, the filter parameters applied a width twice the flight line spacing and length of at least twice the tie line spacing. However due to the nature of some of the aeromagnetic surveys data sets of this study the width had in some cases to be increased but not to exceed 25 % of the suggested length (Table 3.1). The theory behind the above filter parameters is that a corrugation caused by differences between acquisition lines should have a wavelength of twice the acquisition line spacing. Corrugations can also be caused by errors in tie line leveling. If crossover points between tie line and acquisition line have errors then the total extent of the corrugation may extend as far as the next tie line on each side. Thus, the corrugation must have a length (wavelength) of at least twice the tie line spacing.

This decorrugation method utilizes two types of filter: a high pass and low pass filters. The high pass filter is applied perpendicular to the acquisition lines direction, whereas the low pass filter is applied in the acquisition line direction. The aeromagnetic data have been decorrugated by applying the Naudy filter (Dreyer and Naudy, 1968) first followed by a Fuller filter (Fraser et al., 1966) for the high pass filter, and smoothed Fuller for the low pass filter as it will remove any introduced high frequency noise. Decorrugation by this method (Fig. 3.3) removes almost all corrugations and produces well leveled grids.

Table 3.1 Filters parameters used in Naudy-Fuller decorrugation.

Area name	Flight line spacing (m)	Minimum Streak length (m)	Streak width (m)	Dynamic range	
				Minimum adjustment	Maximum adjustment
Area 2	800	10000	2000	-100	100
Al 'Ays	500	6000	1300	-30	30

Survey Merging

It is necessary for data processing and regional interpretation to compile the two separate aeromagnetic surveys of the study area to create a single regional grid. However, the grids of the aeromagnetic data, exhibit mismatch in the overlap area shown in Fig. 3.2, caused by many factors such as time of acquisition, flight altitude, flight line orientation, line spacing. In this study merging or stitching of the grids were made by Intrepid™ Grid_Stitch tools, which enable rapidly combine gridded data sets with high quality results, as seen in , and smoothing the join between the grids so that it becomes invisible during further visualization and geophysical analysis. However, before merging the aeromagnetic surveys into one grid some surveys were downward continued to 150 m. Downward continuation increased signal amplitude at the higher frequency end of the power spectrum, therefore downward continuation was applied using the spectral domain filter (GridFFT) included in the Intrepid™ package which provides a stable downward continuation as it uses damping factor that rolls off the higher frequencies using a low pass Butterworth filter.

The procedure applied to create a single mosaic grid was achieved by first gridding the individual survey data, decorrugation, continuation of each survey grid to 150 m above ground, and finally adjusting surfaces of the grids along the junction with the adjacent grids and correcting the differences along grid edges. To generate unified regional grid, grids must have the same datum, projection and effective overlaps between them.

During stitching of the aeromagnetic grids, surveys needed to be adjusted by adding a correction to the entire grid that needed adjusting and not just along the overlap area. This was done by performing least squares fit of a polynomial along the difference in overlap sample points between the grids. This polynomial was then used to adjust the whole grid. The final stitching stage that was performed was an edge feathering convolution process,

which is a process of iterative local grid smoothing using a 3x3 Laplace convolution kernel and smoothing the seam area using minimum curvature.

Maps Productions

The final merged grid was converted to Arc/info grid for further visualization and mapping. In order to produce a shaded relief image the aeromagnetic grid was processed by Geosoft software. Shading technique produces a grid (shaded grid) with values ranging from 0 to 255 by obtaining an artificial illumination of a surface by determining illumination value for each cell in grid. This is obtained by setting a position for an artificial light source and calculating the illumination values of each cell in relation to neighboring cells, the color shaded relief image was produced by placing the aeromagnetic grid over the created shaded relief grid, then making the aeromagnetic grid transparent.

Output shaded map very effectively highlights trends and pattern in the gridded data that are oriented perpendicular to the direction of illumination. The shaded relief method accentuates the shorter-wavelength components of the data and delineates faults, contacts, folds and other local structures that are associated with horizontal variations in physical properties. This is illustrated in the color shaded relief aeromagnetic map illuminated with azimuth 45° and altitude 45° seen in Fig. 3.3

Reduction to Pole (RTP)

The utility of magnetic data for geologic interpretation is complicated by the fact that, unlike gravity anomalies, magnetic anomalies are usually not located directly above their sources. This is due to the induced magnetization being a vector quantity aligned with the geomagnetic field, resulting in a dipole field whose amplitude and phase vary with latitude. Therefore, a reduction to pole approach has been performed on the magnetic data in order

to reposition the magnetic anomalies directly over their respective sources. This makes anomalies appear to be due to vertical dipole rather than inclined dipole, which can simplify the interpretation of the data (Fig. 3.4).

RTP transforms the total magnetic intensity data to represent an induced magnetic field of 90^{o} inclination. RTP requires knowledge of both the ambient field and source body magnetization directions and makes the simplifying assumption that the rocks in the survey area are all magnetized parallel to the earth's magnetic field (induced magnetization). This is true in the case of rocks with an induced magnetization only, however remnant magnetization will not be correctly dealt with if the direction of eminence is different to the direction of the earth's magnetic field. RTP of bodies with remnant magnetization will result in inclined dipolar anomalies that can be easily identified. Also the RTP transformation is unstable close to the magnetic equator ($<10^{o}$ declination). This is due to the dominance of the horizontal magnetic field vector over the vertical magnetic field vector and often results in N-S trending smearing of the RTP anomalies. However, it is possible to apply correction that prevents this amplification of the north-south anomalies in the data.

The aeromagnetic grid was reduced to pole using the MAGMAP tools of Oasis Montaj™ applying IGRF 1963 parameters. The following formula was applied for RTP;

$$L(\theta) = \frac{1}{[\sin(I_a) + i\cos(I)\cos(D-\theta)]^2} \; if\,(|I_a| < |I|), I_a = I$$

Where

I geomagnetic inclination

I_a inclination for amplitude correction (never less than I)

D geomagnetic declination

$L(\theta)$ Direction of the wave number vector in degrees azimuth

The resultant RTP grid reveals more geological structures and better correlates with geological maps, also it appears that the majority of the magnetic anomalies are induced. This confirms the results of the paleomagnetic investigations carried out by Gettings and Andreasen (1982) and Kellogg and Beckmann (1982). They showed that the direction of the thermo-remnant magnetization (TRM) is close to the Earth's present normal and reverse magnetic field.

Tilt Derivative

Here is a simple method to generate the Tilt derivative (TDR) which was first reported in 1994 but updated by Verduzco et al. (2004). In this study the Tilt derivative was very efficient in mapping weak/subtle magnetic anomalies (Fig.3.5)

The simplified formula of the TDR of the RTP is

$$TDR = \tan^{-1}\left[\frac{VDR}{THDR}\right]$$

Where VDR and THDR are the first vertical derivatives and total horizontal derivatives respectively of the RTP. While VDR can be positive or negative, the THDR is always positive. TDR tends to equalize the amplitude output of RTP anomalies which due to the arctan function restrict amplitudes to values between + π/2 and – π/2 regardless of the amplitudes of the VDR or THDR, another advantage of the TDR is its abilities to discriminate between signal and noise apart from the unlikely case when the noise has similar spectral content to the signal.

Automatic Lineaments Detection

Automatic lineaments extracting for gridded potential field data was proposed by Blakely and Simpson (1986). The routine works by passing a window over a grid and extracting the grid peak (maxima) values for a set of directional criteria. In this study automatic lineaments were extracted from the tilt derivative of TMI using Ridge-Grid of Getgrid™ software (Fig. 3.6). The resulted grid is created as 'flag grid' mode and data were converted to vector format using Arcscan™ (raster to vector conversion extension of ArcGIS 9.3™).

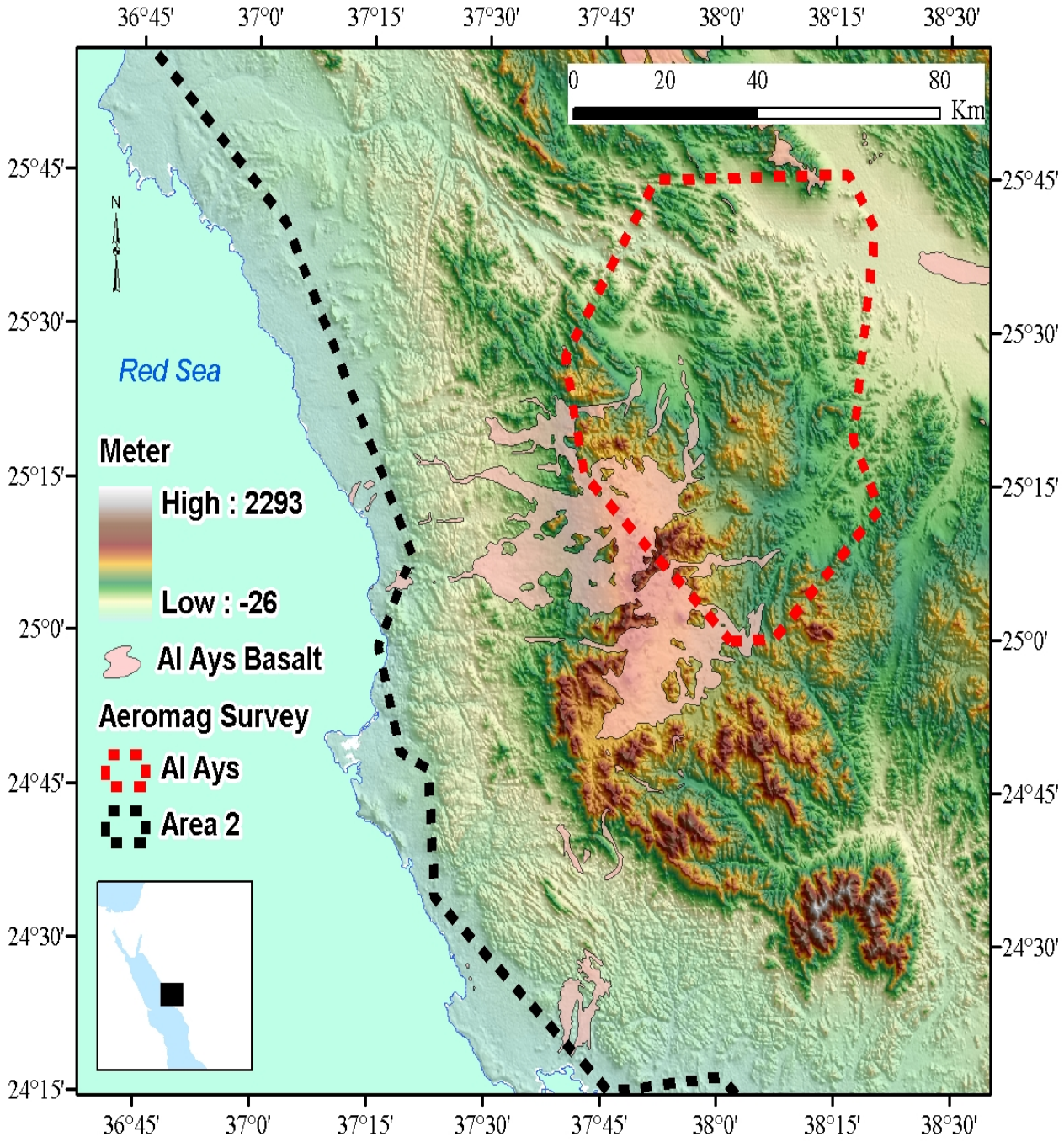

Fig. 3.1 Topography map shown aeromagnetic surveys outlines of Al Ays area.

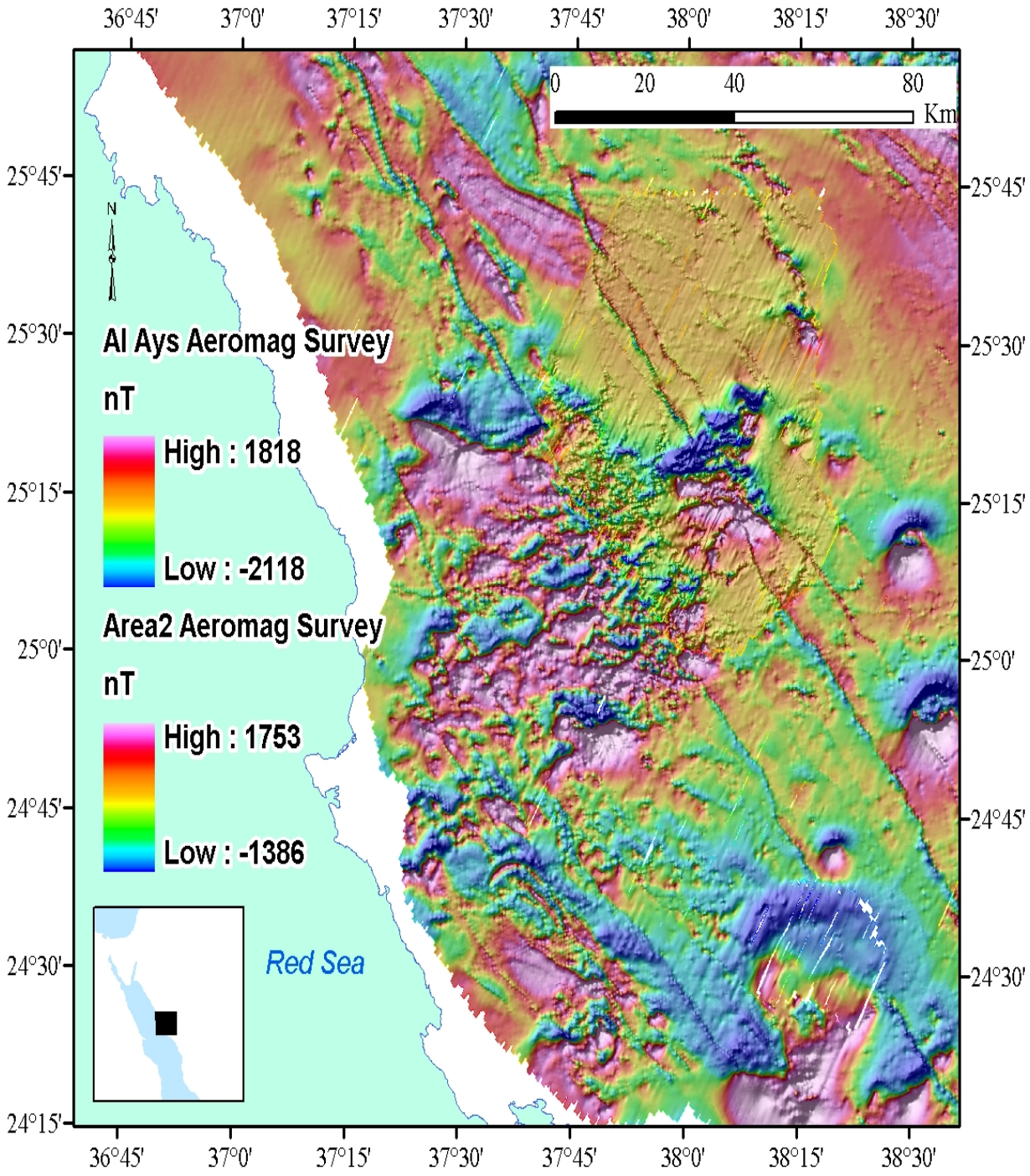

Fig. 3.2 Aeromagnetic surveys before merging and micro levelling.

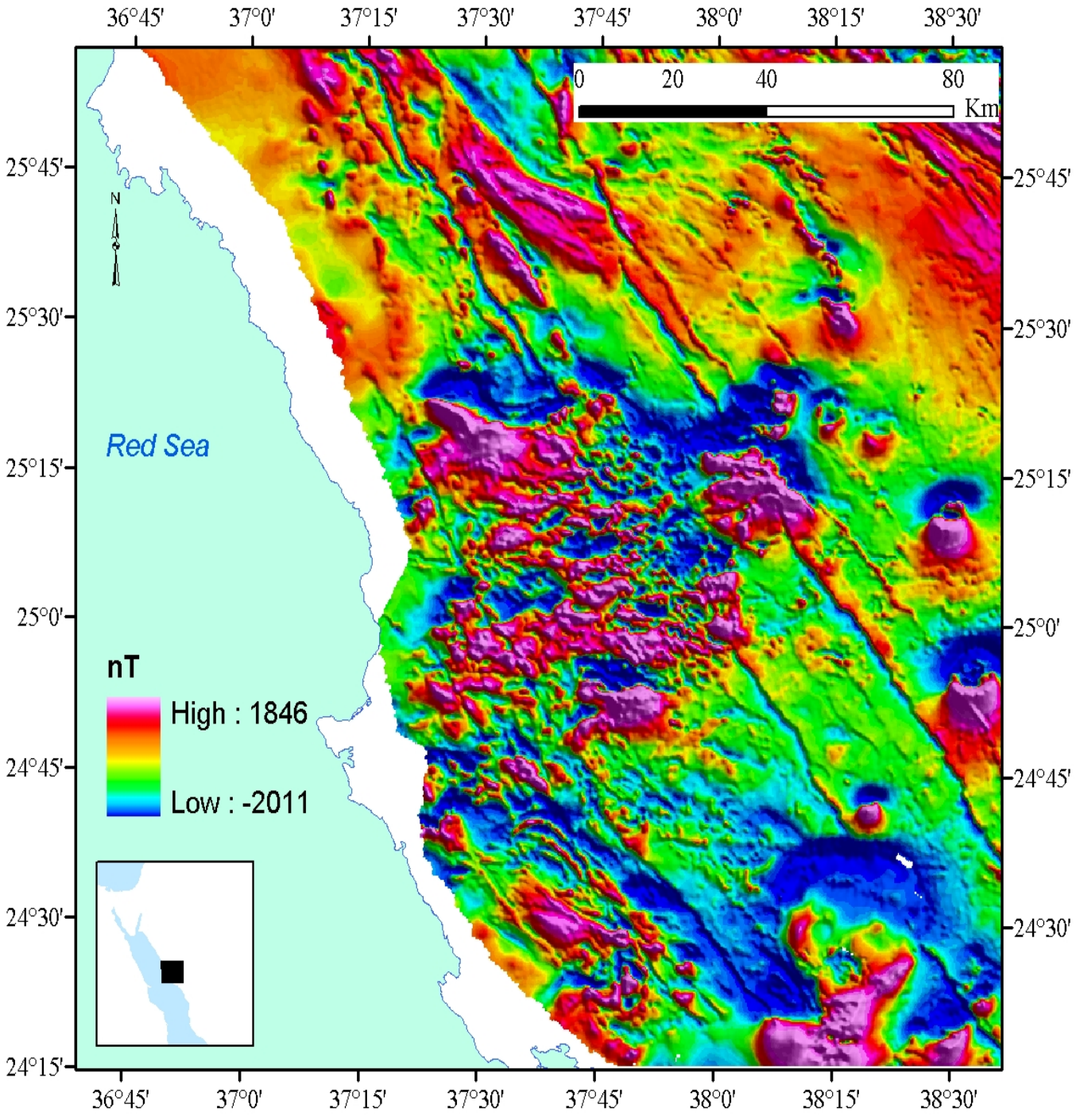

Fig. 3.3 Aeromagnetic surveys after micro leveling and merging into single dataset shown seamless mosaic grid.

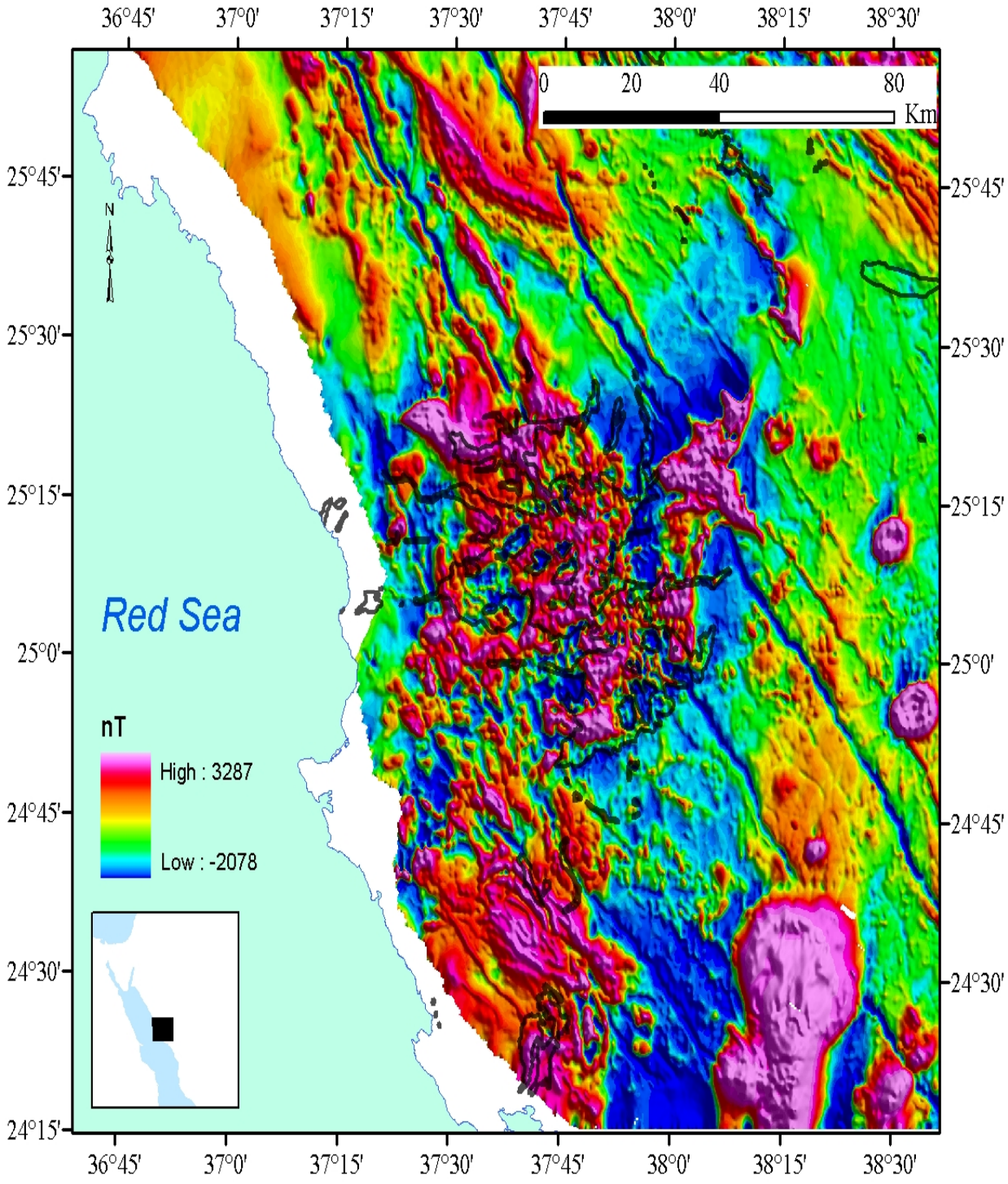

Fig. 3.4 Reduced to pole (RTP) aeromagnetic map of the study area, shown in color shaded-relief illuminated from N45˚E with inclination 45˚

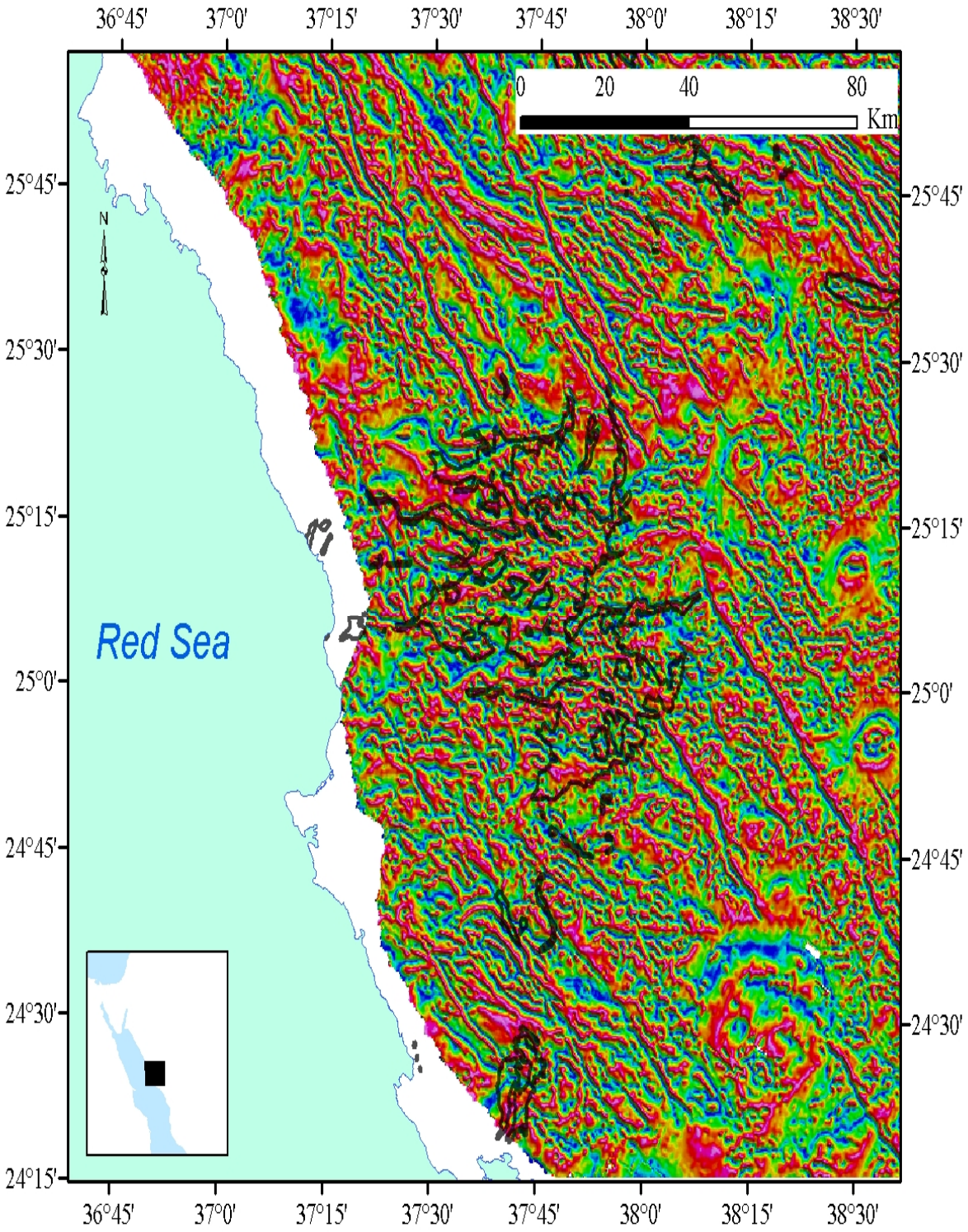

Fig. 3.5 Tilt derivative of the TMI shows detailed geological structures

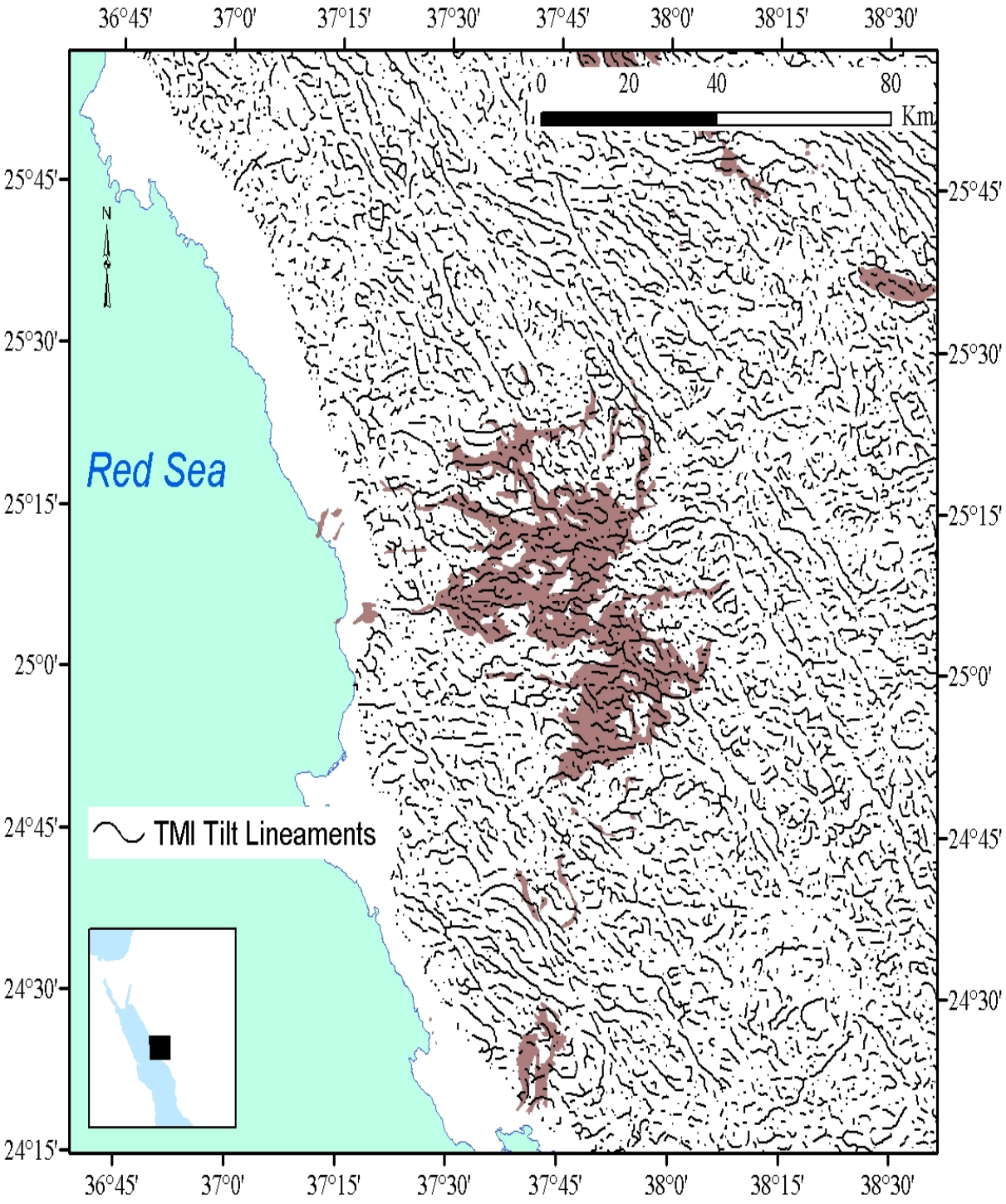

Fig. 3.6 Map shows lineaments of the study area traced automatically.

CHAPTER 4

PETROGRAPHY & GEOCHEMISTRY

Forty three rock samples have been sent to ALS Labs in Canada for geochemical analysis. The applied methods and their accuracy and detection limits are shown below and described in details in appendices B and C.

Sample Preparation Procedures

- **Drying**

Drying are applied only to samples that are excessively wet, in the opinion of the laboratory manager. Drying of excessively wet sample in drying ovens and air drying later .

- **Crushing**

Samples that are too coarse to be put directly into a large pulverizing mill, or where the particle size needs to be reduced before we are able to take a representative split for further pulverization, are crushed using jaw crushers. Coarse crushing of rock chip and drill samples to 70% nominal – 6 mm. fine crushing of rock chip and drill samples to 70% nominal – 2 mm

- **Splitting**

Some samples may require splitting into representative sub samples. Split sample using a riffle splitter. Split sample using riffle splitter or rotary splitter.

- **Pulverizing**

All pulverizing procedures make use of "flying disk" or "ring and puck" style grinding mills. Unless otherwise indicated, all pulverizing procedures guarantee that for most sample types at least 85% of the material will be pulverized to 75 micron (200 mesh) or better. Pulverize split or total sample of up to 250 g to 85% passing 75 micron

Geochemical Analyses Procedures

A) Whole Rock Geochemistry – ME-ICP06 and OA-GRA05

Analysis of major oxides by ICP-AES

Sample Decomposition: Lithium Metaborate/Lithium Tetraborate (LiBO2/Li2B4O7) Fusion* (FUS-LI01)

Analytical Method: Inductively Coupled Plasma – Atomic Emission Spectroscopy (ICP-AES)

A prepared sample (0.200 g) is added to lithium metaborate/lithium tetraborate flux (0.90 g), mixed well and fused in a furnace at 1000°C. The resulting melt is then cooled and dissolved in 100 mL of 4% nitric acid/2% hydrochloric acid. This solution is then analyzed by ICP-AES and the results are corrected for spectral inter-element interferences. Oxide concentration is calculated from the determined elemental concentration and the result is reported in that format.

Element	Symbol	Units	Lower Limit	Upper Limit
Aluminum	Al_2O_3	%	0.01	100
Barium	BaO	%	0.01	100
Calcium	CaO	%	0.01	100
Chromium	Cr_2O_3	%	0.01	100
Iron	Fe_2O_3	%	0.01	100
Magnesium	MgO	%	0.01	100
Manganese	MnO	%	0.01	100

Element	Symbol	Units	Lower Limit	Upper Limit
Phosphorus	P_2O_5	%	0.01	100
Potassium	K_2O	%	0.01	100
Silicon	SiO_2	%	0.01	100
Sodium	Na_2O	%	0.01	100
Strontium	SrO	%	0.01	100
Titanium	TiO_2	%	0.01	100

*Note: For samples that are high in Sulphides, we may substitute a peroxide fusion in order to obtain better results.

B) Four Acid "Near-Total" Digestion

Quantitatively dissolves nearly all elements for the majority of geological materials. Only the most resistive minerals, such as Zircons, are only partially dissolved using this procedure

For 43 samples analyses for 33 element for acid ICP-AES. If ultra-trace levels are not required, the ICP-AES version of the four acid leach is a more economical alternative to using ICP-MS packages. Four acid digestions are able to dissolve most minerals; however, although the term "neartotal" is used, depending on the sample matrix, not all elements are quantitatively extracted. Minimum sample 1g.

Elements and Ranges (ppm

As	(0.2 - 10,000)	Mg	(0.01% - 15%)
Ba	(0.5 - 10,000)	Mn	(5 - 10,000)
Be	(0.05 - 1000)	Mo	(0.05 - 10,000)
Bi	(0.01 - 10,000)	Na	(0.01% - 10%)
Ca	(0.01% - 25%)	Nb	(0.1 - 500)
Cd	(0.02 - 500)	Ni	(0.2 - 10,000)
Ce	(0.01 - 500)	P	(10 -10,000)
Co	(0.1 - 10,000)	Pb	(0.5 - 10,000
W	(0.1 - 10,000)	U	(0.1 - 500)
Y	(0.1 - 500)	V	(1 - 10,000)
Zn	(2 - 10,000)	Ag	(0.02 - 100
Zr	(0.5 - 500		
Cr	(1 - 10,000)	Rb	(0.1 - 500)
Cs	(0.05 - 500)	Re	(0.002 - 50)
Cu	(0.2 - 10,000)	S	(0.01% - 10%)
Fe	(0.01% - 25%)	Sb	(0.05 - 1,000)
Ga	(0.05 - 500)	Se	(1 - 1,000)
Ge	(0.05 - 500)	Sn	(0.2 - 500)
Hf	(0.1 - 500)	Sr	(0.2 - 10,000)
In	(0.005 - 500)	Ta	(0.05 – 100)
K	(0.01% - 10%)	Te	(0.05 - 500)
La	(0.5 - 500)	Th	(0.2 - 500)
Li	(0.2 - 500)	Ti	(0.01% - 10%)
		Tl	(0.02 – 500)

C) Geochemical Procedure – ME-MS61r

(REE Add-on package to ME-MS61)*

Ultra-Trace Level Method Using ICP-MS and ICP-AES

Sample Decomposition: HF-HNO3-HClO4 acid digestion, HCl leach (GEO-4A01)

Analytical Methods: Inductively Coupled Plasma - Atomic Emission Spectroscopy (ICP - AES). A prepared sample (0.25 g) is digested with perchloric, nitric, hydrofluoric and hydrochloric acids. The residue is topped up with dilute hydrochloric acid and analyzed by inductively coupled plasma-atomic emission spectrometry. Following this

analysis, the results are reviewed for high concentrations of bismuth, mercury, molybdenum, silver and tungsten and diluted accordingly. Samples meeting this criterion are then analyzed by inductively coupled plasma-mass spectrometry. Results are corrected for spectral interelement interferences.

NOTE: Four acid digestions are able to dissolve most minerals; however, although the term "*near-total*" is used, depending on the sample matrix, not all elements are quantitatively extracted. Results for the additional rare earth elements will represent the acid leachable portion of the rare earth elements and as such, cannot be used, for instance to do a chondrite plot.

Element	Symbol	Units	Lower Limit	Upper Limit
Silver	Ag	ppm	0.01	100
Aluminum	Al	%	0.01	50
Arsenic	As	ppm	0.2	10 000
Barium	Ba	ppm	10	10 000
Beryllium	Be	ppm	0.05	1 000
Bismuth	Bi	ppm	0.01	10 000
Calcium	Ca	%	0.01	50
Cadmium	Cd	ppm	0.02	1 000
Cerium	Ce	ppm	0.01	500
Cobalt	Co	ppm	0.1	10 000
Chromium	Cr	ppm	1	10 000
Cesium	Cs	ppm	0.05	500
Copper	Cu	ppm	0.2	10 000
Iron	Fe	%	0.01	50
Gallium	Ga	ppm	0.05	10 000
Germanium	Ge	ppm	0.05	500
Hafnium	Hf	ppm	0.1	500
Indium	In	ppm	0.005	500
Potassium	K	%	0.01	10
Lanthanum	La	ppm	0.5	10 000
Lithium	Li	ppm	0.2	10 000
Magnesium	Mg	%	0.01	50

Element	Symbol	Units	Lower Limit	Upper Limit
Manganese	Mn	ppm	5	100 000
Molybdenum	Mo	ppm	0.05	10 000
Sodium	Na	%	0.01	10
Niobium	Nb	ppm	0.1	500
Nickel	Ni	ppm	0.2	10 000
Phosphorous	P	ppm	10	10 000
Lead	Pb	ppm	0.5	10 000
Rubidium	Rb	ppm	0.1	10 000
Rhenium	Re	ppm	0.002	50
Sulphur	S	%	0.01	10
Antimony	Sb	ppm	0.05	10 000
Scandium	Sc	ppm	0.1	10 000
Selenium	Se	ppm	1	1 000
Tin	Sn	ppm	0.2	500
Strontium	Sr	ppm	0.2	10 000
Tantalum	Ta	ppm	0.05	100
Tellurium	Te	ppm	0.05	500
Thorium	Th	ppm	0.2	10 000
Titanium	Ti	%	0.005	10
Thallium	Tl	ppm	0.02	10 000
Uranium	U	ppm	0.1	10 000
Vanadium	V	ppm	1	10 000
Tungsten	W	ppm	0.1	10 000
Yttrium	Y	ppm	0.1	500
Zinc	Zn	ppm	2	10 000
Zirconium	Zr	ppm	0.5	500
Dysprosium	Dy	ppm	0.05	1 000
Erbium	Er	ppm	0.03	1 000
Europium	Eu	ppm	0.03	1 000
Gadolinium	Gd	ppm	0.05	1 000
Holmium	Ho	ppm	0.01	1 000
Lutetium	Lu	ppm	0.01	1 000
Neodymium	Nd	ppm	0.1	1 000
Praseodymium	Pr	ppm	0.03	1 000
Samarium	Sm	ppm	0.03	1 000
Terbium	Tb	ppm	0.01	1 000
Thulium	Tm	ppm	0.01	1 000
Ytterbium	Yb	ppm	0.03	1 000

D) Whole Rock Geochemistry – ME-XRF06

Sample Decomposition: 50% $Li_2B_4O_7$ – 50% $LiBO_2$ (WEI-GRA06)

Analytical Method: X-Ray Fluorescence Spectroscopy)

A calcined or ignited sample (0.9 g) is added to 9.0g of Lithium Borate Flux (50 % - 50 % $Li_2B_4O_7$ – $LiBO_2$), mixed well and fused in an auto fluxer between 1050 - 1100°C. A flat molten glass disc is prepared from the resulting melt. This disc is then analysed by X-ray fluorescence spectrometry.

Element	Symbol	Units	Lower Limit	Upper Limit
Aluminum Oxide	Al_2O_3	%	0.01	100
Barium Oxide	BaO	%	0.01	100
Calcium Oxide	CaO	%	0.01	100
Chromium Oxide	Cr_2O_3	%	0.01	100
Ferric Oxide	Fe_2O_3	%	0.01	100
Potassium Oxide	K_2O	%	0.01	100
Magnesium Oxide	MgO	%	0.01	100
Manganese Oxide	MnO	%	0.01	100
Sodium Oxide	Na_2O	%	0.01	100
Phosphorus Oxide	P_2O_5	%	0.01	100
Silicon Oxide	SiO_2	%	0.01	100
Strontium Oxide	SrO	%	0.01	100
Titanium Oxide	TiO_2	%	0.01	100
Loss On Ignition	LOI	%	0.01	100
	Total	%	0.01	101

Note: Since samples that are high in sulphides or base metals can damage Platinum crucibles, a ME-ICP06 finish method can be selected as an alternative method.

E) OA-GRA05, ME-GRA05

Sample Decomposition: Thermal decomposition Furnace or TGA (OA-GRA05 or ME-GRA05)

Analytical Method: Gravimetric

If required, the total oxide content is determined from the ICP analytic concentrations and loss on Ignition (L.O.I.) values. A prepared sample (1.0 g) is placed in an oven at 1000°C

for one hour, cooled and then weighed. The percent loss on ignition is calculated from the difference in weight.

Method Code	Parameter	Symbol	Units	Lower Limit	Upper Limit
OA-GRA05	Loss on Ignition (Furnace)	LOI	%	0.01	100
ME-GRA05	Loss on Ignition (TGA)	Moisture	%	0.01	100
		LOI	%	0.01	100

F) Geochemical Procedure – ME-MS61r

(REE Add-on package to ME-MS61)* Ultra-Trace Level Method Using ICP-MS and ICP-AES

Sample Decomposition: HF-HNO3-HClO4 acid digestion, HCl leach (GEO-4A01)

Analytical Methods: Inductively Coupled Plasma - Atomic Emission Spectroscopy (ICP - AES)

Inductively Coupled Plasma - Mass Spectrometry (ICP-MS)

A prepared sample (0.25 g) is digested with perchloric, nitric, hydrofluoric and hydrochloric acids. The residue is topped up with dilute hydrochloric acid and analyzed by inductively coupled plasma-atomic emission spectrometry. Following this analysis, the results are reviewed for high concentrations of bismuth, mercury, molybdenum, silver and tungsten and diluted accordingly. Samples meeting this criterion are then analyzed by inductively coupled plasma-mass spectrometry. Results are corrected for spectral interelement interferences.

NOTE: Four acid digestions are able to dissolve most minerals; however, although the term "*near-total*" is used, depending on the sample matrix, not all elements are quantitatively extracted.

Results for the additional rare earth elements will represent the acid leachable portion of the rare earth elements and as such, cannot be used, for instance to do a chondrite plot.

Element	Symbol	Units	Lower Limit	Upper Limit
Silver	Ag	ppm	0.01	100
Aluminum	Al	%	0.01	50
Arsenic	As	ppm	0.2	10 000
Barium	Ba	ppm	10	10 000
Beryllium	Be	ppm	0.05	1 000
Bismuth	Bi	ppm	0.01	10 000
Calcium	Ca	%	0.01	50
Cadmium	Cd	ppm	0.02	1 000
Cerium	Ce	ppm	0.01	500
Cobalt	Co	ppm	0.1	10 000
Chromium	Cr	ppm	1	10 000
Cesium	Cs	ppm	0.05	500
Copper	Cu	ppm	0.2	10 000
Iron	Fe	%	0.01	50
Gallium	Ga	ppm	0.05	10 000
Germanium	Ge	ppm	0.05	500
Hafnium	Hf	ppm	0.1	500
Indium	In	ppm	0.005	500
Potassium	K	%	0.01	10
Lanthanum	La	ppm	0.5	10 000
Lithium	Li	ppm	0.2	10 000
Magnesium	Mg	%	0.01	50
Manganese	Mn	ppm	5	100 000
Molybdenum	Mo	ppm	0.05	10 000
Sodium	Na	%	0.01	10
Niobium	Nb	ppm	0.1	500
Nickel	Ni	ppm	0.2	10 000
Phosphorous	P	ppm	10	10 000

J) Specialty Assay Procedure – OA-GRA10 Moisture

Analytical Method: Gravimetric

A prepared sample (1.0 to 2.0g) is dried in an oven at 105°C for at least 1 hour and then weighed. The difference in weight is then calculated into % Moisture.

Element	Symbol	Units	Lower Limit	Upper Limit
Moisture	N/A	%	0.01	100

H) Assay Procedure – OA-IR05 & OA-IR06

Evaluation of Ores and High Grade Materials

Sample Decomposition: Leco Furnace

Analytical Method: Infrared Spectroscopy

The sample is analyzed for forms of moisture using a Leco analyzer. Where in a prepared sample (0.1 to 0.2 g), it is heated in a furnace at 110°C and 1000°C to release moisture and crystalline water respectively. Water released from the sample is measured by an infrared detection system.

Method Code	Parameter	Symbol	Units	Lower Limit	Upper Limit
OA-IR05	Moisture	H_2O-	%	0.01	100
OA-IR06	Crystalline Water	H_2O+	%	0.01	100

Thin Sections

Representative thin sections have been prepared and studied on using Leitz petrographic microscope with an attached digital camera. Most of the investigated samples are invariably vesicular and porphyritic. Occasionally vesicles are filled with secondary calcite and zeolites and display a typical amygdaloidal texture. The phenocrysts are dominantly forsteritic olivine which quite often has a skeletal form or corrosion embayments thus indicating disequilibrium with the melt. Plagioclase phenocrysts are also quite common in particular in differentiated samples as evident from low mg #. The clinopyroxene is dominantly titanoaugite with a pronounced light brown color. It forms with plagioclase ophitic and subophitic textures. Opaques are present either in euhedral grains or in the form of anhedral granules dispersed in the groundmass that's built of plagioclase laths, clinopyroxenes and rarely olivine with some apatite and other accessories Porphyritic and vesicular textures are the most common. In most of the samples olivine is the main phenocrystal phase; clinopyroxene is very rare as phenocrysts; the differentiated sample with low mg# have plagioclase in the phenocrystal assemblage. Opaques are mostly granular but occasionally occur in euhedral cubes. Since we do not have chemical analyses for minerals, thermodynamic modeling of the crystallization of some samples have been attempted using the widely used MELTS software for this purpose, which is based at the University of Chicago and can be accessed under the following web address:

http://melts.ofm-research.org/Applet/applet_download.html

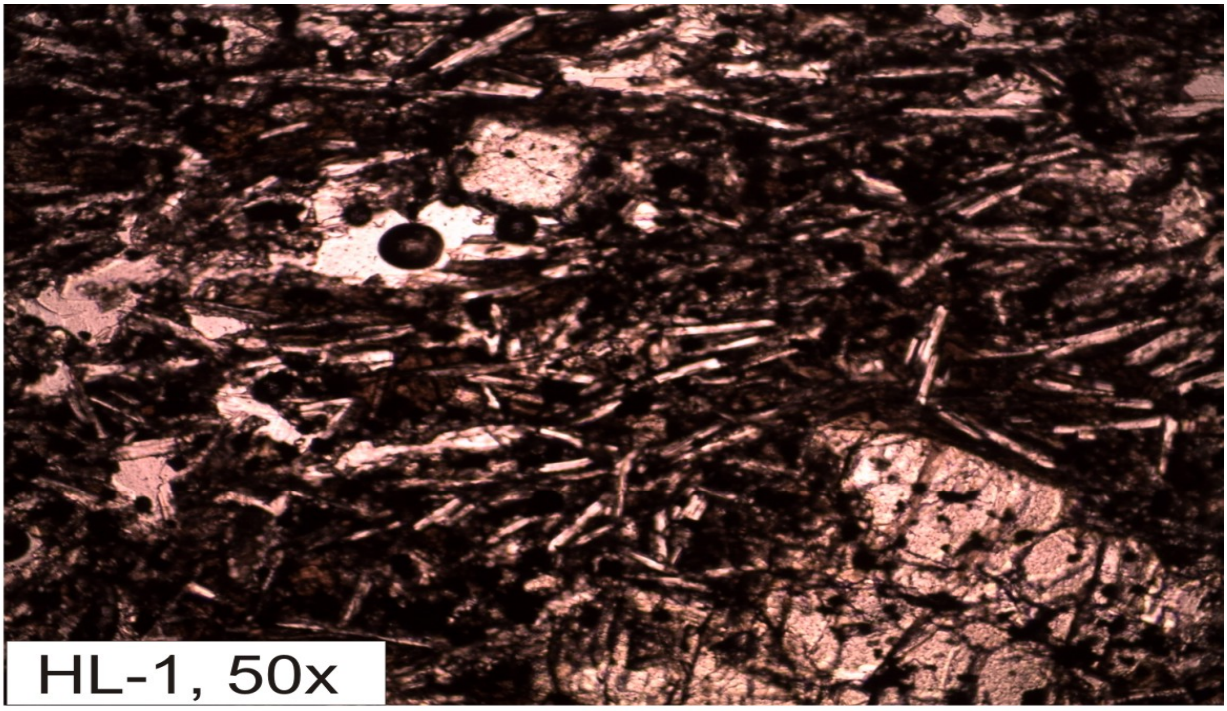

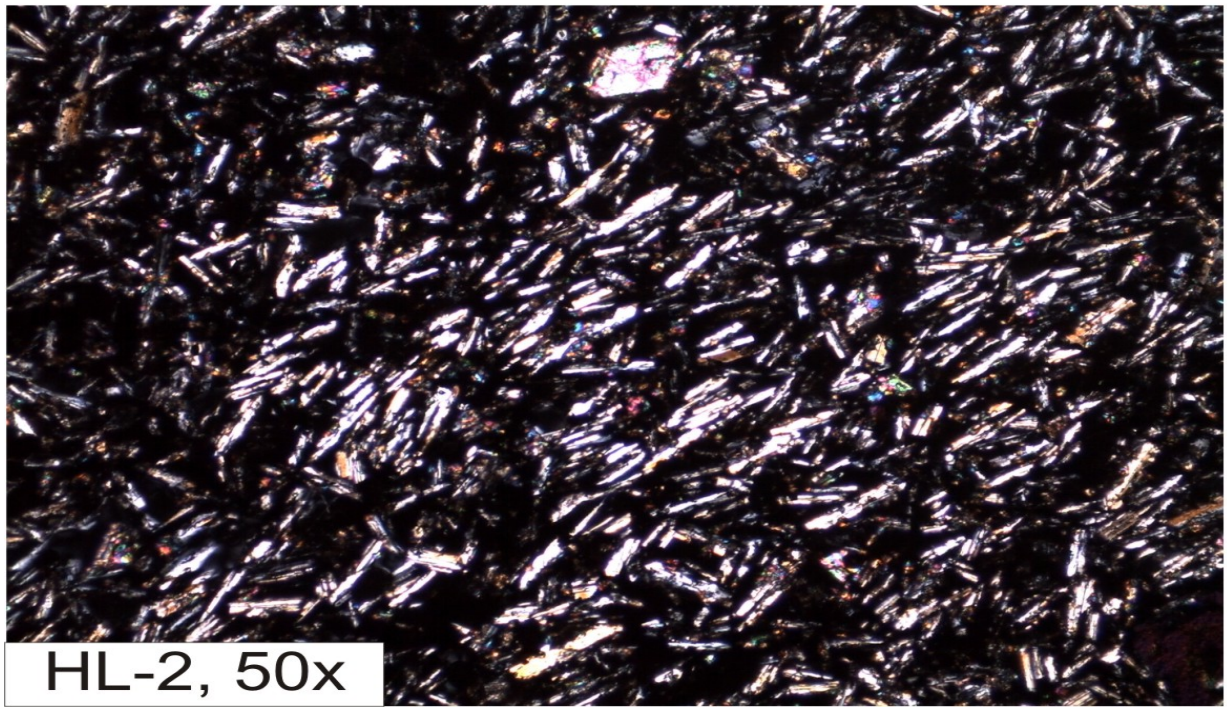

Fig. 4.1. Titano augite and olivine phenocrysts in a groundmass plagioclase laths and titanoaugite and opaques (upper); olivine phenocrysts in a groundmass of plagioclase, pyroxene, and opaques (lower)

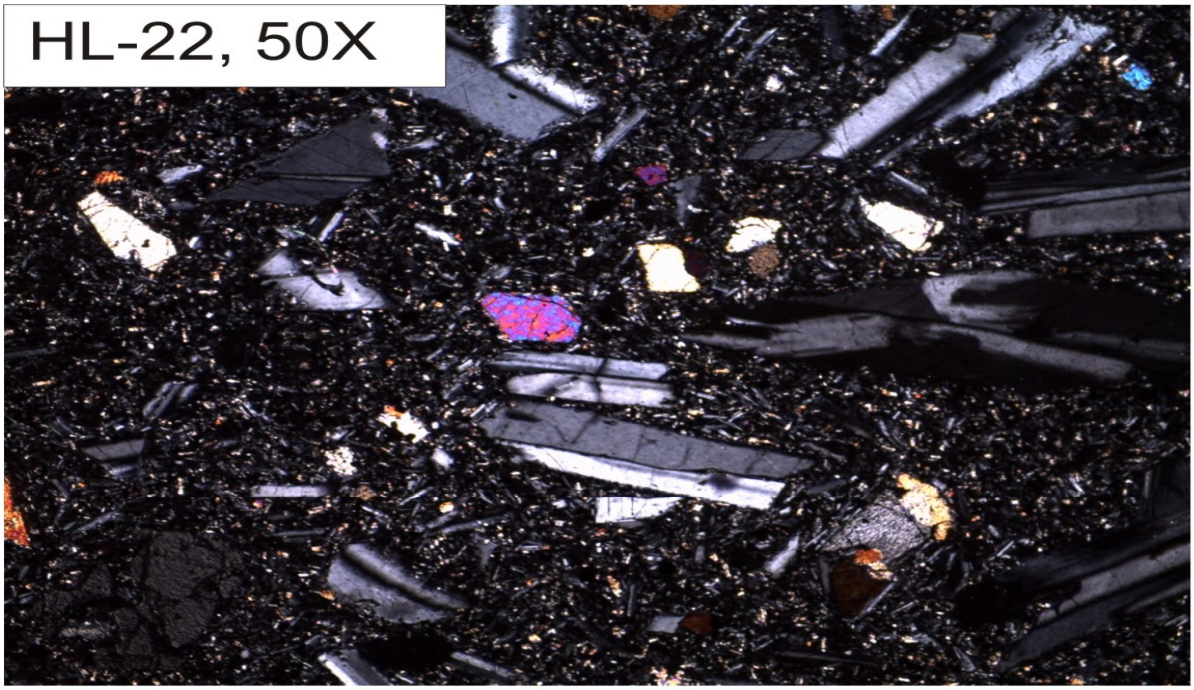

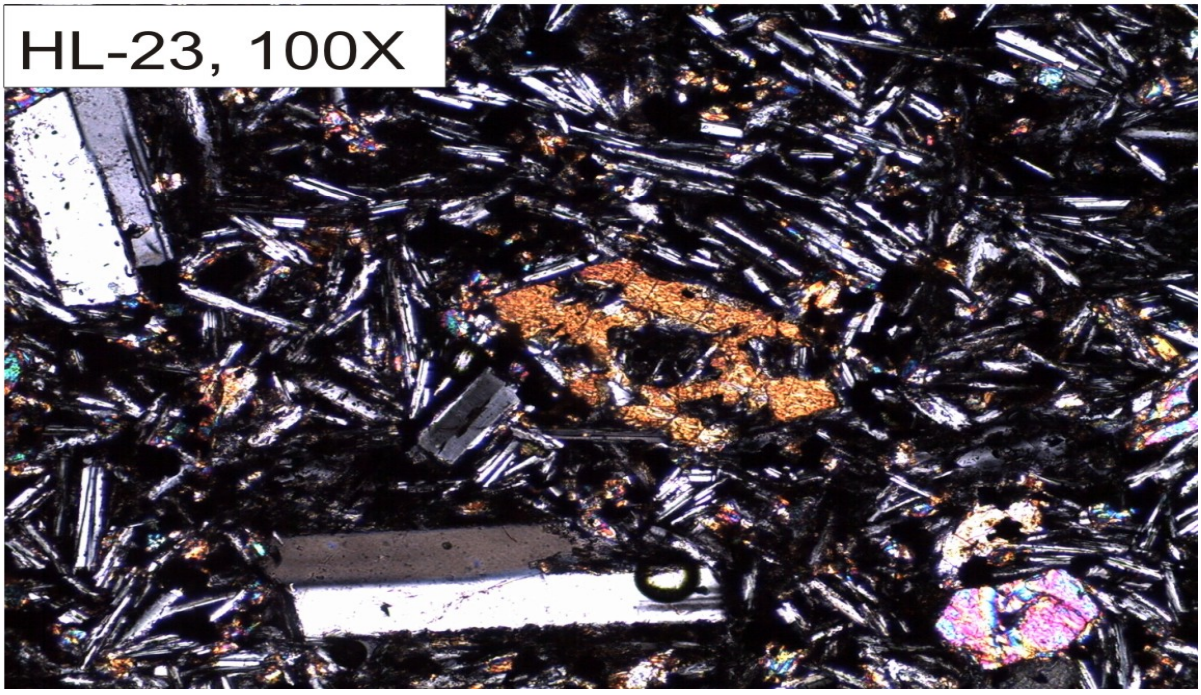

Fig. 4.2 dominantly labradorite and forsteritic olivine phenocrysts in a cryptocrystalline groundmass (upper); skeletal forsteritic olivine and labradorite phenocrysts in a trachoidal groundmass.

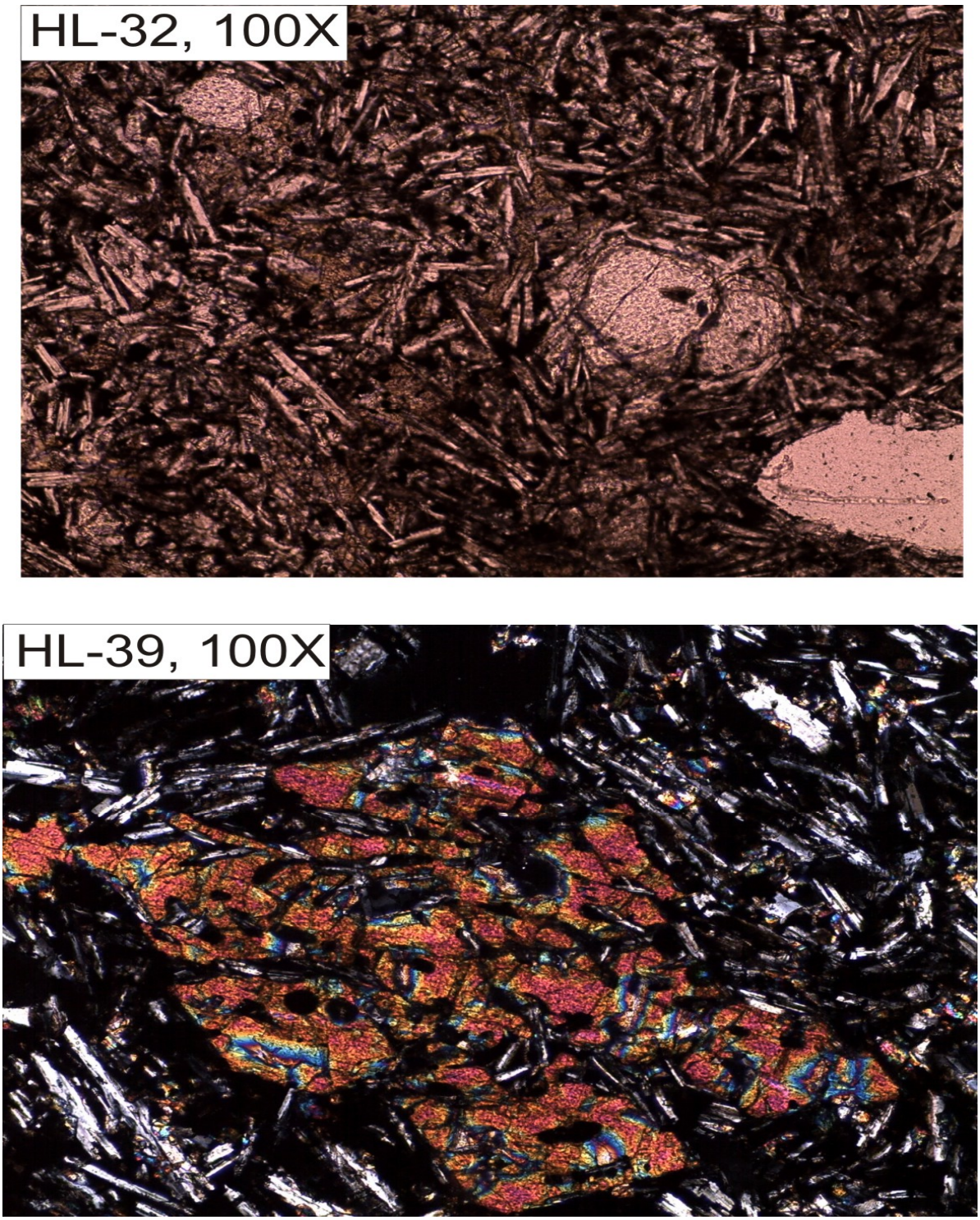

Fig. 4.3 Olivine phenocrysts in a groundmass of brownish titanoaugite and plagioclase displaying sub-ophitic textures (PPL, upper); Skeletal olivine in a groundmass of plagioclase, opaques and granular pyroxene (XPL, lower)

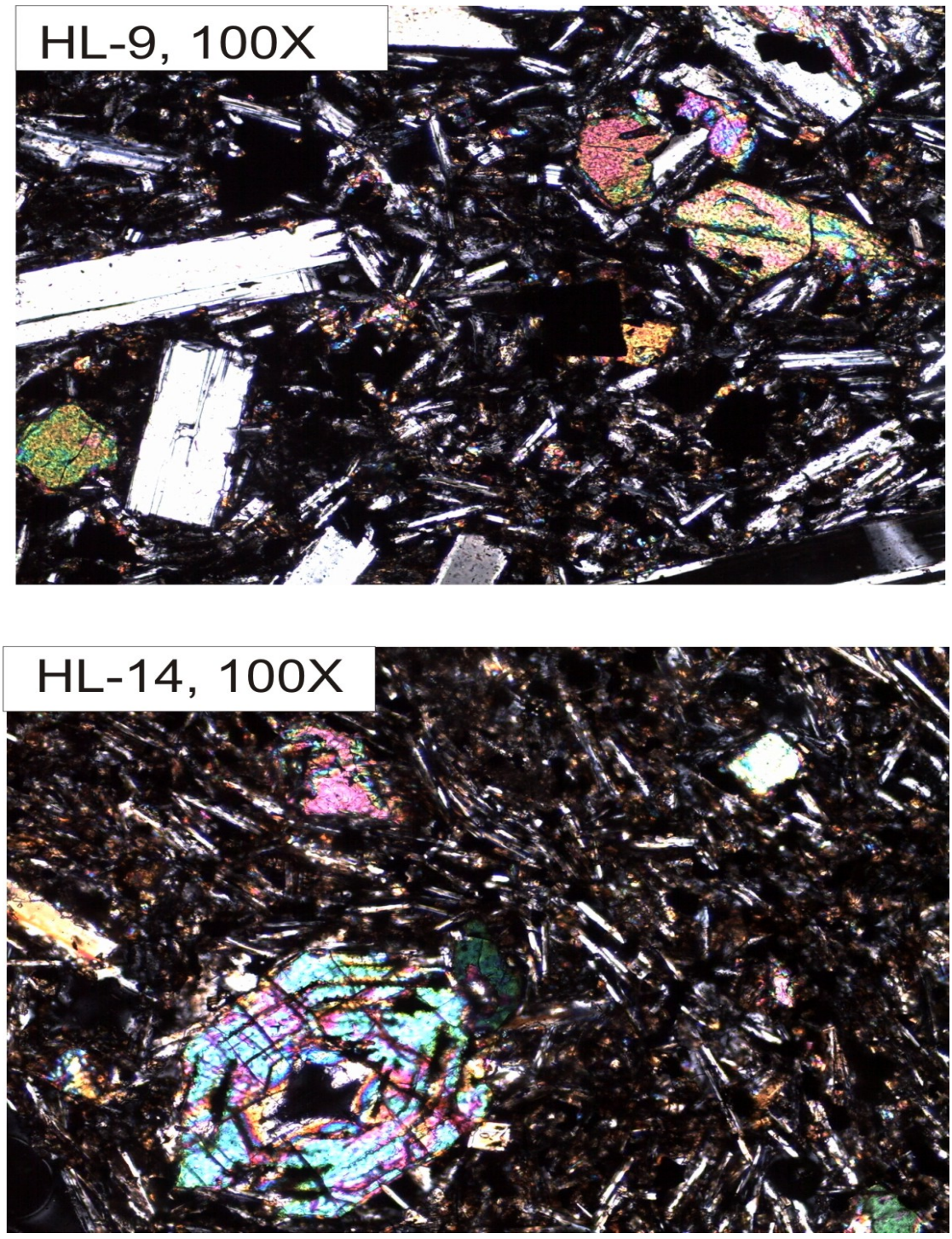

Fig. 4.4. Labradorite, olivine, and euhedral titanomagnetite microphenocrysts in a plagioclase clinopyroxene groundmass (upper); zoned olivine in a plagioclase titanaugite –opaques groundmass (lower).

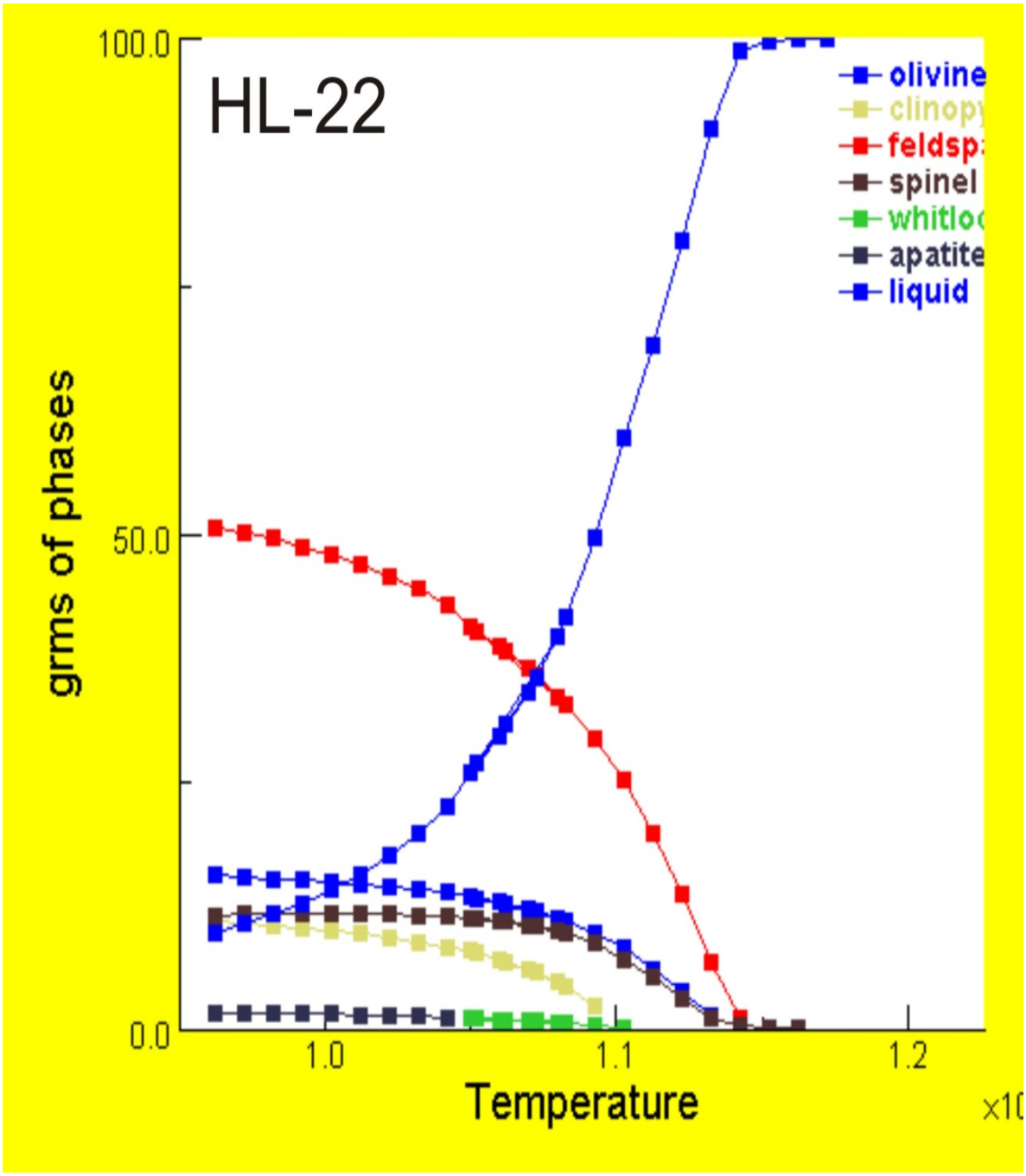

Fig. 4.5 a . Crystallization modeling using the MELTS software (Asimov and Ghiorso, 1998) for HL-22 (highly differentiated melt with mg 39). Note that the temperature is multiplied by 1000. Amount of mineral phases is based on 100 gram melt so it can be equally expressed as wt. %. The differentiated samples HL-22 has a liquidus at about 1172 °C.

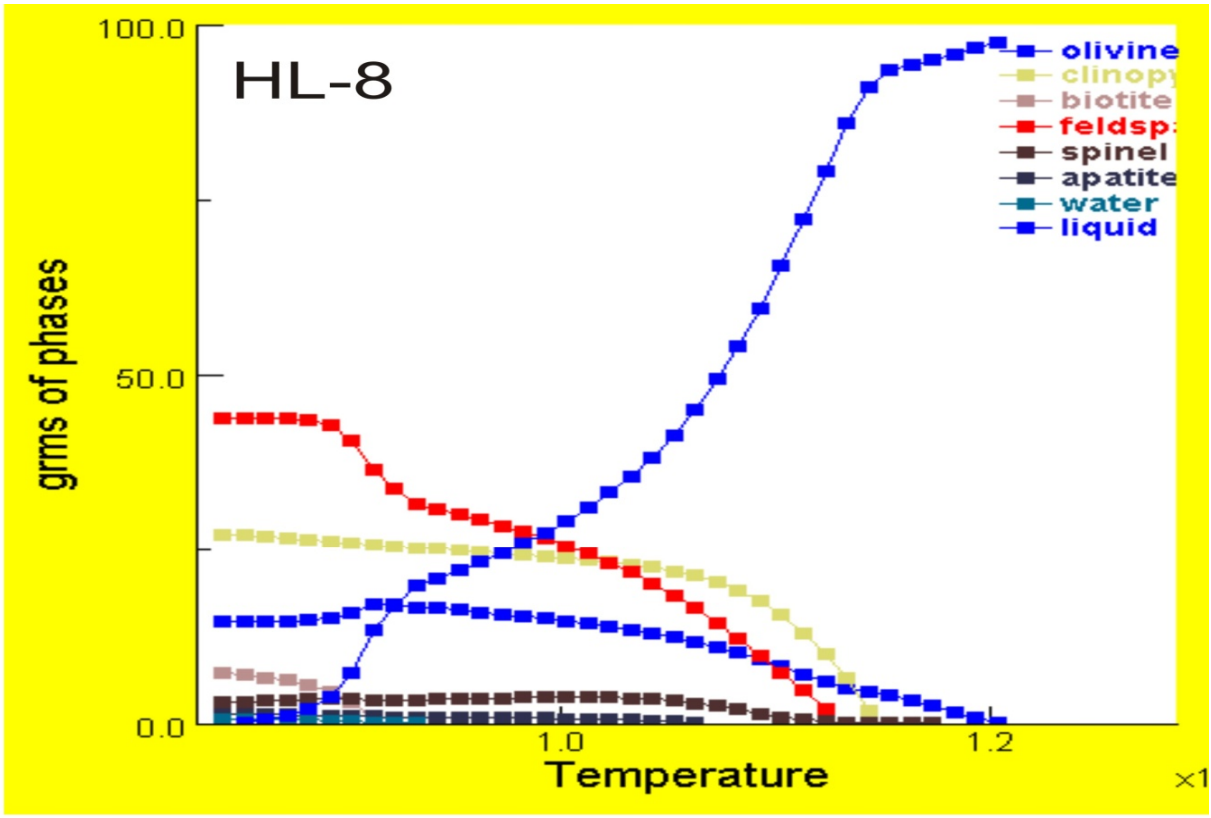

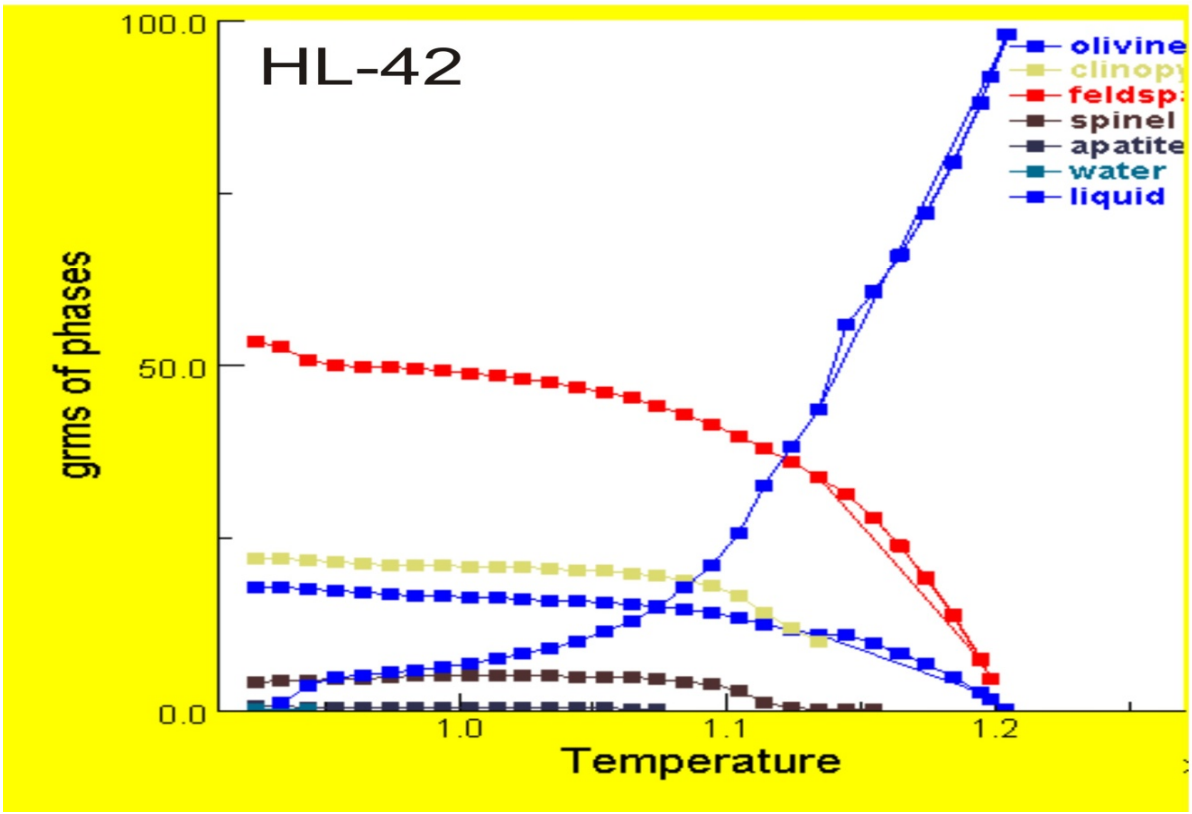

Fig. 4.5 b . Crystallization modeling using the MELTS software for samples HL-8 and HL-42. The liquidus for samples HL-8 and HL-42 is around 1200 °C. The lowest solidus is around 840 °C for sample HL-8.

The sequence of crystallization of the constituent minerals is shown for three samples in Figure 4.5. Since most samples have olivine phenocrysts, some plagioclase as well and rarely pyroxene, the extrusion of the magma must have taken place before the melt became saturated with clinopyroxene i.e at temperatures above 1150 °C. The composition of olivine for the most primitive melt HL-42 is Fo_{62} and the plagioclase (An_{52}).

Four Acid "Near-Total" Digestion

If ultra-trace levels are not required, the ICP-AES version of the four acid leach is a more economical alternative to using ICP-MS packages. Four acid digestions are able to dissolve most minerals; however, although the term "near-total" is used, depending on the sample matrix, not all elements are quantitatively extracted. Minimum sample 1g.

Analytes & Ranges (ppm)								Code	Price per Sample ($)
Ag	0.5-100	Cr	1-10,000	Na	0.01%-10%	Ti	0.01%-10%	ME-ICP61	12.95 Complete package or 8.90 plus 0.55/element
Al	0.01%-50%	Cu	1-10,000	Ni	1-10,000	Tl	10-10,000		
As	5-10,000	Fe	0.01%-50%	P	10-10,000	U	10-10,000		
Ba	10-10,000	Ga	10-10,000	Pb	2-10,000	V	1-10,000		
Be	0.5-1,000	K	0.01%-10%	S	0.01%-10%	W	10-10,000		
Bi	2-10,000	La	10-10,000	Sb	5-10,000	Zn	2-10,000	ME-ICP61m	21.60
Ca	0.01%-50%	Mg	0.01%-50%	Sc	1-10,000				
Cd	0.5-1,000	Mn	5-100,000	Sr	1-10,000				
Co	1-10,000	Mo	1-10,000	Th	20-10,000				

Note: To include Hg to a lower detection limit of 0.01ppm in the suite of elements above, please request method ME-ICP61m instead of ME-ICP61.

Rare Earth & Trace Elements Using ICP-MS

Lithium Borate Fusion

A lithium borate fusion of the sample prior to acid dissolution and ICPMS analysis provides the most quantitative analysis for a broad suite of elements. This technique solubilises most mineral species, including those that are highly refractory.

Analytes & Ranges (ppm)								Code	Price per Sample ($)
Ag	1-1,000	Ga	0.1-1,000	Pb	5-10,000	Tm	0.01-1,000	ME-MS81	22.00 (Sold only as a complete package).
Ba	0.5-10,000	Gd	0.05-1,000	Pr	0.03-1,000	U	0.05-1,000		
Ce	0.5-10,000	Hf	0.2-10,000	Rb	0.2-10,000	V	5-10,000		
Co	0.5-10,000	Ho	0.01-1,000	Sm	0.03-1,000	W	1-10,000		
Cr	10-10,000	La	0.5-10,000	Sn	1-10,000	Y	0.5-10,000		
Cs	0.01-10,000	Lu	0.01-1,000	Sr	0.1-10,000	Yb	0.03-1,000		
Cu	5-10,000	Mo	2-10,000	Ta	0.1-10,000	Zn	5-10,000		
Dy	0.05-1,000	Nb	02-10,000	Tb	0.01-1,000	Zr	2-10,000		
Er	0.03-1,000	Nd	0.1-10,000	Th	0.05-1,000				
Eu	0.03-1,000	Ni	5-10,000	Tl	0.5-1,000				
Combination of Rare Earth & Trace Elements from method ME-MS81 plus whole rock package by method ME-ICP06.								ME-MS81D	33.15 (Sold only as a complete package).

Note: Some base metal oxides and sulfides may not be completely decomposed by the lithium borate fusion. Results for Ag, Co, Cu, Mo, Ni, Pb and Zn will not likely be quantitative by this procedure.

The major, trace and rare earth elements together with the CIPW norms for all samples are listed in Table 2. The Software Igpet version 2010

http://home.comcast.net/~carrvolcano/site/?/page/Igpet_for_Windows_and_Mac

has been used for the construction of chemical variation diagrams, the calculation of the CIPW norms, and plotting of the various chemical classification and tectonic setting diagrams; while CORELDRAW14 was used to edit these diagrams.

The investigated volcanic suite displays narrow major element ranges, that varies from 43.83-47.22 wt% SiO2, 15.37-16.97 wt%Al2O3, 9.8-15.9 wt% Fe2O3, 7.05-12.84 wt%

CaO, 4.32-8.66 wt% MgO, 2.72-4.57 wt% Na2O, 0.36-1.43 wt% K2O, 1.63-3.2 wt% TiO2,0.16-0.25 wt% MnO, and 0.22-0.87 wt% P2O5 (Table 1 in the Appendix).

The Mg-numbers (= molar MgO/MgO + FeO)*100 assuming Fe2+/Fe3+ ratio of 0.85, are low and range between 35 and 59. These values indicate that none of the samples represent a primary magma. All samples are nepheline normative (Table 1 in the Appendix). The samples exclusively plot in the basanite, hawaiite, and alkali olivine basalt fields on the TAS diagram after Le Bas etal 1986 (Fig. 4.6). Furthermore, on the same figure all samples plot in the fields of alkali within plate basalts and the rocks are typically sodic on Irvine and Baragar normative plot (Fig. 4.6 and Appendix B) .

The similarity of the basalts of different episodes indicates that the parent magma remained constant in composition during all sequences of volcanic activities. Fractional crystallization was very slow to produce pronounce variation in the rocks of the successive basalt flows. This variation resulted in the swinging nature of the flows from basalt to trachy-basalt to even tephrite basanite. Major and trace elements are plotted versus mg# as an excellent index for differentiation (Fig. 4.7). Na2O, K2O, Fe2O3, TiO2, and P2O5 increase with decreasing mg# i.e with differentiation, while CaO decreases with differentiation reflecting the separation of both clinopyroxene and plagioclase. SiO2 displays no variation with differentiation (Fig. 4.7). On the other hand, Al2O3 increases at early stages during reflecting olivine and pyroxene fractionation and decreases with plagioclase being a fractionating phase (Table 4.1).

The lunayyir basalts further exhibit a compositional range in trace elements: Cr 70-440, Ni 16-156, Rb 4.9-23.6, Sr 465-825, Ba 93-455, Zn 82-161, Nb 11.5-52.2, Y 21-48, V 135-256, Cs 0.04-0.3, Sc 15-33, Co 35-54, Cu 33-86, Hf 2.6-7.9, Ta 0.7 -4.1, Th 0.9-5.64, U 0.26 -

14.6, Zr 124-375, Mo 4-14, Sn 1-36, Be 0.7-2.1, Pb 2-34, S 0.01-0.58wt%, As 5-11, Cd 0.5 -14, Sb 5-11 ppm, respectively. So the rocks are clearly enriched in HFSE (Nb, Y, Zr).

Selected trace elements are plotted versus mg # (Fig. 4.8). Ni and Cr show as expected decrease with decreasing of mg# demonstrating the role of olivine fractionation, which the most common phenocrystal phase in the investigated rocks; Rb, Y, Zr, Nb, and Ba all as incompatible elements increase with decreasing mg# i.e differentiation. Strontium, on the other hand mimics the trend of Al2O3, an increasing trend at early stages during the fractionation of ferromagnesian minerals and a decreasing trend on the onset of plagioclase fractionation. Most incompatible elements including HFSE show a negative correlation with mg# which indicates that their variation has been acquired through fractional crystallization of ferromagnesian minerals i.e olivine and pyroxene. This is supported at least for the olivine which is the dominant phase in the phenocrystal assemblage (Table 4.1 and Appendix B).

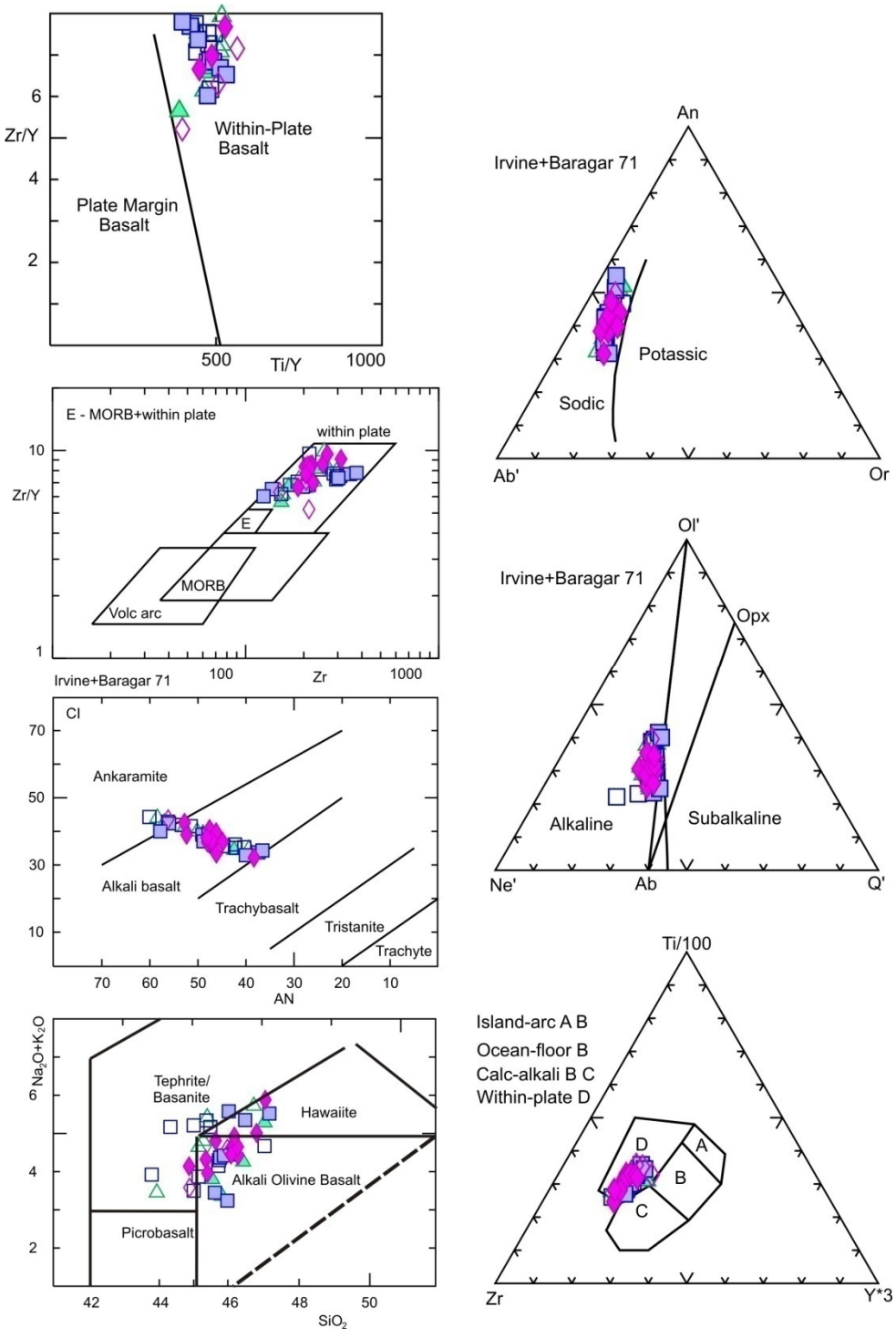

Fig. 4.6. Classification and tectonic setting discrimination diagrams.

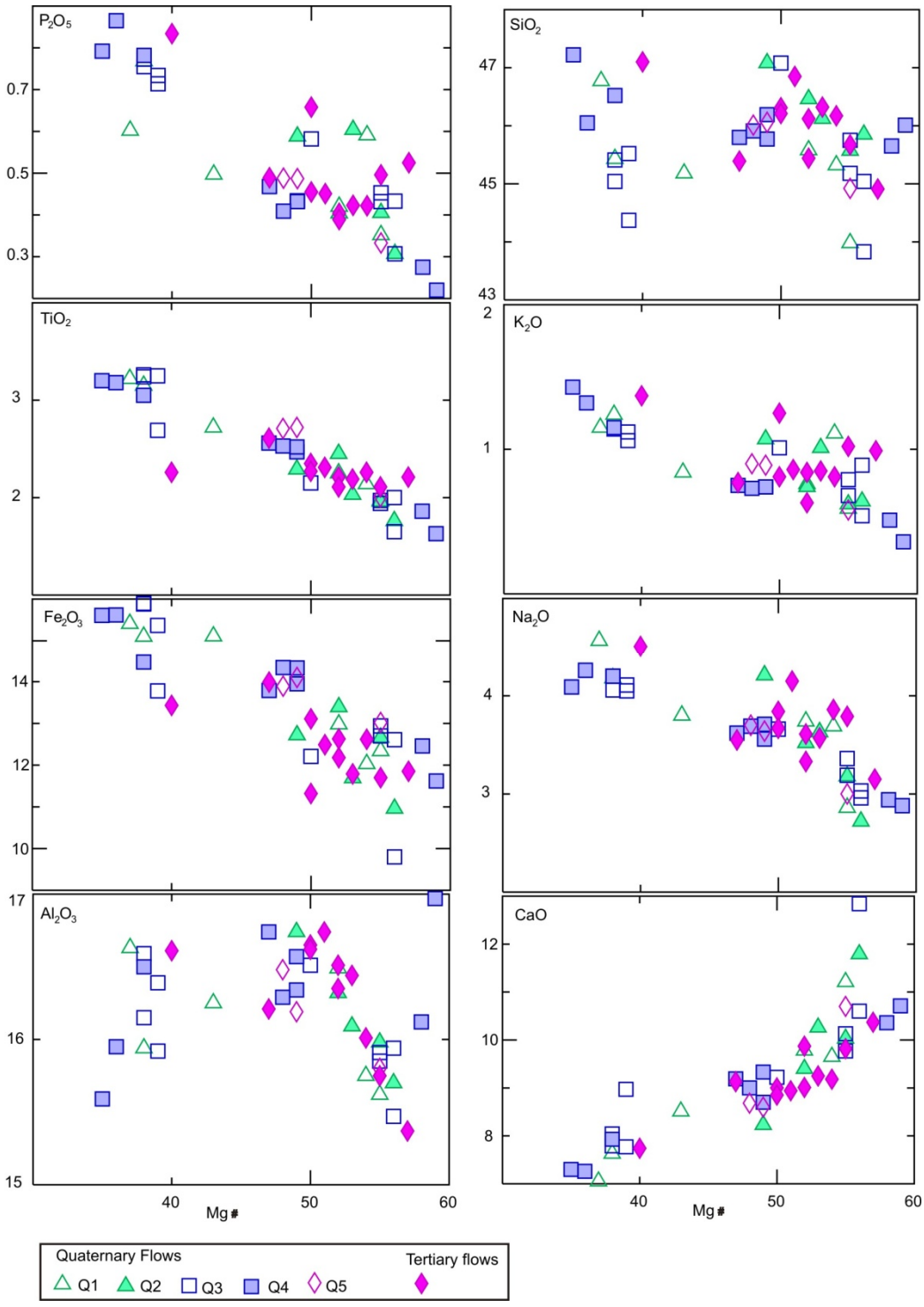

Fig. 4.7 variation of major and minor elements versus mg# for the basalts

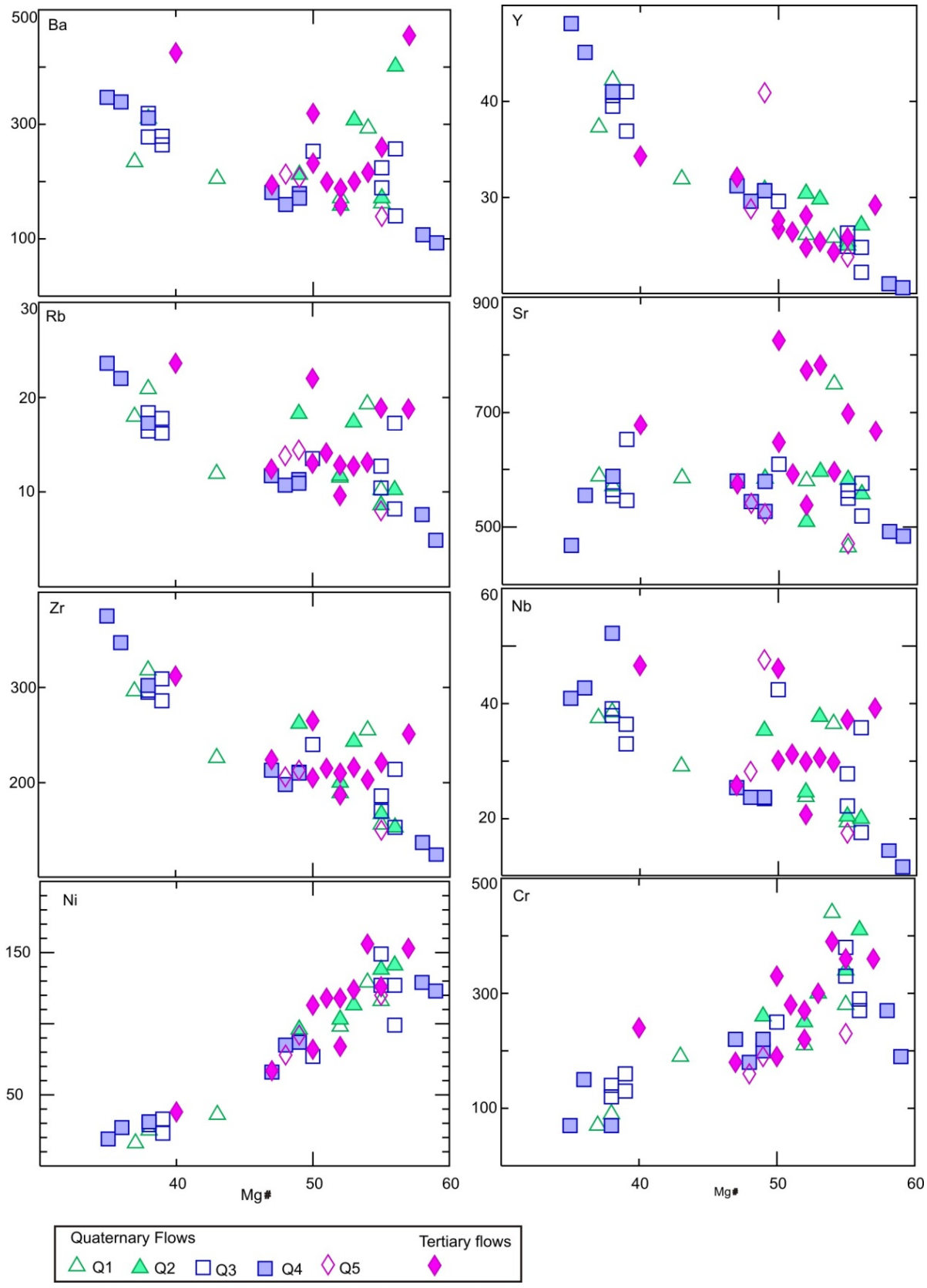

Fig. 4.8 Variation of selected trace elements versus mg # for the basalts .

The Lunayyir Basalts are enriched in REE with a total in the range of 63 ppm (HL-40 with mg # =55) to 219 ppm (HL-39, mg# = 35) and show more or less parallel REE patterns . The LREE are moderately enriched over the HREE (La/Lu)n ranges between 3.5 (for high mg # samples) to 10 (for low mg # sample). This indicates that the variation in the REE content in the samples is controlled by magmatic differentiation rather than degree of partial melting. Furthermore, the flat pattern of the HREE excludes garnet as a phase in the source rock of the investigated basalts. The multi-elements spider patterns are also parallel and indicate that the various flows are related by fractional crystallization rather than different degrees of partial melting. They similar to the pattern of St. Helena alkali basalts. The chemical variation diagrams of the HL basalts suggest that they are cogenetic. This is also supported by the REE and multi-element spiderdiagrams. Further , the magmas are not primary but rather differentiated .

Process identification diagrams based on relative compatibility of certain trace elements have been suggested and used by many authors (e.g. Minster and Allegre, 1978; Clague and Frey, 1982). These diagrams are based on relative behavior of strongly incompatible (hypermagmatophile, C^H) and moderately icompatible (magmatophile, C^M) elements. The ratio will remain constant or increase slightly during closed system fractionation, but will decrease as the degree of partial melting increases. Steep trends that pass through the zero indicate a batch partial melting trends. The Ba/Zr vs Zr and the Ba/Y vs Y plots (Figure 4.10) do not pass through zero and define slightly inclined trends that are in agreement with open system fractionation processes. This is also supported by the binary plots in Figure 4.11 which correspond to fractionation of olivine, pyroxene, and plagioclase and accumulation of apatite (Table 4.1).

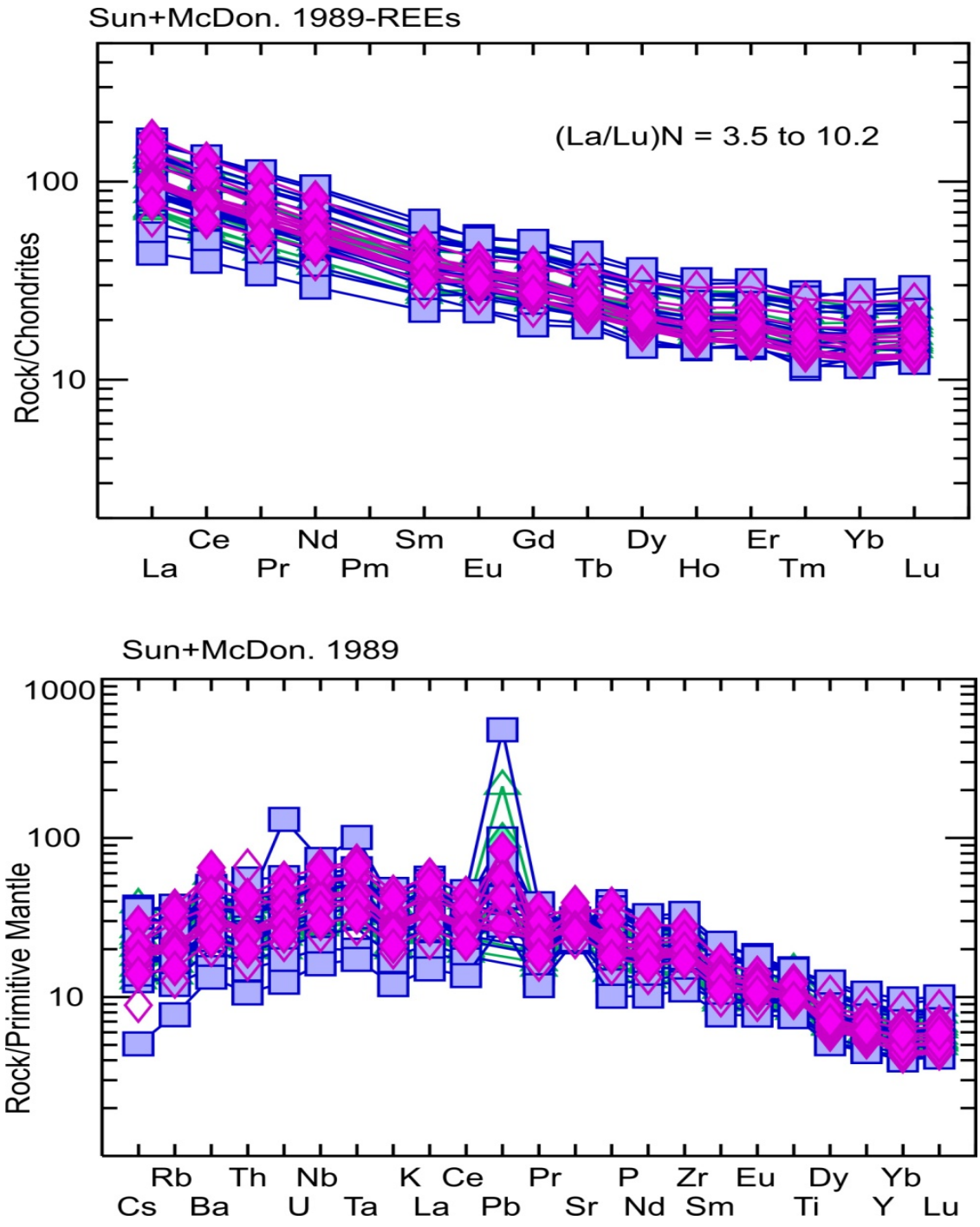

Fig. 4.9. Chondrite normalized REE patterns (upper) and spiderdiagrams of trace elements normalized to primitive mantle (lower) for the investigated rocks. The elements are arranged in order of increasing incompatibility from right to left (normalization after Sun and Hanson 1975).

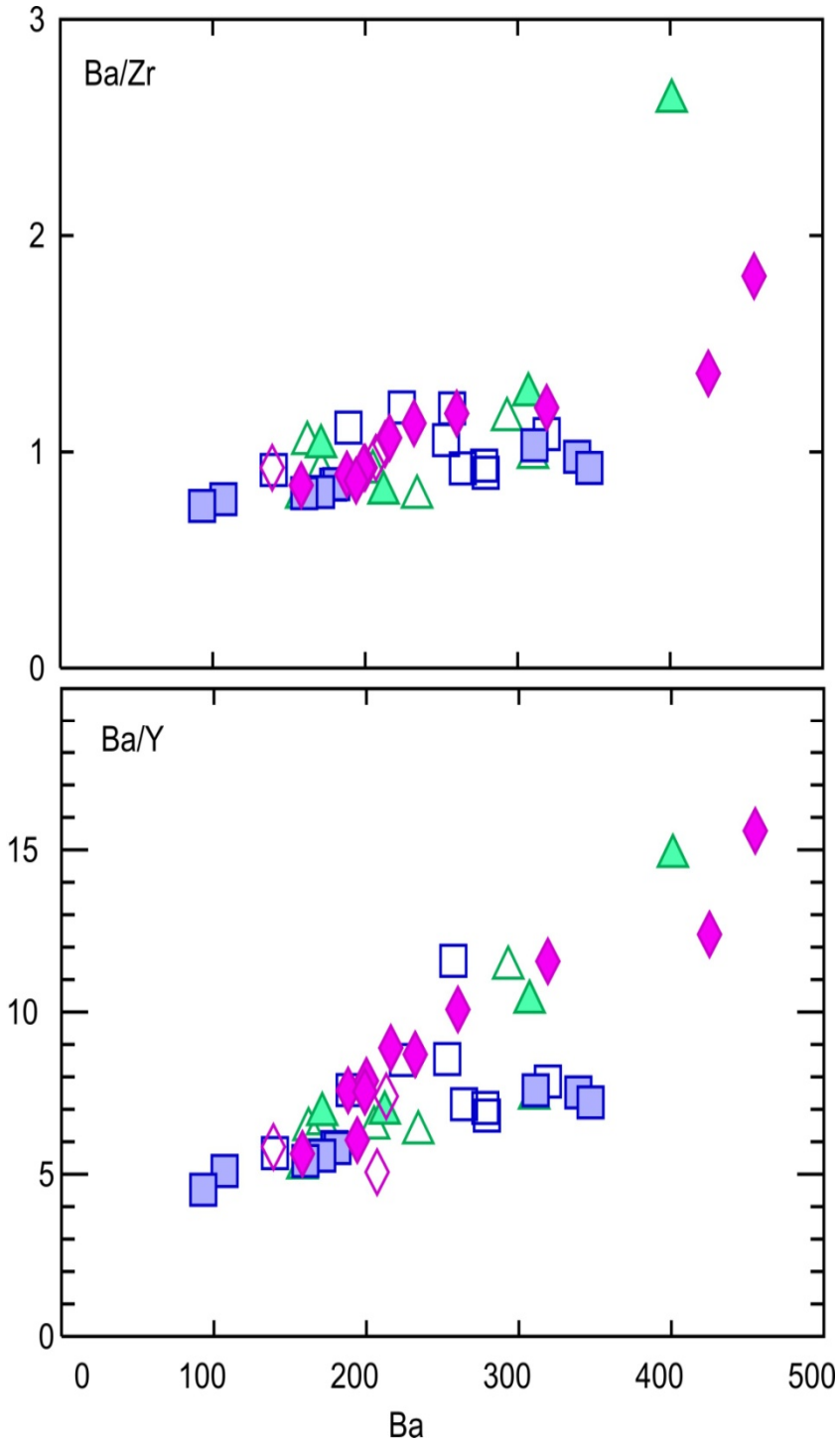

Fig. 4.10. Process identification diagrams using moderately and strongly incompatible elements.

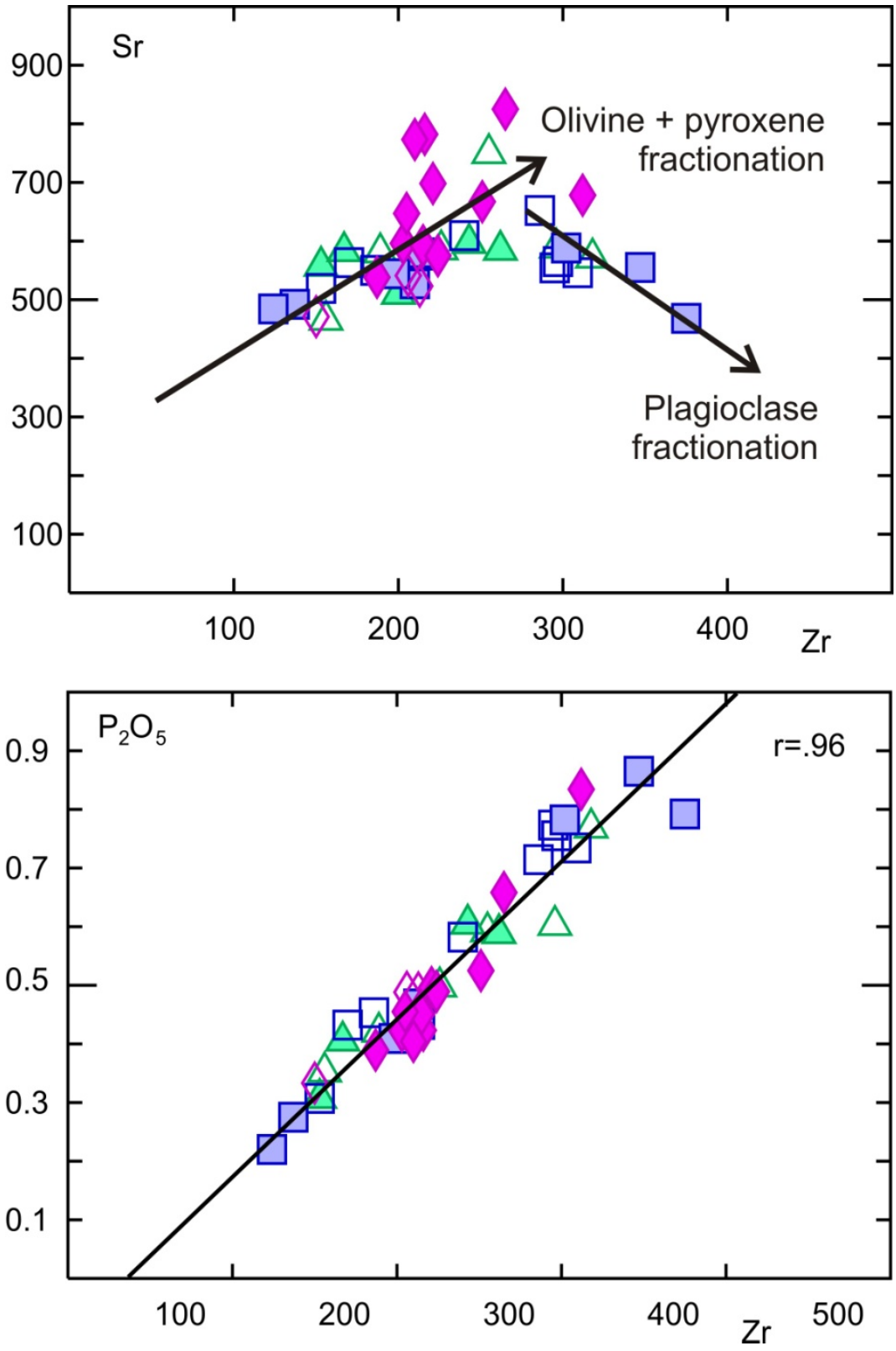

Fig. 4.11 Trace elements binary plots demonstrating the effect of open system fractionation on the chemical evolution of the investigated rocks.

Evolution of magma

Petrography studies of thin sections from Lunayyir flows showed that the basalt contains several phenocrysts of plagioclase and olivine, large phenocrysts of pyroxenes are not common. These phenocrysts were formed, before eruption, in the magma chamber. The similarity of the basalt of different episodes indicates that the parent magma remained constant in composition during all sequences of volcanic activities. Fractional crystallization was very slow to produce pronounce variation in the rocks of the successive basalt flows. This variation resulted in the swinging nature of the flows from basalt to trachy-basalt to even tephrite basanite.

Previous studies of the neighboring lava flows like Harat Khaybar, ithnayn and Kura (Camp et al. 1991) suggested a heterogeneous parent magma unlike the magma filling the chamber below Lunayyir. The Na_2O+k_2+O relation against SiO_2 may show different episode of volcanism, slight variation continued during the successive episodes of eruption the type of rocks mostly of basalt to trachy-basalt and tephrite basanite.(Figures 4.12 and 4.13).

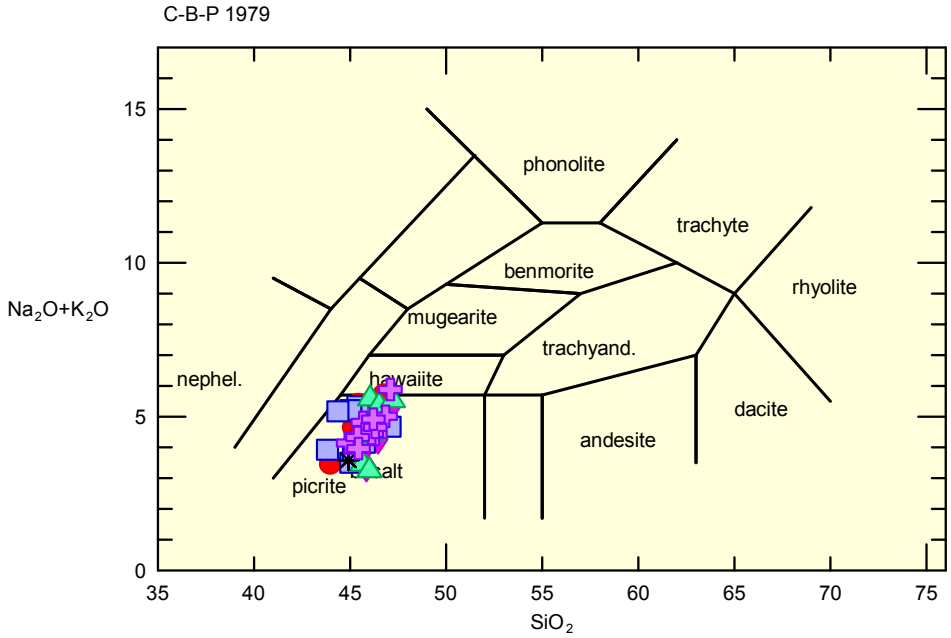

Fig. 4.12 shows all samples occurs in the basaltic to trachy basalt (cox 1980)

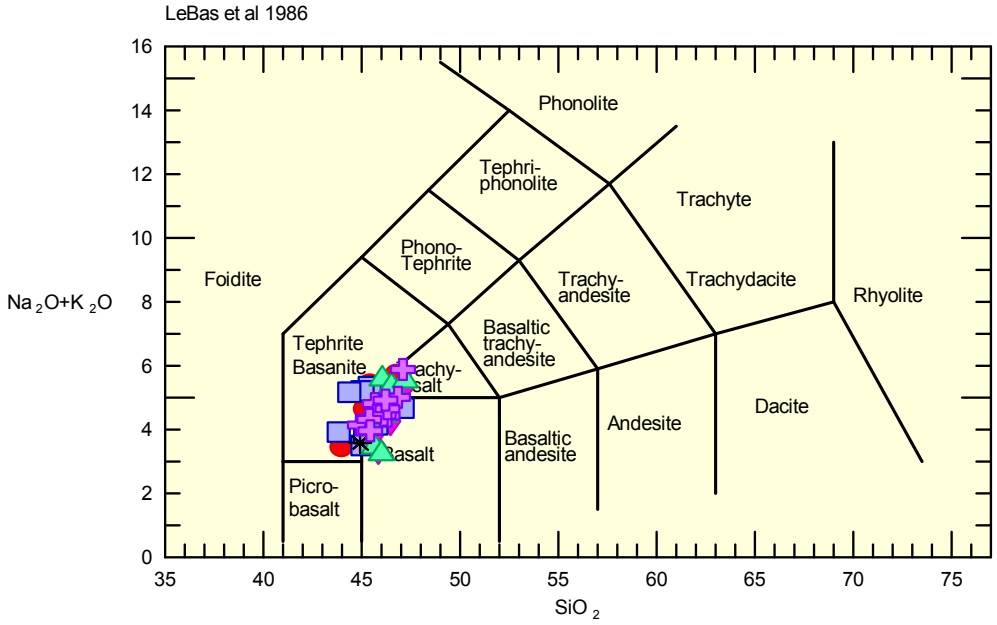

Fig. 4.13 shows all samples occurs in the basaltic to trachy basalt and little at tephrite basanite (Le Bas et al 1986)

Table 4.1 Major, trace, and Rare Earth Elements, and the CIPW normative mineralogy.

	Q1						Q2					Q3								
SAMPLE	HL 20	HL 21	HL 25	HL 31	HL 32	HL 33	HL 9	HL 14	HL 19	HL 27	HL 28	HL 22	HL 23	HL 29	HL 30	HL 34	HL 35	HL 36	HL 41	HL 43
SiO2	45.43	43.98	45.32	46.77	45.18	45.58	46.12	47.08	46.46	45.85	45.57	45.52	45.04	47.08	45.75	45.41	45.04	44.37	45.18	43.83
Al2O3	15.94	15.62	15.75	16.63	16.25	16.49	16.09	16.74	16.32	15.7	15.98	15.92	15.94	16.51	15.91	16.59	16.15	16.39	15.85	15.47
Fe2O3	15.1	12.34	12.03	15.41	15.11	12.98	11.69	12.72	13.39	10.96	12.66	15.37	12.61	12.21	12.94	15.88	15.9	13.78	12.7	9.8
CaO	7.63	11.21	9.65	7.05	8.51	9.78	10.26	8.23	9.4	11.79	10.03	7.77	10.6	9.22	9.77	7.79	8.04	8.97	10.13	12.84
MgO	4.68	7.58	7.02	4.59	5.78	7.07	6.61	6.1	7.34	7.22	7.93	4.87	8.13	6.2	8.09	5.01	4.9	4.38	7.97	6.18
Na2O	4.18	2.86	3.69	4.57	3.8	3.74	3.63	4.21	3.52	2.72	3.18	4.05	2.96	3.66	3.36	4.2	4.06	4.11	3.19	3.03
K2O	1.24	0.59	1.11	1.15	0.84	0.76	1.01	1.07	0.74	0.64	0.62	1.12	0.54	1.01	0.79	1.14	1.15	1.06	0.68	0.89
TiO2	3.15	1.97	2.14	3.22	2.72	2.25	2.03	2.29	2.45	1.76	1.96	3.25	2	2.15	1.94	3.26	3.24	2.69	1.97	1.65
MnO	0.23	0.19	0.19	0.22	0.22	0.19	0.2	0.2	0.2	0.18	0.19	0.23	0.19	0.19	0.2	0.23	0.24	0.22	0.2	0.16
P2O5	0.768	0.352	0.591	0.602	0.497	0.42	0.604	0.588	0.404	0.307	0.405	0.734	0.307	0.582	0.453	0.755	0.773	0.714	0.432	0.433
H2O-	0.17	0.25	0.27	0.15	0.15	0.2	0.16	0.16	0.11	0.43	0.21	0.15	0.15	0.42	0.24	0.17	0.21	0.47	0.23	0.68
H2O+	0.36	0.52	0.65	<0.01	0.09	0.11	0.1	<0.01	<0.01	1.27	0.24	0.25	0.06	0.82	0.34	0.09	0.38	0.69	0.27	1.92
∑	98.878	97.462	98.411	100.36	99.147	99.57	98.504	99.388	100.33	98.827	98.975	99.234	98.527	100.05	99.783	100.53	100.08	97.844	98.802	96.883Tabl
Mg#	38	55	54	37	43	52	53	49	52	56	55	39	56	50	55	38	38	39	55	56
Cr	90	280	440	70	190	210	300	260	250	410	340	130	270	250	380	120	140	160	330	290
Ni	25	116	129	16	36	98	113	96	103	141	138	33	127	77	149	29	31	23	127	99
Rb	20.9	10.2	19.3	18	11.9	11.5	17.4	18.3	11.7	10.2	8.6	17.8	8.2	13.5	12.7	16.4	18.4	16.2	10.4	17.3
Sr	571	465	749	588	585	580	596	584	509	557	582	546	519	609	550	565	554	652	563	576
Ba	310	162	293	234	205	171	307	212	158	401	171	279	140	253	224	278	319	264	189	257
Zn	143	99	89	114	117	94	93	96	108	88	92	141	91	96	95	138	138	122	104	82
Nb	38.5	19.4	36.5	37.5	29.1	23.8	37.7	35.3	24.6	20	20.4	36.4	17.6	42.4	27.8	39.1	37.9	33	22.2	35.8
Y	42.2	25.4	25.8	37.3	31.9	26.1	29.8	30.8	30.4	27.1	25	41	24.8	29.6	26.3	39.5	40.6	36.9	24.9	22.2
V	182	230	161	182	219	197	194	188	256	247	203	205	236	184	191	196	186	135	196	163
Cs	0.3	0.19	0.16	0.18	0.12	0.12	0.21	0.16	0.11	0.14	0.1	0.2	0.1	0.11	0.15	0.17	0.25	0.22	0.1	0.27
Sc	18	25	19	17	19	22	24	18	26	33	24	18	26	21	21	18	18	15	22	22
Co	44.1	51.3	44.6	41.9	49.3	48.1	43.1	43.7	53.1	46.4	49.3	45.9	54.1	39.8	49.5	45.2	45.3	38.4	49.1	35.2
Cu	45	68	51	34	33	61	58	65	60	86	66	46	63	50	55	41	43	34	61	59
Hf	6.8	3.7	5.3	6.4	5.1	4.2	4.9	5.4	4.5	3.6	3.7	6.3	3.4	5.2	4.1	6.3	6.3	6.3	3.6	4.5

Ta	2.4	1.2	2.4	2.4	1.8	1.5	2.3	2.3	1.6	1.2	1.3	2.2	1.1	2.6	1.7	2.4	2.4	2.1	1.3	2
Th	3.03	1.69	2.95	3.55	2.2	1.95	3.22	2.73	1.88	1.74	1.68	2.74	1.38	3.77	2.33	2.87	3.01	2.66	1.79	3.84
U	0.91	0.58	0.9	0.92	0.65	0.61	0.94	0.8	0.54	0.41	0.5	0.82	0.43	0.87	0.69	0.83	0.93	0.94	0.6	0.89
Zr	318	156	255	296	226	189	243	262	200	153	167	309	153	240	186	297	295	286	170	214
Mo	7	9	13	7	13	7	5	8	6	7	9	9	7	9	12	9	10	12	12	7
Sn	2	1	2	18	2	2	2	2	3	1	1	2	2	2	2	2	2	2	1	2
W	1	1	1	1	1	1	1	1	1	1	1	1	1	1	1	1	1	1	5	4
Mo	6	7	12	6	12	6	4	8	5	5	8	8	6	7	10	7	7	10	12	6
Be	1.9	1	1.6	1.8	1.4	1.2	1.5	1.6	1.2	1	1.1	1.7	1	1.5	1.2	1.7	1.8	1.8	1.1	1.5
Pb	4		2	15	2			2	2	4	7			4	2	5	7	5		2
S	0.04	0.21	0.18	0.02	0.45	0.1	0.09	0.01	0.01	0.11	0.37	0.09	0.12	0.1	0.24	0.06	0.07	0.58	0.21	0.01
As		11												5				6		
Bi							2													
Cd				0.6																
Sb				9					5											
	Rare Earth Elements																			
La	34.3	17	30.4	30.9	24.2	20.4	32.1	29	20.4	16.7	17.3	31.7	14.8	31.6	22.6	32.4	32.8	28.9	18.4	25
Ce	71.5	34.9	60.9	62	50	42	63	59	42.7	33	36	67	32.1	60.6	44.9	66.5	67.9	60.5	40	49.7
Pr	9.24	4.55	7.41	7.97	6.29	5.25	7.56	7.33	5.6	4.19	4.53	8.63	4.09	7.15	5.53	8.7	8.73	7.85	5.12	5.75
Nd	38	18.6	28.5	32	25.9	21.5	29.1	28.9	23.1	17.4	18.7	35.3	17.4	27.9	22.4	35.4	36.5	32.4	20.6	22
Sm	8.23	4.24	5.85	6.86	5.74	4.89	6.1	6.11	5.23	4.07	4.24	7.92	4.08	5.67	4.75	7.63	7.86	7.08	4.95	4.56
Eu	2.77	1.56	2.08	2.49	2.1	1.86	1.97	2.11	1.96	1.56	1.65	2.68	1.55	2.1	1.76	2.65	2.76	2.47	1.63	1.5
Gd	9.06	5.01	6.65	8.24	6.86	5.74	6.51	6.53	6.2	5.12	5.16	8.85	4.9	6.57	5.71	8.62	8.94	8.15	5.24	4.76
Tb	1.4	0.8	0.95	1.22	1.02	0.88	0.95	0.99	0.99	0.81	0.81	1.34	0.78	0.98	0.86	1.29	1.35	1.22	0.85	0.78
Dy	7.86	4.75	5.12	7.11	6.13	5.09	5.47	5.87	5.75	5.03	4.82	7.61	4.7	5.53	4.99	7.51	7.64	7.18	4.51	4.08
Ho	1.59	0.94	0.99	1.41	1.23	1.02	1.08	1.16	1.18	1.04	0.99	1.53	0.96	1.1	1.02	1.52	1.5	1.44	0.93	0.81
Er	4.54	2.81	2.84	4.28	3.61	2.98	3.16	3.47	3.44	3.11	2.84	4.5	2.74	3.28	3.01	4.29	4.48	4.15	2.8	2.51
Tm	0.64	0.38	0.38	0.55	0.49	0.41	0.44	0.46	0.48	0.41	0.37	0.59	0.38	0.45	0.39	0.61	0.62	0.57	0.34	0.29
Yb	3.98	2.42	2.38	3.84	3.3	2.58	2.81	3.1	2.92	2.75	2.46	3.98	2.42	2.83	2.63	3.77	3.76	3.66	2.48	2.19
Lu	0.63	0.39	0.36	0.57	0.5	0.4	0.42	0.48	0.46	0.42	0.38	0.6	0.37	0.46	0.4	0.58	0.59	0.55	0.35	0.33
	CIPW norms																			
or	7.53	3.64	6.79	6.86	5.08	4.57	6.13	6.43	4.41	3.93	3.75	6.77	3.28	6.09	4.75	6.79	6.91	6.54	4.13	5.62
ab	31.87	18.69	22.99	34.55	28.14	23.34	23.95	30.79	26.91	21.85	24.00	32.30	21.51	29.71	22.99	29.93	29.32	26.84	22.45	14.13
an	21.65	29.27	23.94	21.65	25.36	26.40	25.28	24.02	26.74	29.83	28.17	22.45	29.38	26.17	26.46	23.25	22.82	24.18	27.65	27.75

ne	2.43	3.56	5.05	2.41	2.57	4.79	4.11	2.95	1.68	1.11	1.93	1.49	2.28	1.03	3.22	3.20	3.04	5.14	2.86	7.18
di	9.91	21.32	17.43	7.92	11.86	16.31	18.51	11.03	14.21	23.20	16.25	9.88	18.21	13.48	16.08	8.82	10.34	14.30	17.04	29.97
ol	11.71	13.52	12.73	12.13	14.30	13.73	11.39	13.39	14.67	10.99	15.97	12.02	15.51	12.56	16.61	13.04	12.53	9.59	15.86	6.05
mt	6.93	5.25	5.46	6.90	6.26	5.53	5.25	5.59	5.77	4.91	5.14	7.04	5.21	5.40	5.08	6.96	6.99	6.35	5.17	4.88
il	6.15	3.91	4.21	6.17	5.28	4.35	3.96	4.42	4.69	3.47	3.81	6.31	3.90	4.17	3.75	6.24	6.26	5.34	3.84	3.35
ap	1.83	0.85	1.42	1.41	1.18	0.99	1.44	1.39	0.94	0.74	0.96	1.74	0.73	1.38	1.07	1.76	1.82	1.73	1.03	1.07
%AN	40.46	61.03	51.01	38.53	47.40	53.08	51.35	43.83	49.84	57.72	54.00	41.01	57.73	46.83	53.51	43.71	43.77	47.39	55.19	66.26

	Q4									Q5			Tertiary									
SAMPLE	HL 12	HL 15	HL 16	HL 24	HL 26	HL 37	HL 38	HL 39	HL 42	HL 1	HL 2	HL 40	HL 3	HL 4	HL 5	HL 6	HL 7	HL 8	HL 10	HL 11	HL 13	HL 17	HL 18
SiO2	45.77	45.8	46.19	46.05	45.91	45.65	46.52	47.22	46.01	46.01	46.06	44.92	45.67	46.17	46.32	46.12	47.1	44.91	46.85	46.31	46.21	45.39	45.44
Al2O3	16.34	16.74	16.57	15.95	16.29	16.12	16.5	15.59	16.97	16.48	16.19	15.8	15.75	16.01	16.44	16.35	16.61	15.37	16.74	16.65	16.62	16.21	16.51
Fe2O3	13.95	13.79	14.33	15.62	14.34	12.46	14.47	15.61	11.62	13.89	14.1	13.02	11.7	12.62	11.79	12.18	13.43	11.85	12.49	13.11	11.32	13.99	12.63
CaO	9.33	9.19	8.7	7.26	9	10.36	7.93	7.3	10.71	8.68	8.6	10.7	9.82	9.18	9.25	9.01	7.74	10.37	8.94	9	8.85	9.13	9.87
MgO	6.67	6.15	6.83	4.48	6.89	8.66	4.42	4.32	8.21	6.53	6.96	7.98	7.33	7.45	6.78	6.47	4.6	7.97	6.66	6.68	5.78	6.27	7.04
Na2O	3.56	3.62	3.71	4.26	3.69	2.94	4.2	4.09	2.88	3.7	3.64	3	3.79	3.86	3.57	3.61	4.51	3.15	4.15	3.84	3.67	3.55	3.33
K2O	0.74	0.75	0.74	1.32	0.73	0.51	1.15	1.43	0.36	0.9	0.89	0.58	1.02	0.81	0.85	0.84	1.37	0.99	0.86	0.81	1.25	0.77	0.63
TiO2	2.47	2.56	2.52	3.18	2.53	1.86	3.05	3.2	1.63	2.71	2.72	2.01	2.11	2.26	2.19	2.21	2.26	2.21	2.31	2.35	2.27	2.61	2.11
MnO	0.21	0.2	0.21	0.25	0.21	0.19	0.21	0.24	0.18	0.21	0.21	0.2	0.18	0.19	0.17	0.18	0.23	0.19	0.18	0.21	0.17	0.21	0.19
P2O5	0.434	0.468	0.432	0.865	0.409	0.275	0.782	0.792	0.22	0.488	0.487	0.333	0.496	0.422	0.423	0.404	0.834	0.525	0.451	0.455	0.658	0.489	0.389
H2O-	0.15	0.22	0.11	0.17	0.12	0.33	0.25	0.15	0.24	0.06	0.13	0.24	0.42	0.22	0.58	0.78	0.22	0.41	0.19	0.18	0.95	0.17	0.42
H2O+	0.12	0.04	<0.01	0.35	<0.01	0.14	0.3	<0.01	0.29	0.03	<0.01	0.18	0.46	0.08	1.64	1.65	0.25	0.89	<0.01	0.2	2.34	0.25	0.38
∑	99.744	99.528	100.34	99.755	100.12	99.495	99.782	99.942	99.32	99.688	99.987	98.963	98.746	99.272	100	99.804	99.154	98.835	99.821	99.795	100.09	99.039	98.939
Mg#	49	47	49	36	48	58	38	35	59	48	49	55	55	54	53	52	40	57	51	50	50	47	52
Cr	200	220	220	150	180	270	70	70	190	160	190	230	360	390	300	270	240	360	280	330	190	180	220
Ni	87	66	87	27	85	129	31	19	123	78	92	120	126	156	124	118	38	153	118	113	82	67	84
Rb	11.3	11.7	10.9	22	10.7	7.6	17.3	23.6	4.9	13.8	14.4	8	18.9	13.1	12.7	12.8	23.6	18.8	14.1	13	22	12.4	9.6
Sr	579	580	527	555	544	492	588	468	484	541	523	471	698	596	782	773	678	667	592	647	825	575	538

Ba	179	181	171	339	160	107	311	347	93	213	207	139	260	216	200	188	425	455	199	232	319	194	158
Zn	112	108	116	149	105	91	133	161	89	133	115	101	86	94	89	89	107	99	92	98	89	117	102
Nb	23.5	25.4	23.7	42.7	23.7	14.4	52.2	40.9	11.5	28.2	47.6	17.5	37.2	29.8	30.6	29.9	46.6	39.2	31.2	30.1	46.1	25.8	20.7
Y	30.7	31.2	30.7	45.1	29.6	21	41	48.1	20.6	28.8	40.9	23.8	25.8	24.3	25.4	24.8	34.3	29.2	26.4	26.7	27.6	32.1	28.1
V	245	234	249	152	233	213	175	169	213	206	216	223	172	234	212	218	139	223	208	215	170	234	225
Cs	0.14	0.13	0.13	0.29	0.1	0.11	0.18	0.28	0.04	0.14	0.12	0.07	0.17	0.17	0.16	0.15	0.23	0.23	0.13	0.16	0.17	0.14	0.11
Sc	23	22	23	17	24	27	19	20	27	22	23	27	25	22	22	22	15	25	19	20	19	23	24
Co	53.2	50.2	54.3	42.1	50.9	50.9	39.7	39.4	50.3	46.1	49.4	50.9	41.8	52.5	46.3	46.9	36.3	50.7	47.8	50	39.5	50.4	51.6
Cu	55	51	52	39	49	73	44	40	60	54	58	68	76	72	68	76	40	66	65	68	54	49	51
Hf	4.7	4.4	4.5	7.3	4.4	2.9	6.5	7.9	2.6	4.3	4.7	3.4	4.7	4.3	4.5	4.4	6.3	5.1	4.4	4.3	5.3	4.9	4.1
Ta	1.5	1.6	1.5	2.6	1.5	0.8	4.1	2.4	0.7	1.6	2.8	1.1	2.3	1.8	1.8	1.8	2.9	2.3	1.9	1.8	2.7	1.6	1.3
Th	1.87	1.87	1.68	3.39	1.76	1.27	3.21	4.69	0.9	2.25	5.64	1.38	3.08	2.1	2.25	2.14	3.68	3.55	2.24	2.21	3.67	2.05	1.66
U	0.64	0.6	0.46	1.07	0.5	0.36	2.75	1.18	0.26	0.65	14.6	0.45	0.89	0.6	0.63	0.61	1.17	0.97	0.59	0.72	0.78	0.62	0.51
Zr	211	213	210	347	198	137	302	375	124	206	213	150	221	203	216	210	312	251	215	205	265	224	187
Mo	7	10	8	11	5	7	6	6	5	6	6	6	9	8	6	4	14	6	5	10	4	8	10
Sn	4	2	2	3	2	1	2	36	2	2	2	1	2	2	2	2	2	7	2	2	2	2	2
W	1	1	1	1	1	4	5	4	4	5	5	5	5	1	1	1	1	1	1	1	1	1	1
Mo	7	9	7	10	4	7	5	5	5	6	5	5	9	7	5	3	13	5	4	9	3	7	9
Be	1.2	1.3	1.2	2.1	1.2	0.9	1.8	2.1	0.7	1.3	1.3	1	1.5	1.2	1.3	1.4	2	1.4	1.2	1.3	1.7	1.3	1.1
Pb	2	5		5	2	3		34	2	2	3		2	6	3	2	3	6		4		4	3
S	0.2	0.17	0.02	0.09	0.02	0.07	0.06	0.03	0.22	0.01	0.01	0.05	0.07	0.03	0.01	0.01	0.24	0.07	0.01	0.06	0.02	0.12	0.21
As			6					6					9					6			5		
Cd								1.4														0.5	
Sb				5															11		9	5	
Rare Earth Elements																							
La	20.9	21.2	20.7	38.4	20.2	12.9	31.9	36.5	10.3	23.8	23.1	15.2	28.8	22.8	24.6	23.4	40	31.6	24.9	23.9	35.4	22.7	18.4
Ce	44.3	45.2	43.2	79.7	42.1	30.3	72.8	81.5	24.2	51.6	51.5	3.7	59.6	46.5	48.4	47.4	79.4	60.8	50	49.2	66.1	47.6	38.4
Pr	5.8	5.91	5.6	10.3	5.49	3.94	9.3	10.65	3.25	6.57	6.75	4.45	7.17	5.89	6.08	6	9.89	7.44	6.37	6.11	8.04	6.2	5.04
Nd	24.2	24.5	23.9	42.6	22.8	16.5	37.7	43.9	13.7	26.4	27.3	18	27.6	23.6	24.7	23.9	38.6	29.6	25.5	24.5	31.4	26.2	21.3
Sm	5.48	5.57	5.34	9.15	5.14	4.06	8.61	9.66	3.42	6.11	6.87	4.27	5.81	5.14	5.38	5.27	7.54	6.19	5.46	5.41	6.34	5.9	4.83
Eu	1.93	2.02	1.94	3.06	1.99	1.31	2.65	2.98	1.29	1.93	1.93	1.51	1.97	1.75	1.68	1.71	2.36	1.99	1.86	1.84	2.15	2.02	1.78
Gd	5.96	6.29	6.08	10.2	6.3	4.15	8.85	10.25	3.88	6.11	7.18	4.62	6.09	5.27	5.24	5.36	7.95	6.39	5.71	5.67	6.75	6.7	5.69
Tb	0.94	0.97	0.95	1.52	0.98	0.72	1.41	1.63	0.69	0.97	1.35	0.78	0.95	0.82	0.79	0.81	1.17	0.97	0.86	0.86	0.98	1.02	0.91
Dy	5.67	5.71	5.78	8.85	5.65	3.88	7.9	9.13	3.74	5.24	7.85	4.31	4.84	4.66	4.56	4.77	6.41	5.41	4.94	5.01	5.22	6.05	5.19

Ho	1.17	1.16	1.16	1.72	1.16	0.82	1.49	1.81	0.82	1.09	1.65	0.94	0.96	0.9	0.89	0.92	1.31	1.07	0.97	0.95	1.04	1.22	1.1
Er	3.38	3.4	3.33	5.1	3.42	2.4	4.46	5.23	2.46	3.25	4.86	2.68	2.9	2.54	2.52	2.61	3.82	3.04	2.78	2.72	3	3.47	3.15
Tm	0.47	0.47	0.44	0.7	0.47	0.32	0.59	0.66	0.3	0.42	0.65	0.37	0.43	0.34	0.34	0.35	0.54	0.42	0.36	0.36	0.39	0.47	0.43
Yb	2.96	3.01	2.91	4.49	2.97	2.07	4.06	4.79	1.98	2.76	4.18	2.37	2.45	2.23	2.1	2.15	3.31	2.66	2.26	2.22	2.44	3.1	2.85
Lu	0.45	0.47	0.45	0.71	0.45	0.31	0.6	0.74	0.31	0.42	0.64	0.34	0.39	0.33	0.33	0.33	0.51	0.4	0.34	0.34	0.37	0.48	0.44
CIPW norms																							
or	4.44	4.51	4.41	7.95	4.36	3.07	6.92	8.56	2.17	5.39	5.32	3.51	6.21	4.88	5.18	5.14	8.29	6.05	5.15	4.86	7.69	4.66	3.83
ab	26.52	27.95	28.37	33.81	26.88	22.56	34.02	35.07	23.67	28.57	28.49	20.53	22.70	26.09	28.53	29.22	32.52	20.80	28.13	27.77	29.77	27.69	25.22
an	26.83	27.69	26.59	20.89	26.00	29.85	23.18	20.22	32.99	26.06	25.50	28.62	23.65	24.43	27.15	26.86	21.52	25.72	24.82	26.20	26.22	26.65	29.04
ne	2.21	1.74	1.78	1.59	2.53	1.52	1.17	0.00	0.66	1.72	1.44	2.97	5.60	3.90	1.42	1.32	3.54	3.66	4.02	2.83	1.39	1.67	2.04
di	14.06	12.67	11.45	8.27	13.35	16.71	9.55	9.25	15.97	11.65	11.69	19.06	18.68	15.48	13.96	13.51	10.03	19.20	13.83	13.06	12.10	13.39	15.14
ol	14.32	13.41	15.71	12.40	15.17	17.09	10.71	10.44	16.22	14.06	15.01	15.39	12.46	14.28	12.95	13.06	12.16	13.41	12.97	14.01	11.07	13.60	14.30
mt	5.85	5.99	5.88	6.91	5.90	4.97	6.72	6.90	4.63	6.19	6.19	5.22	5.39	5.56	5.52	5.57	5.58	5.56	5.59	5.67	5.69	6.10	5.38
il	4.76	4.95	4.82	6.15	4.86	3.60	5.90	6.16	3.16	5.22	5.23	3.91	4.13	4.38	4.29	4.35	4.39	4.34	4.44	4.53	4.49	5.08	4.12
ap	1.02	1.10	1.01	2.04	0.96	0.65	1.84	1.86	0.52	1.15	1.14	0.79	1.18	1.00	1.01	0.97	1.98	1.26	1.06	1.07	1.59	1.16	0.93
%AN	50.29	49.76	48.38	38.19	49.16	56.96	40.53	36.57	58.22	47.70	47.23	58.23	51.02	48.36	48.76	47.90	39.83	55.29	46.87	48.54	46.83	49.05	53.53

CHAPTER 5

EARTHQUAKE DATA ANALYSIS

Earthquake swarms are generated commonly by major strike-slip faulting on transform faults (Sykes 1967;Tatham and Savino 1974) within volcanically active regions. They accommodate with some combination of surface deformation, local resistivity changes, summit deflation, ground cracking, increased heat flow and suggesting some transport of magma within the same region. For a given swarm, the fault plane solutions may exhibit one of two orientations: either both nodal planes are oblique to the epicentral trend, creating an en-echelon fault plane pattern (Hill 1977), or one of the nodal planes coincides with the epicentral trend. Surface deformation modeling studies (Pollard and Holzhausen 1979) have suggested that the strike of en-echelon fissures results from ascending dikes being reoriented by the stress field at the surface.

Saudi Geological Survey (SGS), King Abdulaziz City for science and technology (KACST) and King Saud University (KSU) deployed number of broadband seismic stations at Lunayyir area on April 2009 immediately after starting of earthquake activities (Fig. 5.1 , Table 5.1 and Appendix D). KACST seismic network consists of 10 short-period single component (vertical) seismic stations and one of Broad band, while KSU network composed of 8 seismic stations of short period with the same configuration of KACST stations. Each of short period seismic stations includes short period sensor (SS-1 seismometer), Quantira digitizer as seismic data logger (Q_{330}), Biler (20GB hard disk) for storing of recorded earthquakes; and 12-volt Battery and Solar panel for continuous charging. While, broadband stations were equipped with

Streckeisen STS-2 seismometer. The data acquired with sampling rate of 300 SPS for the broadband and short period as well. The Hard disk was changed every week and moved into the processing center at King Saud University where, the data were retrieved by a sun workstation. The waveform data is also saved as SEED format in the data Base. The continuous raw data as well as the analyzed waveform are saved on DVD. The KSU Data Center receives the raw waveform data and runs the Boulder Real Time Technologies (BRTT) Antelope System. This is a software package for managing real-time seismic network data and performing the basic network operations of detection, association and location of events as well as data archival. A short-term average-to-long-term average (STA/LTA) energy detector runs continuously and detects phase arrivals. The system attempts to locate the event if a number of arrivals are detected by the network within a specified time window.

Table 5.1. Geographic coordinates of KACST and KSU seismic stations at Harrat Lunayyir.

tation Code	Latitude (N)	Longitude (E)	Elevation (m)	Type of Sensor	Data Logger
STN01	25.2554	37.7698	1010	STS-2	Q_{330}
STN02	25.0618	37.6792	559	SS-1	Q_{330}
STN03	25.1851	37.8929	946	SS-1	Q_{330}
STN04	25.2640	37.7805	970	SS-1	Q_{330}
STN05	25.1637	37.5574	393	SS-1	Q_{330}
STN06	25.1934	38.0424	600	SS-1	Q_{330}
STN07	25.4015	37.9651	600	SS-1	Q_{330}
STN08	25.3823	37.6161	600	SS-1	Q_{330}
STN09	24.9631	37.9994	600	SS-1	Q_{330}
STN10	25.0120	37.6592	600	SS-1	Q_{330}
STN11	25.2877	37.8155	956	SS-1	Q_{330}
STN12	25.2708	37.5637	600	SS-1	Q_{330}
STN13	25.0072	38.0650	600	SS-1	Q_{330}
STN14	24.9802	37.8231	600	SS-1	Q_{330}
STN15	25.2204	38.0755	600	SS-1	Q_{330}
STN16	25.4202	37.9542	600	SS-1	Q_{330}
KSU01	25.2134	37.7794	1011	SS-1	Q_{330}
KSU02	25.2423	37.8026	957	SS-1	Q_{330}
KSU03	25.3030	37.7355	962	SS-1	Q_{330}
KSU04	25.2555	37.6571	551	SS-1	Q_{330}
KSU05	25.1989	37.6743	551	SS-1	Q_{330}

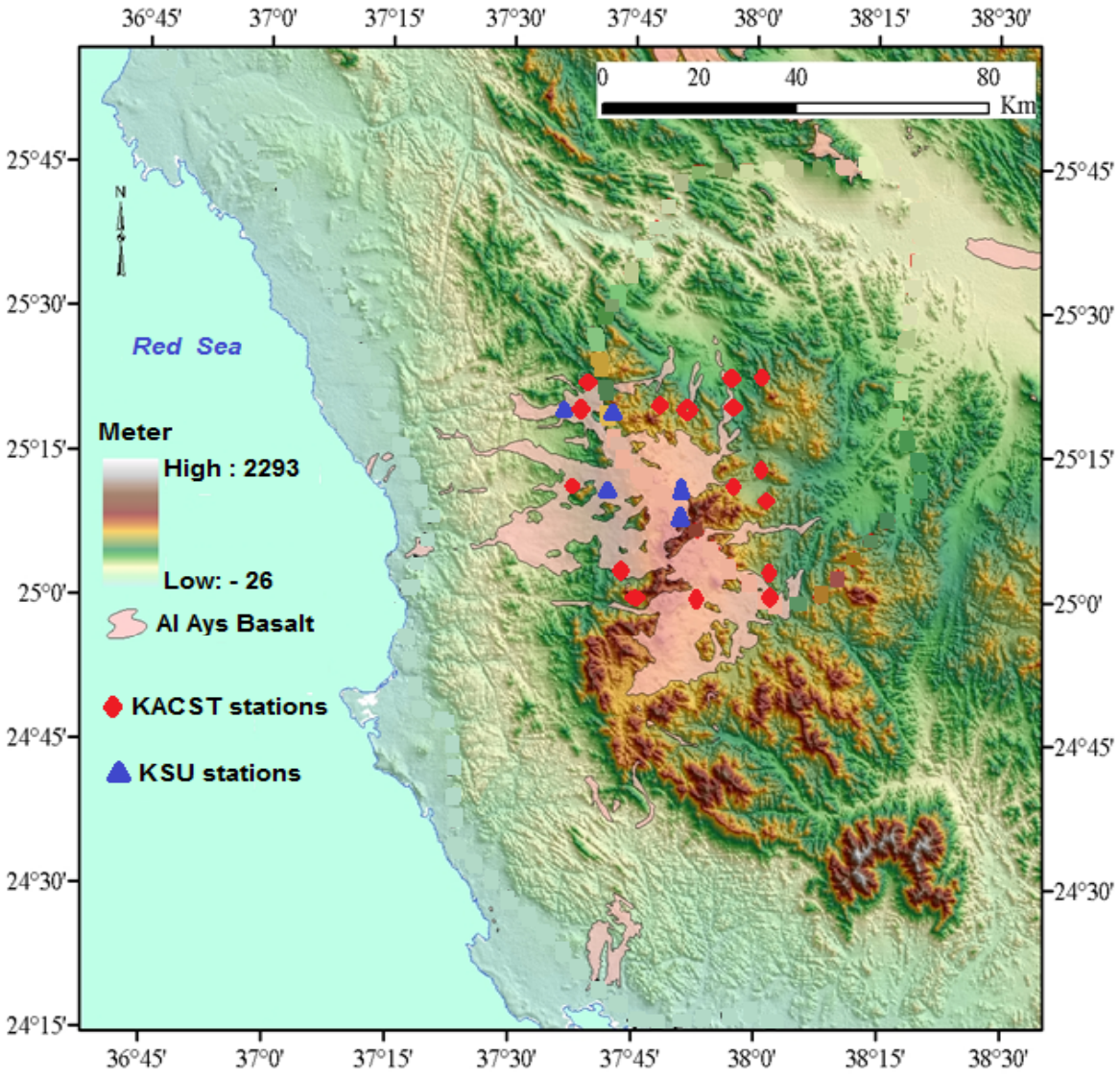

Fig. 5.1 Location map of KACST and KSU seismic stations in Harrat Lunayyir

RATE OF DECAY FOR AFTERSHOCKS SEQUENCE

Kisslinger (1997) stated that, the first aftershocks which occurring within the first 24 or 48 hours after the main shock defines the relevant rupture surface. Several studies around the world during the past years it is indicated that, the occurrence rate of aftershocks, N (t) obeys the modified Omori relation (Benito et al., 2004). The empirical relation for the rate of decay estimation has been suggested by Omori (Utsu, 1961). This relation combine the frequency of aftershocks n(t) per unit time t, following the main shock and represented by:

$$\mathbf{N(t) = K/t^{-c}}$$

Where **K** and **c** are constants and should be estimated for each region. 402 of well-located aftershocks (M ≥2.0) have been used in this study to estimate the rate of decay for Lunayyir earthquake swarm. The cyclic activation for aftershocks was indicated by their heterogeneities. Hence, first month of aftershock observation could be differentiated into three intervals; the first interval from 20 May till 4 June; the second from 5 to 12 June while the third from 13 – 19 June (Fig. 5.2). Each of these intervals has its own rate of decay that differs from the other two as follows;

$\mathbf{N(t) = 37.28\ t^{-0.60}}$, with $R^2 = 0.82$ (*for the first two weeks*),

$\mathbf{N(t) = 20872\ t^{-3.26}}$, with $R^2 = 0.7$ (*for the third week*), and

$\mathbf{N(t) = 5E{+}08\ t^{-5.33}}$, with $R^2 = 0.72$ (*for the last week*)

where **N (t)** being the number of events by day, **t** is the time in days after the main shock, and $\mathbf{R^2}$ is the correlation coefficient. Figure 5.2 indicates that, there are three different rates of decay through the first month of observation for the aftershocks of M ≥ 2.0. Another

noticeable feature for Lunayyir aftershock sequence is the releasing of major part of the cumulative seismic moment during the first hours after the main shock. Excluding the first day (20 May 2009), no event with local magnitude above 4.0 was recorded during the period of recording.

Figure 5.4 shows the recorded events for the period from 7th May - 15th August 2009 with magnitude > 3. It is cleared that more than 90% of the total energy has been released with small events which represents an important observation for releasing the energy continually and there is no chance for occurrence big event. This temporal variation in numbers of events with magnitude ranges could reflect the changing of stress level associated with upward magmatic intrusions.

A moderate (Mw~5.7) earthquake struck Al-Ays on May 19, 2009. The event was large enough to be detected and located by global networks at teleseismic distances. The region is generally believed to be aseismic and large earthquakes are rare in this part of the world. This event serves as a test case to illustrate the SGS location performance and demonstrate what can be done with broadband waveform data. Local information provided by the Saudi Geological Survey, locates this event near the town of Al-Ays, in Harrat Lunayyir (Ash Shaqah). Waveforms of this event and largest eight aftershocks (4 < Mw < 5.7) occurred in Harrat Lunayyir are for the period from April – June, 2009 are shown in Figures 5.5 and 5.6 respectively .

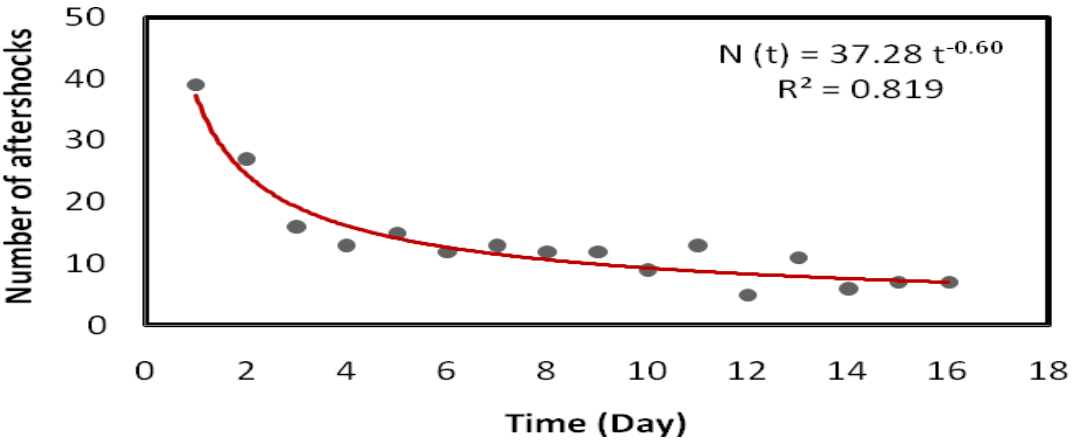

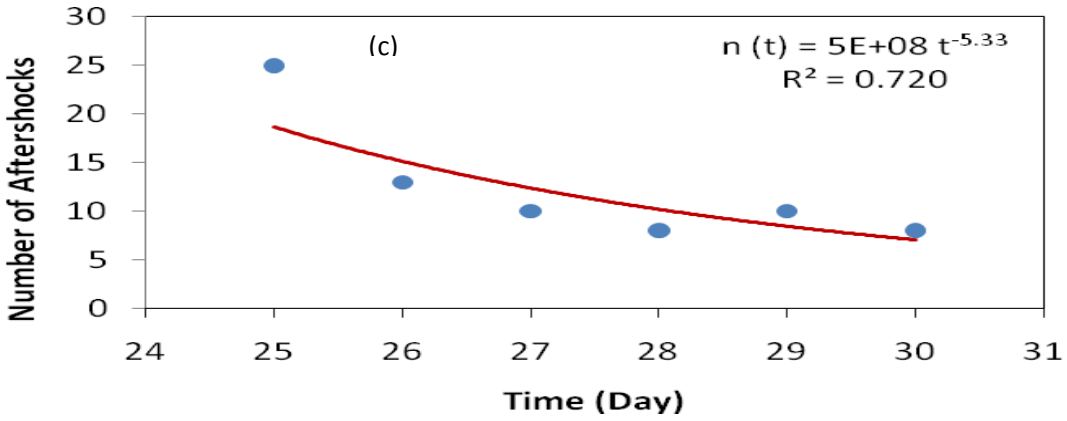

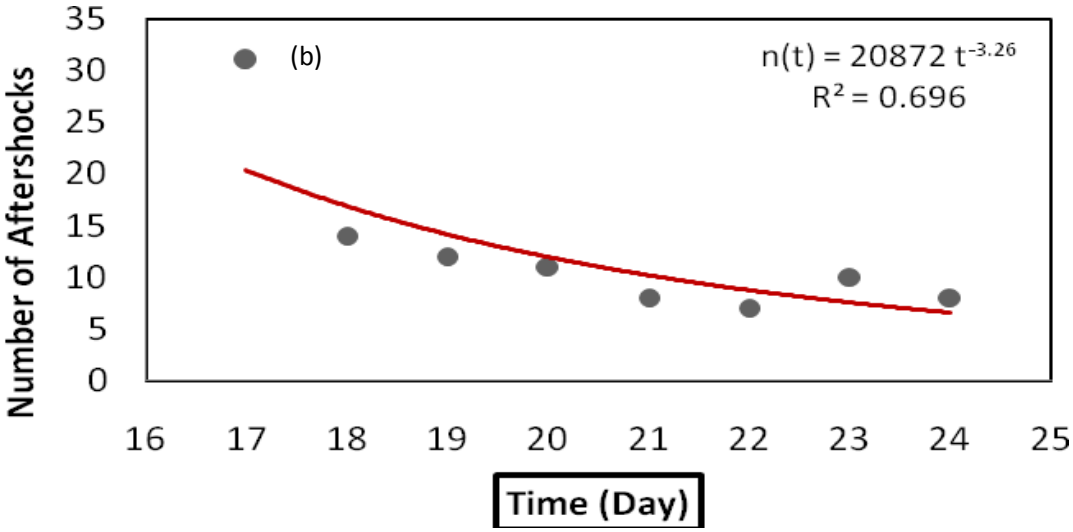

Fig. 5.2 Rate of decay for the aftershock sequence (M ≥ 2).

Fault plane solutions indicate that there are two major structural trends of NE-SW and NW-SE are prevailing at Lunayyir area. Sometimes these directions are slightly deviated into NNE-SSW or NNW-SSE, N-S. The predominant mechanism is normal faulting but it could be contaminated with strike-slip components. Events no.1,2,3,7,8,9,10,11,12,13 and 14 (Fig. 5.7 and table 5.2) have normal faulting mechanism with minor strike–slip components; While events no. 4,5 and 6 have normal faulting mechanism with large strike-slip component. The main trend of extensional stress pattern (*T*-axis) is in NE-SW direction while main trend of compressional stress (*P*-axis) is in NW-SE direction. This is correlated well with the field measurements for the ground cracks and fissures accompanied with the main shock.

In general, these directions correspond to the direction of transform faults crossing the Red Sea and offsetting the median trench and spreading axis of the Red Sea. The main cluster of epicenters corresponds to a cluster of hills composed of ancient Precambrian rocks. The hills were the site of two prehistoric basaltic eruptions as there are two chains of scoria cones sitting on top of them. One chain has five cones and the other three and both are aligned East–West.

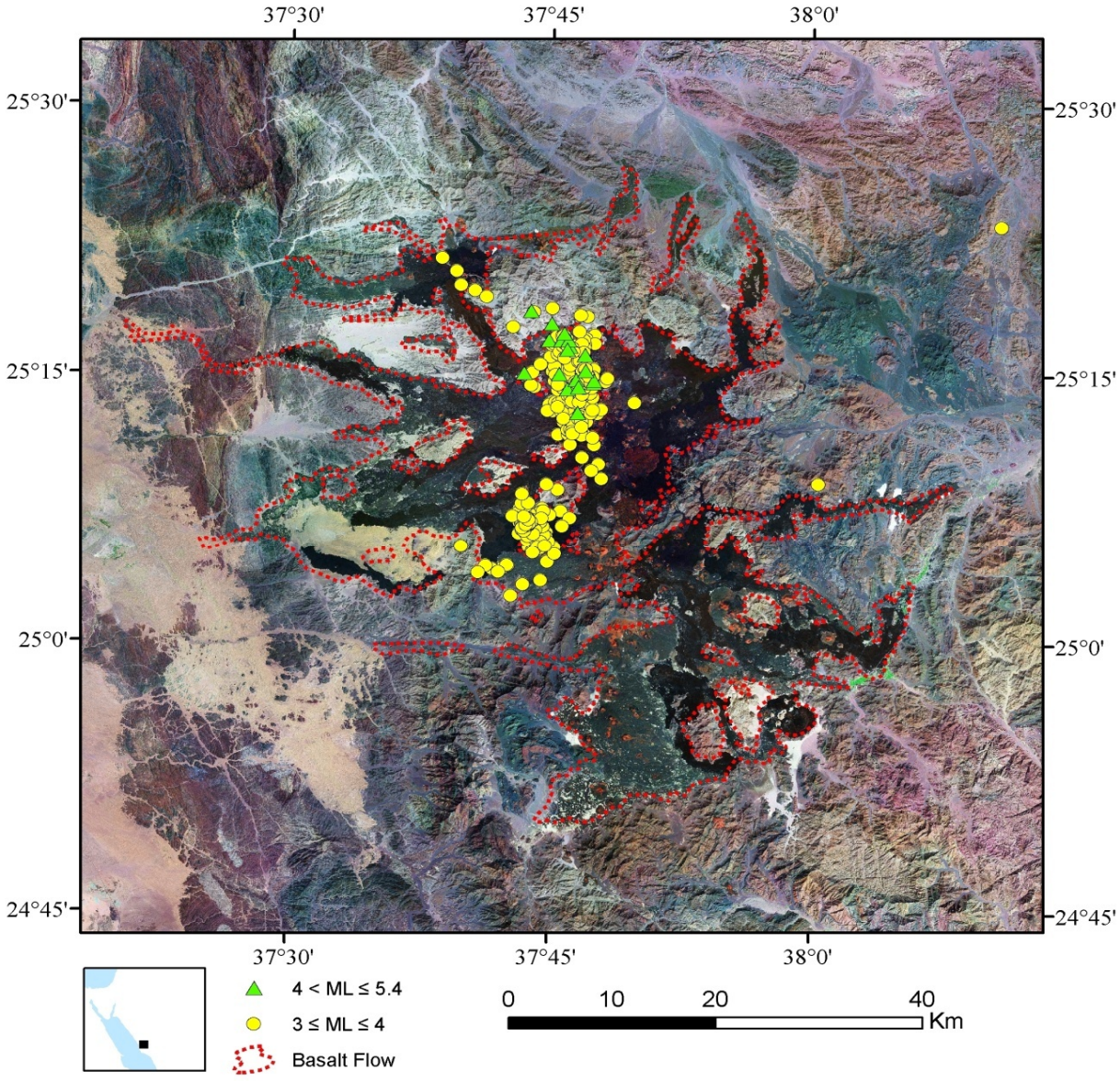

Fig. 5 3. Landsat- color composite image of Harrat Lunayyir showing recent seismicity which were located by the three networks. There is no erosion suggesting it may be the site of the historic eruption of 1000 years ago.

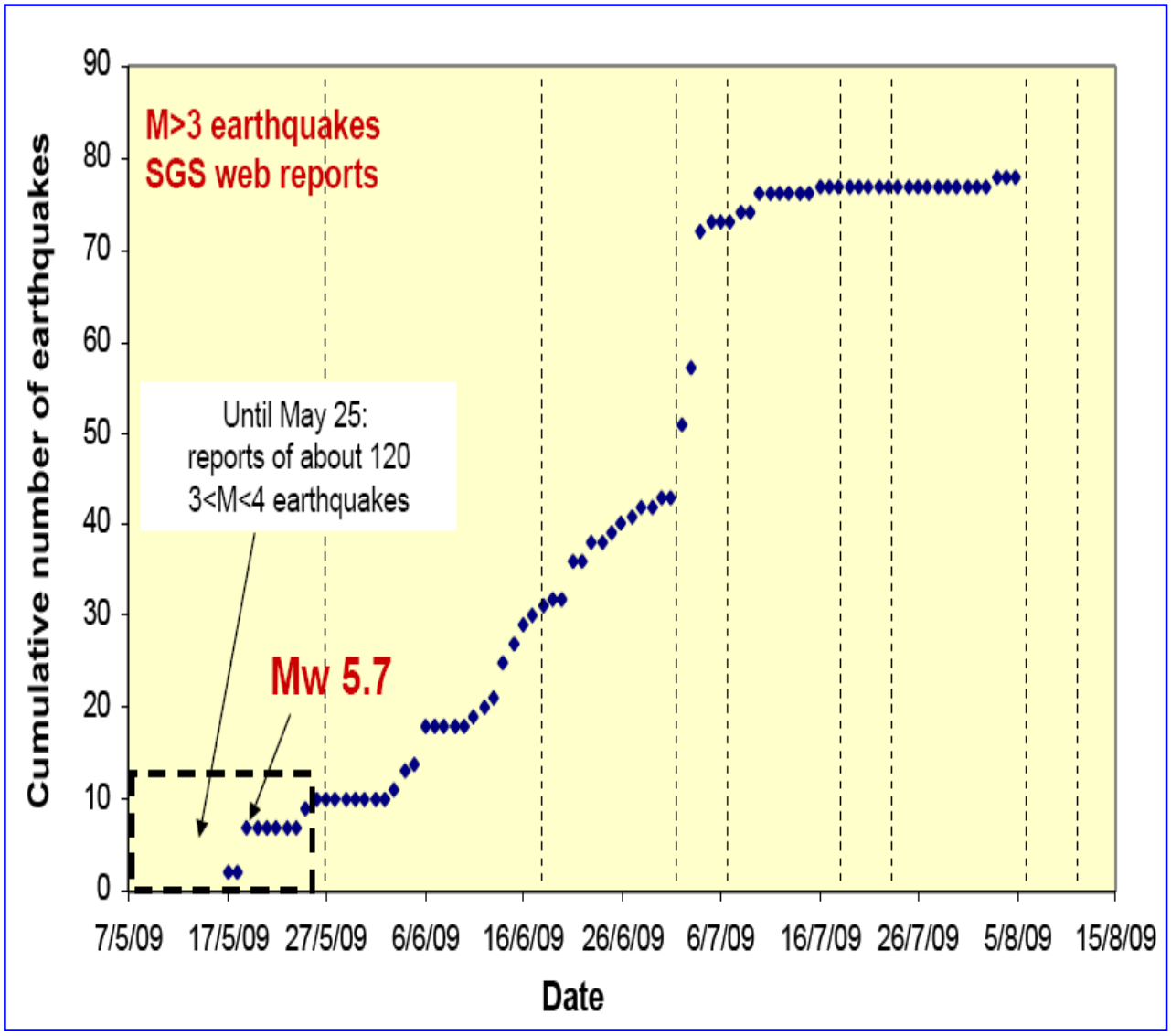

Fig. 5.Σ. A diagram showing the recorded events for the period from 7th May - 15th August 2009 with magnitudes> 3.

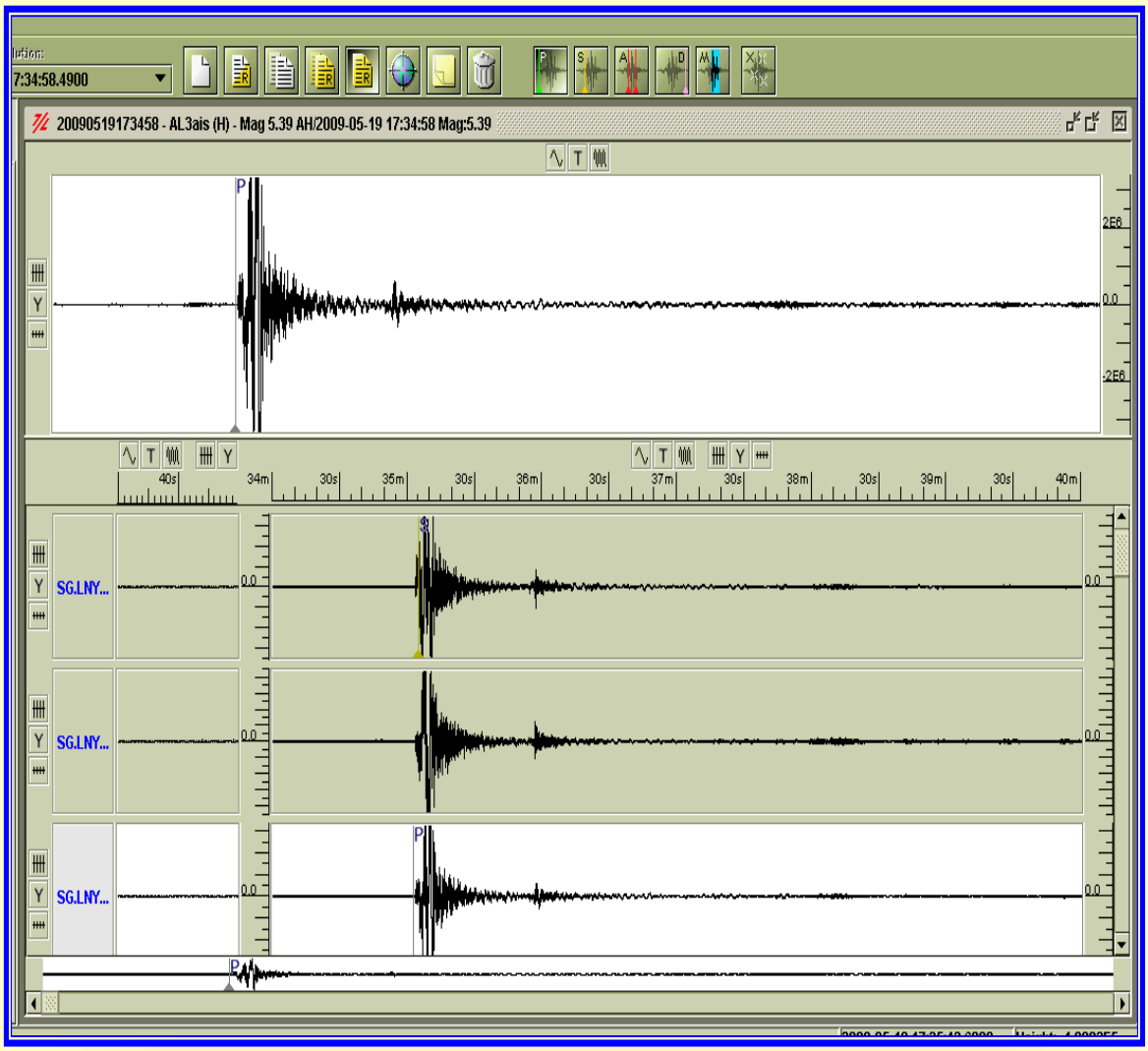

2009-05-19 17:34:58 earthquake (Main shock, M=5.39)

Fig. 5.5 Waveform of the main shock (Mw~5.7).

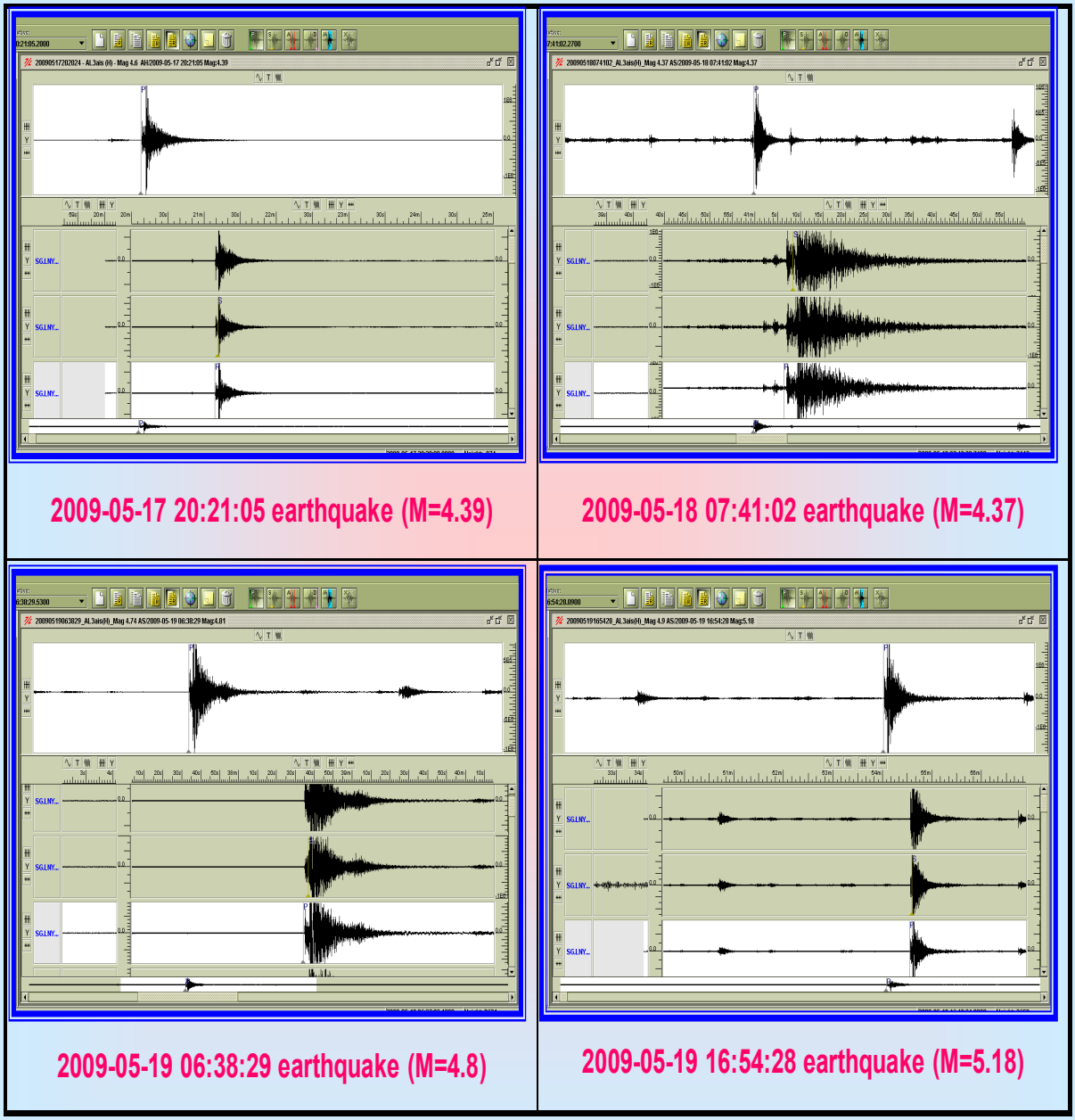

Fig. 5.6 a. Waveforms of large four aftershocks (4.3 < Mw < 5.2)

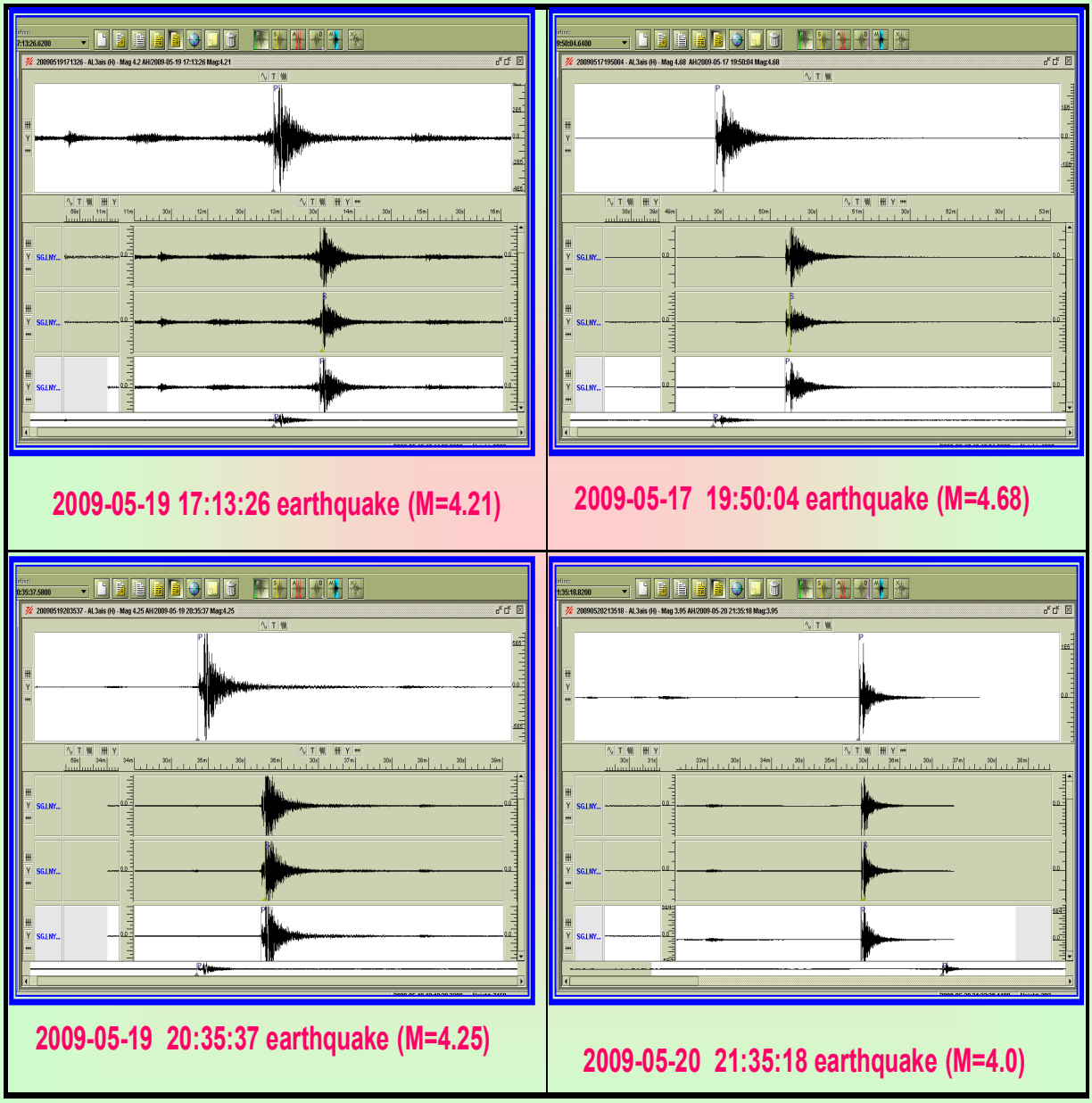

Fig. 5.6 b. Waveforms of large four aftershocks (4 < Mw < 4.7)

We combined waveform data from RAYN-GSN and EIL stations. Figure 5.8 shows the event location and stations used in the focal mechanism study of this event. We followed the grid search procedure described in Walter (1993) to find the best-fitting seismic moment, focal mechanism and depth for all stations using the appropriate velocity model of the Arabian Shield area (Al-Amri et al., 2008). Love and Rayleigh wave group velocities were modeled to estimate average one-dimensional seismic velocity model of the Arabian Shield.

Field investigation and focal mechanism solutions have revealed that the main shock was due to a primary coseismic rupture represented by a N137° (NW-SE) oriented normal faulting. The fault has a displacement of 1.1 m and dip of 48° SW. Secondary ruptures, trending NE-SW to ENE-WSW, have lesser displacements. During May 19th, 2009 earthquake, sympathetic activity occurred on N-S trending faults.

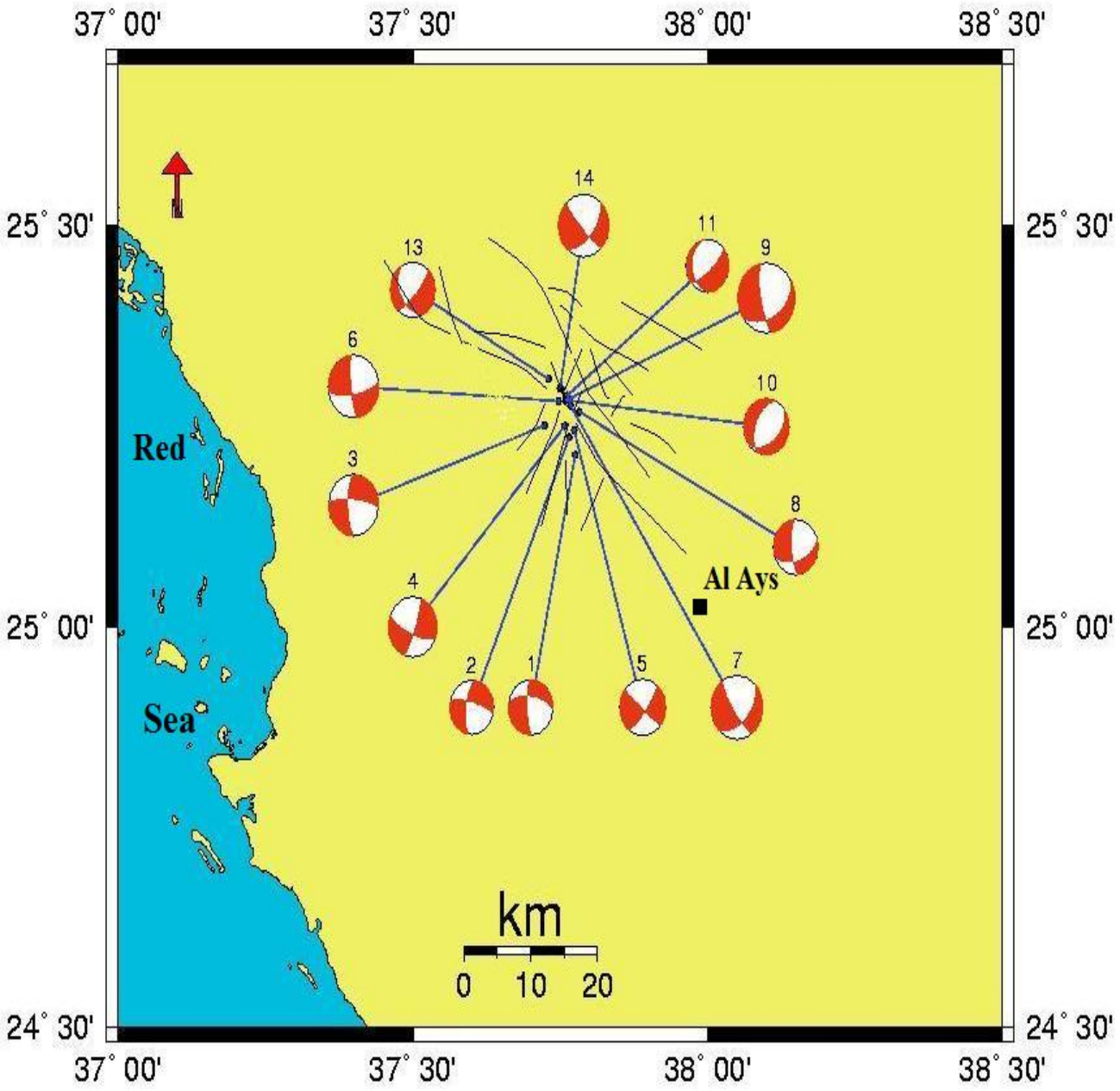

Fig. 5.7 Analysis of fault plane solutions for the largest fourteen events using the PMAN program (Suetsugu, 2003). It indicates that there are two major structural trends of NE-SW and NW-SE are prevailing at Lunayyir area.

Table 5.2 Earthquake parameters used for fault plane solutions

Event No.	Date (yyyy mm dd)	Origin Time h. min. sec	Location		Depth (Km)	Mag.
			Lat. (°N)	Long. (°E)		
1	2009 05 13	23 08 56	25.2148	37.7755	8.89	4.25
2	2009 05 17	19 20 27	25.2368	37.7655	7.78	4.15
3	2009 05 17	19 50 04	25.2515	37.7240	8.02	4.68
4	2009 05 17	20 21 04	25.2505	37.7577	8.13	4.60
5	2009 05 18	07 41 02	25.2453	37.7738	10.62	4.37
6	2009 05 19	06 38 29	25.2818	37.7478	7.76	4.81
7	2009 05 19	16 54 28	25.2763	37.7677	10.10	4.90
8	2009 05 19	17 13 26	25.2685	37.7825	6.37	4.20
9	2009 05 19	17 34 58	25.2820	37.7597	7.81	5.39
10	2009 05 19	18 20 00	25.2820	37.7665	9.62	4.29
11	2009 05 19	19 21 27	25.2885	37.7622	7.20	4.01
12	2009 05 19	19 26 58	25.2733	37.7653	8.23	4.04
13	2009 05 19	20 35 37	25.3093	37.7303	9.30	4.25
14	2009 05 20	19 57 16	25.2975	37.7505	8.49	4.79

Table 5.3. Crustal Velocity model used for determining seismicity parameters (Al-Amri et al. 2008)

Depth (km)	Thickness (km)	V_p (km/s)	V_s (km/s)
0	1	4.0	2.31
1	15	6.2	3.58
16	20	6.8	3.93
36	∞	7.9	4.30

Intensive ruptures, rock falls and land collapses have been observed in the epicentral area of the earthquake. In Al-Ays area, the general degree of damage indicates a maximum predominant intensity of VI (Fig. 7). Ground shaking from the largest event (M 5.4) may have caused light damage. Modified Mercalli Intensities (MMI) reach values of VI. Damage to buildings is expected to be light at these levels. The affected region has low level of urban area (0%) and a low level of cultivated area (0%). In urban areas more damage can be expected than in cultivated or natural areas. Population density in the source region is very low, fortunately not many people were affected. Region of highest ground motions is very sparsely populated as shown in Fig. 5.9 and in table 5.4.

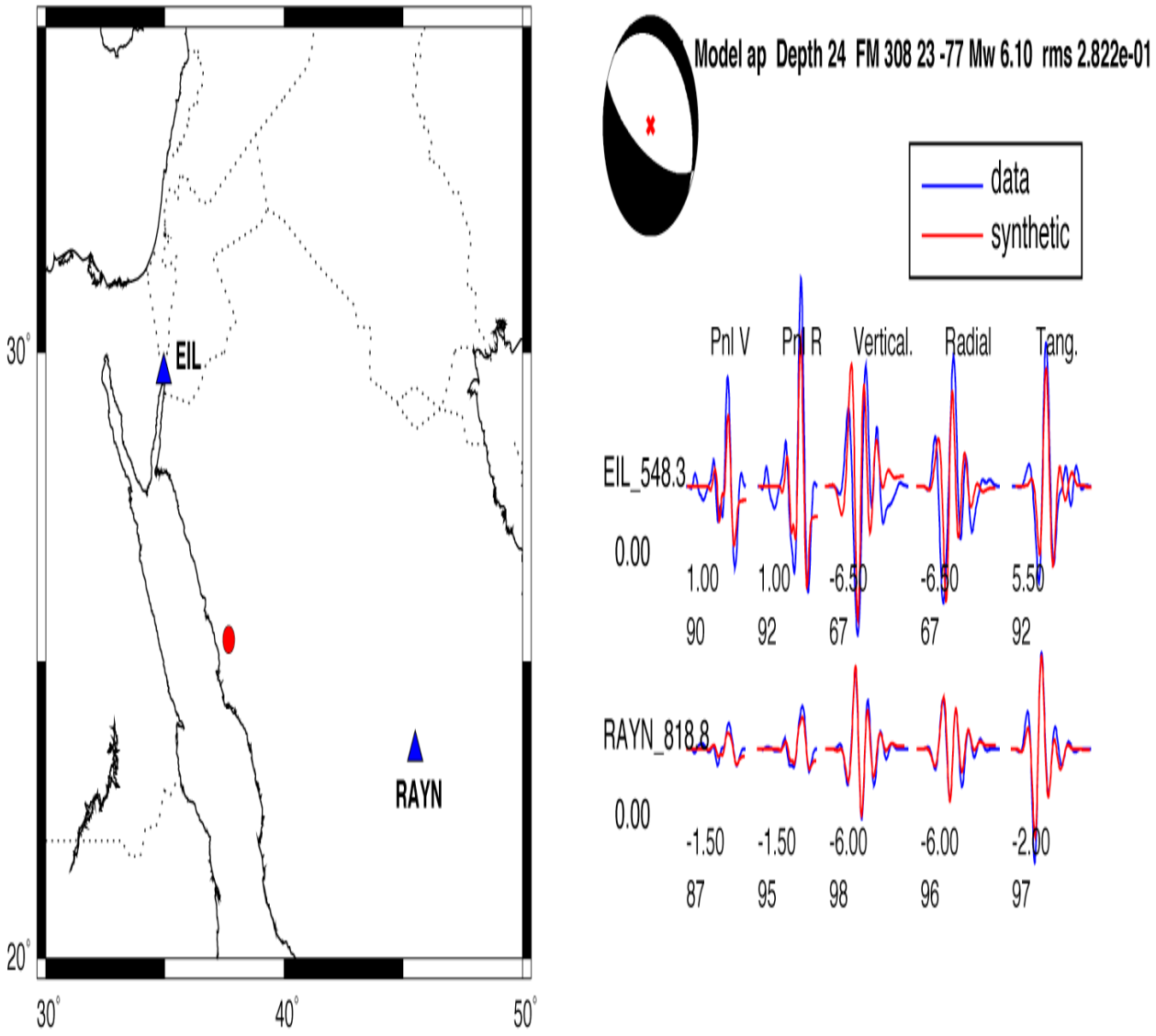

Fig.5.8 Observed (blue) and synthetic (Red) waveforms for the focal mechanism modeling of the May 19 earthquake. The best-fitting focal mechanism is also shown in the figure.

Table 5.4 : Distribution of felt ground motion in cities around Harrat Lunayyir

City	Modified Mercalli Intensity	Remarks
Al-Ayis	VI	**Strong felt**
Umm Laj	From V to less than VI	**Moderate felt**
Yanbu and Al-Wajh	From IV to less than V	**Light felt**
Tabuk and Almadinah	From III to less than IV	**Weak felt**

While the total length of surface rupture was extended up to 8 km and 90 cm of offset with the main shock. Accordingly, the total seismic moment has been calculated through this study as $\mathbf{M_0 = 8.64 \times 10^{24}}$ dyne/cm using the relation

$$\Delta\sigma = 2.5\, M_0/(S)^{3/2}$$

where S is the rupture area that can be estimated by L×(L/2), where L, is the length of surface rupture. Hence, the estimated average stress drop, Δσ, for the mainshock to be about 18.1 bars.

Examination of the total-intensity magnetic anomaly map of the Red Sea (Hall 1979) and remote sensing show that some magnetic anomalies are offset in a northeasterly direction and others are normal to the axial trough lineations. This could be due to the magnetic expression

of transform faults which cause disturbances of the magnetic anomalies. These faults trend in a northeasterly direction, but because of the short distance across the Red Sea it is not possible to ascertain their azimuths accurately from the magnetic anomalies. Hall (1979) mapped large-amplitude, long-wavelength linear magnetic anomalies along the shelves of the northern Red Sea and interpreted them as the expression of oceanic crustal strips of alternating remnant polarization that were emplaced during Tertiary seafloor spreading and subsequently buried by Miocene sedimentary deposits. These anomalies extend onto the coastal plain and inland as far as the exposed margin of the shield, where they are associated with the diabase dike swarm.

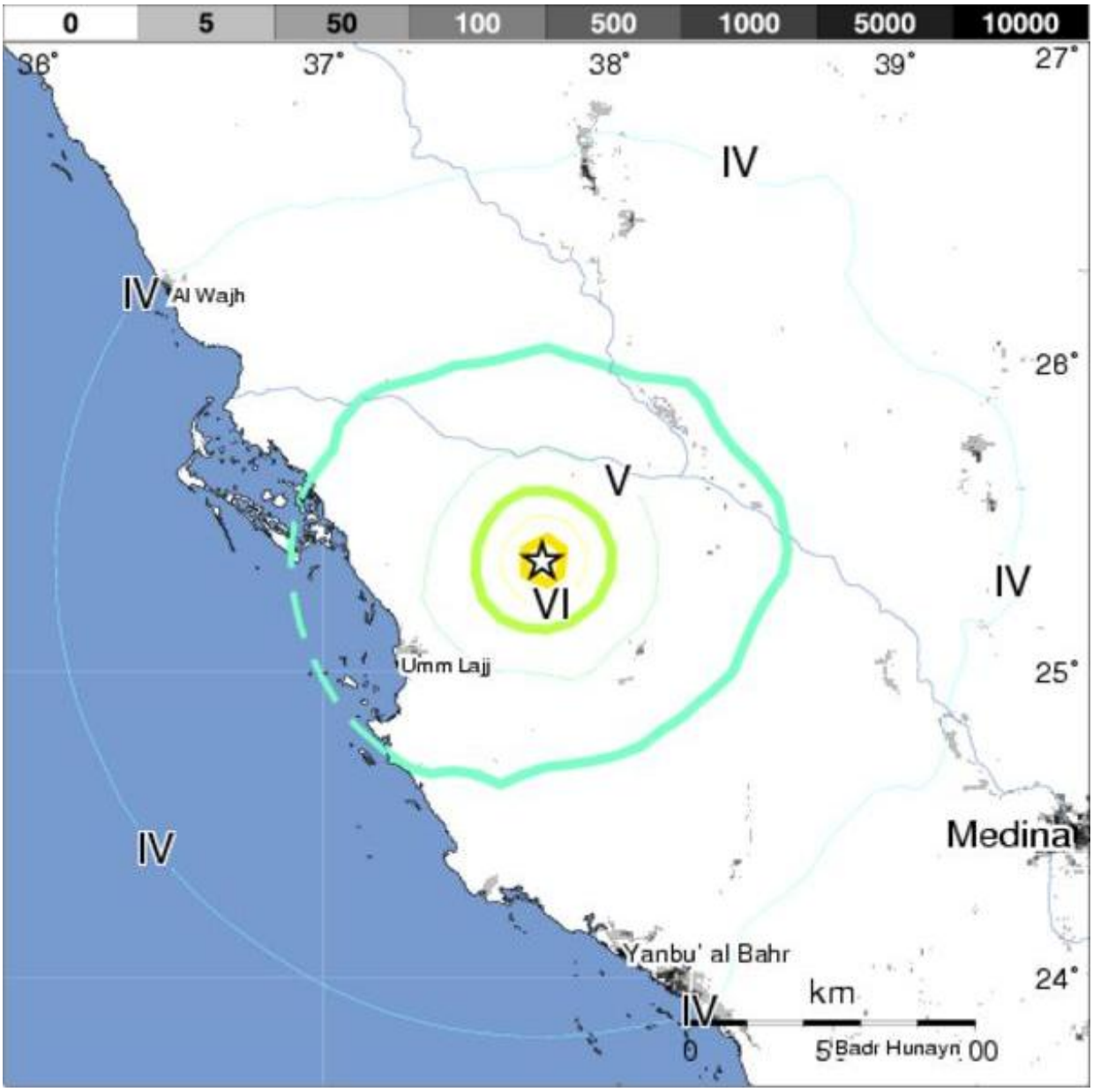

Fig. 5.9. Distribution of maximum intensity based on the largest earthquake affected the area. Population density in the source region is very low, and region of highest ground motions is very sparsely populated.

In order to investigate the relation between the epicentral distribution and the tectonic features, the locations of the faults inferred from the offset of magnetic anomalies were superimposed upon the seismicity map (Fig. 5.11). Alignment of epicenters and the northeast trending faults near latitudes 24.5° N could indicate that this fault extends northeastward on land. The proposed extension of the northeast fault has not been field checked and traced in Umm Laj (coastal plains), because of the presence of thick deposits of unconsolidated sediments.

The scatter of some epicenters in the shield area is due to the complexity of the rift faulting and inaccuracies involved in the calculation of the epicenters because of the poor azimuthal coverage of the existing stations. The low level of seismicity in the coastal plains is caused by the fact that some deep faults existed without surface traces. Marine epicenters are considered of less risk than land earthquakes or seaquakes close to the shore because of the high attenuation of seismic waves travelling through the rather soft and hot upper mantle material beneath the sea.

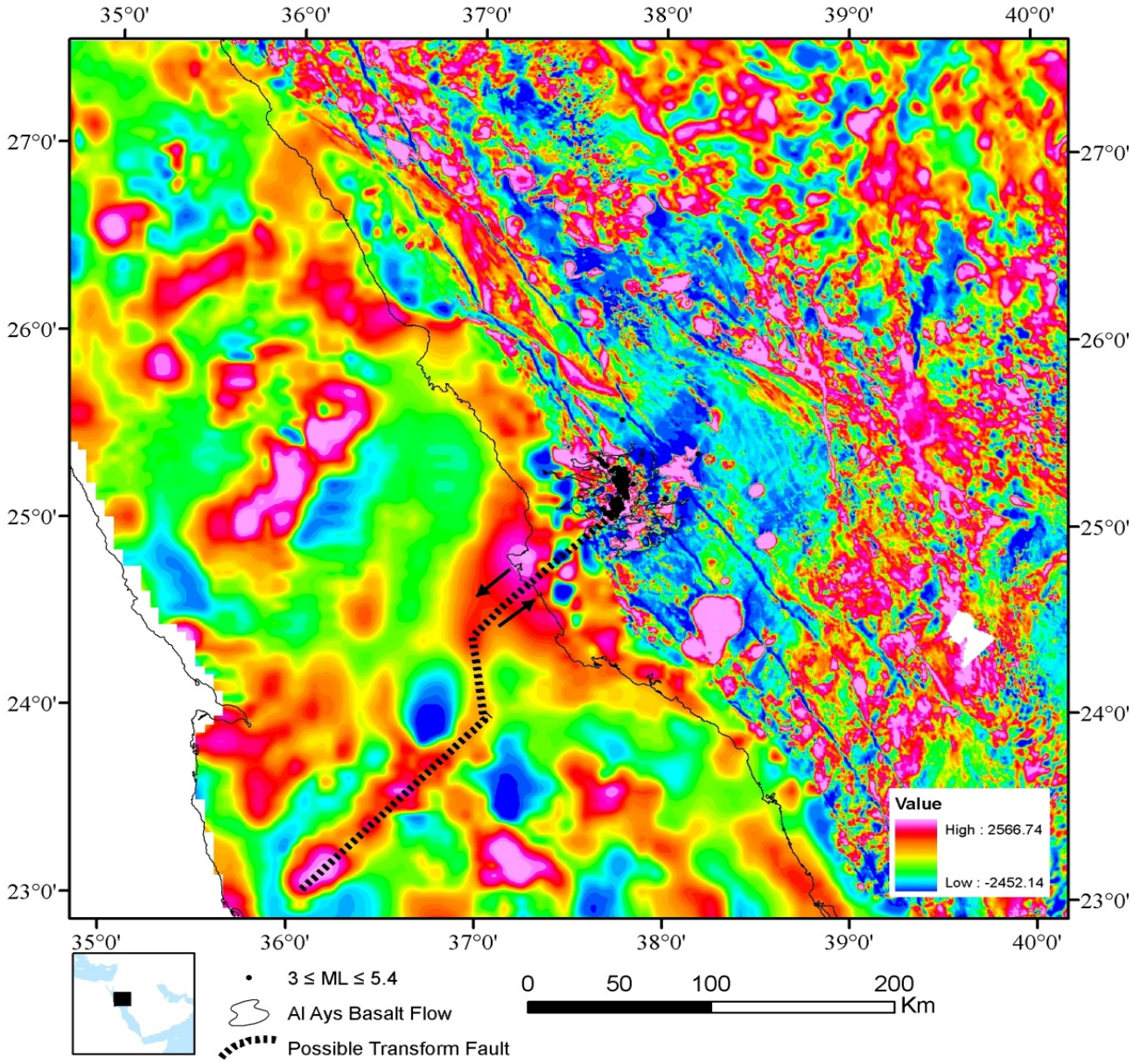

Fig.5.10 Aeromagnetic map showing the relation between the epicentral distribution , tectonic features, and locations of the faults inferred from the offset of magnetic. Alignment of epicenters and the northeast trending faults near latitudes 24.5° N could indicate that this fault extends northeastward on land.

CHAPTER 6

^{40}Ar-^{39}Ar AGE DATING OF BASALTS

Prior to this study no age dating has been carried out on Harrat Lunayyir. However during the mapping the same physical characteristics of the lavas and cones were used to establish the stratigraphy as were used in an earlier study of Harrat Rahat (Camp and Roobol, 1989). The stratigraphic units are believed to be of broadly of similar ages (Roobol, personal communication 2010). An estimate made in this manner for the stratigraphic units of Harrat Lunayyir prior to laboratory dating is given below (Camp and Roobol,1989).

QUATERNARY MAQRAH BASALT.

Qm5 Historic to late prehistoric Less than 4,500 years.
Qm4 0.1 to 0.5 Ma
Qm3 0.5 to 1.0 Ma
Qm2 1.2 to 1.5 Ma
Qm1 1.5 to 1.7 Ma

TERTIARY JARAD BASALT

Tj 2.0 to 8.0 Ma

Detailed geological investigation was carried out during the first year of the project. The project area covers the northwestern corner of Yanbu Al Bahr quadrangle and the southwestern portion of Wadi Alays quadrangle. The result of the detailed geologic survey is shown on in previous sections (Part 1, II and 111). The Precambrian rocks occupy the north and the south parts together with the eastern periphery of the mapped area. In the central zone the Precambrian rocks form isolated inliers. During volcanic activity episodes the relief of the Precambrian rock was high enough to hinder the basalt flow westwards.

Detailed investigation of the basalts lead to the identification of the following succession :

5- Historic to Late Prehistoric lava flows.
4- Prehistoric lava flows and scoria cones.
3- Non eroded lava flows and scoria cones.
2- Eroded lava flows and scoria cones.
1- Eroded lava flows
Unconformity
Tertiary basalt.

The $^{40}Ar/^{39}Ar$ age determination has been carried out at the TerraChron corp Geochronology Laboratory, Toronto, Canada. Each sample was labeled with a HL sample number. The general appearance and physical characteristics of the samples have been examined, and then selected portions for argon analysis. These selected portions were gently crushed and then examined under the binocular microscope to identify the basic phases and to select grains for irradiation. Most of these were fine-grained enough that whole-rock fragments were chosen for irradiation (Appendix A).

The selected rock chips were packaged in aluminum foil and loaded into an aluminum canister, together with a number of grains of the sanidine standard FCT and the Beloc tektite standard, and irradiated in the McMaster Nuclear Reactor, Hamilton, Ontario. The samples were irradiated for a total of 48 Megawatt-hours (approx. 16 hours in the reactor). Once the canister was returned to Toronto, the samples and standards were placed into holes in an aluminum disk and loaded into the ultra-high vacuum sample chamber within the mass spectrometer inlet system. After pumping down, the sample chamber and gas extraction line were baked for at least 12 hours at 150°C to achieve low argon blank levels. The analyses reported here were performed in a single loading of the mass spectrometer.

The first stage in the analysis was to fuse each of the standards in a single heating step, using a Lee Laser Nd-YAG laser operated with frequency doubling, to produce green light of 532 nm wavelength. The evolved gas was then purified by an SAES type 707 Ti-Fe-Zr getter held at 250°C to remove all reactive gases. The remaining noble gas component was let into a VG1200 mass spectrometer equipped with an ion multiplier for analysis of argon. The mass spectrometer was operated in static mode, isolated from the pumps during the analysis. All five natural and irradiation-produced argon isotopes (^{36}Ar through ^{40}Ar) were measured in 20 to 40 successive cycles over about a one-hour period, followed by pumping out of the mass spectrometer. Procedural blanks (in which all steps except the laser heating were followed) were performed before each analysis. The resulting argon isotope measurements were reduced using software have developed in-house, which includes correction for atmospheric contamination, mass discrimination and for interfering nuclear reactions resulting from the irradiation, as well as appropriate statistical analysis of the data, including a detailed treatment of error propagation. The J value (essentially the efficiency of ^{39}Ar production from ^{39}K) was calculated for each standard, using an age of 66.0 Ma for the tektite standard. The J value varies with its position in the container during irradiation and standards are distributed along the length of the container. Each sample analyzed was assigned an appropriate J value for the irradiation, depending on its own position in the irradiation container. The samples were analyzed by an identical procedure, except for the unknown samples, the gas release was done in a series of heating steps, as detailed in the section below. In each heating step, the sample was heated by the laser, generally for 30

seconds, followed by the gas purification and analysis steps as above. In successive heating steps the laser power was gradually increased until the sample was fused in the final step.

Analytical Procedures :

Integrated (Total-gas) age: The age obtained by mathematically summing all of the argon gas fractions extracted during a step-heating analysis. It is essentially equivalent to a traditional K-Ar age, though with somewhat higher precision because it does not require the liquating step necessary in K-Ar analysis. It is also essentially equivalent to a single-step analysis in $^{40}Ar/^{39}Ar$ dating, where all of the sample argon is extracted in a single heating step.

Plateau age: The age obtained by combining several successive heating steps in a step-heating argon analysis. The successive steps to be combined should ideally have ages that are indistinguishable within the analytical errors of the individual steps, and should represent a significant fraction of the total sample argon. On a diagram of age vs. cumulative proportion of ^{39}Ar released, these successive concordant ages appear as a horizontal plateau, hence the name. Ages in this type of diagram are normally computed assuming all sample ^{36}Ar measured is derived from atmosphere. A measure of how well the measured points fit the plateau is given by the goodness-of-fit parameter referred to here as $S/(n-1)$. For a well-fitted plateau this number should be close to one, while significantly larger values indicate a poorer fit.

Isochron age: The age obtained by passing a straight line through several successive heating steps as plotted on a diagram of $^{36}Ar/^{40}Ar$ vs. $^{39}Ar/^{40}Ar$. The successive steps to be combined should fit the line within the analytical errors of the individual steps, and should

represent a significant fraction of the total sample argon. The intercept of the line with the $^{39}Ar/^{40}Ar$ axis corresponds to an age, while its intercept with the $^{36}Ar/^{40}Ar$ axis gives the initial $^{36}Ar/^{40}Ar$ ratio at that time. The isochron treatment is useful when the conventional age spectrum (which is based on the assumption that the initial $^{36}Ar/^{40}Ar$ ratio was that of modern atmosphere) fails to define a plateau age. In this case, if an isochron nevertheless exists with a non-atmospheric $^{36}Ar/^{40}Ar$ ratio, it may indicate a true event in the sample's history. Then the (non-atmospheric) initial argon ratio gives the ambient argon composition at that time. As with the plateau, a measure of how well the measured points fit the isochron line is given by the goodness-of-fit parameter referred to here as $S/(n-2)$. For a well-fitted isochron, this number should be close to one, while significantly larger values indicate a poor fit.

Table 6.1: Summary of the analytical method using $^{40}Ar/^{39}Ar$

Sample. No.	U of T Analysis.	Type of Material	No. of Steps	Integrated Age (ka)	Preferred Age (ka)	Method	$^{40}Ar/^{36}Ar$	ΣS * $(n-f)$
HL-2 (Q5)	P53-035	Whole rock	11	-50 ±118	5 ±81	Isochron	295.5	0.58
HL-14 (Q2)	P53-022	Whole rock	10	478 ±113	511 ±78	Isochron	295.5	0.46
HL-17 (T)	P53-034	Whole rock	16	172 ±304	325 ±89	Isochron	295.5	0.36
HL-26 (Q4)	P53-033	Whole rock	8	352 ±111	191 ±82	Isochron	295.5	0.16
HL-31 (Q1)	P53-029	Whole rock	11	277 ±121	256 ±83	Isochron	295.5	0.44
HL-35 (Q3)	P53-027	Whole rock	11	95 ±109	149 ±110	Isochron	295.5	1.42

* Goodness-of-fit parameter; f is degrees of freedom: $f = 1$ for isochrons forced through 295.5

HL-02 A whole rock chip (**P53-035**) run in 11 steps gives an integrated age of -50 ±118 ka, with integrated Ca/K ratio of 5.59 ±0.01. This integrated age is essentially zero, as the measured integrated $^{40}Ar/^{36}Ar$ of 295.2 ±0.6 is not significantly different from that of the atmospheric ratio of 295.5. Step-heating the sample can potentially improve the radiogenic argon yield (i.e., give higher values of $^{40}Ar/^{36}Ar$) because the atmospheric argon is often more loosely bound to the mineral surfaces and can be preferentially extracted in low temperature steps. This heating can result in more radiogenic argon-rich fractions partitioned to higher temperature steps. Indeed the $^{36}Ar/^{40}Ar$ vs. $^{39}Ar/^{40}Ar$ correlation plot shows that the step-heating successfully produced fractions fanned out to progressively higher potassium to argon ratios, as shown by higher $^{39}Ar/^{40}Ar$ values (the highest temperature fraction 11 has the highest $^{39}Ar/^{40}Ar$ ratio). Nonetheless, in this case none of the 11 fractions have $^{40}Ar/^{36}Ar$ ratios that are significantly higher than 295.5. Thus on this plot, all points fit a line within uncertainties [S/(n−1) = 0.58], and give a Y-intercept corresponding to a $^{40}Ar/^{36}Ar$ ratio of 295.0 ±0.8, in agreement with the modern atmospheric ratio. But the line has essentially zero slope, and poorly constrained $^{39}Ar/^{40}Ar$ intercept that corresponds to an isochron age of 5 ±81 ka, signifying the very recent crystallization of this rock.

Integrated Results:

Age = -49.570 ± 118.120 ka Wt. Mean Age = 5.181 ± 80.888 ka(0.584)

40Ar* / 39K = -4.556 ± 10.857 E-3 Total 39K Vol = 1.5912E-0010 ccNTP/g

Total 40Ar* Vol = -0.725 ± 1.728 E-12

40Ar / 36Ar)sam = 295.24 ± 0.62 Total Atm 40Ar Vol = 8.2000E-0010
(36Ar / 40Ar)sam = 0.00338709 ±0.00000714 Corr 36/40 & 39/40 ratios = 0.072238

(37Ar / 40Ar)sam = 0.59131997 ±0.00155163 Corr 36/40 & 37/40 ratios = 0.037853

(39Ar / 40Ar)sam = 0.19421807 ±0.00041958 Corr 37/40 & 39/40 ratios = 0.782338

37Ca / 39K = 3.045 ± 0.005 38Cl / 39K = 5.751 ± 0.104 E-3

Ca / K = 5.587 ± 0.009 Cl / K = 1.208 ± 0.022 E-3

F1 = -2.172 E-3 F2 = 4.444 E-2

HL-14 A whole rock chip (**P53-022**) run in 10 steps gives an integrated age of 478 ±113 ka, with integrated Ca/K ratio of 5.83 ±0.01. In contrast to HL-2 (above) the integrated $^{40}Ar/^{36}Ar$ ratio of 301.7 ±1.5 is slightly but significantly above the atmospheric ratio of 295.5 and consequently a positive age has been measured. Although the radiogenic yields in the fractions are significantly higher than those in sample HL-2, they are still low (less than 5% radiogenic ^{40}Ar). An age spectrum for the sample is made by assuming that the non-radiogenic Ar in each fraction has $^{40}Ar/^{36}Ar$ ratios of 295.5, similar to how the integrated age has been calculated. At this level of enrichment the calculated ages are very sensitive to small departures from the assumed $^{40}Ar/^{36}Ar$ ratio of 295.5. Thus caution must be used in the interpretation of both the integrated age and the ages of the fractions. The uncertainties in each age are relatively large (again reflecting the small amounts of radiogenic argon). However, within the uncertainties the age spectrum is uniformly flat. This stands in contrast to the Ca/K spectrum that begins at a ratio of 2.01 and climbs to a final value of 9.95 ±0.06.

In contrast to the plateau ages calculated from the fractions and the integrated age, a free fit of the data on the $^{36}Ar/^{40}Ar$ vs. $^{39}Ar/^{40}Ar$ correlation plot makes no assumption about the isotopic composition of the non-radiogenic argon (an isochron is a mixture of non-radiogenic and radiogenic argon, see above) and thus may be a preferable means of age calculation for

non-radiogenic samples. On this plot all of the points fit a line within experimental uncertainties [$S/(n-2)$ =0.52] corresponding to an isochron age of 534 ±343 ka, with a calculated initial $^{40}Ar/^{36}Ar$ ratio of 295.2 ±4.3. This calculated initial ratio is indistinguishable from the modern atmospheric ratio of 295.5. Accordingly, a degree of freedom could be used to fix the initial ratio on this plot at 295.5 (actually 1/295.5, this corresponds to "NIER" on the plot) and refit the points. Treated this way, the points still fit the line within uncertainties [S/(n–1) =0.46] and constrain the age to 511 ±78 ka. As the levels of radiogenic argon are similarly low in the remaining four analyses, we regard the results derived from the isotope correlation plot to be most appropriate means to estimate the ages of these samples.

Integrated Results:

Age = 478.112 ± 113.355 ka	**Wt. Mean Age = 510.564 ± 77.773 ka(0.459)**
40Ar* / 39K = 43.952 ± 10.422 E-3	**Total 39K Vol = 1.4530E-0010 ccNTP/g**
	Total 40Ar* Vol = 6.386 ± 1.514 E-12
(40Ar / 36Ar)sam = 301.71 ± 1.50	**Total Atm 40Ar Vol = 3.0376E-0010 ccNTP/g**
(36Ar / 40Ar)sam = 0.00331442 ±0.00001652	**Corr 36/40 & 39/40 ratios =-0.007631**
(37Ar / 40Ar)sam = 1.48826320 ±0.00780439	**Corr 36/40 & 37/40 ratios =-0.025041**
(39Ar / 40Ar)sam = 0.46846897 ±0.00229752	**Corr 37/40 & 39/40 ratios = 0.924212**
37Ca / 39K = 3.177 ± 0.006	**38Cl / 39K = 4.778 ± 0.111 E-3**
Ca / K = 5.829 ± 0.012	**Cl / K = 1.003 ± 0.023 E-3**
F1 = -2.266 E-3	**F2 = 1.095 E-1**

HL-17 A whole rock chip (**P53-034**) run in 16 steps gives an integrated age of 172 ±304 ka, with integrated Ca/K ratio of 7.39 ±0.02. Its Ca/K spectrum climbs gradually from 3.1 ±0.2 (fraction 1) to a mid-temperature plateau averaging 6.66 ±0.16 (fractions 7 to 13) before climbing steeply to a final value of 22.0 ±0.1 (fraction 16). On the $^{36}Ar/^{40}Ar$ vs. $^{39}Ar/^{40}Ar$ plot, a free fit of all of the points yields an isochron age of 518 ±223 ka [S/(n–·) = 0.32], with an atmospheric initial $^{40}Ar/^{36}Ar$ ratio of 294.6 ±1.0. The same data forced through the atmospheric $^{40}Ar/^{36}Ar$ ratio of 295.5 yield an isochron [S/(n–1) = 0.36] corresponding to an age of 325 ±89 ka.

Integrated Results:

Age = 171.926 ± 303.909 ka	**Wt. Mean Age = 324.796 ± 88.719 ka(0.359)**
40Ar* / 39K = 15.803 ± 27.937 E-3	**Total 39K Vol = 2.3036E-0010 ccNTP/g**
	Total 40Ar* Vol = 3.641 ± 6.436 E-12
(40Ar / 36Ar)sam = 295.91 ± 0.72	**Total Atm 40Ar Vol = 2.6517E-0009 ccNTP/g**
(36Ar / 40Ar)sam = 0.00337946 ±0.00000820	**Corr 36/40 & 39/40 ratios = 0.051653**
(37Ar / 40Ar)sam = 0.34937106 ±0.00114629	**Corr 36/40 & 37/40 ratios = 0.023822**
(39Ar / 40Ar)sam = 0.08675519 ±0.00022941	**Corr 37/40 & 39/40 ratios = 0.674937**
37Ca / 39K = 4.027 ± 0.010	**38Cl / 39K = 5.741 ± 0.227 E-3**
Ca / K = 7.389 ± 0.018	**Cl / K = 1.206 ± 0.048 E-3**
F1 = -2.873 E-3	**F2 = 2.528 E-2**

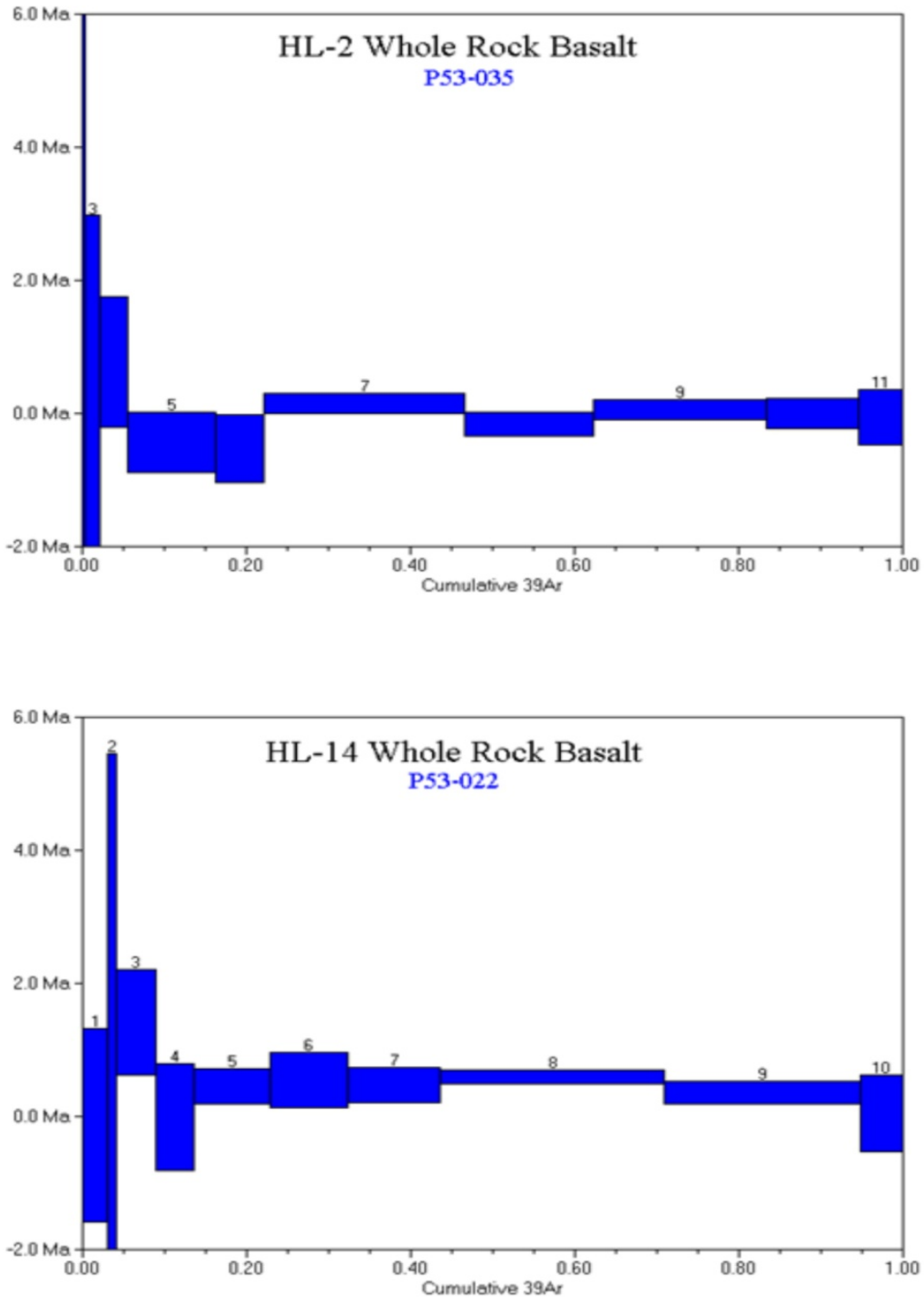

Fig. 6.1 $^{40}Ar/^{39}Ar$ incremental heating release spectra for samples HL-2 and HL-14

HL-26 A whole rock chip (**P53-033**) run in 8 steps gives an integrated age of 352 ±111 ka, with integrated Ca/K ratio of 9.75 ±0.02. Its age-spectrum is uniform except for the final fraction 8 that yields a significantly older apparent age of 2.6 ±0.9 Ma. This old age is also correlated with a significantly high Ca/K value of 34.0 ±0.3. Fractions 1 through 6 on the Ca/K spectrum have relatively uniform values averaging 5.8 ±0.3. On the $^{36}Ar/^{40}Ar$ vs. $^{39}Ar/^{40}Ar$ plot, a free fit of fractions 1 to 7 yields an isochron age of 116 ±143 ka [S/(n−·) = 0.10], with an atmospheric initial $^{40}Ar/^{36}Ar$ ratio of 296.6 ±1.7. The same data forced through the atmospheric $^{40}Ar/^{36}Ar$ ratio of 295.5 yield an isochron [S/(n−1) = 0.16] corresponding to an age of 191 ±82 ka.Fraction 8 (green) lies significantly below this isochron.

Integrated Results:

Age = 351.618 ± 111.180 ka Wt. Mean Age = 208.823 ± 85.253 ka(1.046)

40Ar* / 39K = 32.322 ± 10.221 E-3 Total 39K Vol = 1.1882E-0010 ccNTP/g

Total 40Ar* Vol = 3.841 ± 1.214 E-12

(40Ar / 36Ar)sam = 299.18 ± 1.18 Total Atm 40Ar Vol = 3.0861E-0010 ccNTP/g

(36Ar / 40Ar)sam = 0.00334250 ±0.00001315 Corr 36/40 & 39/40 ratios = 0.011882

(37Ar / 40Ar)sam = 2.02124330 ±0.00849036 Corr 36/40 & 37/40 ratios =-0.015718

(39Ar / 40Ar)sam = 0.38029199 ±0.00148765 Corr 37/40 & 39/40 ratios = 0.914376

37Ca / 39K = 5.315 ± 0.009 38Cl / 39K = 4.945 ± 0.153 E-3

Ca / K = 9.752 ± 0.017 Cl / K = 1.038 ± F1 = -3.791 E-3 F2 = 1.413 E-1

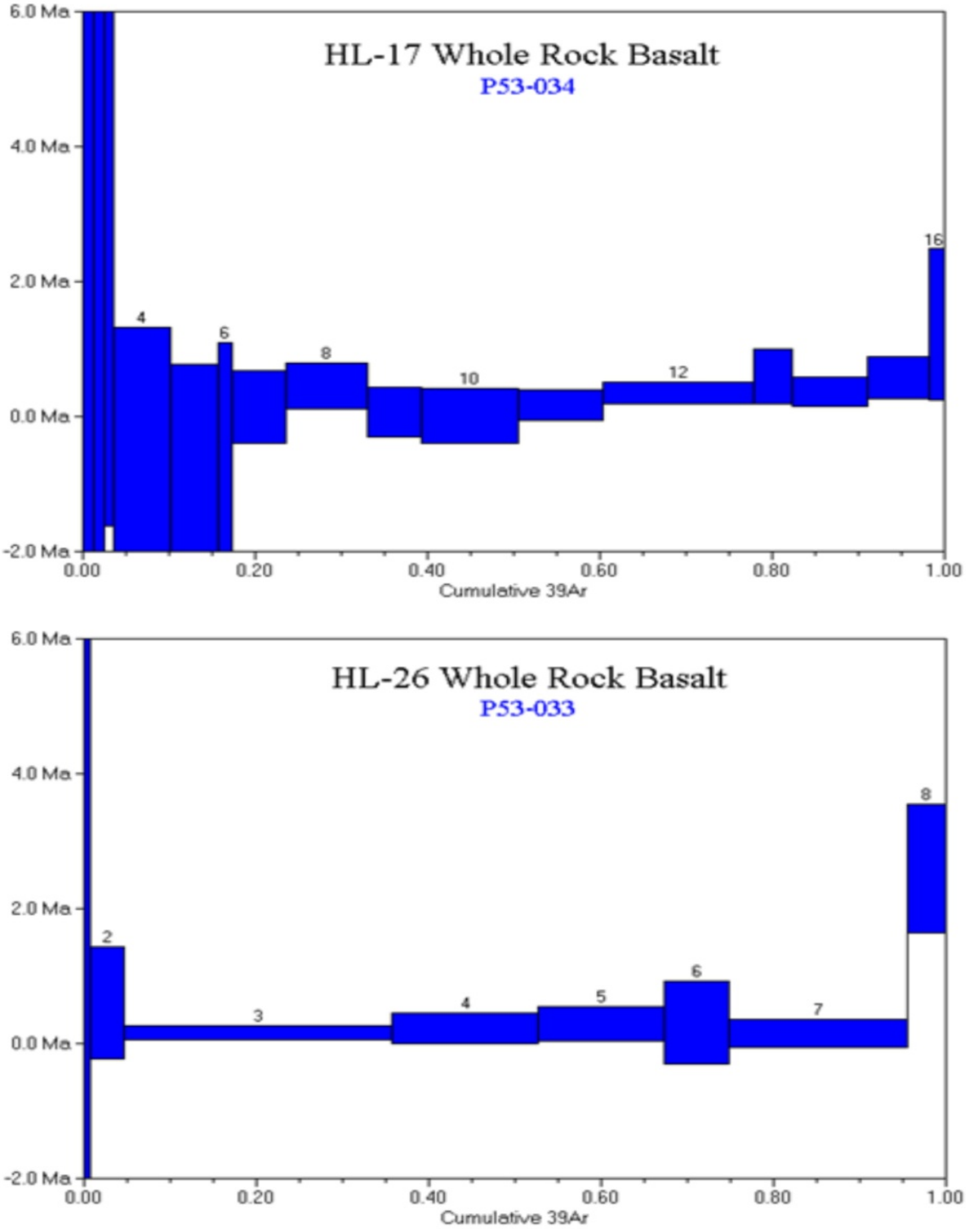

Fig. 6.2 $^{40}Ar/^{39}Ar$ incremental heating release spectra for samples HL-17 and HL-26

HL-31 A whole rock chip (**P53-029**) run in 11 steps gives an integrated age of 277 ±121 ka, with integrated Ca/K ratio of 5.16 ±0.01. On the Ca/K plot, Ca/K ratios increase from 1.96 ±0.14 (fraction 1) to 8.05 ±0.02 in the final fraction. On the $^{36}Ar/^{40}Ar$ vs. $^{39}Ar/^{40}Ar$ plot, the points fit an isochron within the experimental uncertainties [$S/(n-\cdot) = 0.48$] corresponding to an age of 126 ±557 ka, with an atmospheric initial $^{40}Ar/^{36}Ar$ ratio of 297.0 ±6.5. *The same data forced through the atmospheric $^{40}Ar/^{36}Ar$ ratio of 295.5 yield an isochron [$S/(n-1) = 0.44$] corresponding to an age of 256 ±83 ka.*

Integrated Results:

Age = 276.532 ± 121.242 ka	**Wt. Mean Age = 255.929 ± 83.462 ka(0.440)**
40Ar* / 39K = 25.420 ± 11.146 E-3	**Total 39K Vol = 1.2634E-0010 ccNTP/g**
	Total 40Ar* Vol = 3.211 ± 1.408 E-12
(40Ar / 36Ar)sam = 298.52 ± 1.34	**Total Atm 40Ar Vol = 3.1445E-0010 ccNTP/g**
(36Ar / 40Ar)sam = 0.00334988 ±0.00001500	**Corr 36/40 & 39/40 ratios =-0.004327**
(37Ar / 40Ar)sam = 1.11818045 ±0.00532071	**Corr 36/40 & 37/40 ratios =-0.017290**
(39Ar / 40Ar)sam = 0.39771414 ±0.00177142	**Corr 37/40 & 39/40 ratios = 0.925608**
37Ca / 39K = 2.812 ± 0.005	**38Cl / 39K = 4.989 ± 0.155 E-3**
Ca / K = 5.159 ± 0.009	**Cl / K = 1.048 ± 0.033 E-3**
F1 = -2.006 E-3	**F2 = 8.347 E-2**

HL-35 A whole rock chip (**P53-027**) run in 11 steps gives an integrated age of 95 ±109 ka, with integrated Ca/K ratio of 4.75 ±0.01. Its Ca/K spectrum starts at a ratio of 2.54 ±0.03, climbs to a plateau averaging 4.33 ±0.06, before rising to 12.78 ±0.07 in the final fraction. On the $^{36}Ar/^{40}Ar$ vs. $^{39}Ar/^{40}Ar$ plot, a free fit of all of the points yields an isochron age of 368 ±203 ka [$S/(n-\cdot) = 1.41$], with an atmospheric initial $^{40}Ar/^{36}Ar$ ratio of 294.0 ±1.5. The same data forced through the atmospheric $^{40}Ar/^{36}Ar$ ratio of 295.5 give an isochron age of 325 ±89 ka. The $S/(n-1)$ value of 1.42 indicates the points scatter very slightly outside of analytical uncertainties. *The uncertainty on the corresponding isochron age of 149 ±110 ka has been adjusted for the slight scatter of the data points.*

```
Integrated Results:

Age  =  95.365 ± 109.085 ka                    Wt. Mean Age = 148.728 ± 130.980
ka(1.417)

40Ar* / 39K =    8.766 ±  10.027 E-3           Total 39K Vol      =  2.1214E-0010
ccNTP/g

                                               Total 40Ar* Vol =  1.860 ± 2.127 E-
12

(40Ar / 36Ar)sam =   296.05 ±    0.63         Total Atm 40Ar Vol =  1.0050E-0009
ccNTP/g

(36Ar / 40Ar)sam = 0.00337784 ±0.00000715     Corr 36/40 & 39/40 ratios =
0.013954

(37Ar / 40Ar)sam = 0.54481024 ±0.00139134     Corr 36/40 & 37/40 ratios =-
0.005489

(39Ar / 40Ar)sam = 0.21069102 ±0.00045279     Corr 37/40 & 39/40 ratios =
0.811772

37Ca / 39K =  2.586 ± 0.004                   38Cl / 39K =  6.115 ± 0.114 E-3

 Ca / K   =  4.745 ± 0.007                    Cl / K   =  1.284 ±   F1 = -1.845
E-3                              F2 =  4.136 E-2
```

Generally speaking, it is apparent from the plots of Ca/K that in all six samples Ca-rich phases predominate at the highest temperatures. This is a common feature in basaltic rocks. Only in

sample HL-26 is there an indication that a high Ca/K phase may be correlated with a relict or older age. The other samples yield uniform apparent ages throughout their respective age-spectra in spite of the widely varying Ca/K ratios. Thus, the ages can be considered to be representative.

Prior to these analyses, estimates of the ages of the samples were cited as Tertiary to Quaternary. This work places the ages of all six samples firmly in the Quaternary period. Their ages have been summarized in the figure above. The precision of the ages calculated in this study are limited by the small amounts of radiogenic argon compared to the larger amounts of non-radiogenic, or background argon typical in basaltic whole rocks of this age.

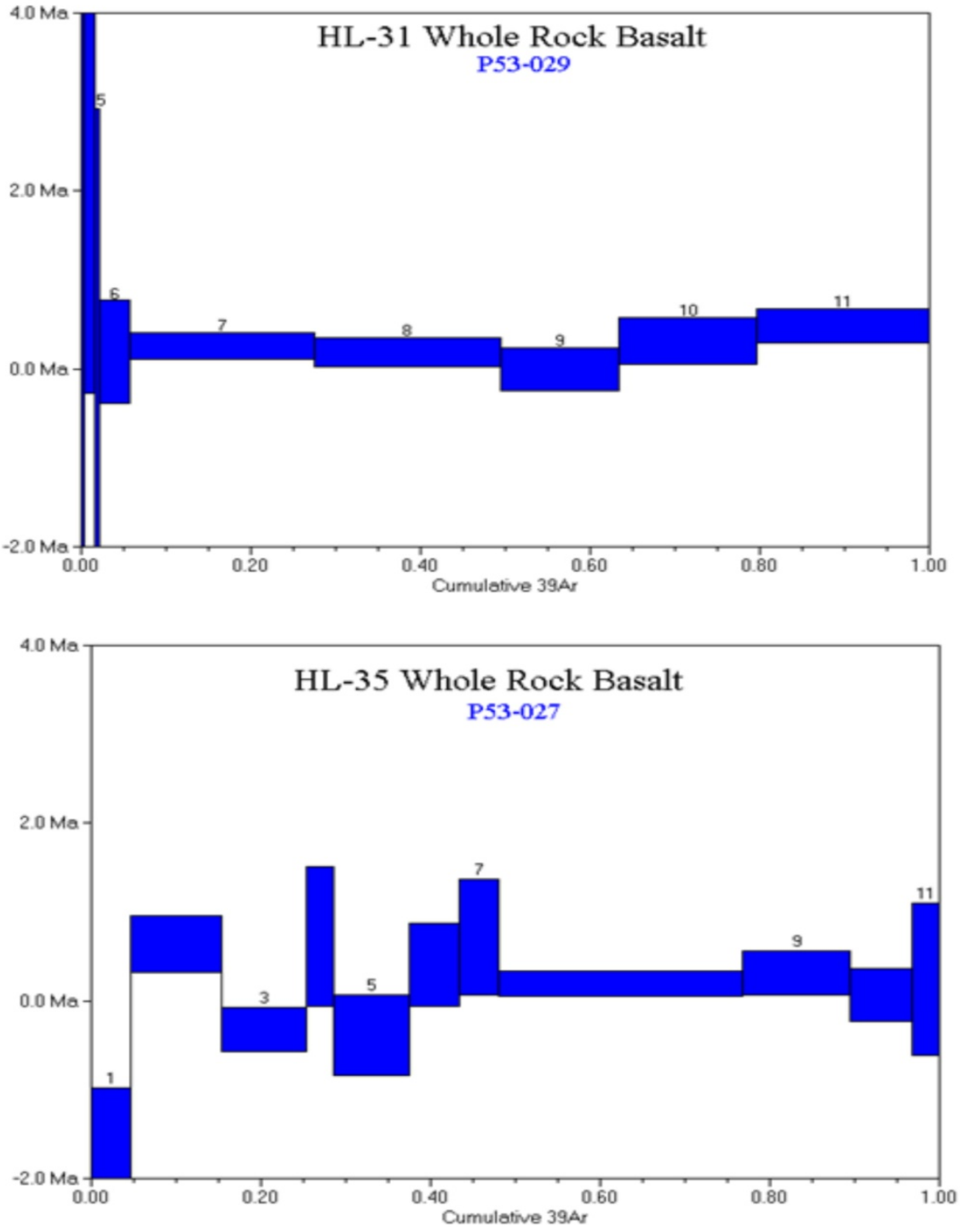

Fig. 6.3 $^{40}Ar/^{39}Ar$ incremental heating release spectra for samples HL-31 and HL-35

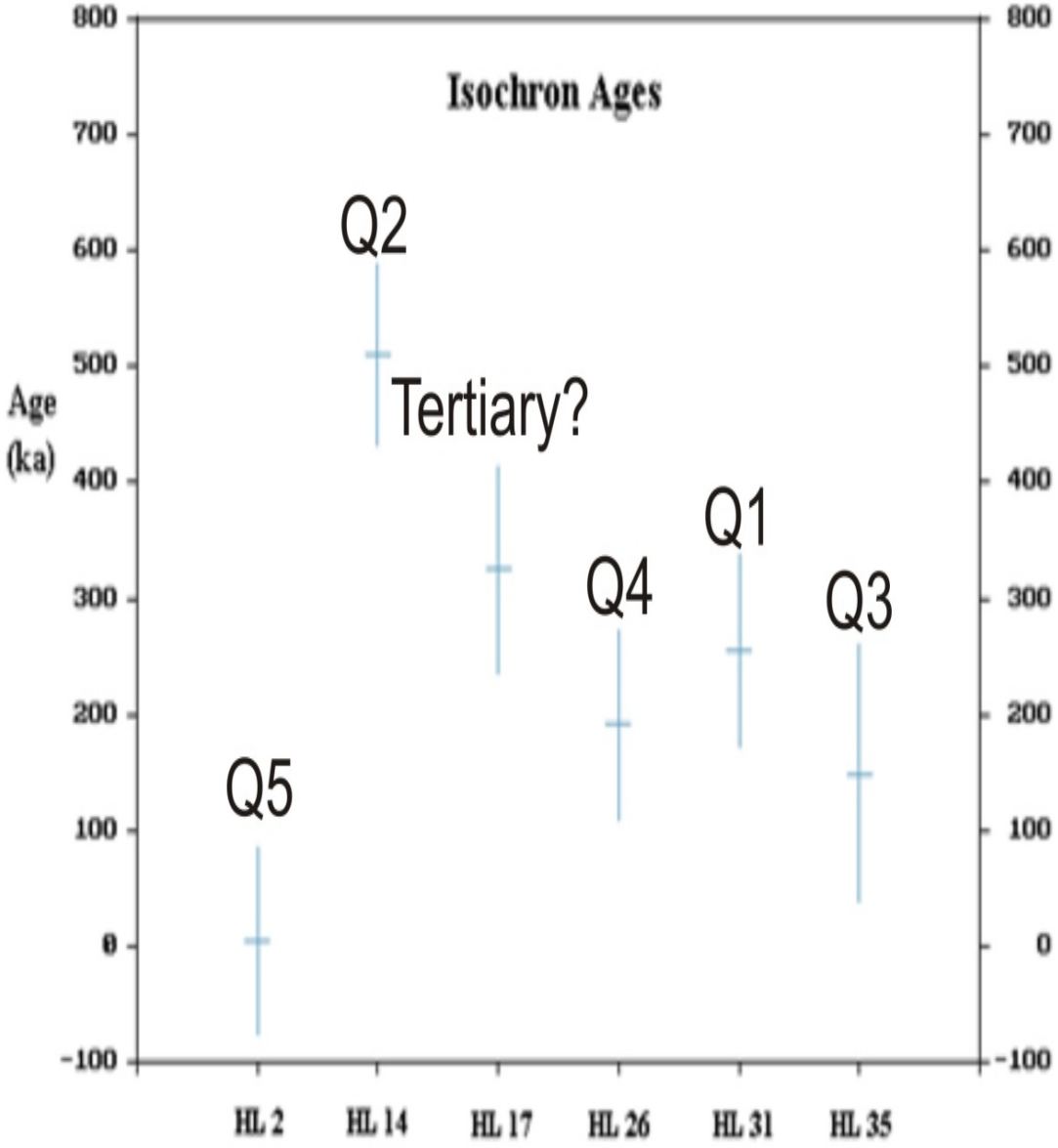

Fig. 6.4 Summary Isochron ages for all samples

CONCLUSIONS & RECOMMENDATIONS

- It can be concluded from this study that recent seismic activities in Harrat Lunayyir is of swarm-type and volcanic-related and occur in the form of sequences, each are lasting up to several months, reaching peak magnitude up to 5.5 and covering a specific tectonic segment of the Harrat. The recent seismic activity indicates a cyclic pattern of events consisting of seismic minima which may represent episodes of accumulation of energy, and seismic maxima which represent the release of energy that can be accumulated to cause larger events in the future. Places of interaction of normal and strike-slip faulting in the Harrat could be the sites of swarm sources and recent stress accumulations. A clustering of swarm activity in time may suggest an episodic source of strain or a constant source with repeated slip along the fault zone.
- The present activity can be termed as a volcano-seismic crisis. In an area where previously there has been little or no seismic activity, the sudden commencement of swarms of activity at shallow depths taken with the presence of fumaroles indicates a possible new cycle of activity. Such events can last for four months and then die out. Alternatively they can continue and escalate leading to felt earthquakes and result in a basaltic eruption. Basaltic eruptions are considered the safest type of volcanic activity and do not usually involve the loss of life and the lava flows can today be diverted away from settlements by building earth banks using bulldozers.
- Field investigations and focal mechanism solutions have revealed that the main shock was due to a primary coseismic rupture represented by a N137° (NW-SE) oriented

normal faulting. The fault has a displacement of 1.1 m and dip of 48° SW. Secondary ruptures, trending NE-SW to ENE-WSW, have lesser displacements. During the May 19th, 2009 earthquake, sympathetic activity occurred on N-S trending faults and secondary effects associated with this event are land collapses and rock falls.

- Analysis of the seismicity data in conjunction with magnetic and geologic information indicate that the seismicity is shallow and the correlation of the offshore epicentral distribution with the major tectonic features is, in general, quite good. However, the low level of seismicity in the shield area and poor correlation with the tectonics might be due to the complexity of faulting, lack of detection of small events and poor or inaccurate azimuthal coverage of stations. Structural patterns inferred from magnetic data and earthquake locations (offshore and onland) provide evidence for continuation of the faulting regime from the northern Red Sea northeastward into the Arabian Shield and Harrat.

- Harrat Lunayyir basalts are typically alkali olivine basalts, hawaiite, and basanites. They are typically porphyritic with olivine being the major phenocrystal phases, which seconded by plagioclase in the differentiated varieties.
- The crystallization of the magmas took place at temperatures in the range of 1200 to about 850 °C. But eruption took place mostly before the magmas got saturated with clinopyroxene at about 1140 degrees.
- It is apparent from the plots of Ca/K that in all six samples Ca-rich phases predominate at the highest temperatures. This is a common feature in basaltic rocks. Only in sample HL-26 is there an indication that a high Ca/K phase may be correlated with a

relict or older age. The other samples yield uniform apparent ages throughout their respective age-spectra in spite of the widely varying Ca/K ratios. Thus, the ages can be considered to be representative.

- The most primitive samples are well below the composition of primary magmas in terms of mg# and the concentration of compatible elements (Ni, Cr). Therefore, most of the flows have suffered fractional crystallization of olivine and plagioclase to a less degree. The latter is not supported by a negative Eu anomaly.
- The strong enrichment in the incompatible elements is a function of lower degree of partial melting of a mantle source that did not change over time and that lacks garnet as a residual phase; the enrichment has been furthered by fractionation.
- The process identification diagrams using magmatophile and hypermagmatophile elements supports the assumption that chemical variability is due to fractionation rather than different degrees of partial melting.
- Prior to these analyses, estimates of the ages of the samples were cited as Tertiary to Quaternary. This work places the ages of all six samples firmly in the Quaternary period. The precision of the ages calculated in this study are limited by the small amounts of radiogenic argon compared to the larger amounts of non-radiogenic, or background argon typical in basaltic whole rocks of this age. The discrepancies in ages and stratigraphic position are due to the small amounts in accumulated argon over the relatively very short period of time.
- The volcanic activity at Harrat Lunayyir started about 500 000 years. There must have been a substantial time between the lowest unit (which has previously assigned a

Tertiary age) and Q1 so that an unconformity has been developed. The last activity could have taken place at about 5000 years ago.

- Geodetic measurements are recommended in order to identify and quantify very recent neotectonic activity and thus, provide prediction of specific future event. Geodetic techniques range from ground technique using strain meters and laser-ranging devices to space technique using very-long-baseline radio interferometry (VLBI) and the global positioning system (GPS).
- It should be pointed out that installation of strong ground-motion instruments in this region will lead to better estimates of the attenuation relationships and accelerations for seismic hazard assessment.

REFERENCES

Al-Amri, A., Rodgers, A., and Al-khalifah, T., (2008). Improving the Level of Seismic Hazard Parameter in Saudi Arabia Using Earthquake Location. Arabian J. of Geosciences, 1, DOI 10.1007/s12517-008-0001-5 , 1-15.

Al-Amri, A. M. and Fnais, M. S. (2009): Seismo-volcanic investigation of 2009 earthquake swarms at Harrat Lunayyir (Ash Shaqah), Western Saudi Arabia. Intern. Jour. Earth Sci. and Engineering, India (in press).

Al-Damegh, K., Sandvol,E. and Barazangi, M. 2005. Crustal structure of the Arabian plate: New constraints from the analysis of teleseismic receiver functions. Earth Planet. Sci. Lett.(231): 177-196

Al Shanti, A. M., (1966): Oolitic iron-ore deposits in Wadi Fatima between Leddah and Mecca, Saudi Arabia. Saudi Arabian Dir. Gen. Min. Resources Bull., vol. 2, 51p.

Ambraseys, A., 1988 Seismicity of Saudi Arabia and adjacent areas, Report 88/11, ESEE, Imperial Coll. Sc. Tech. London, U.K.

Asimov PD, Ghiorso MS (1998) Algorithmic modifications extending MELTS to calculate sub solidus phase relations. Am Mineral 83 (9–10) : 1127–1132

Baer,G. and Hamiel, Y. (2010) : Form and growth of an embryonic continental rift: InSAR observations and modelling of the 2009 western Arabia rifting episode. Geophys. J. Int. 182, 155–167 doi: 10.1111/j.1365-246X.2010.04627.

Barazangi, M., 1981 Evaluation of seismic risk along the western part of the Arabian plate : discussion and recommendations, Bull. Fac. Earth Sc., King Abdulaziz Univ., Jiddah, K.S.A., 4: 77-87.

Benito, B.; Cepeda, J. M.; and Martinez Diaz, J. J. (2004): Analysis of the spatial and temporal distribution of the 2001 earthquakes in El Savador, in Rose, W.I., Bommer, J.J., Lopez, D.L., Carr, M.J., and Major, J.J, eds., Natural hazards in El Salvador: Boulder, Colorado, Geological Society of America Special paper 375, pp. 1-18.

Benoti, M.H., Nyblade, A.A., VanDecar, J.C. and Gurrola, H. 2003. Upper mantle P wave velocity structure and transition zone thickness beneath the Arabian Shield. Geophys. Res. Lett. 30: 1-4

Blakely, R. J. and Simpson, R. W., 1986, Approximating edge of source bodies from magnetic or gravity anomalies: Geophysics, **51,** 1494-1498.

Camp, V.E. and Roobol, M.J., 1991, Geologic Map of the Cenozoic Lava Field of Harrat Rahat, Kingdom of Saudi Arabia: Saudi Arabian Directorate General of Mineral Resources Geoscience

Map GM-1233, scale 1:250,000 with text 37p.

Camp, V.E., and Roobol, M.J., 1992, Upwelling asthenosphere beneath western Arabia and its regional implications: Journal Geophysical Research, v. 97, p.15,255-15,271.

Camp, V.E., Hooper,P.R., Roobol, M.J. and White, D.L., 1987, The Madinah eruption, Saudi Arabia: Magma mixing and simultaneous extrusion of three basaltic chemical types: Bulletin Volcanology, v. 49, p.489-508.

Camp, V.E., Roobol, V.E. and Hooper, P.R., 1989a, The Arabian continental alkali basalt province: Part I. Evolution of Harrat Rahat, Kingdom of Saudi Arabia: Bulletin, Geological Society of America, v. 101, p. 71-95.

Camp, V.E., Roobol, M.J. and Hooper, P.R., 1989, Intraplate alkalic volcanism and magmatic processes along the v600km-long Makkah-Madinah-Nafud volcanic line, western Saudi Arabia: General Assembly of the International association of Volcanology and Chemistry of the Earth's Interior, Continental Magmatism Abstracts, New Mexico Bureau of Mines and Mineral Resources Bulletin 131, p.49.

Camp, V.E., Roobol, M.J. and Hooper, P.R., 1991, The Arabian continental alkali basalt province: Part II. Evolution of Harrats Khaybar, Ithnayn, and Kura, Kingdom of Saudi Arabia: Bulletin, Geological Society of America, v. 103, p.363-391.

Camp, V.E., Roobol, M.J., and Hooper, P.R., 1992, The Arabian continental alkali basalt province: Part III. Evolution of Harrat Kishb, Kingdom of Saudi Arabia: Bulletin, Geological Society of America, v. 104, p. 379-396.

Cox, K.G., 1980. A model for flood basalt volcanism. J. of Petrology, V. 21, P.629-650.

Daradich, A., Mitrovica, J.X., Pysklywec, R.N, Willett, S.D. and Forte, A.M. (2003). Mantle flow, dynamic topography, and rift-flank uplift to Arabian. Geol. Soc. Am. 31:901-904.

Dreyer, H. and Naudy, H., 1968, Non-Linear filtering applied to aeromagnetic profiles: Geophysical Prospecting, **16,** 171-178.

Fraser, D. C., Fuller, B. D., and Ward, S. H., 1966, Some numerical techniques for application in mining exploration: Geophysics, **31,** 1066-1077.

Gettings, M. E. and Andreasen, G. E., 1982, An interpretation of the aeromagnetic anomaly of the Lakathah layered intrusive complex, Kingdom of Saudi Arabia : Ministry of Petroleum and Mineral Resources, Directorate General of Mineral Resources, Jeddah , Saudi Arabia**,** USGS-OF-03-8, 37 p.

Girdler, R. W. (1969): The Red Sea-a geophysical background. In: Degens ET, Ross D. A. (eds): Hot brines and recent heavy metal deposits in the Red Sea. Springer, New York, pp. 59-70

Hall, S. (1979). A total intensity map magnetic anomaly map of the Red Sea and its interpretation. Directorate General of Mineral Resources, Jeddah, Saudi Arabia. Report 275, 260p.

Hansen, S., Schwartz, S., Al-Amri, A. and Rodgers, A. (2006). Combined plate motion and density driven flow in the asthenosphere beneath Saudi Arabia: evidence from shear- wave splitting and seismic anisotropy. Geology, V. 34, no. 10, p. 869 – 872.

Hansen,S., Rodgers, A., Schwartz, S., and Al-Amri, A. (2007). Imaging Ruptured Lithosphere Beneath the Red Sea and Arabian Peninsula. Earth and Planetary Science Letters, 259, 256 – 265.

Hill D.P., (1977): A model for earthquake swarms, *J. Geophys. Res.* 82 (1977), pp. 1347–1352

Johnson, P.R. 1998. Tectonic map of Saudi Arabia and adjacent areas. Deputy Ministry for Mineral Resources Technical Report USGS-TR-98-3 (IR 948).

Johnson, P.R. 2000. Proterozoic geology of Saudi Arabia: Current concepts and issues. Contribution to a workshop on the geology of the Arabian Peninsula, 6th meeting of the Saudi Society for Earth Science, King Abdulaziz City for Science and Technology, Riyadh, Saudi Arabia.

Jónsson, S.; Pallister, J.; McCausland, W., and El-Hadidy, S. (2010): Dyke Intrusion and Arrest in Harrat Lunayyir, western Saudi Arabia, in April-July 2009. Geophysical Research Abstracts, Vol. 12, EGU2010-7704.32 p.

Julia, J., Ammon, C. and Herrmann, R. 2003. Lithosphere structure of the Arabian Shield from the joint inversion of receiver functions and surface-wave group velocities. Tectonophysics 371:1-21

Kellogg, K. S. and Beckmann, G. E. J., 1982, Paleomagnetic investigation of upper proterozoic rocks in the Eastern Arabian Shield, Kingdom of Saudi Arabia : Precambrian Research, **16,** A26-A27.

Kinkar, A., Shawali, A.A., Bankher, K.A., Endo, E., Roobol, M.J. and Wynn, J.C. 1994b. The Al-Madinah-Harrat Rahat volcanic monitoring project summary report. Saudi Arabian Deputy Ministry for Mineral Resources Confidential Report USGS-CR-94-1 (IR909), 47P.

Kisslinger, C., (1997). Aftershocks and fault zone properties. Advances in Geophysics; 38, 1-35.

Klein, B. M.; Economou, E. N. , and Papaconstantopoulos, D. A. (1977): Inverse Isotope Effect and the x Dependence of the Superconducting Transition Temperature in PdH_x and PdD_x. Phys. Rev. Lett. , Vol. 39, No. 9, pp. 574 – 577

Le Bas, M.J., R.W. Le Maitre, A. Streckeisen, and B. Zanettin, A (1977) : chemical classification of volcanic rocks based on the total alkali silica diagram, J. Petrol., 27, 745-750.

Moufti, M.R.H. and Hashad, M.H. 2005. Volcanic hazards assessment of Saudi Arabian Harrats: geochemical and isotopic studies of selected areas of active Makkah- Madinah-Nafud (MMN) volcanic rocks. Final Project Report (LGP-5-27), King Abdlaziz City for Science and Technology, Riyadh, Saudi Arabia.

Pallister, J. S., (1984): Expanatory notes to the geologic map of the Al Lith quadrangle, sheet 20 D., Kingdom of Saudi Arabia.

Pallister, J.; McCausland, W.; Jónsson, S.; Lu. Z.; Zahran, H. M.; El-Hadidy, S.; Aburukbah, A.; Stewart, I.; Lundgern, P.; White, R.; Moufti, M. (2010): Broad accommodation of rift-related extension recorded by dyke intrusion in Saudi Arabia. Nature geoseisnce, Macmillan Publishers Limited, 8p.

Poirier, J. P., and Taher, M.A., 1980 Historical seismicity in the near and middle east, north Africa, and Spain from Arabic documents (VIIth-XVIII century), Bull. Seis. Soc. Am., 70.6, 2185-2201.

Pollard D.D. and Holzhausen G.(1979). On the mechanical interaction between a fluid-filled fracture and the earth's surface. *Tectonophysics*, 53, 27-57.

Roobol, M.J., and Al-Rehaili, M., 1997, Geohazards along the Makkah-Madinah-Nafud (MMN) volcanic line: Saudi Arabian Deputy Ministry for Mineral Resources Technical Report DMMR-TR-97-1, p.125-140.

Roobol, M.J., Bankher, K. and Bamufleh, S. 1994. Geothermal anomalies along the MMN volcanic line including the cities of Al-Madinah Al-Munawwarah and Makkah Al-Mukarramah. Saudi Arabian Deputy Ministry for Mineral Resources Confidential Report DGMR-MADINAH-CR-15-2, 95 p.

Roobol, M.J. and Camp, V.E., 1991a, Geologic map of the Cenozoic Lava Fields of Harrats Khaybar, Ithnayn and Kura, Kingdom of Saudi Arabia: Saudi Arabian Directorate General of Mineral Resources Geoscience Map GH-131, scale 1:250,000 with text 40p.

Roobol, M.J. and Camp, V.E., 1991b, Geologic map of the Cenozoic Lava Field of Harrat Kishb, Kingdom of Saudi Arabia: Saudi Arabian Directorate General of Mineral Resources Geoscience Map GM-132, scale 1:250,000 with text 34p.

SGS 2005. Technical work program of the Saudi Geological Survey (SGS) . Jeddah, Saudi Arabia. 79 p.

SGS 2009. Field Observations from Harrat Lunayyir. Unpublished report, Saudi Geological Survey (SGS) . Jeddah, Saudi Arabia. 15 p.

Silver, P. G., and W. E. Holt (2002), The mantle flow field beneath western North America, Science, 295(5557), 1054-1057.

Stoeser, D.B. and Camp, V.E. 1985. Pan-African microplate accretion of the Arabian Shield, Bull. Geol. Soc. Ame. 6: 817-826.

Suetsugu, D. (2003): PMAN The program for focal mechanism diagram with p-wave polarity data using the equal-area projection. IISEE Lecture Note, Tsukuba, Japan, pp. 44-58.

Sun, S. and Hanson, G. (1975) : Evolution of the mantle: Geochemical evidence from alkali basalt. Geology, V.3, P.297-302.

Sykes, L. R., (1967): Mechnism of earthquakes and nature of faulting on the mid-ocean ridge, J. Geophys. Res., vol. 72, pp. 2131-2153.

Tatham, R. H. and Savino, J. M. (1974): Faulting mechanisms for 2 oceanic earthquake swarms. J. Geophys. Res., Vol. 79, pp. 2643-2652.

Utsu, T. (1961): A statistical study on the occurrence of aftershocks. Geophysics. Mag., 30, pp. 521-605.

Verduzco, B., Fairhead, J. D., and Green, C. M., 2004, New insights into magnetic derivatives for structural mapping: The Leading Edge, **23,** 116-119

Walter, W. (1993). Source parameters of the June 29, l992 Little Skull Mountain earthquake from complete regional waveforms at a single station, *Geophys. Res. Lett.,* 20, 403-406.

Zobin, V.M., 1979, Variations of volcanic earthquakes source parameters before volcanic eruptions, Journ. Volc. Geotherm. Res., 6, 279-293.

RESPONSE TO REVIEWER'S COMMENTS ON THE FINAL REPORT OF ART - 28-95

الردود على مرئيات المحكمين بخصوص التقرير النها ئي للبحث رقم أت-٢٨-٩٥

Reviewer 1 المحكم الاول

١. يجب اضافة شريط ممغنط حاسوبي يحتوى على جميع الخرائط الرقمية التي تم استخلاصها من نتائج الدراسة

تم في التقرير النهائي المنقح إضافة جميع الخرائط الجيولوجية والمغناطيسية الجوية (المجال الكلي – المختزلة الى القطب-المشتقة الثانية) والزلزالية والجيولوجية بمقاييس رسم مختلفة وعالية الدقة.

٢. ربط الواقع الحقلي مع النتائج

تمت في التقرير النهائي ربط نتائج التحليل الجيوكيميائي مع التتابع الطبقي لحرة لونيير بالاضافة الى العمر الجيولوجي الدقيق لكل تتابع طبقي لبراكين الحرة. علاوة على ذلك تم ربط نتائج البيانات الزلزالية والمغناطيسية الجوية مع التراكيب الجيولوجية الواقعة في الحرة والبحر الأحمر.

٣. تطرق الباحثون لخرائط تم الاعتماد على بعضها ولم تضاف في ملاحق التقرير حتى يتمكن المستفيد من مقارنتها مع نتائج هذه الدراسة.

قامت هيئة المساحة الجيولوجية اثناء حادثة العيص باعداد تقرير فني عن المشاهدات الحقلية واشتمل التقرير على مايلي:

أ. مراقبة وتسجيل مستمر للنشاط الزلزالي في الحرة

ب.قياسات تغير درجات الحرارة وغاز الرادون

ت.عمل خرائط ال INSAR لدراسة التشوهات القشرية والإنتفاخات وتم ادراج البيانات الحرارية وغاز الرادون وجميع الخرائط والنماذج في الملحق E وللحصول على تفاصيل اكثر يمكن مخاطبة هيئة المساحة الجيولوجية.

٤. توضيح كيف تم تحقيق الهدف الرابع والخاص بانشاء شبكة جيوديسية في مناطق الزلازل النشطة.

خلال الستة اشهر الثانية من المشروع تم وضع محطتي GPS في موقعين لمحطتي زلازل ولمدة ٣ اشهر لمراقبة التحركات والتشوهات القشرية في الحرة ولم يتم تسجيل أي نتائج يعتمد عليها وبالتالي تم القيام بتحليل صور ال IN SAR كبديل لها والتي لم تكن ضمن اهداف الدراسة واعطت نتائج متوافقة مع اتجاه التراكيب السائدة في منطقة الدراسة.

٥. وصف INSAR لم يحدد اتجاه وتاريخ ونوعية الصور الرادارية.

تم وصف الخرائط بالتفصيل في الفصل الثالث موضحة نوعية الصور الرادارية واتجاهها وتقرير عنها بالإضافة الى ادراج صور وتحاليل اجرتها هيئة المساحة الجيولوجية بالتعاون مع هيئة المساحة الأمريكية (انظر الملحق E) .

٦. معظم المراجع التي اشير اليها في التقرير لم تضمن في قائمة المراجع

تم التأكد من ذلك وتصحيحها وتضمينها في التقرير النهائي المنقح.

٧. معالجة المعلومات المغناطيسية يحتاج الى توضيح اكثر

تم اجراء المطلوب بالتفصيل في الفصل الرابع

٨. طريقة تحديد الأشكال الخطية تحتاج الى توضيح اكثر

تم اجراء المطلوب بالتفصيل في الفصل الرابع وفي القرص الحاسوبي المرفق

٩. اقترح عمل قاعدة معلومات جغرافية رقمية لجميع النتائج التي حصل عليها الباحثون

تم عمل المطلوب وتصنيفها في قاعدة بيانات جغرافية وجميع خرائط منطقة الدراسة مفصلة في القرص الحاسوبي المرفق .

SECOND REVIEWER :

1. Captions of figures in Chapter 3 need more details. More elaboration on the trend of different colors in each map and what do they indicate , will make it better.

All captions along the entire text are explained in details. Structural trends of geologic and aeromagnetic maps in chapters 3 and 4 are identified and delineated.

2. The analytical techniques of petrography and geochemistry (P. 71-72) should include detailed specifications of the analytical equipments and placed in the beginning of chapter 4.

Analytical techniques and procedures of Petrography and Geochemistry are given in details and placed in the beginning of chapter 4 (pages 66 – 76) as well as in Appendix B.

3. Figures on pages 101 and 104 and tables on pages 107 and 109 in chapter 5 have no captions

Corrected and Captions are added.

4. I recommend that at least two points of the conclusion and recommendation should be included in both English and Arabic summaries.

See the revised Arabic and English abstracts as suggested

GLOSSARY

المصطلحات اللاتينية وترجمتها العربية

Arabian Plate	الصفيحه العربيه
Arabian Platform	الرصيف العربي
Arabian Shield	الدرع العربي
Asthenosphere	الغلاف الوهن
Azimuth	الإتجاه الزاوي
Broadband Stations	محطات واسعة المدى
Correlation Coefficient	معامل المضاهاه
Crustal Structure	التركيب القشري
Crustal Thickness	السمك القشري
Harrat Lunayyir	حرة لونيير
Delay Time	زمن التأخير
Epicenter	المركز السطحي للزلزال
Focal Mechanism Solutions	حلول ميكانيكية البؤرة
Fast Polarization	الإستقطاب السريع
Focal Depth	العمق البؤري
Group Velocities	السرع الجماعية

International Association of Seismology & Physics of the Earth (Iasp91)	نموذج حساب معدل السرعه
Frequency	التردد
Aeromagnetics	المغناطيسية الجوية
Magma	صهارة
Lithosphere	الغلاف الصخري
Chronology	العمر الجيولوجي
Broadband seismic station	محطة رصد ذات فتره دوريه واسعة المدى
Longitude (E)	خط الطول
Lower Crust	القشره السفلي
Magnitude	القدر الزلزالي
Mantle	الوشاح (لحاء)
Miocene	فترة الميوسين
Moho Discontinuity	إنقطاع موهو
Monthly Listing	النشرة الزلزاليه الشهريه
Spreading Centers	مراكز التمدد
Tertiary	العصر الثلاثي
Origin Time	زمن حدوث الزلزال عند البؤره
Preliminary Determination of Epicenters (PDE)	التحديد المبدئي لمراكز الزلازل

Plate Tectonics	حركة الصفائح
Polar Projection	إسقاط قطبي
Primary Wave Velocity (Vp)	سرعة الموجات الطوليه
Quaternary	العصر الرابع
Receiver Function	دالة المستقبل
Response Curve	منحنى الإستجابه
Review Events Bulletin (REB)	نشرة الأحداث المراجعه
Rock Density	الكثافه الصخريه
SANDSN	الشبكه السعودية الوطنيه الرقمية للزلازل
Seismic Analysis Code (SAC)	كود التحليل الزلزالي
Seismic Attenuation	التعتيم الزلزالي
Seismic Hazards	خطر زلزالي
Seismic Noise	الضوضاء السيزميه
Seismic Tomography	زلزالية ثلاثية الأبعاد
Seismic Waves	الموجات الزلزاليه
Seismogram	سجل زلزالي
Shear Wave Velocity (Vs)	سرعة موجات القص
Shear Wave Splitting	فصل موجات القص
Spectral Amplitude	السعة الطيفيه

Spectral Analysis	التحليل الطيفي
Surface Wave dispersion	تشتت الموجة السطحي
Surficial Sediments	رواسب سطحيه
Synthetic Waveform	الشكل الموجي المركب
Take-off Angle	زاوية خروج الشعاع عند بؤرة الزلزال
Teleseismic Earthquakes	الزلازل البعيده
Tertiary	العصر الثالث
Theoretical Spectral Rations	النسب الطيفيه النظريه
Thickness	السماكه
Transition Zone	منطقة إنتقاليه
Travel Times	أزمنة المسار
Upper Crust	القشره العلويه
Wave Propagation	الإنتشار الموجي
Waveform Modeling	نمذجة الشكل الموجي

Appendix : A

^{40}Ar-^{39}Ar Dating of Rock Samples

P53-035 HL-2 Whole Rock Basalt Fractions:

No	Name	Temp	Cum 39K	Age	40Ar* / 39K
1	35-01 2.0W 2-D	1	0.00066	-67.244 ± 68.924 Ma	-6.067 ± 6.10
2	35-02 2.5W 2-D	2	0.00385	6.552 ± 10.219 Ma	0.603 ± 0.94
3	35-03 3.0W 2-D	3	0.02119	0.268 ± 2.708 Ma	0.025 ± 0.25
4	33-04 4.0W 3-D	4	0.05544	770.607 ± 977.500 ka	0.071 ± 0.09
5	35-05 4.5W 3-D	5	0.16273	-438.336 ± 455.984 ka	-0.040 ± 0.04
6	35-06 4.5W 20kH	6	0.22168	-528.264 ± 516.313 ka	-0.049 ± 0.05
7	35-07 5.0W 20kH	7	0.46682	147.518 ± 150.067 ka	0.014 ± 0.01
8	35-08 6.0W 20kH	8	0.62311	-157.273 ± 184.490 ka	-0.014 ± 0.02
9	35-09 6.5W 20kH	9	0.83339	55.481 ± 151.237 ka	0.005 ± 0.01
10	35-10 7.0W 20kH	10	0.94672	-1.558 ± 225.242 ka	-0.000 ± 0.02
11	35-11 7.5W 20kH	11	1.00000	-56.191 ± 412.792 ka	-0.005 ± 0.04

No	Name	Cum 36S	40Ar / 36Ar	40ArAcc/g	37Ca / 39K
1	35-01 2.0W 2-D	0.00710	263.25 ± 28.90	5.8E-0012	3.709 ±1.990
2	35-02 2.5W 2-D	0.03291	299.77 ± 6.77	2.1E-0011	1.590 ±0.246
3	35-03 3.0W 2-D	0.15809	295.70 ± 1.98	1.0E-0010	1.772 ±0.059
4	33-04 4.0W 3-D	0.20126	298.72 ± 4.13	3.5E-0011	2.987 ±0.031
5	35-05 4.5W 3-D	0.55206	294.79 ± 0.73	2.9E-0010	2.227 ±0.012
6	35-06 4.5W 20kH	0.61990	293.08 ± 2.34	5.6E-0011	2.970 ±0.020
7	35-07 5.0W 20kH	0.78649	296.64 ± 1.17	1.4E-0010	3.587 ±0.008
8	35-08 6.0W 20kH	0.85742	293.67 ± 2.13	5.8E-0011	3.357 ±0.013
9	35-09 6.5W 20kH	0.94757	296.18 ± 1.86	7.4E-0011	3.057 ±0.012
10	35-10 7.0W 20kH	0.98155	295.47 ± 3.96	2.8E-0011	2.770 ±0.013
11	35-11 7.5W 20kH	1.00000	294.64 ± 6.26	1.5E-0011	2.429 ±0.021

No	38Cl / 39K	40Ar* Vol ccNTP/g	Atm Cont	F1	F2
1	10.015 ± 55.075 m	-635.60 ±-638.58 E-15 (100.5%)	112.2490%	-0.002646	0.002847
2	15.482 ± 5.073 m	305.94 ± 478.03 E-15 (156.2%)	98.5751%	-0.001134	0.002005
3	12.676 ± 1.593 m	67.99 ± 686.84 E-15 (1010.3%)	99.9338%	-0.001264	0.002659
4	5.468 ± 0.846 m	386.11 ± 489.88 E-15 (126.9%)	98.9209%	-0.002131	0.034531
5	7.548 ± 0.333 m	-687.74 ±-715.35 E-15 (104.0%)	100.2397%	-0.001588	0.009221
6	5.989 ± 0.546 m	-455.36 ±-445.00 E-15 (97.7%)	100.8253%	-0.002119	0.037671
7	5.503 ± 0.178 m	528.92 ± 538.09 E-15 (101.7%)	99.6143%	-0.002559	0.075618
8	4.733 ± 0.205 m	-359.49 ±-421.69 E-15 (117.3%)	100.6219%	-0.002395	0.103819
9	5.439 ± 0.154 m	170.63 ± 465.13 E-15 (272.6%)	99.7697%	-0.002180	0.100561
10	5.227 ± 0.263 m	-2.58 ±-373.35 E-15 (14460.1%)	100.0093%	-0.001976	0.127175
11	5.637 ± 0.409 m	-43.78 ±-321.64 E-15 (734.6%)	100.2903%	-0.001733	0.099478

Integrated Results:

Age = -49.570 ± 118.120 ka **Wt. Mean Age = 5.181 ± 80.888 ka(0.584)**

40Ar* / 39K = -4.556 ± 10.857 E-3 ccNTP/g **Total 39K Vol = 1.5912E-0010**

Total 40Ar* Vol = -0.725 ± 1.728 E-12

(40Ar / 36Ar)sam = 295.24 ± 0.62 **Total Atm 40Ar Vol = 8.2000E-0010 ccNTP/g**

(36Ar / 40Ar)sam = 0.00338709 ±0.00000714 **Corr 36/40 & 39/40 ratios = 0.072238**

(37Ar / 40Ar)sam = 0.59131997 ±0.00155163 **Corr 36/40 & 37/40 ratios = 0.037853**

(39Ar / 40Ar)sam = 0.19421807 ±0.00041958 **Corr 37/40 & 39/40 ratios = 0.782338**

37Ca / 39K = 3.045 ± 0.005 **38Cl / 39K = 5.751 ± 0.104 E-3**

Ca / K = 5.587 ± 0.009 **Cl / K = 1.208 ± 0.022 E-3**

F1 = -2.172 E-3 **F2 = 4.444 E-2**

P53-022 HL-14 Whole Rock Basalt Fractions:

No	Name	Temp	Cum 39K	Age	40Ar* / 39K
1	22-01 2.0W 1-D	1	0.03083	-0.135 ± 1.451 Ma	-0.012 ± 0.13
2	22-02 2.5W 1-D	2	0.04062	1.421 ± 4.037 Ma	0.131 ± 0.37
3	22-03 3.0W 1-D	3	0.08931	1.414 ± 0.799 Ma	0.130 ± 0.07
4	22-04 3.5W 1-D	4	0.13610	-4.067 ± 798.208 ka	-0.000 ± 0.07
5	22-05 4.0W 1-D	5	0.22842	459.696 ± 266.640 ka	0.042 ± 0.02
6	22-06 4.5W 1-D	6	0.32319	550.951 ± 417.181 ka	0.051 ± 0.04
7	22-07 5.0W 20kH	7	0.43596	468.260 ± 268.725 ka	0.043 ± 0.02
8	22-08 5.5W 20kH	8	0.70946	597.218 ± 106.598 ka	0.055 ± 0.01
9	22-09 6.5W 20kH	9	0.94756	361.334 ± 164.378 ka	0.033 ± 0.02
10	22-10 6.5W 20kH	10	1.00000	54.356 ± 573.748 ka	0.005 ± 0.05

No	Name	Cum 36S	40Ar / 36Ar	40ArAcc/g	37Ca / 39K
1	22-01 2.0W 1-D	0.08367	294.85 ± 6.93	2.5E-0011	1.095 ± 0.033
2	22-02 2.5W 1-D	0.09679	309.27 ± 40.99	4.0E-0012	1.233 ± 0.163
3	22-03 3.0W 1-D	0.13781	317.32 ± 13.24	1.2E-0011	1.548 ± 0.028
4	22-04 3.5W 1-D	0.16177	295.40 ± 20.24	7.3E-0012	1.271 ± 0.026
5	22-05 4.0W 1-D	0.20144	309.40 ± 8.44	1.2E-0011	1.319 ± 0.012
6	22-06 4.5W 1-D	0.28153	303.97 ± 6.60	2.4E-0011	1.590 ± 0.016
7	22-07 5.0W 20kH	0.36852	303.39 ± 4.65	2.6E-0011	2.069 ± 0.013
8	22-08 5.5W 20kH	0.66182	302.74 ± 1.32	8.9E-0011	3.860 ± 0.010
9	22-09 6.5W 20kH	0.94616	299.43 ± 1.81	8.6E-0011	4.832 ± 0.018
10	22-10 6.5W 20kH	1.00000	296.19 ± 7.28	1.6E-0011	5.422 ± 0.033

No	38Cl / 39K	40Ar* Vol ccNTP/g	Atm Cont	F1	F2
1	10.427 ± 1.189 m	-55.60 ±-597.48 E-15 (1074.6%)	100.2192%	-0.000781	0.014914
2	11.262 ± 3.455 m	185.74 ± 528.08 E-15 (284.3%)	95.5461%	-0.000879	0.034196
3	7.303 ± 0.505 m	919.92 ± 520.25 E-15 (56.6%)	93.1251%	-0.001104	0.066629
4	4.181 ± 0.468 m	-2.54 ±-498.71 E-15 (19625.6%)	100.0349%	-0.000906	0.088383
5	4.605 ± 0.361 m	566.87 ± 328.86 E-15 (58.0%)	95.5063%	-0.000941	0.107275
6	4.215 ± 0.391 m	697.40 ± 528.16 E-15 (75.7%)	97.2133%	-0.001134	0.068102

7	4.176 ±	0.334 m	705.33 ± 404.84 E-15	(57.4%)	97.4003%	-0.001476	0.094449
8	4.451 ±	0.152 m	2.18 ± 0.39 E-12	(17.9%)	97.6098%	-0.002754	0.122047
9	4.519 ±	0.202 m	1.15 ± 0.52 E-12	(45.5%)	98.6870%	-0.003446	0.134799
10	3.944 ±	0.535 m	38.06 ± 401.80 E-15	(1055.6%)	99.7678%	-0.003868	0.169372

Integrated Results:

Age = 478.112 ± 113.355 ka **Wt. Mean Age = 510.564 ± 77.773 ka(0.459)**

40Ar* / 39K = 43.952 ± 10.422 E-3 ccNTP/g **Total 39K Vol = 1.4530E-0010**

Total 40Ar* Vol = 6.386 ± 1.514 E-12

(40Ar / 36Ar)sam = 301.71 ± 1.50 **Total Atm 40Ar Vol = 3.0376E-0010 ccNTP/g**

(36Ar / 40Ar)sam = 0.00331442 ±0.00001652 **Corr 36/40 & 39/40 ratios =- 0.007631**

(37Ar / 40Ar)sam = 1.48826320 ±0.00780439 **Corr 36/40 & 37/40 ratios =- 0.025041**

(39Ar / 40Ar)sam = 0.46846897 ±0.00229752 **Corr 37/40 & 39/40 ratios = 0.924212**

37Ca / 39K = 3.177 ± 0.006 **38Cl / 39K = 4.778 ± 0.111 E-3**

Ca / K = 5.829 ± 0.012 **Cl / K = 1.003 ± 0.023 E-3**

F1 = -2.266 E-3 **F2 = 1.095 E-1**

P53-034 HL-17 Whole Rock Basalt Fractions:

No	Name	Temp	Cum 39K	Age	40Ar* / 39K
1	34-01 2.0W 23-N	9	0.01309	0.915 ± 6.384 Ma	0.084 ± 0.59
2	34-02 2.3W 23-N	9	0.02575	-0.289 ± 17.233 Ma	-0.027 ± 1.58

3	34-03 2.6W 23-N	10	0.03590	2.622 ±	4.249 Ma	0.241 ±	0.39
4	34-04 2.8W 23-N	11	0.10146	-0.433 ±	1.751 Ma	-0.040 ±	0.16
5	34-05 3.4W 23-N	11	0.15662	-1.376 ±	2.153 Ma	-0.126 ±	0.20
6	34-06 3.5W 23-N	12	0.17290	-1.084 ±	2.182 Ma	-0.100 ±	0.20
7	34-07 3.7W 23-N	13	0.23525	140.601 ±	532.419 ka	0.013 ±	0.05
8	34-08 4.0W 24-N	14	0.33073	448.054 ±	337.565 ka	0.041 ±	0.03
9	34-09 5.0W 24-N	30	0.39266	65.283 ±	371.673 ka	0.006 ±	0.03
10	34-10 3.5W 20kH	31	0.50449	10.751 ±	399.356 ka	0.001 ±	0.04
11	34-11 4.7W 20kH	32	0.60412	168.478 ±	229.441 ka	0.015 ±	0.02
12	34-12 5.0W 20kH	33	0.77869	352.153 ±	155.026 ka	0.032 ±	0.01
13	34-13 5.2W 20kH	34	0.82400	592.476 ±	399.897 ka	0.054 ±	0.04
14	34-14 5.0W 20kH	36	0.90990	366.958 ±	211.062 ka	0.034 ±	0.02
15	34-15 5.5W 20kH	37	0.98268	573.940 ±	311.519 ka	0.053 ±	0.03
16	34-16 6.6W 20kH	38	1.00000	1.367 ±	1.118 Ma	0.126 ±	0.10

No	Name	Cum 36S	40Ar / 36Ar	40ArAcc/g	37Ca / 39K
1	34-01 2.0W 23-N	0.07944	295.86 ± 2.49	2.1E-0010	1.672 ± 0.112
2	34-02 2.3W 23-N	0.16293	295.40 ± 6.16	2.2E-0010	2.427 ± 0.515
3	34-03 2.6W 23-N	0.19676	297.36 ± 3.03	9.0E-0011	1.879 ± 0.094
4	34-04 2.8W 23-N	0.37228	295.12 ± 1.54	4.7E-0010	2.460 ± 0.031
5	34-05 3.4W 23-N	0.53362	294.39 ± 1.73	4.3E-0010	2.710 ± 0.043
6	34-06 3.5W 23-N	0.56852	294.31 ± 2.39	9.3E-0011	2.223 ± 0.069
7	34-07 3.7W 23-N	0.62869	295.84 ± 1.30	1.6E-0010	3.129 ± 0.020
8	34-08 4.0W 24-N	0.68418	297.32 ± 1.38	1.5E-0010	3.951 ± 0.017

9	34-09 5.0W 24-N	0.71444	295.82 ±	1.80	8.0E-0011	3.458 ± 0.024
10	34-10 3.5W 20kH	0.77886	295.54 ±	1.64	1.7E-0010	3.716 ± 0.030
11	34-11 4.7W 20kH	0.82403	296.38 ±	1.20	1.2E-0010	3.526 ± 0.013
12	34-12 5.0W 20kH	0.90919	297.20 ±	0.75	2.3E-0010	3.712 ± 0.010
13	34-13 5.2W 20kH	0.92950	298.62 ±	2.13	5.4E-0011	3.669 ± 0.021
14	34-14 5.0W 20kH	0.96817	297.42 ±	1.11	1.0E-0010	5.689 ± 0.028
15	34-15 5.5W 20kH	0.99312	299.45 ±	2.17	6.6E-0011	7.481 ± 0.024
16	34-16 6.6W 20kH	1.00000	303.62 ±	6.83	1.8E-0011	11.997 ± 0.057

No	38Cl / 39K	40Ar* Vol ccNTP/g	Atm Cont	F1	F2
1	6.367 ± 4.513 m	0.25 ± 1.77 E-12 (698.2%)	99.8798%	-0.001193	0.000782
2	17.666 ± 8.225 m	-0.08 ± -4.62 E-12 (5957.8%)	100.0350%	-0.001731	0.000905
3	5.426 ± 3.756 m	564.19 ± 914.74 E-15 (162.1%)	99.3749%	-0.001340	0.002694
4	6.133 ± 0.990 m	-0.60 ± -2.43 E-12 (404.2%)	100.1293%	-0.001755	0.004804
5	3.470 ± 2.326 m	-1.61 ± -2.51 E-12 (156.4%)	100.3770%	-0.001933	0.004682
6	9.524 ± 2.141 m	-373.87 ±-751.92 E-15 (201.1%)	100.4056%	-0.001586	0.005812
7	5.882 ± 0.441 m	185.62 ± 702.92 E-15 (378.7%)	99.8838%	-0.002232	0.020545
8	4.691 ± 0.345 m	905.97 ± 682.66 E-15 (75.4%)	99.3881%	-0.002818	0.043801

9	7.197 ±	0.572 m	85.60 ± 487.36 E-15	(569.3%)	99.8934%	-0.002467	0.045961
10	5.073 ±	0.440 m	25.46 ± 945.61 E-15	(3714.6%)	99.9851%	-0.002651	0.041695
11	5.667 ±	0.285 m	355.45 ± 484.09 E-15	(136.2%)	99.7041%	-0.002515	0.050458
12	7.368 ±	0.219 m	1.30 ± 0.57 E-12	(44.0%)	99.4268%	-0.002648	0.049239
13	4.353 ±	0.376 m	568.52 ± 383.80 E-15	(67.5%)	98.9555%	-0.002617	0.052972
14	4.554 ±	0.843 m	667.53 ± 383.99 E-15	(57.5%)	99.3533%	-0.004058	0.079384
15	3.804 ±	0.308 m	884.62 ± 480.24 E-15	(54.3%)	98.6803%	-0.005337	0.130752
16	5.023 ±	0.934 m	501.55 ± 410.21 E-15	(81.8%)	97.3247%	-0.008558	0.171012

Integrated Results:

Age = 171.926 ± 303.909 ka **Wt. Mean Age = 324.796 ± 88.719 ka(0.359)**

40Ar* / 39K = 15.803 ± 27.937 E-3 **Total 39K Vol = 2.3036E-0010 ccNTP/g**

Total 40Ar* Vol = 3.641 ± 6.436 E-12

(40Ar / 36Ar)sam = 295.91 ± 0.72 **Total Atm 40Ar Vol = 2.6517E-0009 ccNTP/g**

(36Ar / 40Ar)sam = 0.00337946 ±0.00000820 **Corr 36/40 & 39/40 ratios = 0.051653**

(37Ar / 40Ar)sam = 0.34937106 ±0.00114629 **Corr 36/40 & 37/40 ratios = 0.023822**

(39Ar / 40Ar)sam = 0.08675519 ±0.00022941 **Corr 37/40 & 39/40 ratios = 0.674937**

37Ca / 39K = 4.027 ± 0.010 **38Cl / 39K = 5.741 ± 0.227 E-3**

Ca / K = 7.389 ± 0.018 **Cl / K = 1.206 ± 0.048 E-3**

F1 = -2.873 E-3 **F2 = 2.528 E-2**

P53-033 HL-26 Whole Rock Basalt Fractions:

No	Name	Temp	Cum 39K	Age	40Ar* / 39K
1	33-01 2.0W 22-N	1	0.00730	3.422 ± 5.446 Ma	0.315 ± 0.50
2	33-02 3.0W 22-N	2	0.04570	606.958 ± 826.243 ka	0.056 ± 0.08
3	33-03 3.5W 22-N	3	0.35779	164.402 ± 107.115 ka	0.015 ± 0.01
4	33-04 4.0W 20kH	4	0.52673	230.637 ± 225.705 ka	0.021 ± 0.02
5	33-05 4.5W 20kH	5	0.67384	290.683 ± 252.615 ka	0.027 ± 0.02
6	33-06 4.7W 20kH	6	0.74817	310.001 ± 617.233 ka	0.028 ± 0.06
7	33-07 5.0W 20kH	7	0.95486	145.166 ± 209.666 ka	0.013 ± 0.02
8	33-08 6.5W 20kH	8	1.00000	2.595 ± 0.948 Ma	0.239 ± 0.09

No	Name	Cum 36S	40Ar / 36Ar	40ArAcc/g	37Ca / 39K
1	33-01 2.0W 22-N	0.04517	301.29 ± 9.40	1.4E-0011	2.572 ± 0.111
2	33-02 3.0W 22-N	0.09201	300.70 ± 7.21	1.4E-0011	3.772 ± 0.038
3	33-03 3.5W 22-N	0.20127	300.41 ± 3.25	3.4E-0011	3.035 ± 0.008
4	33-04 4.0W 20kH	0.42943	297.29 ± 1.76	7.0E-0011	2.616 ± 0.011
5	33-05 4.5W 20kH	0.67914	297.29 ± 1.57	7.7E-0011	3.500 ± 0.012
6	33-06 4.7W 20kH	0.80640	297.39 ± 3.80	3.9E-0011	4.006 ± 0.030
7	33-07 5.0W 20kH	0.97152	297.40 ± 2.76	5.1E-0011	10.221 ± 0.020
8	33-08 6.5W 20kH	1.00000	338.55 ± 17.85	8.8E-0012	18.541 ± 0.171

No	38Cl / 39K	40Ar* Vol ccNTP/g	Atm Cont	F1	F2
1	23.445 ± 7.457 m	272.96 ± 434.78 E-15 (159.3%)	98.0795%	-0.001834	0.011223
2	6.638 ± 0.831 m	254.61 ± 346.66 E-15 (136.2%)	98.2692%	-0.002691	0.087056
3	4.307 ± 0.252 m	560.39 ± 365.15 E-15 (65.2%)	98.3651%	-0.002165	0.214357
4	5.107 ± 0.237 m	425.56 ± 416.49 E-15 (97.9%)	99.3992%	-0.001866	0.056236
5	5.623 ± 0.407 m	467.05 ± 405.93 E-15 (86.9%)	99.3976%	-0.002497	0.059174
6	4.915 ± 0.785 m	251.69 ± 501.18 E-15 (199.1%)	99.3632%	-0.002858	0.066585
7	4.670 ± 0.258 m	327.70 ± 473.32 E-15 (144.4%)	99.3610%	-0.007291	0.283944
8	3.414 ± 0.981 m	1.28 ± 0.47 E-12 (36.5%)	87.2839%	-0.013225	0.476145

Integrated Results:

Age = 351.618 ± 111.180 ka **Wt. Mean Age = 208.823 ± 85.253 ka(1.046)**

40Ar* / 39K = 32.322 ± 10.221 E-3 ccNTP/g **Total 39K Vol = 1.1882E-0010**

Total 40Ar* Vol = 3.841 ± 1.214 E-12

(40Ar / 36Ar)sam = 299.18 ± 1.18 **Total Atm 40Ar Vol = 3.0861E-0010 ccNTP/g**

(36Ar / 40Ar)sam = 0.00334250 ±0.00001315 **Corr 36/40 & 39/40 ratios = 0.011882**

(37Ar / 40Ar)sam = 2.02124330 ±0.00849036 **Corr 36/40 & 37/40 ratios =- 0.015718**

(39Ar / 40Ar)sam = 0.38029199 ±0.00148765 **Corr 37/40 & 39/40 ratios = 0.914376**

37Ca / 39K = 5.315 ± 0.009 **38Cl / 39K = 4.945 ± 0.153 E-3**

Ca / K = 9.752 ± 0.017 **Cl / K = 1.038 ± 0.032 E-3**

F1 = -3.791 E-3 **F2 = 1.413 E-1**

P53-029 HL-31 Whole Rock Basalt Fractions:

No	Name	Temp	Cum 39K	Age	40Ar* / 39K
1	29-01 2.0W 15-N	1	0.00014	99.854 ± 220.521 Ma	9.437 ± 21.42
2	29-02 2.3W 15-N	2	0.00019	-60.950 ± 469.007 Ma	-5.509 ± 41.68
3	29-03 3.0W 15-N	3	0.00303	-10.730 ± 17.254 Ma	-0.983 ± 1.58
4	29-04 3.5W NB 1	4	0.01570	4.040 ± 4.307 Ma	0.372 ± 0.40
5	29-05 3.7W 15-N	5	0.02077	-1.662 ± 4.581 Ma	-0.153 ± 0.42
6	29-06 4.0W 20kH	6	0.05722	193.947 ± 574.097 ka	0.018 ± 0.05
7	29-07 4.5W 20kH	7	0.27417	253.081 ± 150.115 ka	0.023 ± 0.01
8	29-08 4.6W 20kH	8	0.49479	190.398 ± 165.345 ka	0.018 ± 0.02
9	29-09 5.0W 20kH	9	0.63456	-4.420 ± 240.327 ka	-0.000 ± 0.02
10	29-10 5.0W 20kH	10	0.79653	314.044 ± 260.352 ka	0.029 ± 0.02
11	29-11 6.0W 20kH	11	1.00000	485.346 ± 191.012 ka	0.045 ± 0.02

No	Name	Cum 36S	40Ar / 36Ar	40ArAcc/g	37Ca / 39K
1	29-01 2.0W 15-N	0.00359	338.58 ± 111.52	1.1E-0012	5.171 ± 9.638
2	29-02 2.3W 15-N	0.00516	274.25 ± 148.64	4.9E-0013	26.779 ± 35.184
3	29-03 3.0W 15-N	0.04599	287.38 ± 12.66	1.3E-0011	423.372 ± 334.149 m
4	29-04 3.5W NB 1	0.08995	308.22 ± 14.16	1.4E-0011	1.066 ± 0.073
5	29-05 3.7W 15-N	0.10348	288.71 ± 18.28	4.3E-0012	1.352 ± 0.233
6	29-06 4.0W 20kH	0.15573	296.98 ± 4.39	1.6E-0011	2.214 ± 0.037

7	29-07 4.5W 20kH	0.37238	298.27 ±	1.66	6.8E-0011	1.969 ± 0.007
8	29-08 4.6W 20kH	0.57212	297.80 ±	2.01	6.3E-0011	2.266 ± 0.010
9	29-09 5.0W 20kH	0.67635	295.44 ±	3.52	3.3E-0011	2.347 ± 0.010
10	29-10 5.0W 20kH	0.82475	299.24 ±	3.14	4.7E-0011	3.453 ± 0.009
11	29-11 6.0W 20kH	1.00000	301.65 ±	2.47	5.5E-0011	4.388 ± 0.011

No	38Cl / 39K	40Ar* Vol ccNTP/g	Atm Cont	F1	F2
1	-202.303 ± 257.253 m	164.65 ± 372.14 E-15 (226.0%)	87.2757%	-0.003688	0.002888
2	1.181 ± 1.569	-35.37 ±-266.47 E-15 (753.4%)	107.7499%	-0.019102	0.009492
3	7.016 ± 10.685 m	-352.91 ±-565.77 E-15 (160.3%)	102.8260%	-0.000302	0.000674
4	13.992 ± 2.465 m	594.85 ± 634.95 E-15 (106.7%)	95.8738%	-0.000761	0.009339
5	-2.529 ± 6.049 m	-97.78 ±-269.44 E-15 (275.5%)	102.3515%	-0.000964	0.015573
6	3.851 ± 1.064 m	82.10 ± 243.04 E-15 (296.0%)	99.5028%	-0.001579	0.047233
7	5.483 ± 0.292 m	637.63 ± 378.25 E-15 (59.3%)	99.0727%	-0.001404	0.060067
8	5.352 ± 0.280 m	487.81 ± 423.65 E-15 (86.8%)	99.2293%	-0.001616	0.075161
9	4.204 ± 0.259 m	-7.17 ±-390.06 E-15 (5436.7%)	100.0219%	-0.001674	0.093031
10	4.070 ± 0.277 m	590.76 ± 489.81 E-15 (82.9%)	98.7499%	-0.002463	0.108943
11	4.992 ± 0.253 m	1.15 ± 0.45 E-12 (39.4%)	97.9612%	-0.003130	0.141884

Integrated Results:

Age = 276.532 ± 121.242 ka **Wt. Mean Age = 255.929 ± 83.462 ka(0.440)**

40Ar* / 39K = 25.420 ± 11.146 E-3 ccNTP/g **Total 39K Vol = 1.2634E-0010**

Total 40Ar* Vol = 3.211 ± 1.408 E-12

(40Ar / 36Ar)sam = 298.52 ± 1.34 **Total Atm 40Ar Vol = 3.1445E-0010 ccNTP/g**

(36Ar / 40Ar)sam = 0.00334988 ±0.00001500 **Corr 36/40 & 39/40 ratios =- 0.004327**

(37Ar / 40Ar)sam = 1.11818045 ±0.00532071 **Corr 36/40 & 37/40 ratios =- 0.017290**

(39Ar / 40Ar)sam = 0.39771414 ±0.00177142 **Corr 37/40 & 39/40 ratios = 0.925608**

37Ca / 39K = 2.812 ± 0.005 **38Cl / 39K = 4.989 ± 0.155 E-3**

Ca / K = 5.159 ± 0.009 **Cl / K = 1.048 ± 0.033 E-3**

F1 = -2.006 E-3 **F2 = 8.347 E-2**

P53-027 HL-35 Whole Rock Basalt Fractions:

No	Name	Temp	Cum 39K	Age	40Ar* / 39K
1	27-01 2.0W 16-N	12	0.04653	-2.002 ± 1.019 Ma	-0.184 ± 0.09
2	27-02 2.5W 16-N	13	0.15308	638.832 ± 314.227 ka	0.059 ± 0.03
3	27-03 3.2W 16-N	14	0.25304	-327.300 ± 250.256 ka	-0.030 ± 0.02
4	27-04 4.0W 21-N	15	0.28526	726.615 ± 787.259 ka	0.067 ± 0.07
5	27-05 4.5W 20kH	16	0.37548	-389.381 ± 450.793 ka	-0.036 ± 0.04
6	27-06 4.6W 20kH	17	0.43447	401.536 ± 468.889 ka	0.037 ± 0.04
7	27-07 4.9W 20kH	18	0.48032	717.269 ± 645.306 ka	0.066 ± 0.06
8	27-08 5.0W 20kH	19	0.76737	191.394 ± 144.222 ka	0.018 ± 0.01
9	27-09 6.0W 20kH	20	0.89548	316.778 ± 250.914 ka	0.029 ± 0.02
10	27-10 6.5W 20kH	21	0.96793	65.060 ± 298.831 ka	0.006 ± 0.03
11	27-11 7.0W 20kH	22	1.00000	249.480 ± 856.515 ka	0.023 ± 0.08

No	Name	Cum 36S	40Ar / 36Ar	40ArAcc/g	37Ca / 39K
1	27-01 2.0W 16-N	0.24008	293.28 ± 1.12	2.4E-0010	1.385 ± 0.017
2	27-02 2.5W 16-N	0.37035	298.50 ± 1.49	1.3E-0010	2.343 ± 0.009
3	27-03 3.2W 16-N	0.43953	292.79 ± 2.05	7.0E-0011	2.427 ± 0.010
4	27-04 4.0W 21-N	0.47257	299.56 ± 4.46	3.3E-0011	2.306 ± 0.021
5	27-05 4.5W 20kH	0.53022	292.01 ± 4.00	5.8E-0011	2.283 ± 0.012
6	27-06 4.6W 20kH	0.56092	299.92 ± 5.24	3.1E-0011	2.079 ± 0.018
7	27-07 4.9W 20kH	0.59399	301.20 ± 5.23	3.3E-0011	2.252 ± 0.022
8	27-08 5.0W 20kH	0.83943	296.78 ± 0.97	2.5E-0010	2.414 ± 0.006
9	27-09 6.0W 20kH	0.93739	297.88 ± 1.90	9.8E-0011	2.658 ± 0.009
10	27-10 6.5W 20kH	0.98376	296.08 ± 2.68	4.7E-0011	3.674 ± 0.022
11	27-11 7.0W 20kH	1.00000	298.32 ± 9.79	1.6E-0011	6.966 ± 0.037

No	38Cl / 39K	40Ar* Vol ccNTP/g	Atm Cont	F1	F2
1	11.178 ± 0.713 m	-1.82 ± -0.92 E-12 (50.9%)	100.7582%	-0.000988	0.003674
2	7.151 ± 0.502 m	1.33 ± 0.65 E-12 (49.2%)	98.9962%	-0.001671	0.030702
3	6.279 ± 0.285 m	-637.84 ±-487.66 E-15 (76.5%)	100.9259%	-0.001732	0.055972
4	6.829 ± 0.756 m	456.64 ± 494.86 E-15 (108.4%)	98.6436%	-0.001645	0.036130
5	4.726 ± 0.301 m	-684.94 ±-792.89 E-15 (115.8%)	101.1964%	-0.001628	0.057082

6 5.655 ± 0.572 m 461.86 ± 539.39 E-15 (116.8%) 98.5254% -0.001483 0.063694

7 4.422 ± 0.528 m 641.41 ± 577.18 E-15 (90.0%) 98.1066% -0.001606 0.050089

8 6.038 ± 0.161 m 1.07 ± 0.81 E-12 (75.4%) 99.5676% -0.001722 0.045248

9 5.355 ± 0.261 m 791.36 ± 626.89 E-15 (79.2%) 99.2026% -0.001896 0.055328

10 6.108 ± 0.487 m 91.92 ± 422.20 E-15 (459.3%) 99.8032% -0.002621 0.088566

11 5.022 ± 0.732 m 156.01 ± 535.66 E-15 (343.3%) 99.0531% -0.004969 0.189383

Integrated Results:

Age = 95.365 ± 109.085 ka **Wt. Mean Age = 148.728 ± 130.980 ka(1.417)**

40Ar* / 39K = 8.766 ± 10.027 E-3 **Total 39K Vol = 2.1214E-0010 ccNTP/g**

Total 40Ar* Vol = 1.860 ± 2.127 E-12

(40Ar / 36Ar)sam = 296.05 ± 0.63 **Total Atm 40Ar Vol = 1.0050E-0009 ccNTP/g**

(36Ar / 40Ar)sam = 0.00337784 ±0.00000715 **Corr 36/40 & 39/40 ratios = 0.013954**

(37Ar / 40Ar)sam = 0.54481024 ±0.00139134 **Corr 36/40 & 37/40 ratios =- 0.005489**

(39Ar / 40Ar)sam = 0.21069102 ±0.00045279 **Corr 37/40 & 39/40 ratios = 0.811772**

37Ca / 39K = 2.586 ± 0.004 **38Cl / 39K = 6.115 ± 0.114 E-3**

Ca / K = 4.745 ± 0.007 **Cl / K = 1.284 ± 0.024 E-3**

F1 = -1.845 E-3 **F2 = 4.136 E-2**

APPENDIX : B

DESCRIPTION OF ROCK SAMPLES

&

PETROGRAPHIC ANALYSIS

- **Sample collection**

A number of about 46 samples of the volcanic rocks we taken from the five different quaternary volcanic layers and from the tertiary local flows which no longer flow as individual layer. The samples taken about 3 kg each and we take double one as reference sample the sample number from lower to upper quaternary and from tertiary age.

layer	Sample no
Q5 quaternary	**2- 40- 1**
Q4	**24-38-16-12-37-15-39-26-42**
Q3	**22-35-30-41-34-36-43-29-23**
Q2	**28- 9- 14- 27- 19**
Q1	**33- 20- 25- 32- 21- 31**
T tertiary	**4- 13- 3- 6-8-7- 18- 10- 17- 11- 5**

Hand specimen description of Samples

hand specimen description for the sample taken for each layer can summarized as below

Layer no	Sample no	Description
Q1	**33- 20- 25- 32- 21- 31**	Grey color highly vesicular , fine massive rocks with Amygdales (size vary from fine to 1cm) calcite is seen filling the cavities some copper minerals are found as very small partials , some viscous show orientation
Q2	**28- 9- 14- 27-**	Grayish black color locally vesicular , rocks with Amygdales (size vary from fine to 1cm

	19	) filing by zeolite , some viscous show orientation, olivine mineral is visible in fine grains (fig1,2,3)
Q3	**22-35-30-41-34-36-43-29-23**	Grayish black color vesicular , some viscous show orientation, with Amygdales (size vary from fine to 1cm) filing by zeolite ,and calcite is seen filling the cavities olivine and plagioclase mineral is visible in fine grains, and surface show baking to exposed sediment (fig.4) .some samples closed to be daibase.
Q4	**24-38-16-12-37-15-39-26-42**	Black massive vesicular is locally , some viscous show orientation (fig.5), with (size vary Amygdales from fine to 1cm) filing by zeolite , and calcite is seen filling the cavities olivine and plagioclase mineral is visible in fine grains, and surface show baking to exposed sediment . porphritic texture seen.
Q5	**2- 40- 1**	Black gerish vesicular high , some viscous show lantculler orientation, with Amygdales filing by zeolite , , and surface show peaking to exposed sediment ..
T	**4- 13- 3- 6-8-7-18- 10- 17- 11-5**	Black very fine grains, massive vesicular is locally filing by zeolite . olivine mineral is visible in fine grains, and surface show baking to exposed sediment

Locally vesicular

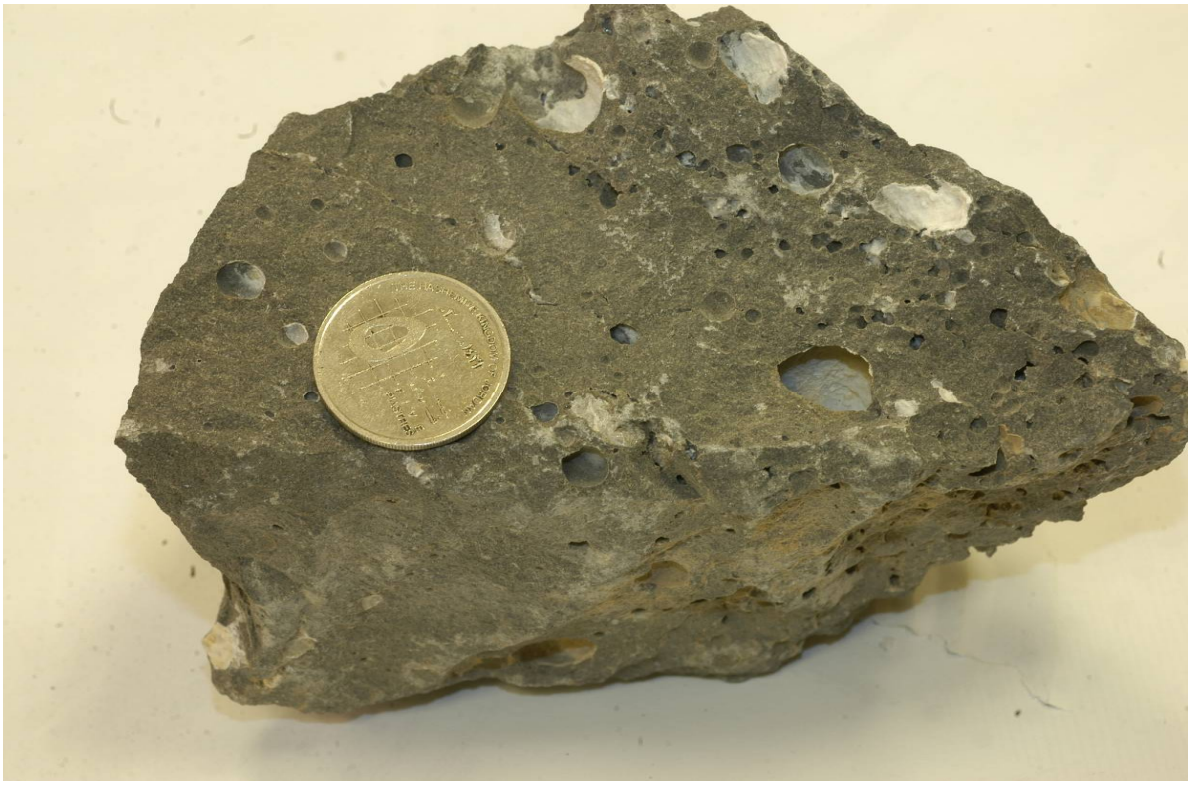

Amygdales (size vary from fine to 1cm) filing by zeolite

Amygdales (size vary from fine to 1cm) filing by zeolite

baking of exposed sediment at the surface

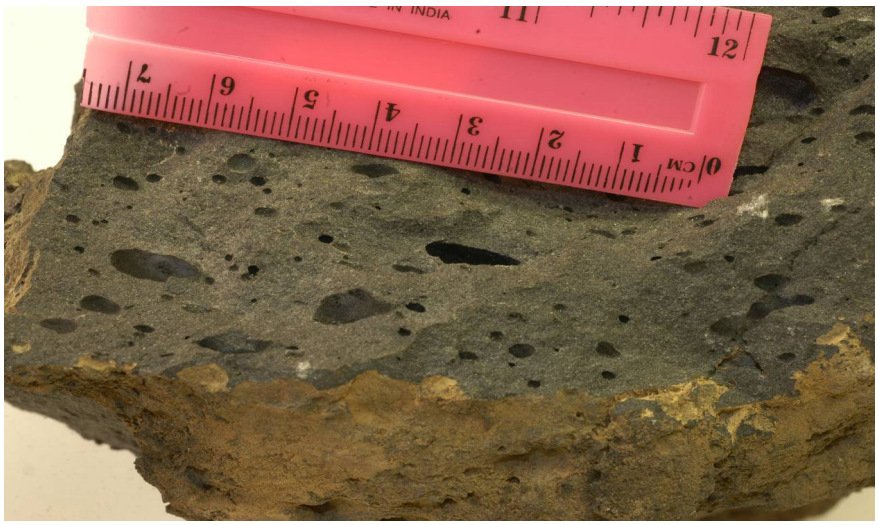

a

b

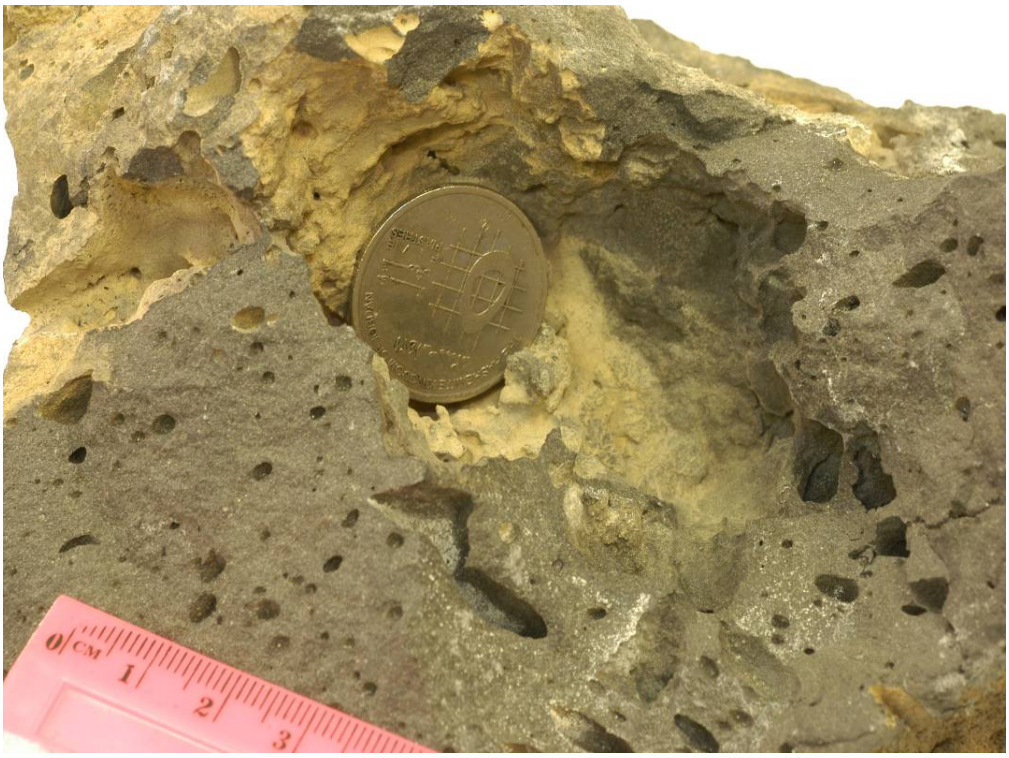

c

a,b and c some viscous with different sizes show orientation

Analytical Methods

10 Samples prepared for petrographic study, 43 samples for geochemical analysis (major, minor and trace elements including the rare earths) by inductively coupled plasma Mass spectrometry (ICP-MS). 6 samples analyzed to isotopic and geochronological analyses. The table blew shows the samples type from the different flows and the analytical method

Sample type	Analytical methods	Sample no	Total sample
Volcanic	Age dating	Q1(20-25),Q2(14-28) Q3(22-23),Q4(24-26) Q5(2-40)	6
Volcanic	petrographic study	Q1(29-32),Q2(14-9) Q3(22-23),Q4(16-39) Q5(1-2)	10
Volcanic	geochemical analysis	Sample 1 to 43	43

The petrography study:

Eight samples were studied from the different layers ,the detailed study under microscope show different textures in the different layer of volcanic rocks , also show similarity in some slides in minerals composition the detailed study can be shown as below from different layers :

Sample HL 29(fig.1,2) from layer Q3

Texture: Vesicular, vesicles match up to 30% of the rock. The cavities exhibit variable shapes as elongate, lenticular and even irregular.

Composition:

1- Plagioclase 40%. The plagioclase is mostly labradorite (extinction angle 35º) occurs as minute lath (0.2- 0.3mm).
2- Pyroxene 50%. The pyroxene crystals are too small to verify . They are within the average of 0.02 mm.
3- The opaque minerals mount up to 10% of the rock, The rock is classified as vesicular basalt.

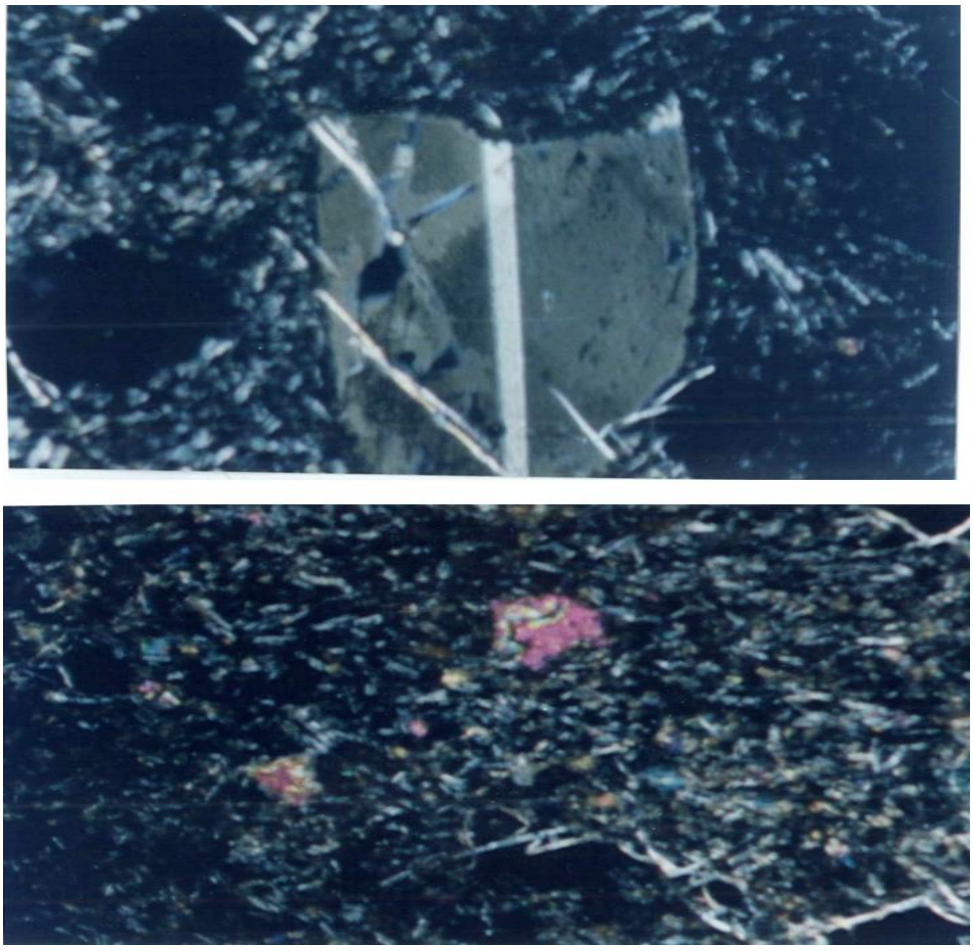

Fig1,2

Sample HL 22 from layer Q3

Texture: The texture is vesicular, fine-grained porphyritc.

Constituents:

1- Plagioclase 40%. The plagioclase which is labradorite occurs as relatively large laths forming phenocrysts.
2- Pyroxene 45%.The pyroxene is found as minute subhedral crystals approximately 0.01mm.
3- Olivine 10%. The olivine occurs as euhedral crystals.
4- Opaque minerals 5%.

Sample HL 1 from layer Q5(fig3)

The rock is vesicular olivine basalt

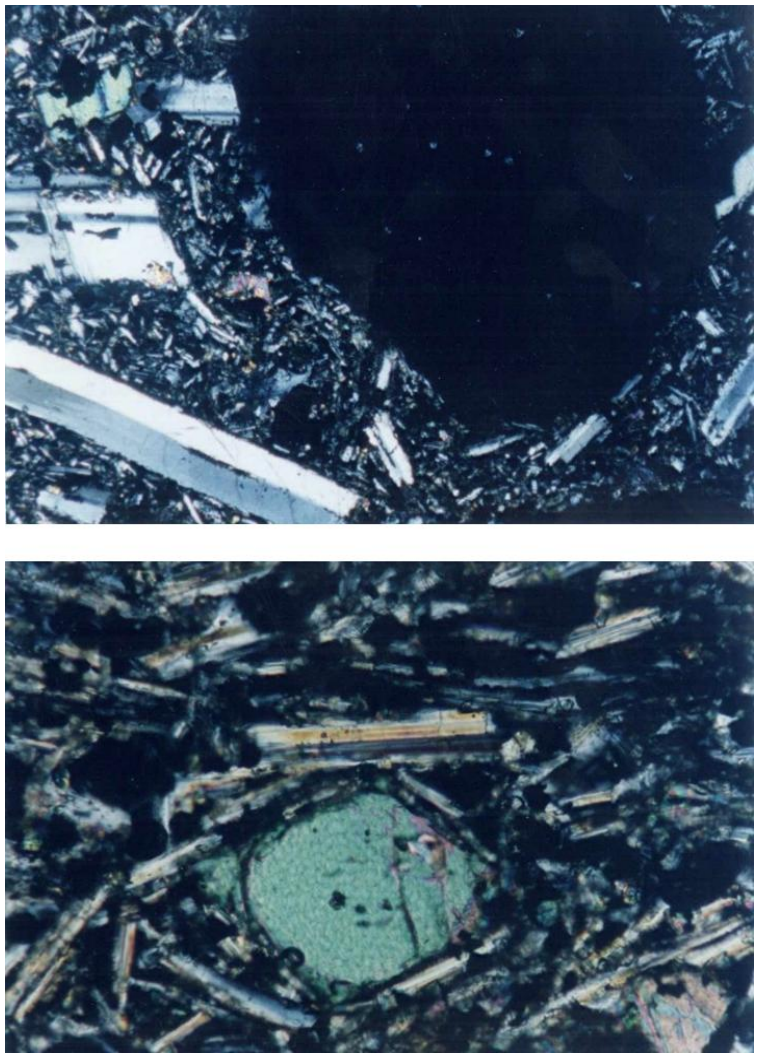

Fig 3 vesicular olivine basalt

Texture: Vesicular and fine-grained porphyritic. The vesicles are few and show orientation.

Composition:

1- Plagioclase 45%. Plagioclase lath average length is 0.8 mm.
2- Pyroxene 40%. The pyroxene occurs in the groundmass as minute crystals and sometimes found as relatively larger crystals (0.3mm) with diffused boundaries.
3- Olivine 9%. The crystals are relatively large to form phenocrysts. The olivine crystals are euhedral and show distortion.
4- Opaque 6%. The equidimentional shape indicates magnetite.

Sample HL 2 from layer Q5(fig 5)

The rock is vesicular olivine basalt

Texture: Fine-grained vesicular.

Composion:

1- Plagioclase 43%. Most of the plagioclase laths have an average length of 0.2 o.3 mm.
2- Pyroxene 40%. It is found as minute (0.04mm) crystals in the matrix.
3- Olivine 6%. The olivine occurs as euhedral crystals commonly distorted.
4- Opaque minerals 11%.

Sample HL 16 from layer Q4 The rock is olivine basalt

Texture: hyalopilitic

Constituents:

1- Plagioclase 55%. The average length of the plagioclase lath is 0.5mm. Some of these laths were distorted.
2- Pyroxene 40 %. The pyroxene occurs as anhedral crystals with diameter within the range 0.2- 0.3mm.

3-Olivine 10 %. The olivine occurs as subhedral crystals and show alteration to serpentine along fractures.

4- Opaque minerals 7%.

5-Iddingsite found as an alteration of olivine and as a trace.

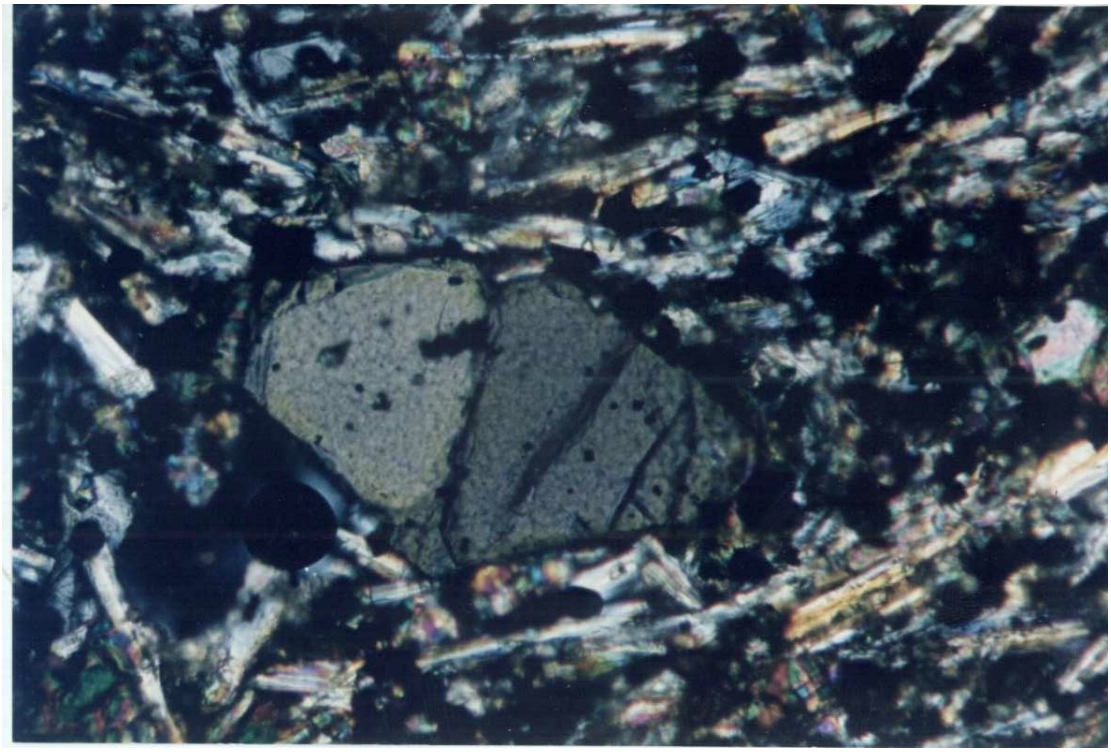

Fig 5 olivine basalt

Sample HL 39 from layer Q4

The rock is vesicular olivine basalt

Texture: Vesicular with large cavities reaching up to 8mm. The cavities are rounded and elongate found oriented due to the flow of the magma.

Mineral composition:

1- Plagioclase 50%.The average length of the plagioclase laths is 0.3mm.
2- Pyroxene 35%. Pyroxene is found only in the matrix as minute crystals.
3- Olivine 7%.
4- Opaque minerals 8%.

Sample HL 14 from layer Q2

Texture: Highly vesicular. The pores approximately 22% of the rock. The cavities are irregular but oriented due to the lava flow.

Constituents:

1- Plagioclase 50%. The plagioclase laths vary in length from 0.1 to 0.6mm. larger laths sometimes broken. The plagioclase bytonite to labradorite. The plagioclase laths sometimes found rapping the olivine.

2- Pyroxene 35%. It occurs as minute (0.01-0.03)crystals with diffused boundaries.

3- Olivine 10%. It is found as euhedral crystals with average size of 0.2 to 1.0mm.

4- Opaque minerals 5%.

Sample HL 9 from layer Q2 The rock is vesicular olivine basalt

Texture: Vesicular with large vesicles (3-6 mm) and exhibit variable shapes rounded, elongate and oval.

Mineral composition:

1- Plagioclase 40%. It occurs as minute lath in the groundmass and as phenocrysts reaching 0.5 to 1.5 mm. Broken laths are common. The plagioclase is laboratories.

2- Pyroxene 40%. Larger crystals exhibit brown color.

3- Olivine 10%. Distortion is common among olivine crystals.

4- Opaque minerals 10%. The opaque minerals are larger than in other samples.

APPENDIX : C

GEOCHEMICAL ANALYSIS

Forty three rock samples sent to ALS labs in Canada for geochemical analysis as shown in table 1. The analyses were done for 85 element , major oxides , Rare earth &trace elements. To show preliminary different relationships among these elements as well as types of volcanic rocks and origin of magma, we applied different diagrams and models. Previous investigators classified the basaltic flows into two groups according to the erosional surfaces. These are the older tertiary and the relatively younger Quaternary basalt. The Quaternary basalt was subdivided into five units depending on field observations.

Basalt classification

Chemical analyses were received from ALS Laboratories in Canada. The analyses cover 43 samples, each sample was analyzed for 72 elements and 14 oxides of major elements. Evaluation of these chemical data at the moment is preliminary. At present we concentrated on data leading to the classification of the basalt in each episode of eruption.

In Fig 2, the silica (SiO_2) was plotted against the total alkalis (Na_2O + K_2O) for all units of the basalt to determine the field of these rocks in igneous classification, As shown on the figure the rocks of the Tertiary and the Quaternary basalt cluster in one area. All rocks are almost similar except for slight variations. These slight variations are even noted within one

unit. According to plot of alkalis against silica the basalt of Lunayyir is classified as trachy-basalt as compared to Le Bas et al. (1986) diagram. As a conclusion the classification of the basalt in all layers found to be fluctuating between basalt, trachy-basalt and tephrite basanite.

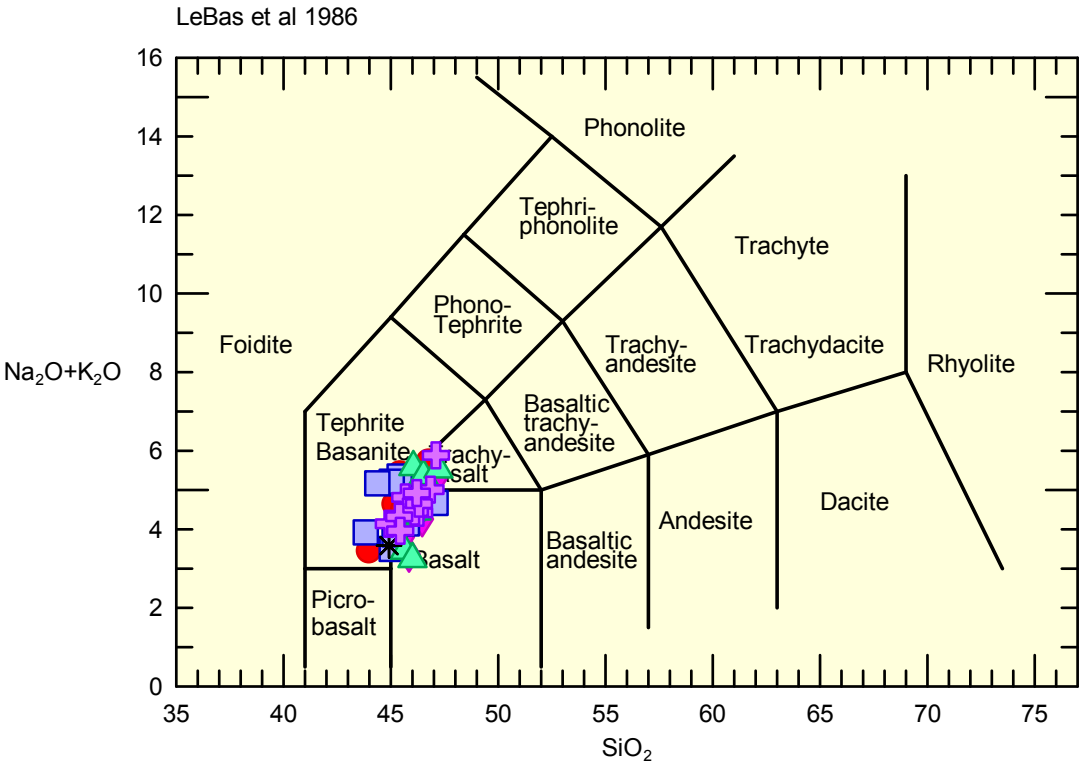

Figure 2 (SiO_2) against the total alkalis (Na_2O + K_2O) all layers

Qm4

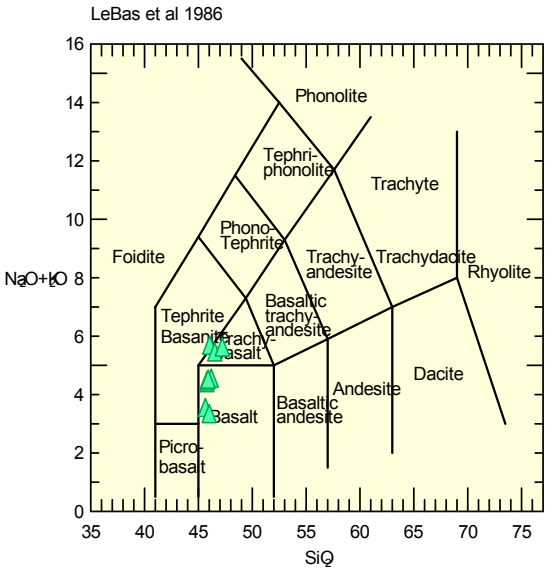

Qm2

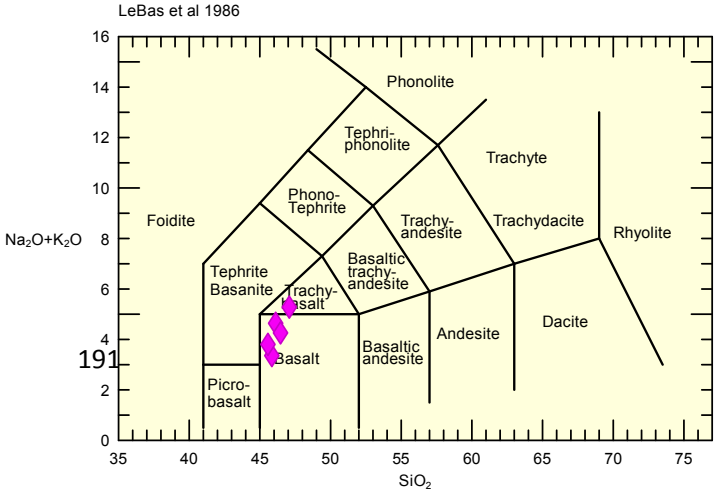

Tertiary

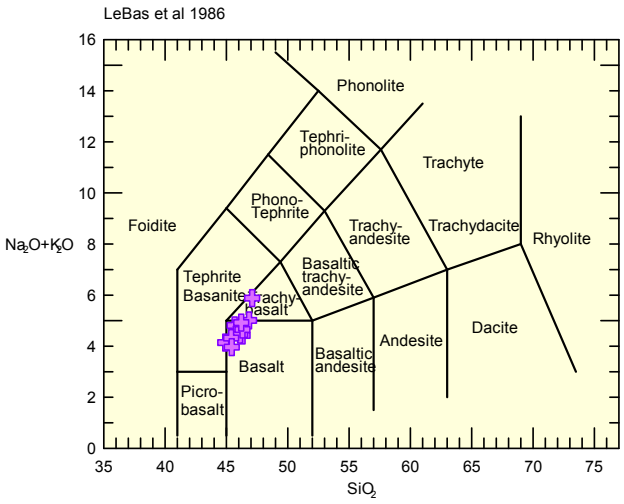

Fig. 3 (SiO_2) against the total alkalis (Na_2O + K_2O) for QM2,QM4&Tertiary

Several plots were made to understanding the relationship between silica and other major oxidizes for different layers. The relation between K_2o V Sio_2 and Na_2o V Sio_2 is linear and increases directly proportional, and the other relations between Mgo and Sio_2 show inversely proportional (figure 4). This indicates that the minerals are formed during magma crystallization.

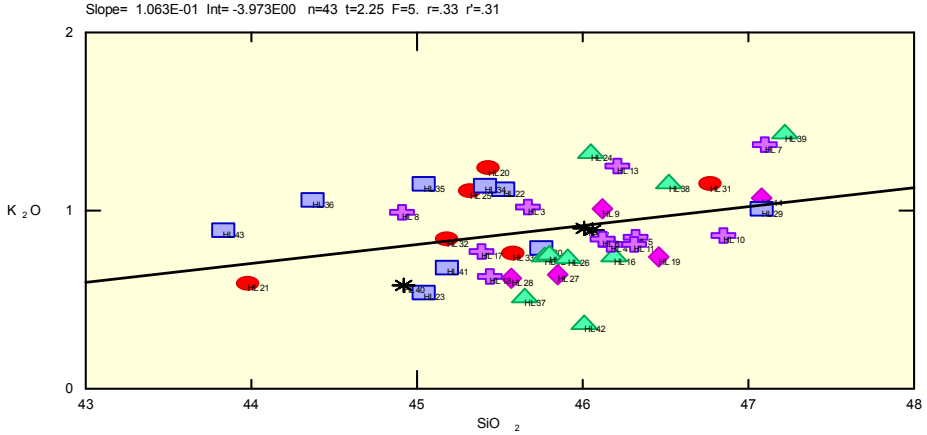

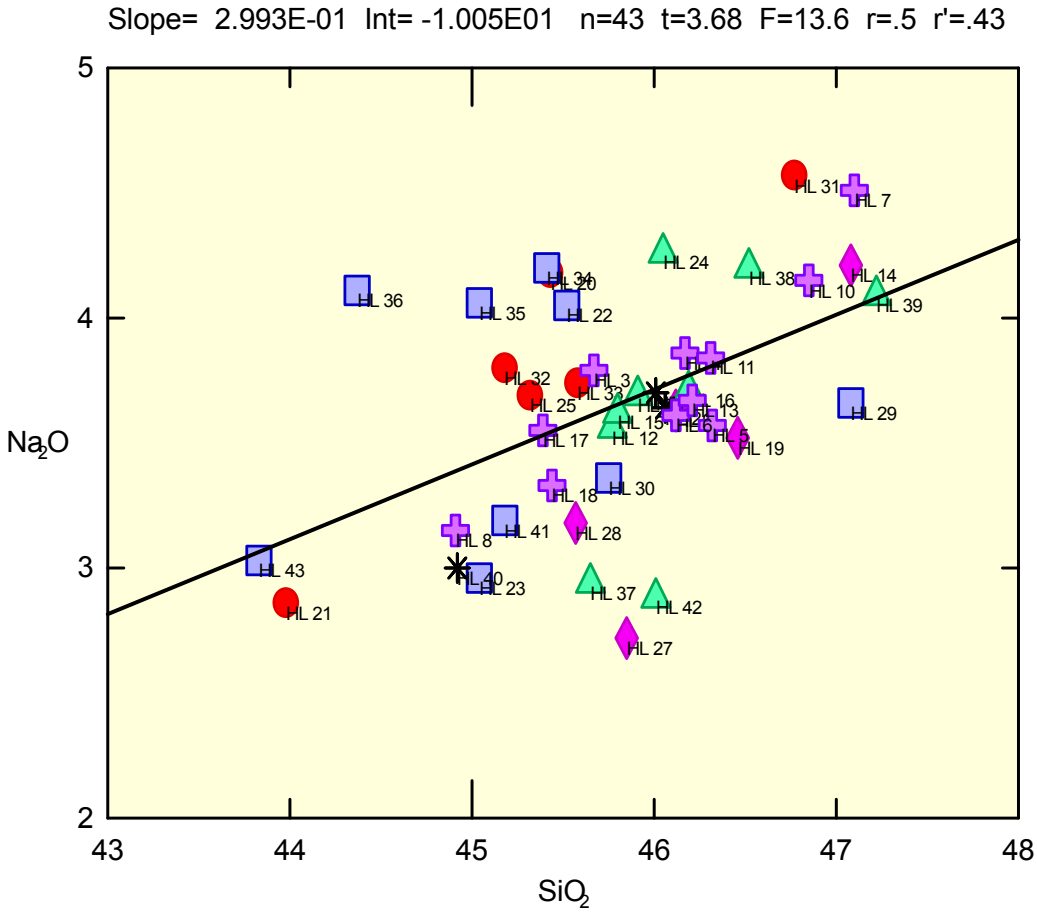

Fig.4 Major Oxides Elements

SAMPLE DESCRIPTIOI	SIO2 %	AL2O3 %	FE2O3 %	CAO %	MGO %	NA2C %	K2O %	CR2C %	TIO2 %	MNO %	P2O5 %	SRO %	BAO %	LOI %	TOTAL %	H2O %	H2O_ %
HL 20	45.43	15.94	15.1	7.63	4.68	4.18	1.24	0.01	3.15	0.23	0.768	0.06	0.04	0.43	98.89	0.17	0.36
HL 21	43.98	15.62	12.34	11.21	7.58	2.86	0.59	0.03	1.97	0.19	0.352	0.06	0.02	1.65	98.45	0.25	0.52
HL 25	45.32	15.75	12.03	9.65	7.02	3.69	1.11	0.04	2.14	0.19	0.591	0.08	0.04	0.95	98.6	0.27	0.65
HL 31	46.77	16.63	15.41	7.05	4.59	4.57	1.15	0.01	3.22	0.22	0.602	0.07	0.02	-0.53	99.79	0.15	<0.01
HL 32	45.18	16.25	15.11	8.51	5.78	3.8	0.84	0.02	2.72	0.22	0.497	0.07	0.02	0.08	99.1	0.15	0.09
HL 33	45.58	16.49	12.98	9.78	7.07	3.74	0.76	0.02	2.25	0.19	0.42	0.07	0.02	0.62	100	0.2	0.11
HL 9	46.12	16.09	11.69	10.26	6.61	3.63	1.01	0.03	2.03	0.2	0.604	0.07	0.04	0.92	99.3	0.16	0.1
HL 14	47.08	16.74	12.72	8.23	6.1	4.21	1.07	0.03	2.29	0.2	0.588	0.07	0.02	-0.5	98.84	0.16	<0.01
HL 19	46.46	16.32	13.39	9.4	7.34	3.52	0.74	0.03	2.45	0.2	0.404	0.06	0.02	-0.78	99.55	0.11	<0.01
HL 27	45.85	15.7	10.96	11.79	7.22	2.72	0.64	0.04	1.76	0.18	0.307	0.06	0.05	1.84	99.12	0.43	1.27
HL 28	45.57	15.98	12.66	10.03	7.93	3.18	0.62	0.04	1.96	0.19	0.405	0.07	0.02	0.52	99.18	0.21	0.24
HL 22	45.52	15.92	15.37	7.77	4.87	4.05	1.12	0.02	3.25	0.23	0.734	0.07	0.03	-0.14	98.8	0.15	0.25
HL 23	45.04	15.94	12.61	10.6	8.13	2.96	0.54	0.03	2	0.19	0.307	0.06	0.02	0.33	98.75	0.15	0.06
HL 29	47.08	16.51	12.21	9.22	6.2	3.66	1.01	0.03	2.15	0.19	0.582	0.07	0.03	0.65	99.59	0.42	0.82
HL 30	45.75	15.91	12.94	9.77	8.09	3.36	0.79	0.04	1.94	0.2	0.453	0.07	0.03	0.69	100.05	0.24	0.34
HL 34	45.41	16.59	15.88	7.79	5.01	4.2	1.14	0.02	3.26	0.23	0.755	0.07	0.03	-0.58	99.81	0.17	0.09
HL 35	45.04	16.15	15.9	8.04	4.9	4.06	1.15	0.02	3.24	0.24	0.773	0.07	0.04	0.33	99.94	0.21	0.38
HL 36	44.37	16.39	13.78	8.97	4.38	4.11	1.06	0.02	2.69	0.22	0.714	0.07	0.03	1.73	98.53	0.47	0.69
HL 41	45.18	15.85	12.7	10.13	7.97	3.19	0.68	0.04	1.97	0.2	0.432	0.07	0.02	0.69	99.11	0.23	0.27
HL 43	43.83	15.47	9.8	12.84	6.18	3.03	0.89	0.03	1.65	0.16	0.433	0.07	0.03	5.34	99.75	0.68	1.92
HL 12	45.77	16.34	13.95	9.33	6.67	3.56	0.74	0.02	2.47	0.21	0.434	0.07	0.02	-0.18	99.4	0.15	0.12
HL 15	45.8	16.74	13.79	9.19	6.15	3.62	0.75	0.03	2.56	0.2	0.468	0.07	0.02	-0.11	99.28	0.22	0.04
HL 16	46.19	16.57	14.33	8.7	6.83	3.71	0.74	0.02	2.52	0.21	0.432	0.06	0.02	-0.87	99.46	0.11	<0.01
HL 24	46.05	15.95	15.62	7.26	4.48	4.26	1.32	0.02	3.18	0.25	0.865	0.06	0.04	-0.14	99.21	0.17	0.35
HL 26	45.91	16.29	14.34	9	6.89	3.69	0.73	0.02	2.53	0.21	0.409	0.06	0.02	-0.75	99.35	0.12	<0.01
HL 37	45.65	16.12	12.46	10.36	8.66	2.94	0.51	0.03	1.86	0.19	0.275	0.06	0.01	0.21	99.34	0.33	0.14
HL 38	46.52	16.5	14.47	7.93	4.42	4.2	1.15	0.01	3.05	0.21	0.782	0.07	0.03	-0.13	99.22	0.25	0.3
HL 39	47.22	15.59	15.61	7.3	4.32	4.09	1.43	0.01	3.2	0.24	0.792	0.06	0.04	-0.62	99.28	0.15	<0.01
HL 42	46.01	16.97	11.62	10.71	8.21	2.88	0.36	0.02	1.63	0.18	0.22	0.06	0.01	0.45	99.33	0.24	0.29
HL 1	46.01	16.48	13.89	8.68	6.53	3.7	0.9	0.02	2.71	0.21	0.488	0.06	0.02	-0.68	99.02	0.06	0.03
HL 2	46.06	16.19	14.1	8.6	6.96	3.64	0.89	0.02	2.72	0.21	0.487	0.06	0.02	-0.82	99.14	0.13	<0.01
HL 40	44.92	15.8	13.02	10.7	7.98	3	0.58	0.03	2.01	0.2	0.333	0.06	0.02	0.75	99.39	0.24	0.18
HL 3	45.67	15.75	11.7	9.82	7.33	3.79	1.02	0.04	2.11	0.18	0.496	0.07	0.03	0.92	98.93	0.42	0.46
HL 4	46.17	16.01	12.62	9.18	7.45	3.86	0.81	0.04	2.26	0.19	0.422	0.07	0.03	0.07	99.17	0.22	0.08
HL 5	46.32	16.44	11.79	9.25	6.78	3.57	0.85	0.03	2.19	0.17	0.423	0.09	0.02	1.1	99.02	0.58	1.64
HL 6	46.12	16.35	12.18	9.01	6.47	3.61	0.84	0.03	2.21	0.18	0.404	0.08	0.02	1.74	99.24	0.78	1.65
HL 7	47.1	16.61	13.43	7.74	4.6	4.51	1.37	0.03	2.26	0.23	0.834	0.08	0.05	0.28	99.11	0.22	0.25
HL 8	44.91	15.37	11.85	10.37	7.97	3.15	0.99	0.03	2.21	0.19	0.525	0.07	0.05	1.55	99.24	0.41	0.89
HL 10	46.85	16.74	12.49	8.94	6.66	4.15	0.86	0.03	2.31	0.18	0.451	0.07	0.02	-0.52	99.23	0.19	<0.01
HL 11	46.31	16.65	13.11	9	6.68	3.84	0.81	0.04	2.35	0.21	0.455	0.07	0.02	-0.06	99.48	0.18	0.2
HL 13	46.21	16.62	11.32	8.85	5.78	3.67	1.25	0.02	2.27	0.17	0.658	0.09	0.04	1.97	98.91	0.95	2.34
HL 17	45.39	16.21	13.99	9.13	6.27	3.55	0.77	0.02	2.61	0.21	0.489	0.06	0.02	0.26	98.98	0.17	0.25
HL 18	45.44	16.51	12.63	9.87	7.04	3.33	0.63	0.02	2.11	0.19	0.389	0.06	0.02	0.22	98.46	0.42	0.38

APPENDIX : D

EARTHQUAKE DATA & PARAMETERS

Earthquake Parameters for magnitudes ≥ 3.0 located in Harrat Lunayyir in May and June of 2009

Day	Month	Year	Hour	Min.	Sec.	Lat.	Long.	Depth	Mag.
5	5	2009	9	28	21	25.09000	37.72980	4.18	3.00
11	5	2009	7	38	26	25.12050	37.72530	4.25	3.00
12	5	2009	4	8	32	25.13000	37.72800	4.08	3.00
14	5	2009	3	12	30	25.21500	37.77070	7.80	3.00
14	5	2009	6	41	13	25.22070	37.77180	9.04	3.00
15	5	2009	18	13	11	25.22420	37.76720	9.19	3.00
17	5	2009	0	18	39	25.20020	37.77870	8.42	3.00
18	5	2009	7	11	57	25.23720	37.76670	9.28	3.00
18	5	2009	23	14	36	25.24470	37.77670	8.52	3.00
12	6	2009	7	48	55	25.24200	37.78000	9.63	3.00
2	5	2009	0	39	58	25.10300	37.73550	7.61	3.01
2	5	2009	3	46	50	25.12620	37.74230	6.66	3.01
2	5	2009	23	41	25	25.10000	37.74600	4.52	3.01
9	5	2009	16	58	53	25.12120	37.73280	5.93	3.01
10	5	2009	16	34	52	25.11830	37.73450	4.90	3.01
15	5	2009	13	55	29	25.21080	37.77230	8.80	3.01
19	5	2009	0	5	59	25.27180	37.75800	7.16	3.01
19	5	2009	0	7	46	25.25380	37.77070	8.00	3.01
25	5	2009	18	49	33	25.17330	37.78020	7.37	3.01
3	6	2009	7	18	27	25.29430	37.71320	10.11	3.01
10	6	2009	18	19	59	25.21400	37.79430	5.56	3.01
27	6	2009	9	26	1	25.19170	37.79000	18.70	3.01
1	5	2009	22	42	38	25.09770	37.74520	6.98	3.02
8	5	2009	23	12	47	25.09080	37.74520	6.73	3.02
9	5	2009	22	52	43	25.11450	37.72930	5.36	3.02
10	5	2009	6	9	32	25.10770	37.72870	6.29	3.02
10	5	2009	7	38	22	25.11550	37.73170	5.89	3.02
10	5	2009	17	28	4	25.10620	37.73580	5.56	3.02
13	5	2009	19	52	12	25.21650	37.77070	11.15	3.02

17	5	2009	8	31	34	25.27330	37.75680	7.60	3.02
19	5	2009	6	55	43	25.25980	37.73970	7.14	3.02
19	5	2009	11	26	24	25.24930	37.77750	8.79	3.02
20	6	2009	20	53	49	25.30520	37.77770	8.72	3.02
5	5	2009	10	23	14	25.09630	37.72850	4.62	3.03
5	5	2009	10	23	14	25.09630	37.72850	4.62	3.03
9	5	2009	0	48	11	25.08430	37.73350	4.09	3.03
10	5	2009	12	53	33	25.10230	37.73120	2.99	3.03
10	5	2009	16	42	5	25.09980	37.72880	3.81	3.03
14	5	2009	10	57	56	25.22020	37.77150	9.24	3.03
17	5	2009	8	21	44	25.19750	37.77020	8.08	3.03
20	5	2009	7	13	1	25.26970	37.77480	6.29	3.03
14	6	2009	12	21	43	25.27870	37.77900	9.26	3.03
16	9	2009	10	7	20	25.24700	37.80370	7.44	3.03
8	5	2009	18	11	24	25.10950	37.74320	3.58	3.04
11	5	2009	3	30	38	25.10620	37.72330	3.88	3.04
11	5	2009	11	10	52	25.12120	37.73020	3.33	3.04
12	5	2009	0	28	27	25.11050	37.72920	5.55	3.04
15	5	2009	7	38	47	25.21980	37.76080	10.26	3.04
15	5	2009	13	40	50	25.22770	37.76800	9.37	3.04
15	5	2009	16	23	42	25.19850	37.76700	9.80	3.04
15	5	2009	16	50	39	25.19920	37.76620	9.49	3.04
16	5	2009	8	7	22	25.20150	37.77580	10.71	3.04
18	5	2009	9	37	44	25.23120	37.76830	10.53	3.04
18	5	2009	16	43	18	25.25680	37.77230	7.64	3.04
25	5	2009	8	55	19	25.23330	37.78420	8.84	3.04
6	5	2009	13	0	55	25.08650	37.73500	4.87	3.05
6	5	2009	23	14	28	25.09580	37.73730	6.17	3.05
11	5	2009	4	55	15	25.12000	37.72350	4.80	3.05
16	5	2009	13	30	58	25.21300	37.77580	10.13	3.05
18	5	2009	2	31	37	25.24400	37.76900	8.59	3.05
18	5	2009	13	42	0	25.25200	37.77420	7.98	3.05
19	5	2009	13	47	54	25.25750	37.77280	8.31	3.05
19	5	2009	14	23	54	25.26080	37.77450	7.62	3.05

21	5	2009	1	9	44	25.26570	37.76280	8.74	3.05
26	6	2009	6	58	23	25.18500	37.79130	5.66	3.05
6	5	2009	21	27	0	25.08570	37.73300	3.80	3.06
10	5	2009	16	9	58	25.05860	37.74130	8.36	3.06
12	5	2009	18	30	12	25.11070	37.72670	4.81	3.06
18	5	2009	20	1	19	25.25830	37.77220	6.61	3.06
24	5	2009	17	45	7	25.14970	38.00620	10.87	3.06
23	6	2009	10	47	18	25.21800	37.79800	6.06	3.06
9	5	2009	17	44	52	25.14350	37.75680	6.89	3.07
10	5	2009	17	31	42	25.10200	37.73400	5.69	3.07
15	5	2009	18	25	31	25.22430	37.76930	8.77	3.07
15	5	2009	19	32	36	25.22270	37.77200	8.68	3.07
18	5	2009	17	34	20	25.26320	37.78280	7.29	3.07
18	5	2009	20	3	28	25.26100	37.77450	7.58	3.07
19	5	2009	3	42	13	25.25950	37.77430	6.58	3.07
1	5	2009	0	28	1	25.06980	37.70520	9.27	3.08
8	5	2009	17	8	42	25.10150	37.74380	8.60	3.08
11	5	2009	5	6	15	25.12800	37.72730	5.12	3.08
14	5	2009	7	56	37	25.21380	37.77400	8.58	3.08
16	5	2009	12	58	32	25.21280	37.77480	9.33	3.08
17	5	2009	5	18	33	25.20650	37.78400	7.69	3.08
18	5	2009	3	37	43	25.26620	37.76380	6.29	3.08
18	5	2009	14	56	37	25.25320	37.77150	7.80	3.08
19	5	2009	10	9	48	25.25330	37.77070	8.82	3.08
24	5	2009	0	3	47	25.16130	37.78920	6.80	3.08
14	6	2009	3	10	45	25.25570	37.79030	7.90	3.08
1	5	2009	2	21	13	25.07250	37.70880	7.42	3.09
2	5	2009	16	25	13	25.07580	37.74770	4.04	3.09
11	5	2009	17	12	15	25.11800	37.72750	5.37	3.09
13	5	2009	10	22	50	25.20930	37.76220	8.72	3.09
13	5	2009	17	39	30	25.20620	37.76232	8.23	3.09
14	5	2009	2	31	3	25.20330	37.77450	7.72	3.09
17	5	2009	1	43	49	25.20880	37.77650	9.63	3.09
19	5	2009	7	48	42	25.21700	37.79200	8.34	3.09

29	5	2009	9	56	15	25.31170	37.75080	7.90	3.09
6	6	2009	4	1	4	25.25170	37.78080	9.16	3.09
14	6	2009	1	2	37	25.25380	37.78170	9.35	3.09
2	5	2009	11	17	16	25.10370	37.74620	5.88	3.10
2	5	2009	14	45	2	25.08950	37.75370	6.57	3.10
11	5	2009	13	48	28	25.11500	37.73430	4.53	3.10
12	5	2009	19	45	35	25.11550	37.72920	4.75	3.10
15	5	2009	5	42	2	25.22258	37.74830	7.39	3.10
17	5	2009	12	59	40	25.20920	37.77670	9.30	3.10
18	5	2009	17	6	49	25.25270	37.77500	8.21	3.10
19	5	2009	3	28	36	25.28220	37.78100	7.54	3.10
19	5	2009	5	24	38	25.25370	37.77350	7.82	3.10
9	5	2009	14	32	50	25.11330	37.74070	4.53	3.11
9	5	2009	15	48	15	25.11970	37.72950	6.01	3.11
14	5	2009	20	3	27	25.21070	37.77320	9.49	3.11
17	5	2009	17	18	52	25.24330	37.75900	9.51	3.11
20	5	2009	18	25	18	25.30820	37.73250	7.75	3.11
22	5	2009	0	10	18	25.28680	37.76200	6.00	3.11
13	6	2009	16	41	5	25.25170	37.77930	10.79	3.11
2	5	2009	16	52	31	25.08320	37.75450	5.68	3.12
9	5	2009	19	10	54	25.10230	37.72000	3.33	3.12
12	5	2009	0	21	49	25.11250	37.72330	5.29	3.12
13	5	2009	1	48	35	25.13950	37.72270	5.05	3.12
13	5	2009	23	30	46	25.21400	37.77620	8.72	3.12
14	5	2009	5	33	45	25.22320	37.77100	9.41	3.12
15	5	2009	3	58	44	25.21870	37.76750	7.99	3.12
15	5	2009	17	32	52	25.21950	37.77070	11.38	3.12
17	5	2009	9	52	52	25.22470	37.77050	8.37	3.12
18	5	2009	19	16	15	25.25420	37.77430	8.34	3.12
19	5	2009	11	9	7	25.24880	37.76780	8.23	3.12
19	5	2009	14	53	53	25.25480	37.76780	8.46	3.12
2	5	2009	12	47	1	25.11720	37.76870	5.13	3.13
9	5	2009	14	39	16	25.10420	37.73100	4.96	3.13
12	5	2009	2	10	11	25.10920	37.72350	4.11	3.13

14	5	2009	11	45	55	25.23000	37.77570	9.76	3.13
14	5	2009	19	38	49	25.15380	37.79880	24.42	3.13
16	5	2009	5	15	25	25.19550	37.77650	9.18	3.13
18	5	2009	3	8	10	25.25330	37.76070	6.75	3.13
18	5	2009	6	32	53	25.25000	37.77120	9.19	3.13
18	5	2009	10	21	25	25.22570	37.77000	11.03	3.13
19	5	2009	2	26	41	25.27820	37.78200	6.71	3.13
19	5	2009	11	1	1	25.25880	37.77570	6.77	3.13
30	4	2009	23	2	56	25.38900	38.18080	11.05	3.14
2	5	2009	9	42	11	25.12350	37.75980	3.61	3.14
13	5	2009	2	18	16	25.19450	37.75680	8.80	3.14
14	5	2009	14	45	6	25.21030	37.77630	11.58	3.14
14	5	2009	21	43	33	25.21980	37.77170	9.97	3.14
15	5	2009	11	18	53	25.21950	37.75250	7.55	3.14
15	5	2009	19	29	30	25.22450	37.76980	8.66	3.14
16	5	2009	8	16	13	25.20580	37.77500	10.47	3.14
16	5	2009	10	59	23	25.20900	37.77500	9.17	3.14
19	5	2009	8	14	35	25.29000	37.77680	7.07	3.14
19	5	2009	16	10	9	25.26200	37.77400	7.64	3.14
14	6	2009	1	9	21	25.27570	37.78150	6.21	3.14
12	5	2009	11	27	48	25.11180	37.72950	3.94	3.15
13	5	2009	0	57	1	25.09000	37.66500	9.08	3.15
15	5	2009	12	35	22	25.21980	37.77020	10.75	3.15
15	5	2009	15	52	57	25.22280	37.76650	8.89	3.15
16	5	2009	1	29	52	25.19980	37.76880	8.15	3.15
16	5	2009	17	14	44	25.22620	37.76080	7.70	3.15
19	5	2009	15	29	14	25.25020	37.78020	8.00	3.15
20	5	2009	7	28	58	25.25480	37.78080	7.83	3.15
1	5	2009	0	40	58	25.07220	37.70980	8.46	3.16
1	5	2009	2	35	10	25.06630	37.70080	9.86	3.16
5	5	2009	11	58	16	25.10770	37.74120	7.16	3.16
14	5	2009	15	37	27	25.22500	37.75120	7.54	3.16
15	5	2009	8	14	0	25.22500	37.77220	9.47	3.16
17	5	2009	6	39	21	25.20520	37.77150	7.19	3.16

18	5	2009	4	48	52	25.23800	37.76370	8.92	3.16
18	5	2009	15	13	54	25.27800	37.75070	7.05	3.16
19	5	2009	0	43	56	25.26170	37.77170	7.14	3.16
19	5	2009	15	38	53	25.25900	37.77420	7.22	3.16
20	5	2009	2	31	14	25.27150	37.76950	8.21	3.16
20	5	2009	13	56	41	25.16720	37.79570	23.62	3.16
13	5	2009	14	25	42	25.21320	37.76570	9.46	3.18
18	5	2009	22	15	14	25.26770	37.76200	7.56	3.18
19	5	2009	0	25	54	25.25250	37.77380	8.09	3.18
19	5	2009	8	0	58	25.22100	37.78820	8.23	3.18
24	5	2009	15	39	48	25.27600	37.76600	7.63	3.18
11	5	2009	6	22	22	25.10480	37.72520	4.19	3.19
16	5	2009	22	50	19	25.21250	37.77920	10.03	3.19
18	5	2009	5	49	1	25.24250	37.76170	8.23	3.19
18	5	2009	9	16	42	25.22430	37.82980	9.03	3.19
2	5	2009	7	8	9	25.09220	37.73900	6.58	3.20
13	5	2009	18	6	27	25.22250	37.78150	9.83	3.20
13	5	2009	21	32	57	25.21550	37.77707	8.84	3.20
15	5	2009	13	8	59	25.22620	37.75960	8.16	3.20
15	5	2009	20	8	0	25.22580	37.77280	7.91	3.20
16	5	2009	19	35	3	25.27720	37.77200	8.53	3.20
17	5	2009	23	47	16	25.24500	37.76880	9.04	3.20
17	5	2009	23	56	34	25.23080	37.76180	8.45	3.20
18	5	2009	5	44	39	25.24050	37.77350	7.21	3.20
19	5	2009	3	5	21	25.23400	37.78330	8.33	3.20
14	5	2009	23	49	40	25.22100	37.77120	9.43	3.21
15	5	2009	17	8	3	25.21220	37.77130	9.36	3.21
18	5	2009	13	7	21	25.26700	37.74930	7.71	3.21
19	5	2009	14	28	26	25.25370	37.77600	8.42	3.21
21	6	2009	4	14	41	25.21450	37.78820	5.07	3.21
12	5	2009	6	25	40	25.11670	37.72870	4.62	3.22
13	5	2009	21	18	29	25.18530	37.76850	10.13	3.22
13	5	2009	23	36	56	25.21570	37.77480	8.42	3.22
14	5	2009	14	48	26	25.22050	37.75850	8.07	3.22

16	5	2009	22	19	51	25.20270	37.77870	8.62	3.22
17	5	2009	2	58	31	25.21130	37.77200	7.58	3.22
18	5	2009	6	41	20	25.23620	37.76920	8.25	3.22
19	5	2009	8	18	54	25.25380	37.77470	8.20	3.22
29	4	2009	9	47	39	25.04420	37.71270	8.87	3.23
5	5	2009	13	41	36	25.09520	37.74820	4.19	3.23
8	5	2009	22	3	6	25.09520	37.74100	7.85	3.23
14	5	2009	16	34	23	25.22650	37.75830	9.26	3.23
17	5	2009	13	18	28	25.20700	37.77930	8.10	3.23
18	5	2009	11	23	24	25.24080	37.75650	9.38	3.23
18	5	2009	18	28	20	25.28170	37.76220	6.57	3.23
20	5	2009	0	18	11	25.26850	37.77450	8.14	3.23
20	5	2009	3	53	25	25.25000	37.75420	9.94	3.23
23	6	2009	6	29	23	25.23000	37.78000	10.80	3.23
24	6	2009	16	44	40	25.21750	37.78970	7.83	3.23
11	5	2009	19	26	15	25.11220	37.72280	5.51	3.24
14	5	2009	21	19	12	25.22030	37.77130	9.23	3.24
17	5	2009	11	43	15	25.21870	37.76600	8.57	3.24
18	5	2009	21	54	24	25.25970	37.77550	7.76	3.24
12	5	2009	10	5	53	25.11000	37.72770	4.58	3.25
13	5	2009	1	5	21	25.11830	37.72500	4.03	3.25
15	5	2009	9	31	58	25.24400	37.80180	9.65	3.25
16	5	2009	21	49	12	25.19650	37.78080	9.22	3.25
17	5	2009	11	54	16	25.21620	37.75180	8.07	3.25
19	5	2009	0	55	50	25.24800	37.77480	6.99	3.25
1	5	2009	23	8	14	25.06570	37.68130	13.10	3.26
11	5	2009	4	48	51	25.11270	37.72080	4.80	3.26
12	5	2009	3	45	10	25.11320	37.73150	3.36	3.26
17	5	2009	4	59	56	25.20630	37.78370	7.32	3.26
17	5	2009	13	21	5	25.20170	37.77920	8.71	3.26
15	5	2009	2	52	53	25.22120	37.77200	9.48	3.27
15	5	2009	15	14	29	25.22820	37.76930	9.23	3.27
15	5	2009	15	16	9	25.22220	37.76850	10.36	3.27
16	5	2009	18	12	56	25.20600	37.77670	8.24	3.27

17	5	2009	10	9	45	25.19550	37.77080	8.21	3.27
20	5	2009	0	5	52	25.27230	37.77420	7.15	3.27
15	6	2009	2	34	46	25.27080	37.78100	6.96	3.27
9	5	2009	22	26	39	25.10230	37.72730	4.84	3.28
15	5	2009	13	25	1	25.22700	37.77020	7.67	3.28
19	5	2009	13	27	12	25.26330	37.77520	8.25	3.28
20	5	2009	3	15	32	25.26100	37.76750	9.17	3.28
13	5	2009	20	11	59	25.21550	37.76850	10.00	3.29
15	5	2009	21	29	56	25.22630	37.77600	7.20	3.29
16	5	2009	7	55	53	25.26520	37.75780	8.01	3.29
18	5	2009	20	42	12	25.28700	37.79120	7.40	3.29
12	5	2009	21	56	10	25.12170	37.71880	2.22	3.30
15	5	2009	11	39	11	25.22500	37.75430	7.30	3.30
18	5	2009	6	57	59	25.22400	37.75680	9.30	3.30
18	5	2009	20	57	42	25.28370	37.78300	7.72	3.30
20	5	2009	15	58	4	25.25850	37.76830	8.97	3.30
26	5	2009	1	34	31	25.22900	37.78970	8.22	3.30
1	5	2009	15	47	4	25.09670	37.73470	10.38	3.31
15	5	2009	20	35	52	25.22670	37.77520	8.65	3.31
18	5	2009	5	14	50	25.22250	37.76170	8.56	3.31
18	5	2009	9	22	48	25.23270	37.76830	11.15	3.31
5	6	2009	21	54	22	25.23620	37.78020	9.47	3.31
14	5	2009	0	50	34	25.21070	37.77500	8.30	3.32
2	5	2009	13	49	32	25.10930	37.76130	7.00	3.33
13	5	2009	0	42	20	25.13100	37.72900	4.99	3.33
15	5	2009	19	44	35	25.22730	37.77270	8.02	3.33
17	5	2009	2	8	13	25.21160	37.77750	9.92	3.33
18	5	2009	8	11	5	25.23780	37.76150	10.15	3.33
18	5	2009	10	11	51	25.22030	37.75620	9.68	3.33
18	5	2009	19	0	29	25.30400	37.78450	7.42	3.33
12	5	2009	14	3	13	25.10770	37.72330	3.15	3.34
18	5	2009	15	49	45	25.27270	37.75980	7.38	3.34
19	5	2009	1	7	36	25.28400	37.75520	7.35	3.34
19	5	2009	15	50	45	25.56870	37.76930	7.26	3.34

12	5	2009	21	36	16	25.12670	37.72120	3.93	3.36
15	5	2009	4	0	37	25.21870	37.76680	8.21	3.36
16	5	2009	1	45	10	25.22330	37.76970	8.32	3.36
18	5	2009	15	12	34	25.27830	37.75150	7.47	3.36
13	5	2009	14	8	18	25.22320	37.77300	8.99	3.37
14	5	2009	19	17	7	25.20350	37.77100	9.91	3.37
14	5	2009	15	21	0	25.21320	37.77300	10.39	3.38
20	5	2009	23	20	44	25.26770	37.77880	7.93	3.38
4	6	2009	0	9	57	25.33280	37.66280	9.39	3.38
25	6	2009	10	40	30	25.25280	37.79030	9.62	3.38
18	5	2009	4	16	8	25.27250	37.75480	6.39	3.39
18	5	2009	14	55	7	25.25450	37.77200	7.87	3.39
19	5	2009	16	17	6	25.27050	37.77150	8.03	3.39
5	6	2009	22	10	9	25.24180	37.78900	9.29	3.39
13	6	2009	6	40	1	25.23270	37.78070	6.67	3.39
10	5	2009	17	30	8	25.11970	37.74920	8.02	3.40
5	6	2009	4	22	5	25.32230	37.68730	7.24	3.40
1	5	2009	17	46	54	25.07200	37.68870	14.84	3.41
14	5	2009	4	56	17	25.21980	37.76970	7.21	3.41
12	5	2009	3	35	12	25.12370	37.74350	6.61	3.42
13	5	2009	20	15	35	25.21200	37.77470	8.61	3.42
14	5	2009	0	47	5	25.21030	37.77500	8.21	3.42
14	5	2009	8	30	30	25.22380	37.77130	8.89	3.42
15	5	2009	15	31	21	25.22730	37.76820	9.71	3.42
19	5	2009	23	43	32	25.28650	37.76070	7.43	3.42
18	5	2009	6	19	9	25.25220	37.73170	10.10	3.43
18	5	2009	13	39	17	25.24500	37.77880	5.65	3.43
18	5	2009	16	18	53	25.24930	37.76970	8.55	3.43
19	5	2009	10	6	30	25.26250	37.77430	7.35	3.43
15	5	2009	4	45	29	25.22730	37.76630	7.00	3.44
17	5	2009	19	3	53	25.25220	37.77600	9.10	3.44
19	5	2009	6	41	17	25.26650	37.76850	6.87	3.44
16	5	2009	18	4	7	25.20430	37.77100	7.45	3.45
19	5	2009	16	38	28	25.26930	37.76830	7.61	3.45

29	4	2009	16	35	58	25.05480	37.72400	9.01	3.46
9	5	2009	18	46	21	25.10500	37.73230	5.96	3.46
10	5	2009	18	59	59	25.11450	37.72700	3.94	3.46
16	5	2009	11	18	38	25.22500	37.75850	10.01	3.46
13	5	2009	21	12	45	25.19500	37.76630	10.58	3.47
11	6	2009	5	31	42	25.22930	37.77770	11.43	3.47
12	5	2009	23	25	17	25.13050	37.72270	4.88	3.48
19	5	2009	1	51	29	25.27920	37.79170	7.94	3.48
21	5	2009	21	15	34	25.27880	37.76350	7.29	3.48
13	5	2009	21	20	20	25.19870	37.76850	9.83	3.49
17	5	2009	3	27	47	25.23200	37.78680	7.77	3.49
20	5	2009	17	11	35	25.27650	37.76100	8.66	3.49
30	5	2009	8	31	57	25.26280	37.77730	6.50	3.49
14	5	2009	4	9	54	25.21880	37.77070	9.32	3.50
14	5	2009	8	1	45	25.22250	37.77380	8.33	3.50
18	5	2009	23	43	35	25.27900	37.75250	7.33	3.51
18	5	2009	23	43	35	25.27900	37.75250	7.33	3.51
20	5	2009	5	14	9	25.26680	37.77330	9.04	3.51
8	5	2009	19	22	24	25.08820	37.74030	4.44	3.52
27	6	2009	0	4	28	25.22490	37.77680	6.75	3.52
14	5	2009	12	47	2	25.20550	37.77780	10.19	3.53
17	5	2009	12	30	9	25.22430	37.77220	10.26	3.53
10	5	2009	18	12	49	25.12320	37.74120	5.22	3.54
14	5	2009	23	25	15	25.22120	37.76780	10.58	3.54
15	5	2009	4	3	3	25.21950	37.76650	7.86	3.54
15	5	2009	14	49	44	25.22480	37.76930	9.66	3.54
17	5	2009	6	26	7	25.22100	37.75650	7.86	3.54
20	6	2009	12	59	12	25.27170	37.77080	6.07	3.54
19	5	2009	16	20	43	25.26950	37.76900	7.75	3.55
12	5	2009	3	40	55	25.11670	37.74150	6.46	3.56
18	5	2009	13	37	18	25.24400	37.77860	8.22	3.56
15	5	2009	4	51	56	25.22480	37.77000	10.03	3.57
18	5	2009	7	19	44	25.22730	37.76150	10.42	3.57
14	5	2009	17	16	27	25.22280	37.77020	9.11	3.58

18	5	2009	0	32	29	25.25320	37.75100	7.76	3.58
15	5	2009	10	27	51	25.23700	37.77800	10.92	3.59
12	5	2009	22	2	51	25.12830	37.72720	4.42	3.60
17	5	2009	4	41	57	25.19400	37.77950	6.77	3.61
17	5	2009	12	0	24	25.21680	37.74670	10.55	3.61
21	5	2009	22	3	15	25.26250	37.77620	6.74	3.62
13	5	2009	21	41	10	25.21300	37.77420	9.61	3.63
16	5	2009	23	40	50	25.23050	37.78280	8.48	3.63
19	5	2009	19	44	19	25.28570	37.75530	8.39	3.63
17	5	2009	8	12	14	25.26470	37.75680	8.96	3.64
17	5	2009	16	39	49	25.24730	37.77080	10.18	3.64
10	5	2009	18	12	11	25.11680	37.72730	5.40	3.65
13	5	2009	22	33	57	25.20030	37.76820	9.41	3.65
18	5	2009	7	59	16	25.26820	37.75730	8.39	3.65
4	6	2009	1	6	42	25.32780	37.67620	8.31	3.65
20	6	2009	11	18	54	25.27500	37.77000	8.90	3.65
12	5	2009	3	2	30	25.11020	37.72780	4.96	3.66
17	5	2009	14	39	44	25.25250	37.77620	8.55	3.66
18	5	2009	8	24	25	25.23100	37.76610	10.63	3.66
13	5	2009	19	16	13	25.23170	37.78620	8.43	3.67
18	5	2009	4	40	37	25.25780	37.75280	7.25	3.67
18	5	2009	11	24	13	25.20980	37.76180	10.25	3.67
15	5	2009	20	42	6	25.21750	37.76880	6.69	3.68
30	4	2009	19	42	36	25.06900	37.69470	14.66	3.69
13	5	2009	22	29	17	25.19950	37.76680	8.57	3.69
18	5	2009	7	47	52	25.23600	37.75630	9.44	3.69
8	5	2009	22	5	9	25.09000	37.73800	6.54	3.70
13	5	2009	0	2	20	25.21030	37.77470	7.71	3.70
13	5	2009	23	49	40	25.21350	37.77520	8.89	3.70
17	5	2009	4	23	49	25.23420	37.78820	8.78	3.70
19	5	2009	19	33	21	25.28380	37.76430	8.56	3.70
14	5	2009	4	39	43	25.22070	37.77200	8.60	3.71
18	5	2009	7	29	23	25.23770	37.76600	8.58	3.73
18	5	2009	8	41	17	25.21550	37.76050	10.40	3.73

18	5	2009	0	54	8	25.24020	37.73070	8.34	3.74
13	5	2009	22	14	39	25.14820	37.74650	6.77	3.75
9	5	2009	14	5	27	25.10870	37.73070	5.30	3.82
14	5	2009	14	1	34	25.22170	37.75470	8.51	3.85
14	5	2009	14	32	47	25.24730	37.77950	10.33	3.85
15	5	2009	8	48	26	25.22450	37.76750	10.04	3.87
14	5	2009	1	16	34	25.22070	37.75900	7.42	3.88
19	5	2009	19	50	43	25.26970	37.77450	8.85	3.89
13	5	2009	18	35	45	25.22750	37.78230	8.73	3.91
12	5	2009	22	51	14	25.11880	37.71380	6.83	3.92
17	5	2009	20	1	31	25.23880	37.73400	7.89	3.92
18	5	2009	13	25	32	25.26970	37.75600	8.64	3.93
13	5	2009	23	47	18	25.21020	37.77200	8.78	3.97
24	6	2009	5	39	50	25.23030	37.77830	7.16	3.97
17	5	2009	20	28	27	25.24430	37.75320	9.16	3.99
19	5	2009	19	21	27	25.28850	37.76220	7.20	4.01
19	5	2009	19	26	58	25.27330	37.76530	8.23	4.04
17	5	2009	19	20	27	25.23680	37.76550	7.78	4.15
19	5	2009	17	13	26	25.26850	37.78250	6.37	4.20
13	5	2009	23	8	56	25.21480	37.77550	8.89	4.25
19	5	2009	20	35	37	25.30930	37.73030	9.30	4.25
19	5	2009	18	20	0	25.28200	37.76650	9.62	4.29
18	5	2009	7	41	2	25.24530	37.77380	10.62	4.37
22	6	2009	11	2	42	25.24270	37.79080	9.87	4.47
17	5	2009	20	21	4	25.25050	37.75770	8.13	4.60
17	5	2009	19	50	4	25.25150	37.72400	8.02	4.68
20	5	2009	19	57	16	25.29750	37.75050	8.49	4.79
19	5	2009	6	38	29	25.28180	37.74780	7.76	4.81
19	5	2009	16	54	28	25.27630	37.76770	10.10	4.90
19	5	2009	17	34	58	25.28200	37.75970	7.81	5.39

APPENDIX : E

Measurements of Radon Concentration & Thermal variations in Water Wells as well as In SAR and SRTM maps for Harrat Lunayyir. Data Taken and Analyzed by the Saudi Geological Survey

Radon concentration in water wells in (pCi/L)					
Date	Al Farea area	Al Ayis area	Al Hadma area		Earthquake Frequencies
	Radon concentration in well no. 36	Radon concentration in well no. 73	Radon concentration in well no. HT2	Radon concentration in well no. HT7	
11/5/2009	203	136	311		541
18/5/2009	221	231	440	920	521
22/5/2009	209	55	253	851	249
23/5/2009	200	154	320	1056	193
24/5/2009	202	122	429	1240	216
25/5/2009	275	145	361	1188	169
26/5/2009	170	157	401	1243	153
27/5/2009	178	229	409	1320	198
28/5/2009	129	137	387	1325	181
29/5/2009	160	118	337	1422	156
30/5/2009	244	117	368	1431	139
31/5/2009	163	116	280	1391	187
1/6/2009	85	251	320	1285	181
2/6/2009	265	272	310	1361	187
3/6/2009	234	174	260	1018	199
4/6/2009	231	251	195	1289	189
5/6/2009	239	262	225	1381	245
6/6/2009	147	382	256	1266	182
7/6/2009	282	265	364	1266	
8/6/2009	274	239	339	1287	
9/6/2009	297	219	343	1349	
10/6/2009	247	278	231	1382	
11/6/2009	243	252	460	1280	
12/6/2009	312	227	437	1172	
13/6/2009	233	228	374	1385	
17/6/2009	230	175	300	1229	
18/6/2009	247	249	265	1309	
19/6/2009	259	134	288	1238	
20/6/2009	230	Out of order	487	1196	
21/6/2009	234	103	399	1308	
22/6/2009	159	109	393	1173	
23/6/2009	183	193	497	1340	

24/6/2009	175	179	373	1258	
25/6/2009	245	261	355	1206	
26/6/2009	160	231	384	1166	
27/6/2009	187	210	554	1248	
28/6/2009	221	178	500	1207	
29/6/2009	186	271	337	1208	
30/6/2009	223	239	362	1266	
1/7/2009	211	166	309	1249	
2/7/2009	232	150	472	1064	
3/7/2009	257	202	294	1187	
4/7/2009	169	150	286	1299	
5/7/2009	Out of order	Out of order	221	1250	
6/7/2009	226	117	359	1238	
7/7/2009	Out of order	156	310	1320	
8/7/2009	Out of order	185	278	1197	
9/7/2009	280	262	363	1279	

Locations of High Thermal Wells in 2010

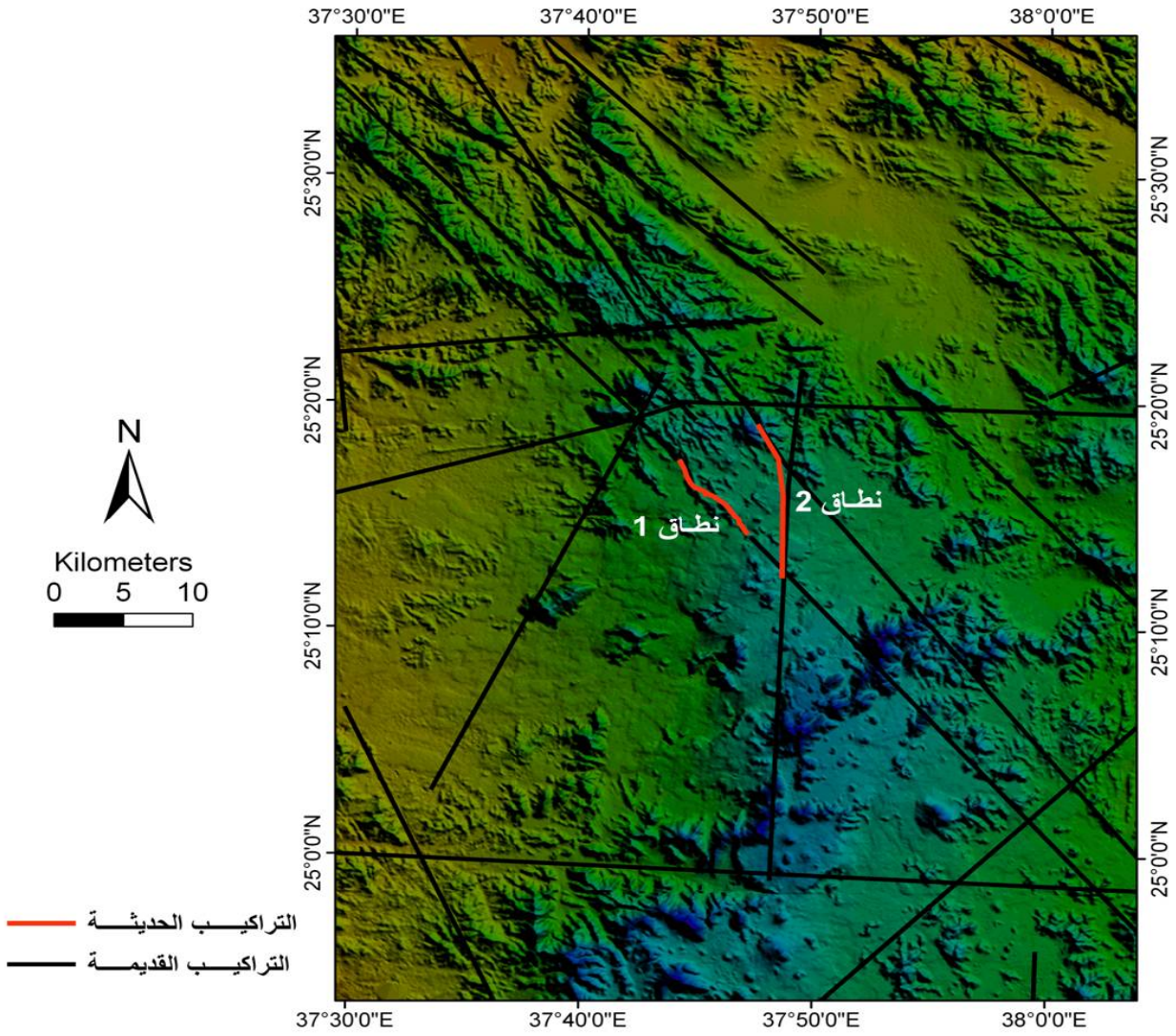

Old and New Structural features from SRTM Images

Half-Graben model from In SAR

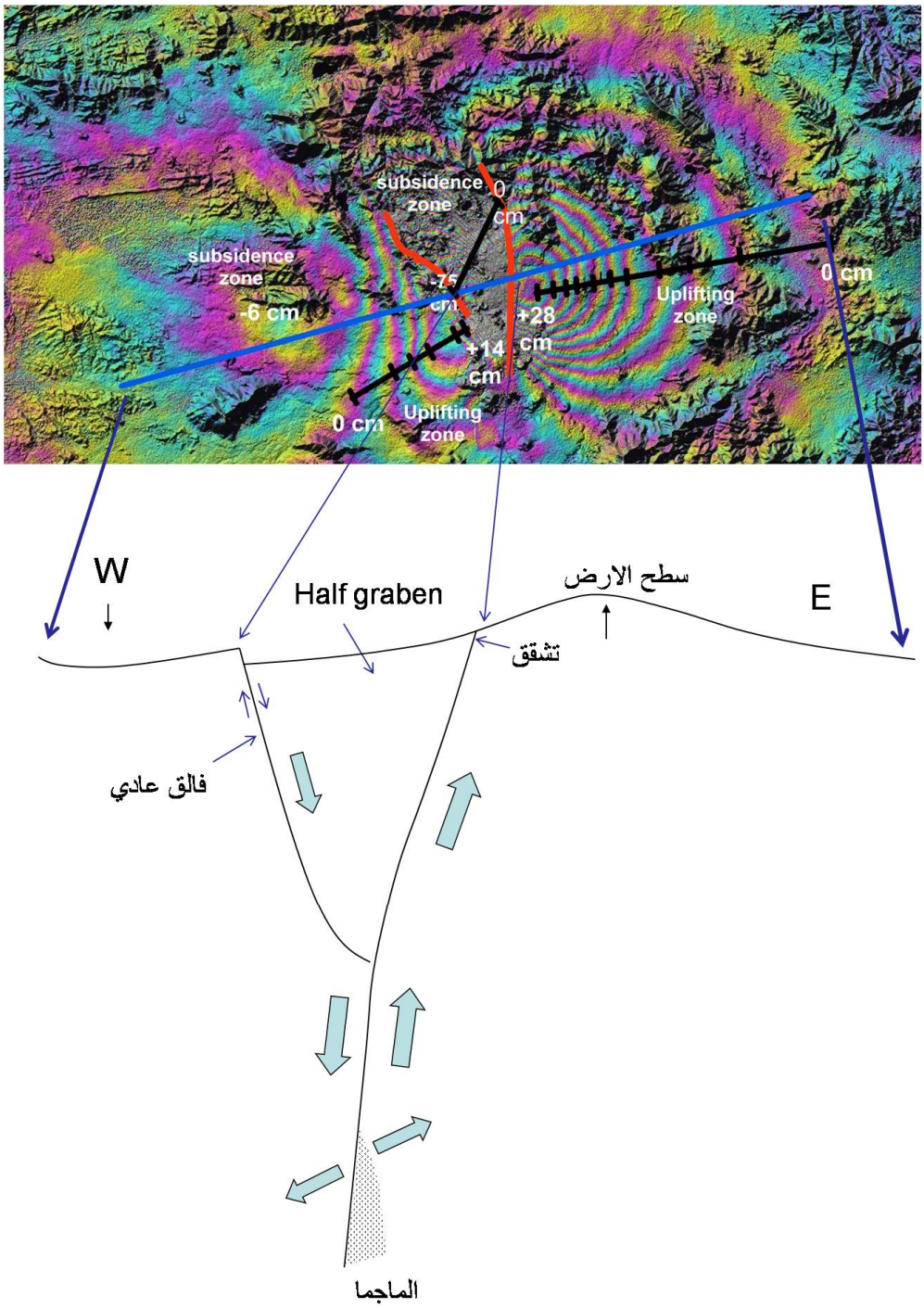

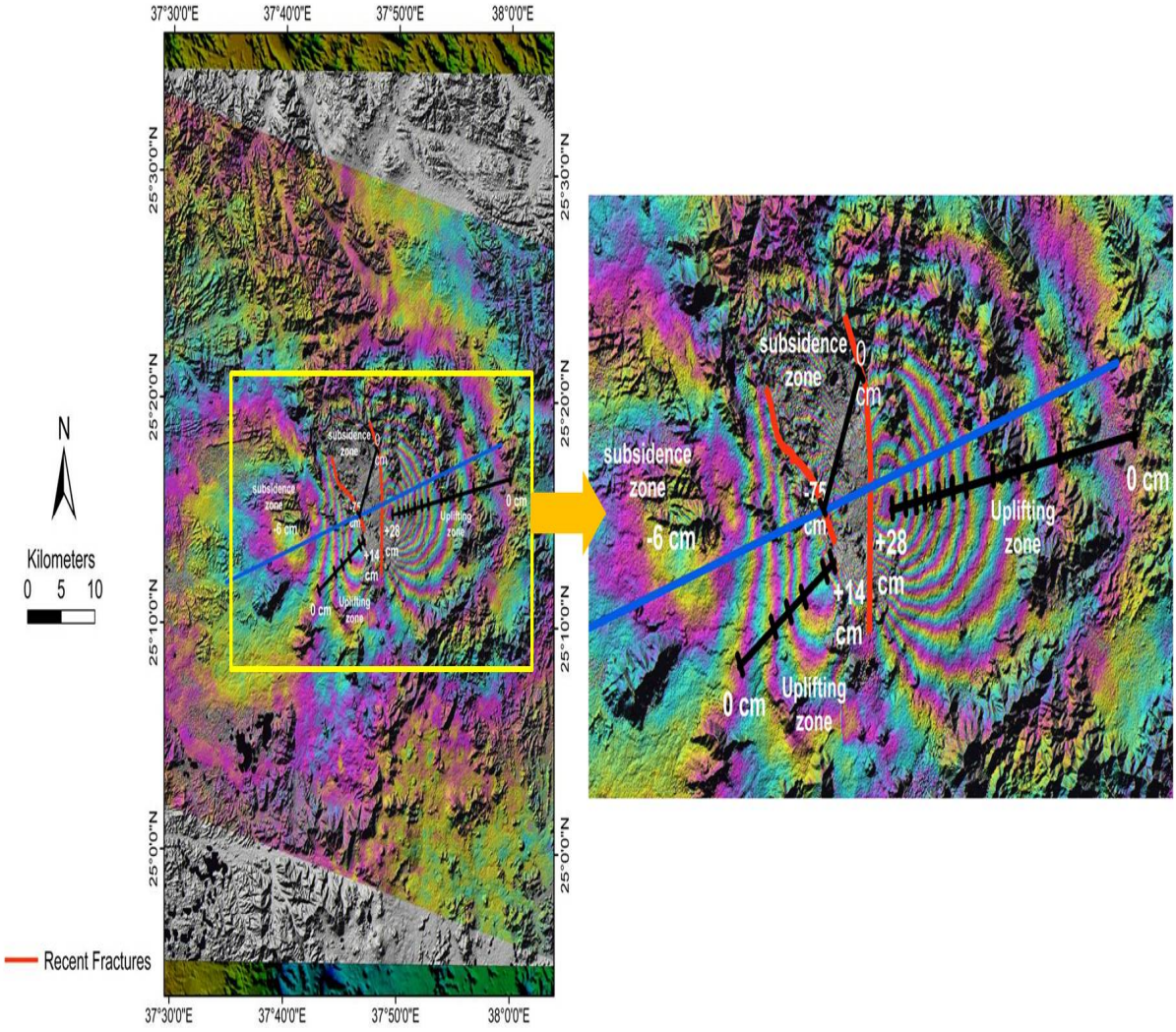

Analysis of In SAR Maps

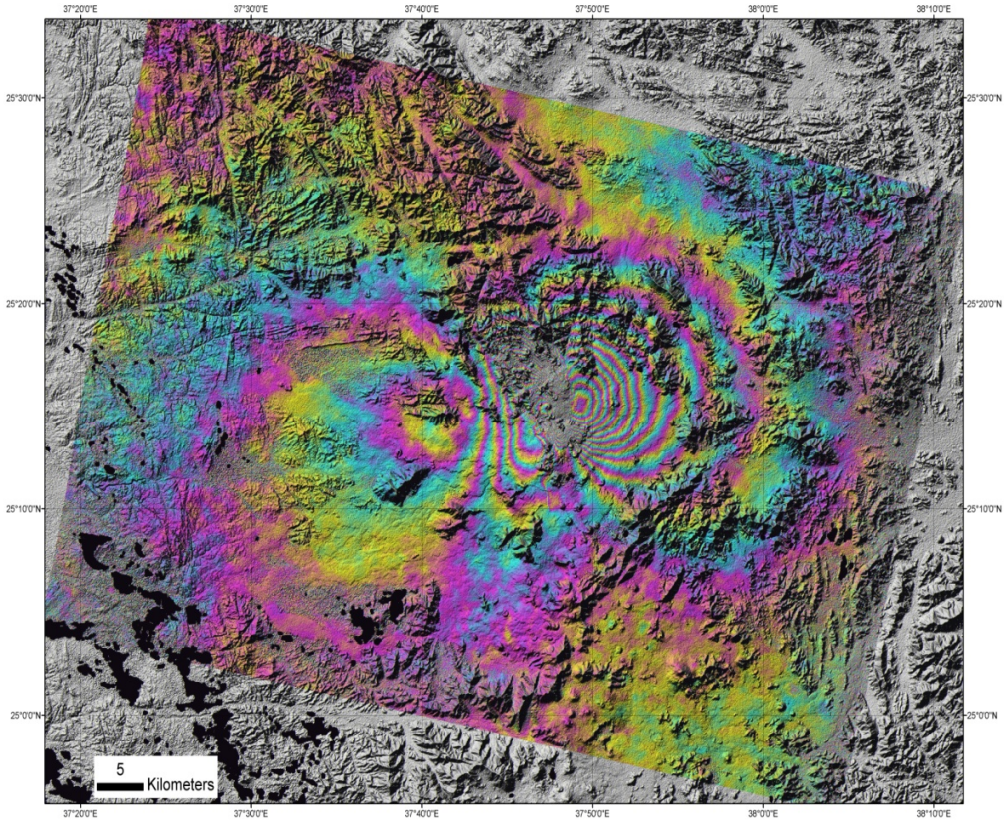

In SAR Over Hill Shade

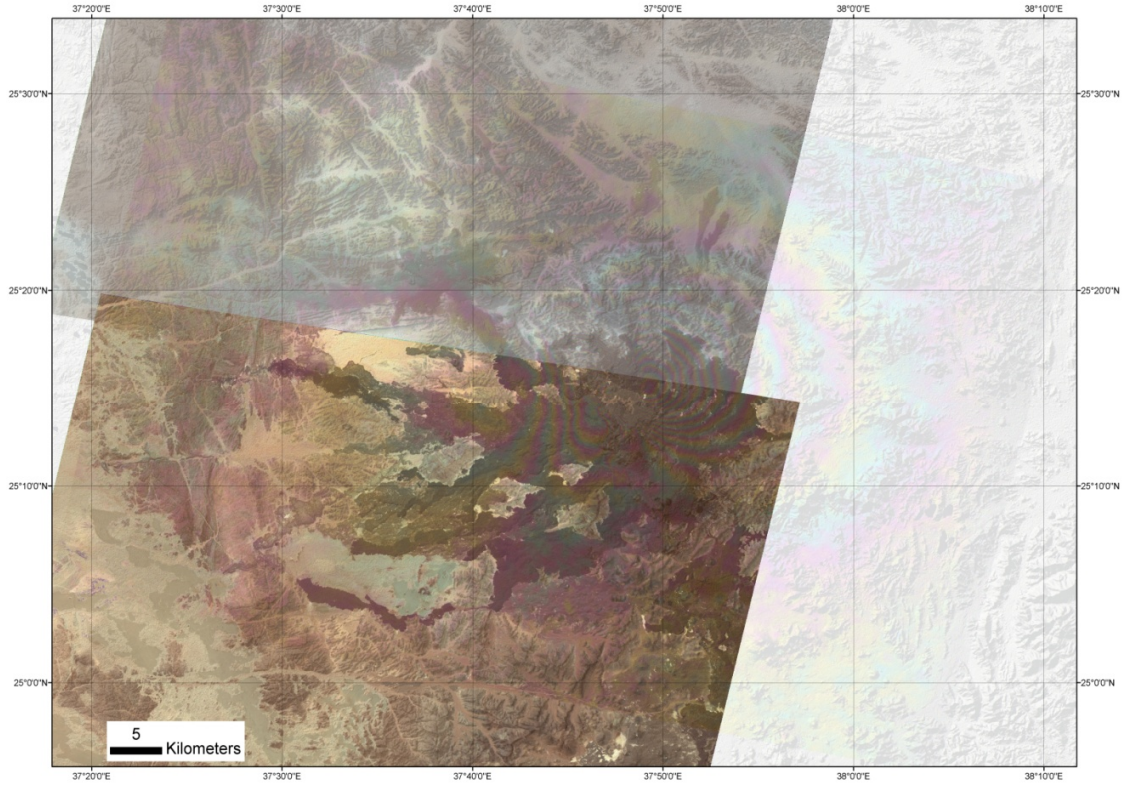

In SAR Over Hill Shade Over ASTER

Observed Inteferogram over Google Earth image

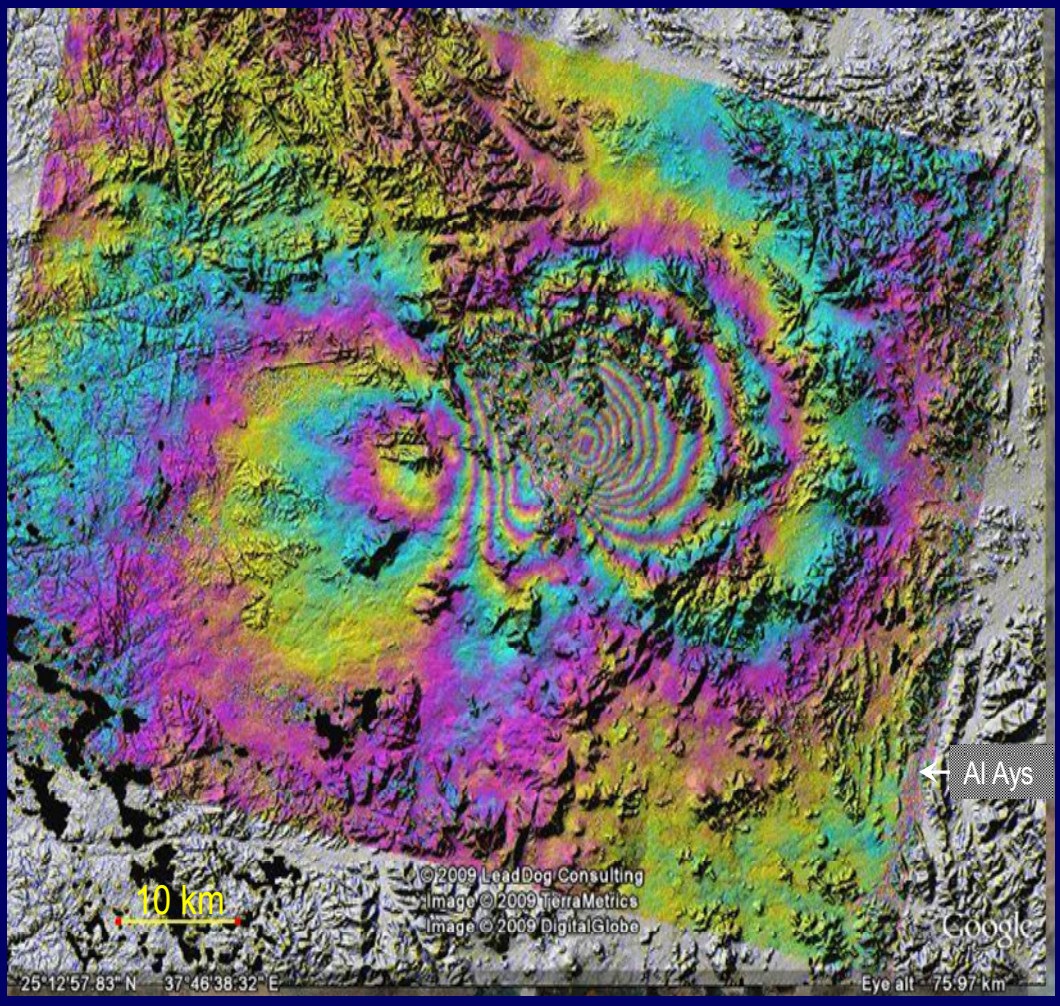

USGS Flip back and forth with previous image to better locate ground features

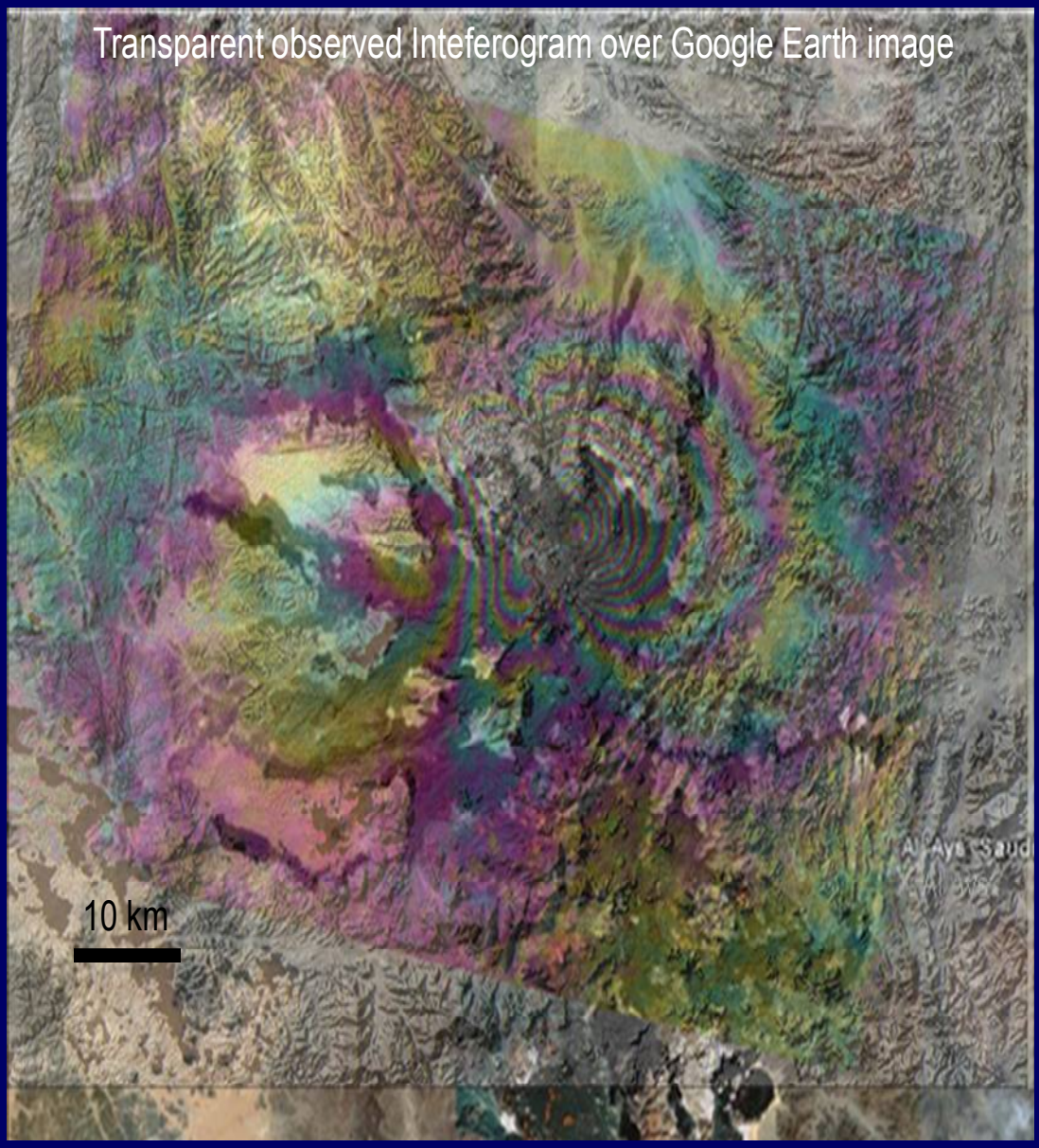

USGS Flip back and forth with previous image to better locate ground features

Observed

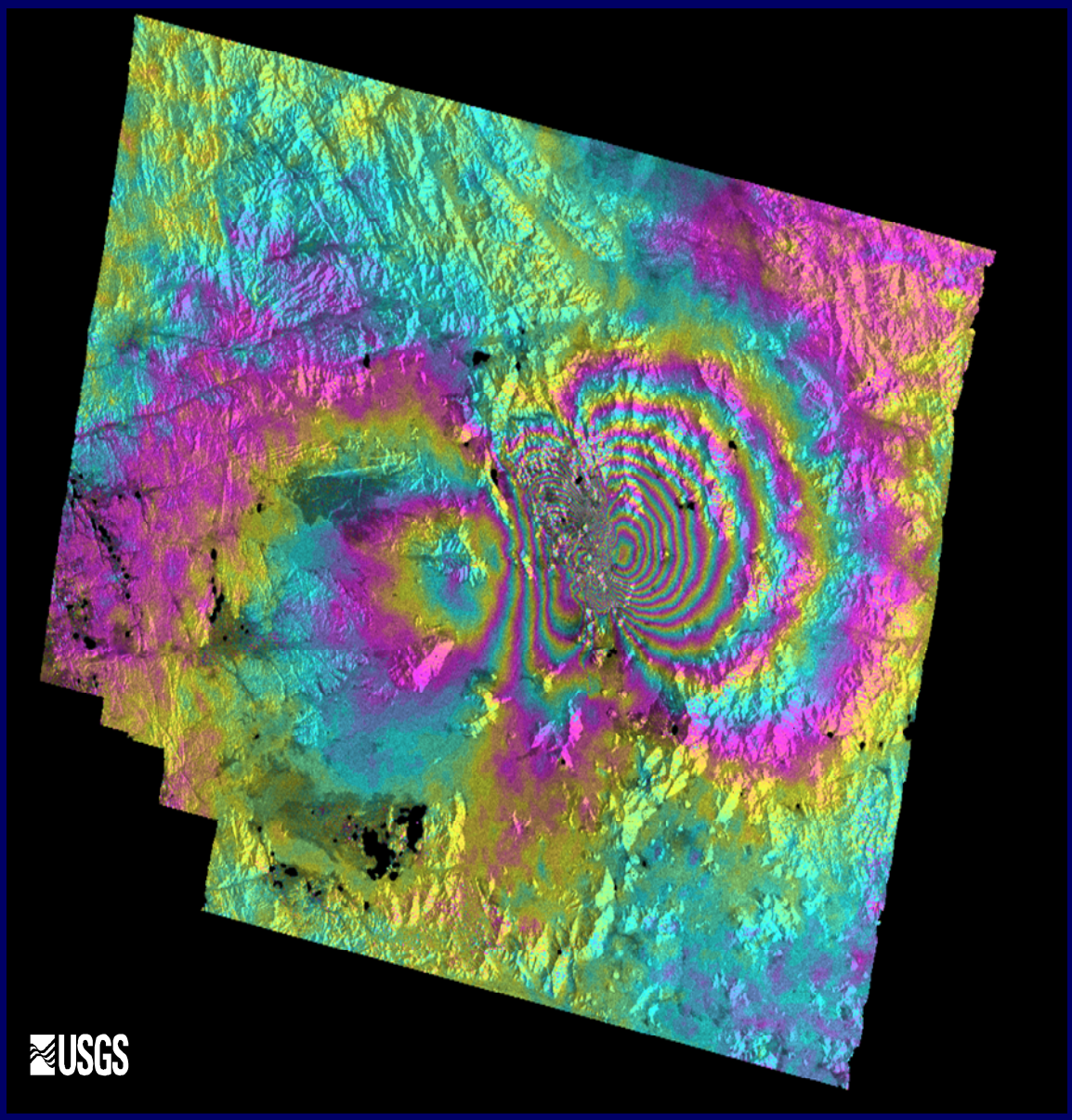

Residual

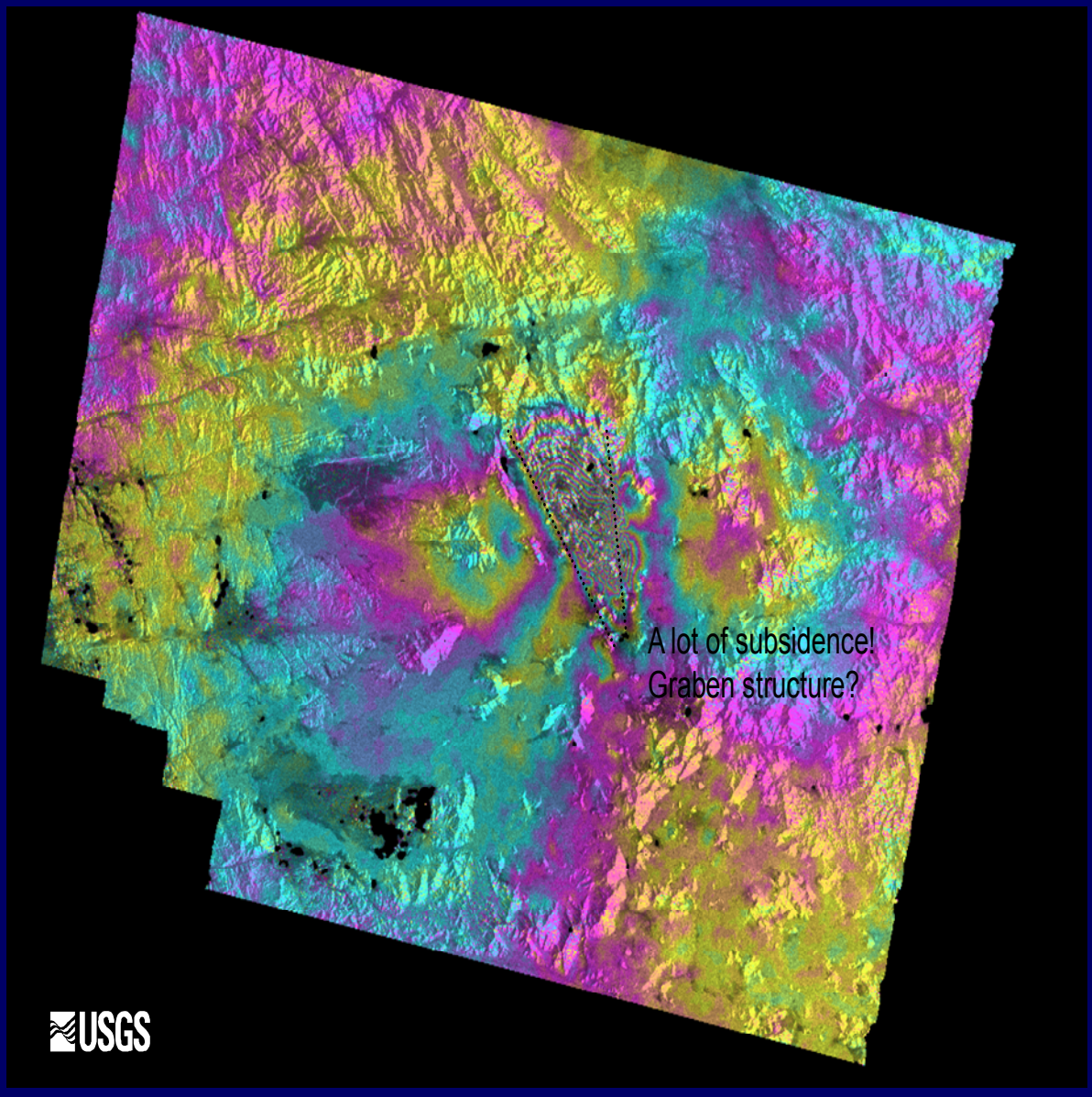

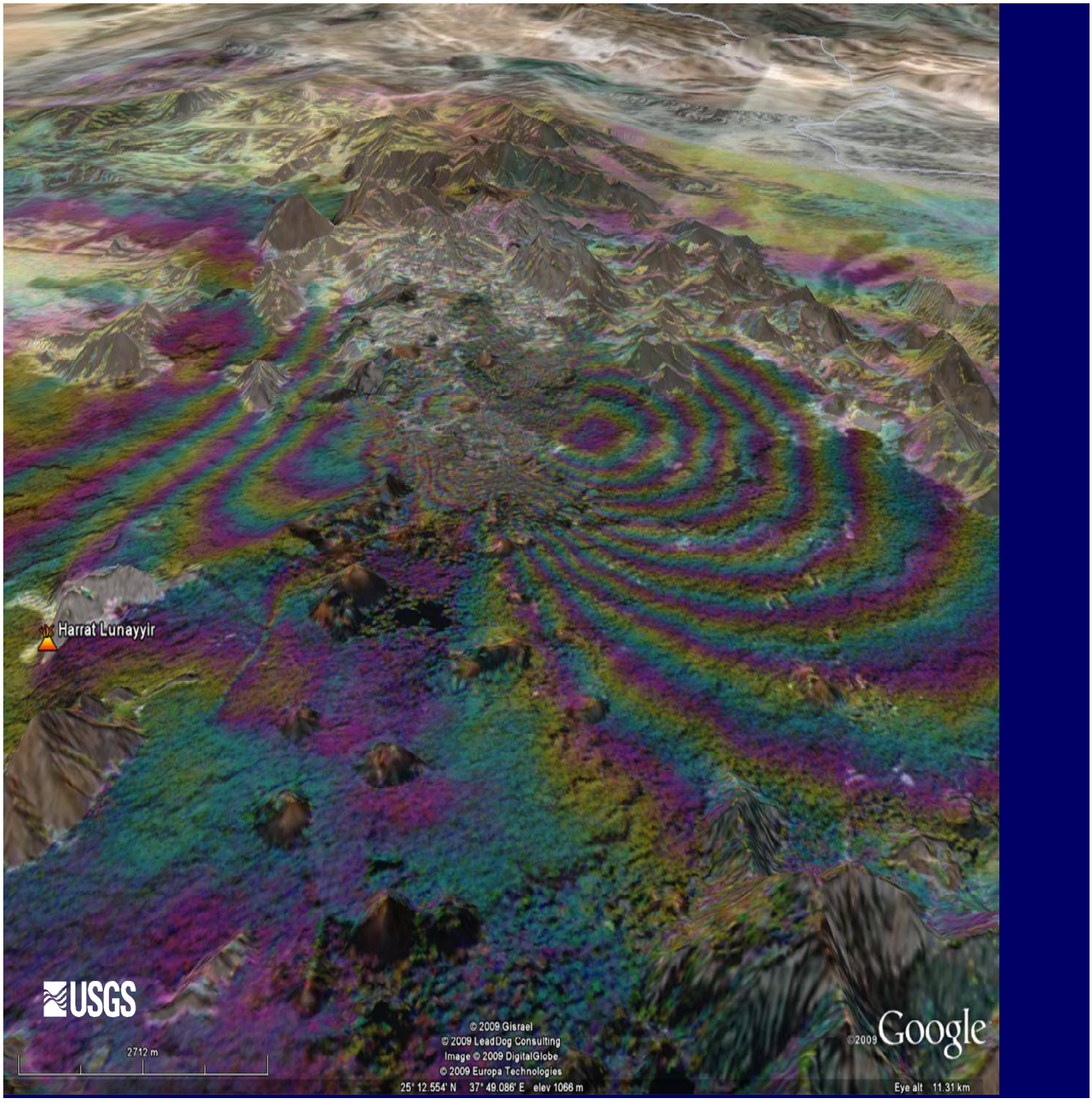
Harrat Lunayyir
USGS
2712 m
© 2009 Gisrael
© 2009 LeadDog Consulting
Image © 2009 DigitalGlobe
© 2009 Europa Technologies
25° 12.554' N 37° 49.086' E elev 1066 m
©2009 Google
Eye alt 11.31 km

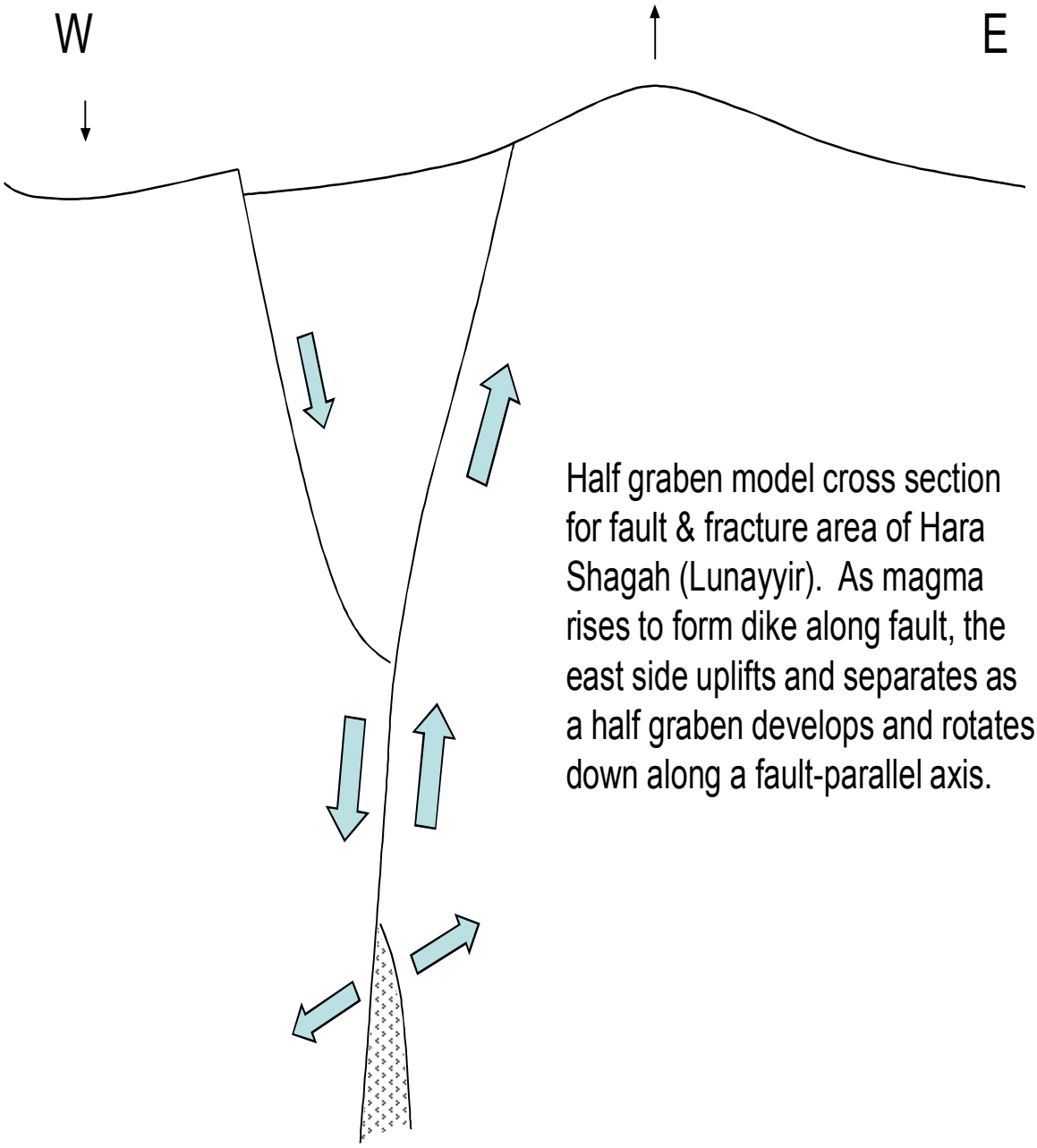

Half graben model cross section for fault & fracture area of Hara Shagah (Lunayyir). As magma rises to form dike along fault, the east side uplifts and separates as a half graben develops and rotates down along a fault-parallel axis.

Deformation Monitoring with Radar Interferometry: How it works

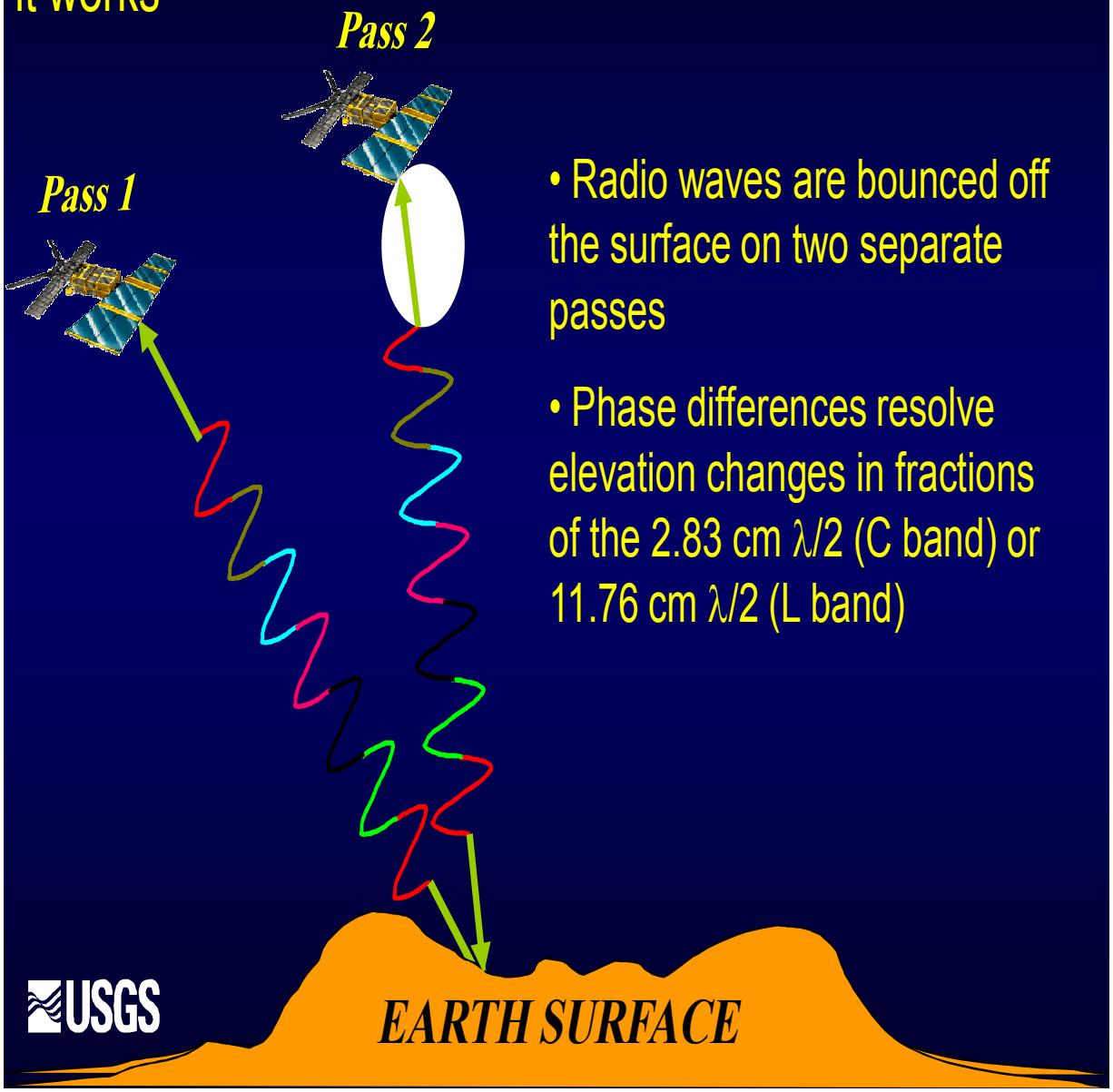

- Radio waves are bounced off the surface on two separate passes
- Phase differences resolve elevation changes in fractions of the 2.83 cm $\lambda/2$ (C band) or 11.76 cm $\lambda/2$ (L band)

الشقوق الحديثة الناتجة عن النشاط الزلزالي الحالي

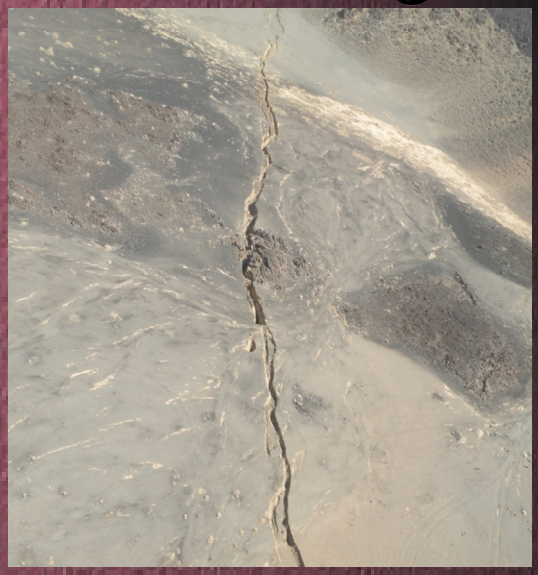

Modeled

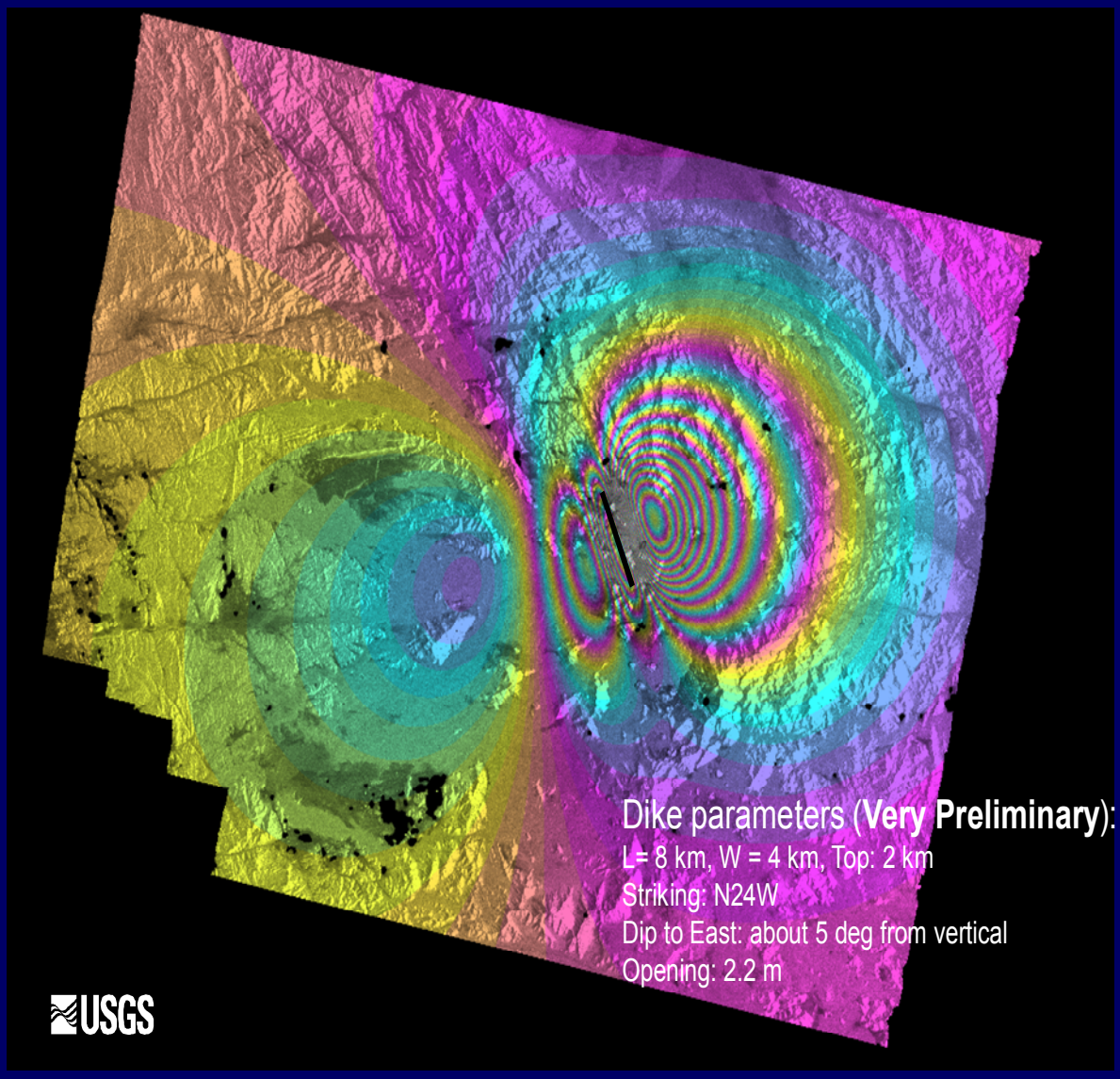
Dike parameters (**Very Preliminary**):
L= 8 km, W = 4 km, Top: 2 km
Striking: N24W
Dip to East: about 5 deg from vertical
Opening: 2.2 m
USGS